Università degli Studi di Milano – Bicocca

Facoltà di Scienze Matematiche, Fisiche e Naturali

Doctorate in Materials Science – XXIV cycle

A Combined Computational and Experimental Study of Spectroscopic Evidences by Dopants and Defects in Semiconducting and Insulating Oxides

Ph.D. Dissertation of

Federico Gallino

Thesis presented for the degree of *Doctor Europaeus*
and
For the degree of *Doctor Europaeus* in *Materials Science* of the Network *Physics and Chemistry of Advanced Materials* (PCAM)

Supervisor	*Dean of the Doctorate*
Dr. Cristiana Di Valentin	Prof. Gian Paolo Brivio
External Supervisor	*PCAM Chairman*
Dr. Yuemin Wang	Prof. Gian Paolo Brivio

A.A. 2011/2012

Dedicated to
Giorgia

Acknowledgments

My first and deeply-felt thanks are for Dr. Cristiana Di Valentin, my supervisor, guide and example throughout the course of the Doctorate. I will always be indebted to her for the teaching, the encouragement and the support in difficult times at work and in life.

I would like to express my acknowledgements to Prof. Gianfranco Pacchioni for his wise advices and thoughtful discussions. It was a honour to join a research group of extremely high scientific level. My thanks go to all the members (present and past) of the Quantum Chemistry group of the Department of Materials Science for their scientific and human qualities and in particular to Dr. Livia Giordano, Dr. Gloria Preda, Dr. Stefano Prada, Dr. Umberto Martinez and Dr. Fenggong Wang.

The work presented in this thesis is largely based on a collaboration with the group directed by Dr. Yuemin Wang in the Department of Physical Chemistry I, Ruhr University Bochum. I am extremely grateful to Dr. Yuemin Wang for the opportunity to join his group during my six-months-stay in Bochum. I would like to thank him for the supervision, the precious and numerous discussions, and his lectures that have extended my scientific knowledge also to an experimental expertise. I would like to express my gratitude to all the members of the Department of Physical Chemistry I for the kindness and stimulating working atmosphere and in particular to Dr. Hengshan Qiu and Dr. Lanying Jin. My special thanks to Dr. Heshmat Noei, a friend more than a colleague. I want to thank the Department of Physical Chemistry I for financial support of my stay in Bochum.

During my Ph.D. I had also the opportunity to continue a fruitful collaboration with the experimental group of Prof. Elio Giamello of the University of Turin, from where my scientific research started with my Master Degree. I would like to express my gratitude to all the group, and in particular to Prof. Elio Giamello and Dr. Mario Chiesa, for the exciting joint research and for having introduced me to the Quantum Chemistry group of Prof. Gianfranco Pacchioni.

I am indebted to Prof. Gian Paolo Brivio for the skilful organization of the Doctorate Programme and for the opportunity to work in a stimulating European Universities network.

I would like to thank the PCAM Research Training Program and the CARIPLO Foundation for supporting my stay in Bochum and for the financial support through an Advanced Materials Grant 2009 ("*Development of second generation photocatalysts for energy and environment*").

Last but not least, I wish to thank my parents and my sister for the constant and infinite support. This work would not have been possible without their presence and helpfulness.

Contents

PART I

OVERVIEW AND BACKGROUND TOPICS

CHAPTER 1

Introduction

1.1 Metal Oxides and Defects

Metal oxides represent a class of ceramic materials with an extraordinary range of applications due to their variety, their chemical stability and their numerous fascinating chemical and physical properties involving bulk and surface layers. Piezoelectricity, superconductivity, magnetism, acid-base and redox properties are some of the characteristics that point metal oxides as valuable and reliable materials for technological applications ranging from transparent conductors to gas sensors, to optoelectronics and spintronics devices, to fuel cells and heterogeneous catalysts [1,2,3,4,5]. Metal oxides include insulators (*e.g.* MgO), metals (*e.g.* V_2O_3 and Re_2O_3), wide-band gap and narrow-band gap semiconductors (*e.g.* TiO_2 and Ti_2O_3, respectively) and even superconductors since the discovery of high-temperature superconductivity in copper oxide based materials [6]. Among metal oxides the alkaline-earth oxides *Ae*O represent typical ionic crystals, insulating and crystallizing with the NaCl crystal structure at normal conditions. The class of transition metal oxides (TMO) shows, instead, the widest range of electronic

properties because of the incomplete filling of the d shells. The variety of crystal structures and the variation in the spin, charge and orbital states resulting from the presence of d electrons explain the large diversity in the electronic properties and the potential applications of these materials. Recently S. F. Matar *et al.* [7] proposed a simple method based on the electronegativity, χ, [8,9] and the chemical hardness, η, [10,11] to predict the electronic and chemical properties of metal oxides. According to this scheme oxides can be grouped in four classes as represented in Figure 1.1.

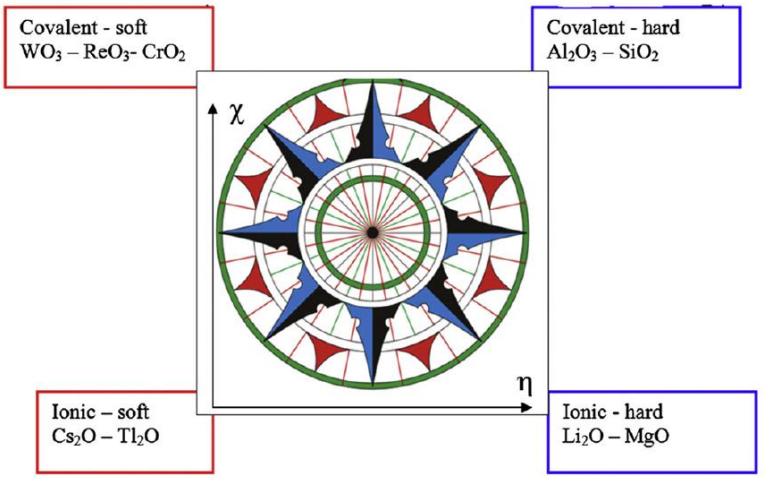

Figure 1.1. Subdivision of metal oxides in classes using the χ-η map approach as proposed by Matar *et al.* [7]. Courteously reproduced from Ref. [7].

The main goal of scientists is to understand the origin of metal oxides properties in order to learn how to manipulate and tune them through the modification of stoichiometry and crystal structure and/or through the introduction of defects. Defects and impurities, in particular, often play a crucial role in determining the properties of the materials. In semiconductors the incorporation of small amounts of impurities determines the electrical conductivity [12], dilute concentrations of magnetic defects may induce ferromagnetism in otherwise non-magnetic materials [13], and the presence of impurities or vacancies on oxide surfaces can severely affect the chemical (sensing [14] and catalytic [15,16]) properties of the solid. Defects such as vacancies and interstitial atoms mediate dopant diffusion in microelectronic devices [17,18], affect the performance of photo-active devices [19], and the efficiency of devices for converting sunlight to electrical power [20]. The

nature and the type of defect states, the degree of non-stoichiometry, the anisotropy and the broad range of the resulting properties of the doped-material pave the way to fascinating possibilities and new physics of metal oxides. The richness and variety of the metal oxides research field demand an interdisciplinary approach and have recently favoured the birth of various forms of *defect engineering*, aimed at controlling defect behavior within the solid [21]. However, despite the worldwide interest and effort of the scientific community, even in the case of apparently simple oxide systems, it has not yet been possible to reach a general consensus on many defect related issues and so far, with a few exceptions, the properties of metal oxides are still poorly known and under-exploited in comparison with metals.

In the vast context of the doped and defective metal oxide properties, the present introduction is restricted to well-defined themes, which have been addressed in this thesis and are subject of increasing interest in literature.

1.1.1 Electrical Properties

In general, impurities and defects may be divided in deep and shallow defects depending on whether they create localized states located in the band gap, or resonate within the continuum of the host bands (valence or conduction band), respectively. For example, a defect state located within the gap and below the conduction-band minimum (CBM) is observed for hydrogen in MgO [22] or oxygen vacancies in Al_2O_3 [23] while a defect state located above the CBM is found for hydrogen in ZnO [24] and oxygen vacancies in In_2O_3 [23].

Shallow impurities induce bound states in the optical gap very close to the band edges and their electronic properties are described by a hydrogenic model, *i.e.* the effective-mass theory (EMT) [25,26]. The electron (or hole) in a shallow state that is resonant with the host band, will drop to the band edge and occupy a perturbed-host state (PHS [27,28]) rather than the defect level. It can therefore be treated as independent of all other electrons of the system and it is weakly bound by the screened long-range Coulombic tail of the impurity potential, $-e^2/\varepsilon r$ (where ε is the dielectric constant of the crystal). The calculated binding energy from the nearest band edge is less than 0.1 eV and the effective Bohr radius is significantly large compared with the interatomic distance. Shallow defects determine the electrical conductivity of the material that can be of *p*-type (holes as free carriers) or *n*-type (electrons as free

carriers) depending on whether the defects are acceptors or donors, respectively.

Conversely, deep defects induce states within the band gap and well-separated from band edges, strongly bound essentially by the short-range part of the defect potential. Deep level states can act as recombination (or killer) centres or as traps, limiting therefore the lifetime of carriers. Deep defects create levels described by localized wave functions and even if they are occupied, they usually do not contribute to the conductivity due to the localized nature of the state and the high activation energy. Deep defects are also expected to respond only weakly to external perturbations such as pressure or temperature. The theoretical description of these impurities has been a major challenge, also because they require relaxation of the unperturbed host crystal around the defect.

The accurate control of the conductivity in metal oxides represents a fundamental issue. In semiconductors, in particular, the incorporation of a relatively small concentration of native point defects and impurities (down to 10^{-14} cm^{-3} or 0.01 ppm) can significantly affect the electrical and optical properties of the system [29]. The achievement of good bipolar (*p*-type and *n*-type) conductivity in semiconductors is a prerequisite for the design of almost all the electronic and optoelectronic devices. However, most materials exhibit an asymmetry in their ability to be *n*-type or *p*-type doped (see Fig. 1.2). For example, ZnO is a good *n*-type conductor via intrinsic or extrinsic dopants but, so far, it has not been possible to achieve a significant and reliable *p*-type doping [30,31].

The difficulties and limitations in doping of semiconductors are related to many factors: low solubility, compensation by low-energy native defects, deep impurity levels, and structural bi-stability known as *AX* and *DX* centres [32]. The solubility is the maximum concentration that the impurity can attain in the material under thermodynamic equilibrium. An increasing amount of the impurity (higher chemical potential) does not necessarily imply a higher concentration of impurities incorporated in the material because they can precipitate in other phases (*i.e*. metal clusters, other metal oxides). However the main obstacle to an effective doping is the compensation by native point defects or foreign impurities. Finally, even if the material is successfully doped, a maximum dopant concentration limit exists, known as *doping limit*. In particular, it has been proved [33] that the capacity to dope a material is related to the position of the valence band maximum (VBM), ε_{VBM}, with respect to a phenomenological *p*-like pinning energy, ε^{p}_{pin}, and to the position

of the conduction band minimum, ε_{CBM}, with respect to a *n*-like pinning energy, ε^{n}_{pin}. A material with $\varepsilon^{n}_{pin} \ll \varepsilon_{CBM}$ cannot be doped *n*-type while a material with $\varepsilon^{p}_{pin} \gg \varepsilon_{VBM}$ cannot be doped *p*-type.

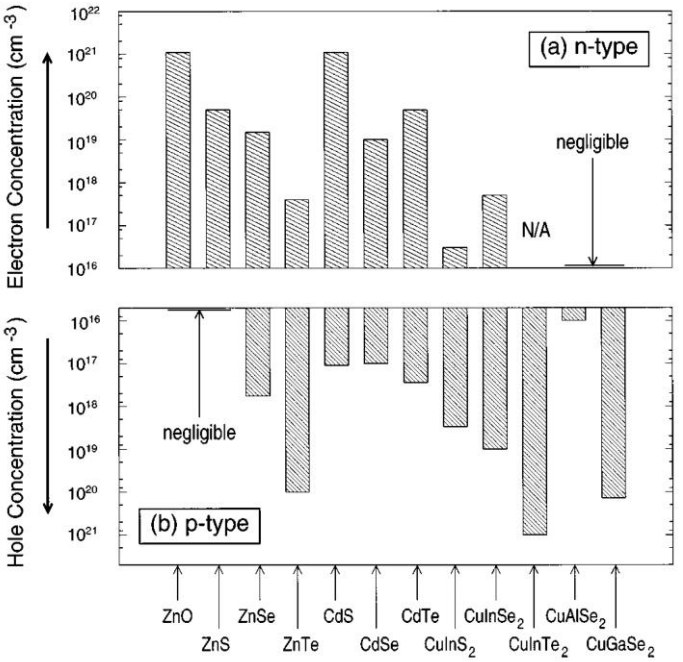

Figure 1.2. Experimental maximum carrier concentrations for a) *n*-type and b) *p*-type doping of various semiconductors as reported in Ref. [34]. N/A means no data are available. Courteously reproduced from Ref. [34].

1.1.2 Band-Gap Engineering

The successful application of semiconducting oxides also depends on the possibility of band-gap engineering. In particular, over the last decade an outstanding effort has been made by the scientific community in designing new strategies for improving the harvesting of solar light and its conversion into other forms of energy or chemical reactivity (water splitting [35,36] or organic decomposition [37,38]), through band gap electron-hole excitation in semiconducting metal oxides. In photo-electrochemical applications, for example, the light is either absorbed by the semiconducting material, or the latter behaves as an electron conductor for electrons injected from dye molecules, which are adsorbed on its surface (*i.e.* in dye-sensitized solar cells).

In both cases, the exact position of the band edges play a decisive role for the efficiency of the process. In the case of the dye-sensitization, the CBM has to match the lowest excited state of the dye molecule to enable effective electron transfer. If the CBM is too high in energy (*i.e*. higher than the excited state of the dye molecules), electron injection from the dye into the conduction band is unsuccessful.

A good deal of effort has been devoted to lowering the threshold energy for excitation [39,40,41,42,43]. Much work has been performed to refine convenient and efficient synthetic procedures to dope or functionalize semiconductor samples of various nature (single crystals, powders, nanocrystals, thin films, and nanotubes). In particular, nanocrystals present a broader range of parameters that can affect their electronic band gaps in comparison with bulk semiconductors [44]. In Figure 1.3 some of these parameters are reported, including size, shape, and composition.

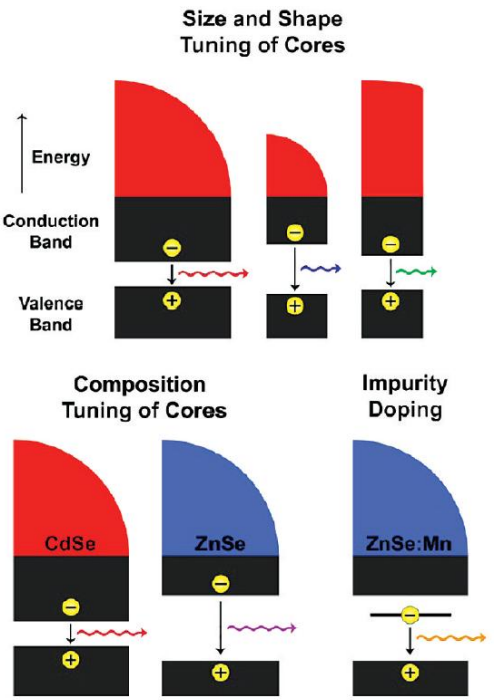

Figure 1.3. Some of the parameters affecting the band gap of semiconductor nanocrystals (specifically: size and shape, composition and impurity doping). Courteously reproduced from Ref. [44].

1.1.3 Magnetic Properties

The opportunity to introduce spin functionality (*i.e*. ferromagnetism / spin polarization) in nonmagnetic oxide systems through doping with magnetic impurities has recently fired up the scientific community to look for effective and reliable diluted magnetic semiconducting oxides (DMSO) [13]. In particular, the insertion of homogeneous and dilute (a few percent) concentration of a magnetic dopant can ensure that the original set of properties of the undoped material could remain almost unaffected, thereby exploiting the best of both fields (*i.e*. optoelectronics and spintronics).

In order to design an effective DMSO, the dopant has to possess three prerequisites, and specifically it has to (i) carry a magnetic moment in its stable charge state [45,46], (ii) exhibit ferromagnetic coupling between the other dopants within a certain range of magnetic interaction, and (iii) have a thermodynamic solubility above the percolation threshold [45,47].

The research activity on DMSO is mainly focused on two wide band gap *n*-type metal oxides, namely TiO_2 and ZnO and was originally prompted by the observation of ferromagnetism in diluted Co-doped TiO_2 [48] and Mn-doped ZnO [49] (see Fig. 1.4).

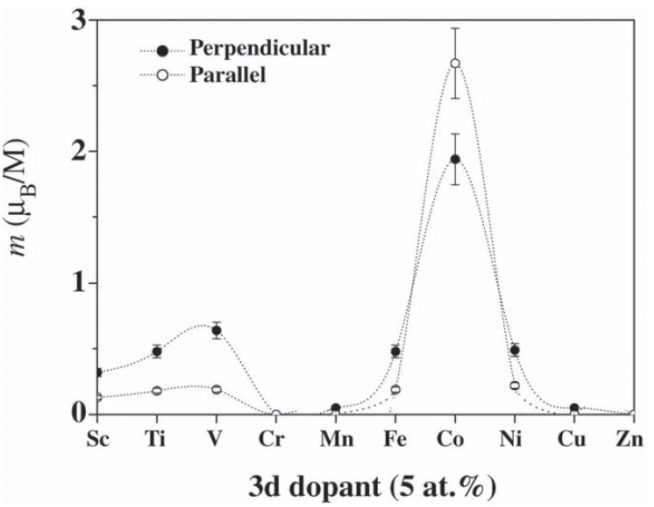

Figure 1.4. Measured magnetic moment of M-doped ZnO films at room temperature, with M representing first-row transition metals. Solid circles represent data for the field applied perpendicular to the film plane and open circles represent data for the field applied in the plane of the film. The moment is expressed as μ_B/M. Courteously reproduced from Ref. [50].

Despite the numerous works and the significant advances in the field, several issues are still under debate in literature [13]. In particular, the reliability of experiments is still unsatisfactory, mainly because of the difficulties in obtaining uniform doping and avoiding clustering which are highly affected by the doping methodology and the experimental conditions. In addition, the magnetic interaction mechanism is still far from being undoubtedly proved. In fact, the conventional mechanism of ferromagnetic exchange working for bulk ferromagnets (*e.g.*, magnetite, maghemite, ferrites) cannot be applied to DMSO. Since magnetic dopants are in a diluted concentration in the system, the mean separation between neighbouring dopants is so large that the ferromagnetism is *carrier*-mediated. In this context, different mechanisms are possible and have been suggested, including the presence of itinerant carriers (RKKY), polarons, F-centres, etc. [13]. This lack of comprehension has triggered several theoretical studies aimed at creating new models of ferromagnetism and at directing experimental works [51,52]. However, initial expectations were not fulfilled by actual results and theoretical groups showed a substantial disagreement even on the qualitative results. In a recent work, Zunger *et al.* [53] questioned the reliability of the reported theoretical predictions pointing at the severe limitations of pure density functional theory approximations in correctly and accurately describing band gap values and spin localization, both essential components when investigating transition metal doped semiconductors. Anyway, so far the field remains equally controversial on the theoretical front as on the experimental side.

1.2 Background of the Present Study

The most promising and powerful approach to study defects in metal oxides is a joint use of highly sophisticated experimental and modelling techniques [54,55,56,57].

Computer modelling is a valuable tool in solid-state and material science since it effectively complements experimental evidences by providing an atomistic insight in complex materials and processes. Ab-initio electronic structure methods, that do not depend on system-specific parameters, play a crucial role not only in the interpretation of existing experimental data, but also in directing new experimental efforts. Unfortunately, no universal quantum-mechanical method exists that is suitable for all materials and

phenomena but a hierarchy of computational techniques facing the compromise between accuracy and efficiency is available (see Fig. 1.5).

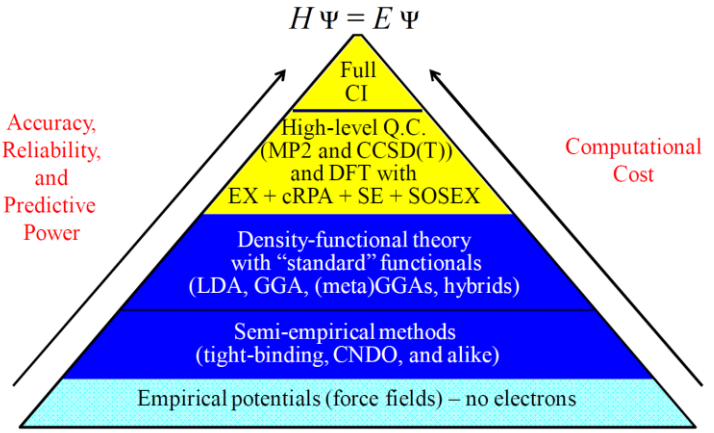

Figure 1.5. Ladder of the state of the art of the electronic structure theory methods as a function of accuracy, reliability, predictive power and computational cost. Courteously reproduced from Ref. [58].

In the next Chapter we will show that in the framework of the density functional theory (DFT), the methods are distinguished on the basis of their approximation of the exchange-correlation (XC) energy. No method is able to accurately describe all the properties of the system under consideration. Therefore the choice of the computational approach will depend on the system, on the properties analyzed, and on the compromise between accuracy and computational costs. We will show that for the description of the oxides properties under investigation in this study, a good compromise between accuracy and computational expense is achieved by the hybrid B3LYP functional [59,60].

In conjunction with advanced and effective experimental techniques such as electron paramagnetic resonance spectroscopy (EPR), high resolution electron energy loss spectroscopy (HREELS) and ultra-high vacuum Fourier transform infrared spectroscopy (UHV-FTIR), we have been able to provide a detailed and atomistic description of a number of open issues concerning the chemistry and physics of doped metal oxides. EPR spectroscopy is a powerful tool for identifying and characterizing paramagnetic entities and it has been successfully applied in continuous wave (CW) and pulsed experiments on polycrystalline materials in the group of Prof. E. Giamello (University of

Turin, Italy). HREEL and UHV-FTIR spectroscopies have been effectively used in the group of Dr. Y. Wang (Ruhr University of Bochum, Germany) to investigate vibrations and electronic excitations of both bulk and surface species on well-defined single crystal surfaces and powder samples.

During my Doctorate, besides my computational research under supervision of Dr. C. Di Valentin (University of Milan-Bicocca, Italy), I had also the opportunity to achieve direct experience of these experimental techniques by performing EPR measurements in the group of Prof. E. Giamello and HREELS experiments in the group of Dr. Y. Wang within the Physics and Chemistry of Advanced Materials (PCAM) European Doctoral Programme.

In order to optimize the doping strategies and to address a number of open issues, we have therefore been able to provide an atomistic description of dopants and defects in metal oxides through a combined and multidisciplinary approach. The tight connection between quantum-chemical methods, using sophisticate theoretical tools for probing structure and property relationships, and advanced experimental techniques yields invaluable information on the oxides properties affected by defects. In the following a brief introduction to the properties investigated in this work is reported.

1.2.1 Investigated Properties

Defects and impurities incorporated in metal oxides often modify the electronic structure of the system. A description of the electronic structure modifications can be provided by theoretical methods. In particular, in the density functional theory framework the defect levels can be approximated to the corresponding single-particle Kohn-Sham eigenvalues and their position in the material gap and dispersion in the *k*-space are commonly investigated through the density of states and the band structure analysis. A good reproduction of the experimental band gap is an essential pre-requisite to identify the correct position of defect states. However, orbital-independent density functional theory approximations [local density approximation (LDA) and generalized gradient approximation (GGA)] show severe limitations in correctly and accurately describing band gap values. A practical, although not perfect, solution is represented by hybrid exchange-correlation functionals having positive effects on both the reliability of the computed defect energetics and spin localization [61]. The electronic structure can be experimentally investigated by a number of spectroscopies using electrons of

various energies as well as photons in the x-ray or ultraviolet-visible energy ranges. For example, electron energy loss experiments provide information about the gap states, the position and the shape of the deep level absorption thresholds, while photon spectroscopies (*e.g.*, XPS and UPS) describe the valence band shape and/or the core level positions. Angle-resolved UPS experiments allow the band dispersion to be plotted along high-symmetry lines of reciprocal space (*e.g.*, MgO [62], SrTiO3 [63], TiO2 [64,65]) that is directly comparable with the computed band structure. However, the single-particle description of energy levels introduced in the gap by defect centres is not well justified if electronic transitions are involved between different defect charge states. A better approximation is provided by the transition energy levels that are directly comparable with spectroscopic evidences (*e.g.*, ionization energy and photoluminescence emission) [66,67,68]. One of the major and more original contributions of this work of thesis is the development of an approach to compute the transition energy levels using the CRYSTAL code [69,70,71] for periodic calculations based on Gaussian atomic functions. This approach introduces a large simplification in the calculation of the transition energy levels by an efficient use of the Janak's theorem [72].

An impurity can enter in the host lattice in different positions (*i.e.*, substitutional to a cation or anion, interstitial) and in different concentrations (*i.e.*, isolated atom or small cluster of atoms). A thorough theoretical description of the relative stability of the various conceivable models provides key information for experimentalists for the identification of effective doping mechanisms or for determining the favourable conditions to achieve the desired doping. The thermodynamics of defects is here addressed in terms of (zero-temperature) formation energies that are functions of the total electronic energies. In principle the free Gibbs energies should be considered, however the use of the total electronic energies is justified by the small contributions from vibrational entropy, that are estimated typically in the range between 0 and 10 k, where k is the Boltzmann constant [68]. The plot of formation energies of the various defects as a function of the oxygen chemical potential, that can be expressed also in terms of oxygen partial pressure, is a valuable information for experimentalists to check the most stable impurity in the adopted experimental conditions or to find out the best doping conditions to obtain the desired impurities. Finally, the evaluation of the formation energy at different Fermi levels allows to determine the most stable charge state of the defect.

If the impurity carries unpaired electron(s), it is a paramagnetic centre and

can be investigated by electron paramagnetic resonance. This powerful technique is strongly connected to quantum chemistry, since it provides an experimental tool to measure the wave function of the unpaired electron(s). A careful comparison of computed and measured electron paramagnetic resonance parameters (*i.e.*, *g*-tensor, hyperfine coupling constants and quadrupole coupling constants) provides an unambiguous assignment of the paramagnetic impurity.

The interaction of these centres can result in collective magnetic interactions, *e.g.* ferromagnetism. The latter is here investigated in terms of total energy differences of the ferromagnetic and the antiferromagnetic states for diluted defect concentrations. A number of configurations with impurities at different distance is addressed. Hybrid exchange-correlation functional is adopted to overcome the limitations of local and semilocal functionals in describing strongly localized unpaired charge carriers.

Finally, the adsorption of small molecules on metal oxide surface is investigated in terms of adsorption energies and vibrational frequencies. The identification of how the species adsorb on a specific surface can be achieved only through a combined experimental and computational study. The use of infrared spectroscopy on polycrystalline sample provides a preliminary information about the possible species forming on all the available metal oxide surfaces. The comparison with the frequencies observed on a precise single crystal surface, through high-resolution electron energy loss spectroscopy (HREELS), and with the computed frequencies, obtained for a density functional theory model, yields an unambiguous assignment of the IR bands. The various coverage phases are investigated by means of thermal desorption spectroscopy (TDS) and their relative adsorption enthalpies are compared with the computed electronic binding energies corrected for vibrational contributions. In this way a complete picture of the reactivity of the surface towards gaseous molecules is provided.

1.2.2 Structure of the Thesis

The main objective and the major value of this work is to provide a combined setup of theoretical and experimental techniques to simulate and measure a number of properties altered and/or induced by defects in three representative and technologically relevant oxides: zinc oxide (ZnO), zirconium dioxide (ZrO_2) and magnesium oxide (MgO).

Zinc oxide and zirconium dioxide are wide-gap semiconductors with a vast set of technological applications generally related to the inclusion of defects and impurities and spanning from optoelectronics to spintronics devices and photocatalysis. They are the subjects of Part II and Part III, respectively. A detailed description of their structure and chemical-physical properties is provided in the respective background sections.

Part II deals with the main subject of this work: bulk and surface zinc oxide properties.

After synthesis, ZnO commonly presents *n*-type conductivity and in Chapter 3 some of the most common donor defects (specifically: hydrogen interstitial and substitutional to oxygen, zinc interstitial and oxygen vacancy) have been investigated in terms of thermodynamic and optical transition energy levels. The good agreement with existing experimental data provides a powerful validation of the computational method presented in Sec. 2.1.5.1.

In Chapter 4 copper doping of ZnO has been analyzed under different perspectives, spanning from the presence of donor and acceptor states, to magnetic interactions, to cluster tendency and to the interaction with oxygen vacancies. In particular, in conjunction with HREELS experiments, for the first time the inclusion of copper donor impurities in bulk ZnO has been observed which, on the basis of our calculations, we have assigned to interstitial copper species.

In Chapter 5, the most promising shallow acceptor candidate for *p*-type doping of ZnO, *i.e*. nitrogen substitutional to oxygen, is investigated. First, nitrogen has been observed in polycrystalline sample and characterized in terms of hyperfine and quadrupolar coupling constants through a combined EPR and theoretical study. Secondly, the nitrogen doping process has been analysed upon the sputtering with ammonia of the mixed-terminated ZnO $(10\bar{1}0)$ surface through TDS experiments. The effectiveness of the doping process and the fundamental role of post-treatment oxidation were proved. The defective states within the optical gap have been estimated using HREELS measurements with a 66 eV electron primary energy. The computation of the transition energy levels have then demonstrated that nitrogen acts as a deep acceptor species in ZnO, disappointing the hopes to achieve *p*-type conductivity through nitrogen-doping.

In order to get more insight in the nitrogen doping mechanism, the reactivity of ZnO single crystal and powders towards ammonia has been addressed by a combined theoretical and HREEL and UHV-FTIR study, in

Chapter 6. Different coverages have been considered and, while at low concentration only molecularly adsorbed species have been observed, at a full monolayer coverage the repulsive steric interactions between adsorbates have been shown to induce the formation of an ordered adlayer with (2 x 1) periodicity, presenting alternating molecular NH_3 and singly deprotonated NH_2 moieties adsorbed on cationic sites.

Part III is focused on ZrO_2, specifically the tetragonal polymorph which is commonly stabilized by impurities. In particular, here the interest is related to the titanium doping of the material, which was experimentally found to induce a large red shift of the optical absorption edge. In Chapter 7 we proposed a rationalization of this experimental observation based on the computation of the optical transition levels of Ti species. The possible interaction with oxygen vacancies has also been considered.

In Part IV the nitrogen doping of MgO, recently proposed as potential route to achieve room temperature ferromagnetism has been investigated. This work was divided in two parts.

In Chapter 8 the electronic structure and the spin properties of nitrogen impurities have been theoretically studied, considering also possible charge transfers with magnesium or oxygen vacancies.

Finally, in Chapter 9 we show how a trapped N_2^- radical anion in the polycrystalline material has been identified and characterized through a combined EPR and DFT study.

CHAPTER 2

Methods

2.1 Computational Methods

2.1.1 The Schrödinger Equation

Quantum mechanical simulations of a solid with N electrons and M nuclei is based on the solution of the many-body (time-independent) Schrödinger equation:

$$\mathbf{H}_{\text{tot}}\,\Psi(R_1,\ldots R_M\,;r_1,\ldots r_N) = E_{tot}\,\Psi(R_1,\ldots R_M\,;r_1,\ldots r_N) \tag{2.1}$$

where Ψ is the wave-function of the system associated to the energy E_{tot} and r and R are the spatial coordinates of electrons and nuclei, respectively. The total (non-relativistic) Hamiltonian operator, $\mathbf{H_{tot}}$, can be decomposed in kinetic and potential operators of nuclei and electrons:

$$(\mathbf{T}_{\text{e}} + \mathbf{T}_{\text{n}} + \mathbf{V}_{\text{ee}} + \mathbf{V}_{\text{en}} + \mathbf{V}_{\text{nn}})\Psi(\mathbf{R},\mathbf{r}) = E_{tot}\,\Psi(\mathbf{R},\mathbf{r}) \tag{2.2}$$

The exact solution of Eq. (2.2) provides all the physical-chemical properties of the system. Unfortunately, even for small molecules this equation is too complex to be solved and several approximations are needed. The most common assumption is to consider nuclear and electronic motions as independent in the *Born-Oppenheimer* approximation [73] because of the mass

difference of electrons and nuclei. The exact wave function Ψ can be written as an expansion in the complete set of electronic functions, $\Phi_\nu(\mathbf{R},\mathbf{r})$, with expansion coefficients, $\Lambda_\nu(\mathbf{R})$, being functions of the nuclear coordinates:

$$\Psi(\mathbf{R},\mathbf{r}) = \sum_\nu \Lambda_\nu(\mathbf{R})\Phi_\nu(\mathbf{R},\mathbf{r}) \tag{2.3}$$

$\Phi_\nu(\mathbf{R},\mathbf{r})$ are solutions of the *electronic Hamiltonian* $\mathbf{H_e}(\mathbf{R})$:

$$\begin{gathered}\mathbf{H}_e(\mathbf{R})\Phi_\nu(\mathbf{R},\mathbf{r}) = E_\nu^e(\mathbf{R})\Phi_\nu(\mathbf{R},\mathbf{r}) \\ \mathbf{H}_e = \mathbf{T}_e + \mathbf{V}_{ee} + \mathbf{V}_{en}\end{gathered} \tag{2.4}$$

In the *Born-Oppenheimer* and *adiabatic* approximations, where the form of the total wave function is restricted to one electronic surface, the Schrödinger equation becomes:

$$(\mathbf{T}_n + E_\nu(\mathbf{R}))\Lambda_\nu(\mathbf{R}) = E_{tot}\Lambda_\nu(\mathbf{R}) \tag{2.5}$$

The solution of the *electronic* Schrödinger Eq. (2.4), with the nuclear positions **R** as parameters, results in a *potential energy surface* (PES) that represents the basis for solving the nuclear motion (*i.e.* vibrations and rotations).

The *Born-Oppenheimer* approximation does not account for correlated dynamics of ions and electrons and therefore it breaks down for systems where this contribution cannot be negligible, for example:

- polaron-induced superconductivity;
- dynamical Jahn-Teller effect at defects in crystals;
- some phenomena of diffusion in solids;
- non-adiabaticity in molecule–surface scattering and chemical reactions;
- relaxation and some transport issues of charge carriers (e^- or h^+).

These limits can be severe, nevertheless, we will use the *Born-Oppenheimer* approximation in the following.

2.1.2 Basic principles of the Density Functional Theory

Even if the exact expressions of the operators in Eq. (2.2) are known, the Schrödinger equation cannot be solved because the dynamics of a many-electron system is very complex and the electron-electron interaction, $\mathbf{V_{ee}}$, requires elaborate computational methods to be evaluated. A significant

simplification is provided by the *Hartree-Fock* (HF) or *Wave Function Theory* (WFT) that introduces independent-particle models, where the motion of one electron is considered to be dependent only on the average electron-electron interactions. The contribution to the energy due to the mutual relationships between electrons, known as correlation energy, can be included only by means of a high level of *Configuration Interactions*. However, the computational cost heavily depends on the system size and therefore this method is generally limited to systems with 10-100 electrons. The alternative to WFT is the *Density Functional Theory* (DFT) [74,75] that has now become the preferred method for electronic structure theory for complex systems, in part because its cost scales more favourably with system size and yet it competes well in accuracy except for very small systems. DFT is based on the electronic density of the system, $\rho(\mathbf{r})$, according to the two Hohenberg and Kohn theorems [76]:

"Any observable magnitude of a stationary non-degenerated ground state can be calculated exactly from its electronic density".

"The electronic density of a stationary non-degenerated ground state can be calculated exactly determining the density that minimizes the energy of the ground state".

The energy becomes a functional of ρ, $E^{DFT}[\rho]$, and compared to Eq. (2.2) it may be divided into three parts: kinetic energy, $T[\rho]$, attraction between nuclei and electrons, $E_{ne}[\rho]$, forming an external potential $V_{ext}(\mathbf{r})$, and electron-electron repulsion, $E_{ee}[\rho]$ (the nuclear-nuclear repulsion, $E_{nn}[\rho]$, is a constant within the *Born-Oppenheimer* approximation).

$$E^{DFT}[\rho] = T[\rho] + E_{ne}[\rho] + E_{ee}[\rho] \tag{2.6}$$

While the WFT depends on a 3N-dimensional wave function for a system with N electrons, in principle DFT can describe a material in terms of its three dimensional electronic density, independent of the system size. However, so far any attempts to design such *orbital-free* DFT resulted in low performance especially because of the poor description of the kinetic energy and their accuracy is still too scarce to be of general use [77,78]. The success of modern DFT methods is based on the idea suggested by Kohn and Sham (KS) in 1965 [79]. In their approach to DFT a reference system of fictitious non-interacting electrons moving in an effective potential, $V_{eff}(\mathbf{r})$, is associated in its ground

state to the same density of the real system of interacting electrons, $\rho(\mathbf{r})$. The latter can therefore be written in terms of non-interacting one-electron orbitals, ϕ_i:

$$\rho(\mathrm{r}) = \sum_{a}^{occ.} n_s \left|\phi_a^{KS}(\mathrm{r})\right|^2 \rightarrow \rho^{exact}(\mathrm{r}) \tag{2.7}$$

The ground state wave function of the non-interacting system is a Slater determinant Φ^{KS} built on one-electron orbitals, ϕ_i, solutions of the Kohn-Sham Eq. (2.8), where $\hat{f}^{KS}$ is the one electron operator defined in Eq. (2.9):

$$\hat{f}^{KS}\phi_i^{KS}(\mathrm{r}) = \varepsilon_i^{KS}\phi_i^{KS}(\mathrm{r}) \tag{2.8}$$

$$\hat{f}^{KS} = -\tfrac{1}{2}\nabla^2 + V_{eff}(\mathrm{r}) \tag{2.9}$$

$V_{eff}(\mathbf{r})$ consists of the external potential $V_{ext}[\mathbf{r}]$, the classical Coulomb component $U_J(\mathbf{r};[\rho])$ of the electron-electron interaction V_{ee} and the potential $V_{xc}(\mathbf{r};[\rho])$ associated to the exchange-correlation energy functional $E_{xc}[\rho]$.

$$V_{eff}(\mathrm{r}) = V_{ext}(\mathrm{r}) + U_J(\mathrm{r};[\rho]) + V_{xc}(\mathrm{r};[\rho]) = -\sum_{A}^{M}\frac{Z_A}{\mathrm{r}_{1A}} + \int\frac{\rho(\mathrm{r}_2)}{\mathrm{r}_{12}}d\mathrm{r}_2 + \frac{\delta E_{xc}[\rho]}{\delta\rho(\mathrm{r})} \tag{2.10}$$

It is worth noting that $U_J(\mathbf{r};[\rho])$ contains also the interaction of the electron with itself (*self-interaction*, see Sec. 2.1.3) whose correction must be taken into account in the unknown potential $V_{xc}(\mathbf{r};[\rho])$. The total energy in Eq. (2.6) becomes:

$$E^{KS}[\rho] = T_S[\rho] + E_{ne}[\rho] + J[\rho] + E_{xc}[\rho] \tag{2.11}$$

The KS model is closely related to HF method providing identical formulas to the kinetic, $T_S[\rho]$ (the subscript S denotes that it is calculated from a Slater determinant), electron-nuclear, $E_{ne}[\rho]$, and Coulomb electron-electron energies, $J[\rho]$. The part that remains after subtraction of E^{KS} from the exact energy defines the exchange-correlation energy, $E_{xc}[\rho]$, that consists of a kinetic correlation energy (first parenthesis in Eq. (2.12)) and a potential correlation and exchange energy (second parenthesis in Eq. (2.12)).

$$E_{xc}[\rho] = (T[\rho] - T_S[\rho]) + (E_{ee}[\rho] - J[\rho]) = T_c + U_{xc} \tag{2.12}$$

E_{xc}, which is a rather small fraction of the total energy, is the only unknown functional. Therefore, unlike HF methods that use an exact Hamiltonian but obtain an approximated solution of the wave function, in DFT approaches the Hamiltonian is approximated but the electronic density of the system is exact. Unfortunately, so far it does not exist a systematic way to improve DFT results by a better description of the exchange-correlation functional [54]. J. P. Perdew [80,81] suggested a roadmap for functional development, known as Jacob's ladder, where one can expect or at least hope for an improvement in the accuracy for each step up the ladder: local density approximation (LDA), gradient generalized approximation (GGA), higher order gradient or meta-GGA methods and hybrid or hyper-GGA functional (see Fig. 2.1).

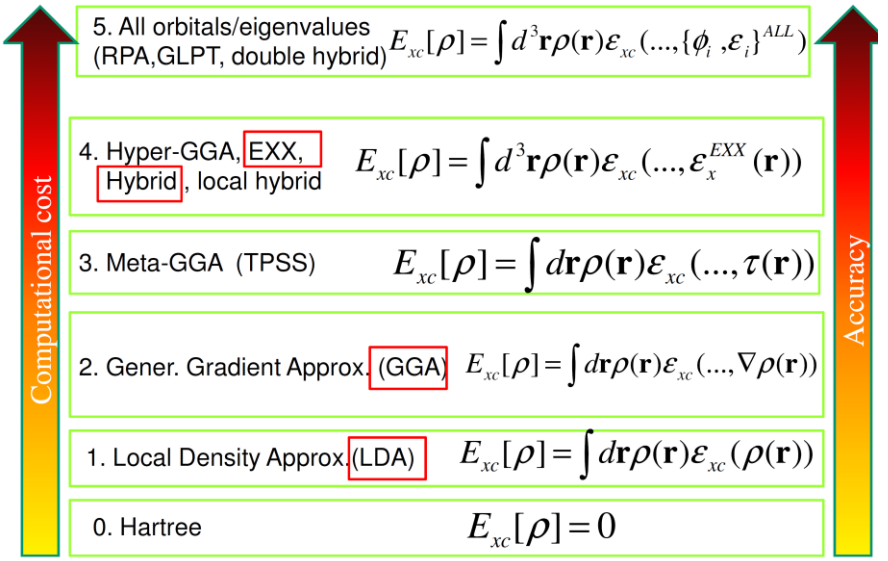

Figure 2.1. Jacob's Ladder proposed by J. P. Perdew [80,81] to improve the exchange-correlation functional. For a detailed explanation of the terms in the figure and the relative methods we refer the reader to Sec. 2.1.3. Courteously reproduced from Ref. [82].

An exhaustive overview of DFT is far beyond the purposes of this introduction (see textbooks [83,84,85,86]). In the following we will briefly address only the main DFT methods and the criteria we considered in the choice of the functional used in the present work.

2.1.3 DFT Methods

The first two rungs of the Jacob's ladder are occupied by the so-called o*rbital-independent functionals* (see Fig. 2.1). They rely explicitly on the density and are in turn divided into strictly local, LDA, and semilocal, GGA.

In the LDA approximation the exchange-correlation energy is evaluated for a homogeneous electron gas [79]. Its main success comes from the description of extended systems, such as metals, where the approximation of a slowly varying electron density is quite valid. However, even if it is an *exact* and simple DFT method and presents some significant advantages (*i.e.* cancellation of errors between the approximate exchange and correlation holes, *vide infra*) it is severely affected by several failures (*e.g.* underestimation of the exchange energy by ~10% for molecular systems and overestimation of electron correlation by a factor close to 2 with consequent overestimation of bonding strength).

Many of these quantitative limits are remedied using the GGA approach that includes informations on the deviations from the electron gas homogeneity only by considering the gradients of the spin-polarized charge densities, $\nabla\rho(r)$. GGA functionals are distinguished in *parameter-free* and *empirical* functionals according to whether parameters are determined from exact theoretical conditions (*e.g.* PW91, PBE [87,88]) or from fits to experimental data (*e.g.* LYP [60,89]), respectively. Over the years, several improvements of these functional were proposed such as revPBE [90], with the goal of obtaining more accurate atomic absolute energies and molecular atomization energies and RPBE [91], with the aim of achieving improved chemisorptions energies for small molecules on metal surfaces.

Both LDA and GGA methods suffer from serious formal deficiencies that can result in qualitatively incorrect computations. In the following we will briefly focus on the two main deficiencies that occur with LDA and GGA functionals: the presence of self-interaction and the absence of a derivative discontinuity in the exchange-correlation energy.

- self-interaction error: each electron in the system is repelled from an average charge density, including a spurious repulsion from itself. A complete error cancellation is guaranteed for the exact exchange-correlation functional, but only partial cancellation is obtained in either the LDA or the GGA. For localized states, the spurious self-interaction destabilizes the system while for delocalized states the error is much smaller because the spurious contribution to the Coulomb potential comes from a greater average distance. In this sense

LDA or GGA usually fail in the quantitative treatment of localized states. Moreover, the self-interaction error causes an incorrect long-range behaviour of the Kohn-Sham potential [92,93].

- absence of derivative discontinuity in the exchange-correlation energy: the exact energy of a N-electron system behaves as a series of linear segments at the varying of the electron occupancy N [94]. Thus, E_{tot} has to be piecewise linear with respect to fractional occupancy N, but its derivative must be discontinuous as N passes through integers [95]. The physical meaning is made explicit referring to the chemical potential μ, defined as functional derivative of the total energy with respect to the charge density in Eq. (2.13).

$$\mu = \partial E_{tot} / \partial \rho(\mathrm{r}) \tag{2.13}$$

By definition also the chemical potential must exhibit a discontinuity and in particular, its absolute value should be equal to the ionization potential I_P if the integer number of electrons is approached from below, and it should be equal to the electron affinity E_A if the number of electrons is approached from above. Since LDA and GGA exchange-correlation potentials are continuous in the density and in its gradient, these potentials do not exhibit any particle number discontinuity. They average over the discontinuity and the value of the highest occupied Kohn-Sham orbital, that is rigorously equal to the chemical potential, differs therefore from I_P by approximately half the derivative discontinuity in these DFT methods [96].

A natural and potentially highly advantageous idea to overcome LDA and GGA limits is to use Kohn-Sham orbitals, themselves being functionals of the density, as ingredients in approximate exchange-correlation functional, known as orbital-dependent functionals [97,98].

Orbital-dependent functionals. There are four main classes of orbital-dependent functionals:

1. The meta-generalized-gradient-approximation (MGGA).

They use kinetic energy density τ (that is orbital-dependent by definition) or the Laplacians $\nabla^2\rho_\sigma$ in the construction of $E_{xc}[\rho]$. They are close in spirit to the traditional semilocal, explicit density functionals GGA, as they use the orbitals in a mostly semilocal way. Instead of LDA and GGA they can satisfy the constraint of freedom from self-correlation by employing so-called iso-

orbital indicators [99,100,101] but the self-interaction error is only slightly reduced. Therefore, even if they are the most accurate semilocal functionals they are still significantly hampered by the problems of LDA and GGA functionals.

2. Self-interaction correction (SIC) scheme.

Originally proposed by Perdew [92,102], it is a correction scheme of exchange-correlation functionals based on the idea that the exchange-correlation energy of the density of a single, fully occupied orbital must exactly cancel that orbital's self-interaction energy. The self-interaction energy terms are therefore subtracted on an orbital-by-orbital basis and for this reason the SIC scheme is counted in the family of orbital-dependent functionals. The SIC scheme is an *ad hoc* scheme and although, in principle, it can be applied to any given functional approximation, it has predominantly been used to correct LDA. While in the solid-state community the SIC scheme has successfully been used for describing strongly correlated systems [103,104], the results for molecules appeared less favourable. This failure can be explained by considering that part of the self-interaction error of semilocal functionals is needed to model correlation effects, in particular the *static* correlation (*vide infra*) [105,106,107,108,109]. Thus, it has been suggested that the self-interaction error in a many-electron system should be scaled down instead of removed completely.

3. Hybrid functionals.

The physical principle, upon which hybrid functionals are based, is the *Adiabatic Connection Theorem* (ACT) [110]. First of all we assume a many-electron Hamiltonian in the form of Eq. (2.14) with $0 \leq \lambda \leq 1$.

$$H_\lambda = T + V_{ext}(\lambda) + \lambda V_{ee} \tag{2.14}$$

where the external potential operator V_{ext} is equal to V_{ne} for $\lambda = 1$, but for intermediate λ values $V_{ext}(\lambda)$ is adjusted such that the density remains constant. For the $\lambda = 0$ case, the electrons are non-interacting and the exact solution to the Schrödinger equation is given as a Slater determinant, while the $\lambda = 1$ case corresponds to the real interacting electrons system. If we define the exchange-correlation hole h_{xc} as the reduced probability of finding an electron 2 at a position $\mathbf{r}_2$ given that an electron 1 is located at $\mathbf{r}_1$, the ACT connects $E_{xc}[\rho]$ and the corresponding hole potential $\mathbf{V_{xc}}(\lambda)$ through Eq. (2.15).

$$E_{xc} = \int_0^1 \left\langle \Psi_\lambda \left| V_{xc}^{hole}(\lambda) \right| \Psi_\lambda \right\rangle d\lambda \tag{2.15}$$

Assuming $\mathbf{V_{xc}}$ to be linear in λ, in the crudest approximation the integral is given as the average of the values at the two end-points (λ = 0, λ = 1). If the KS orbitals were identical to the HF orbitals, the integral for λ = 0 is the exact exchange energy given by the Hartree-Fock theory. Approximating the integral for λ = 1 by the LDA result, Becke proposed the *Half-and-Half* method [111] based on Eq. (2.16).

$$E_{xc} = \frac{1}{2}\left(\left\langle \Psi_0 \left| V_{xc}^{hole}(0) \right| \Psi_0 \right\rangle + \left\langle \Psi_1 \left| V_{xc}^{hole}(1) \right| \Psi_1 \right\rangle\right) = 0.5 \cdot E_x^{exact} + 0.5 \cdot E_{xc}^{LDA}[\rho] \tag{2.16}$$

Becke defined such functional hybrid functional viewing it as a true mixture of HF and DFT approaches. A significant improvement over this simple method can be obtained by refining the approximate integration of $E_{xc}[\rho]$ and a practical way is provided by Eq. (2.17).

$$E_{xc} = bE_x^{exact} + (1-b)E_x^{app} + E_c^{app} \tag{2.17}$$

where the superscript *app* denotes the approximate functional E_{xc}^{app}, typically LDA or GGA, that has been split in the exchange and correlation parts. It is noteworthy that Eq. (2.17) mixes the approximate and exact exchange linearly, but the approximate correlation is taken as is.

This can be motivated taking into account the description of the *static* and *dynamical* correlation in LDA and GGA. *Dynamical* correlation [112] is due to the reduction expected in the many-electron wave function when two electrons approach each other and because of the screening, it is inherently a short-range effect. *Static* or long-range correlation [112] arises from degeneracies or near degeneracies of several Slater determinants. It has been proved that the semilocal GGA correlation, E_c^{app}, agrees closely with the dynamical correlation [113] while the difference between the semilocal GGA exchange E_x^{app} and the exact exchange E_x^{exact} arises from the effective inclusion of static correlation in E_x^{app} [114]. Thus, dynamical correlation is well modelled by semilocal correlation but semilocal exchange differs from exact exchange by static correlation, and therefore a linear mix of E_x^{app} and E_x^{exact} as in Eq. (2.17) is needed.

A generalization and improvement of Eq. (2.17) considers a higher number of parameters and a combination of LDA and GGA functionals. In this context, the most popular hybrid functional is the B3LYP method [59,60] defined by Eq. (2.18).

$$E_{xc}^{B3LYP} = (1-a)E_x^{LDA} + aE_x^{exact} + b\Delta E_x^{B88} + (1-c)E_c^{LDA} + cE_c^{LYP} \quad (2.18)$$

where the *a*, *b* and *c* parameters were determined by fitting to experimental data and their values are $a = 0.20$, $b = 0.72$ and $c = 0.81$. This functional works extremely well for atoms and molecules [115], despite its *ad hoc* construction, and it has become the most popular functional in the chemistry community. However, the use of the LYP correlation (experimental parameters dependent) results in a functional that does not reduce to the LDA in the limit of an uniform electron gas and sometimes it may induce errors in applications to solids and surfaces (*e.g.* metals).

This formal deficiency is absent with either the B3PW91 functional or with one-parameter functionals based on either the LDA or PBE GGA. In particular, the simplest of the hybrid functionals in use for solids is the PBE0 [116] functional defined by Eq. (2.19).

$$E_{xc}^{PBE0} = E_{xc}^{PBE} + a(E_x^{HF} - E_x^{PBE}) = aE_x^{exact} + (1-a)E_x^{PBE} + E_c^{PBE} \quad (2.19)$$

where E_x^{PBE} and E_c^{PBE} are the exchange and correlation components of the semilocal PBE functional, respectively. A mixing factor of $a = 1/4$ is argued from theoretical grounds and not derived from fits, although other empirical choices for *a* have been explored. Other approaches point to increase the functional flexibility either by means of the introduction of the kinetic energy density as in MGGA methods (*i.e.* MGGA hybrid functionals [117]) or by means of the partition of the exchange term into short-range (SR) and long-range (LR) parts according to Eq. (2.20).

$$E_{xc}^{hyb} = aE_x^{SR\_exact} + (1-a)E_x^{SR\_app} + bE_x^{LR\_exact} + (1-b)E_x^{LR\_app} + E_c^{app} \quad (2.20)$$

The PBE-based screened hybrid functional obtained excluding the long-range portion of the exact exchange by setting $b = 0$ is known as HSE [118,119,120, 121,122] and has been found to provide an excellent description of metals in particular [122].

It is noteworthy that the hybrid functionals exhibit an accuracy superior to

that of the LDA or GGA ones for a wide range of properties for which they were not fitted (*e.g.* molecular structures, vibration frequencies, electrical and magnetic properties). The evaluation of the nonlocal exchange in periodic solids is highly more computationally expensive compared to the LDA and GGA functionals [75]. However, hybrid functionals still show shortcomings: because they contain only a fraction of exact exchange, they are not self-interaction-free nor do they generally possess the correct derivative discontinuity.

4. Functionals combining exact exchange and compatible correlation

This class of functionals includes the most recent and advanced approaches that try to use at the same time the exact exchange and a correlation that accounts for both short range and long range contributions.

The first subclass, called hyper generalized gradient approximation (HGGA) [123] or local hybrid functionals [124], is based on the idea of combining exact exchange with an existing semilocal functional that models dynamical correlation and an exchange-like functional that models static correlation. The latter is the only unknown element but its development is far from easy.

A completely different approach concerns the perturbative scheme that expands the exchange-correlation energy in a Rayleigh-Schrödinger-like perturbation series, with the electron-electron interaction acting as the perturbation. The first DFT-based perturbation theory approach was developed by Görling and Levy [125,126,127]. All the pertubative approaches make use of not only the occupied KS orbitals but also the unoccupied ones. They can achieve systematic convergence to the exact result but at the price of a very high computational cost.

A last subclass reported of functionals is the random-phase approximation (RPA) based on an exact representation of the exchange-correlation energy in the form of the adiabatic-connection fluctuation-dissipation theorem [128,129]. This approach can describe Van der Waals interactions and generally reproduces long-range correlation well [130]. However, it misses important short-range correlation effects and therefore it is regarded as the complement of semilocal correlation functionals which mainly represent short-range correlation.

A group of functionals that cannot be categorized into one of the classes presented above includes the DFT+*U* functionals, first introduced by

Anisimov and co-workers in order to improve the theoretical description of strongly correlated systems [131,132]. The approach is based on the idea of selecting a small number of localized orbitals and treating the correlation associated to them in a special way. In particular, an additional ($U-J$) parameter is added to the total DFT energy functional to mimic an effective onsite Coulomb (U) and exchange (J) between electrons with the same orbital angular momentum. The main advantage of DFT+U is the modest additional computational cost respect to hybrid functionals that are much more demanding because of the evaluation of nonlocal Fock exchange in a periodic solid. The ($U-J$) term is an empirical parameter and the value has to be determined investigating its dependency on the variable of interest. However, a more rigorous approach is to determine ($U-J$) from first principles, *i.e.* via constrained DFT [133] where the electron occupation on a particular site is held fixed. The main drawbacks are that ($U-J$) is derived from an unphysically constrained situation, and the underlying DFT calculations still suffer from approximate exchange-correlation problems.

In conclusion of this overview we stressed that generally each functional considered here belongs to a gradually higher step of Jacob's ladder resulting in an improved accuracy (see Fig. 2.1). However, the possible benefits of these approaches come at a heavy price sacrificing an essential part of what made DFT attractive in the first place, namely, modest computational cost gained through insightful modelling of physical quantities (*i.e.* LDA and GGA). Furthermore, no functional is able to correctly describe all the properties of the system under consideration. There is no universal recipe in the choice of the functional. It will depend on the system, on the properties analyzed, and on the compromise between accuracy and computational costs. In Section 2.1.5 we will focus on the key properties considered in this study, emphasizing the critical and problematic issues of DFT functionals and explaining the choices made.

2.1.4 Computational Packages

In this Section we briefly report some basic details on the two main computational packages used in this work, the CRYSTAL code and the GAUSSIAN code.

2.1.4.1 CRYSTAL Code

The CRYSTAL code is the main package used in the present studies [69,70,71]. This software was conceived more than thirty years ago [134,135] as an extension to periodic systems of powerful ab-initio molecular codes [136,137,138] and it was developed by means of the main contribution of the researchers of the Theoretical Chemistry Group in Torino (Italy) and of the Computational Materials Science Group in Daresbury (UK). The exchange-correlation functionals implemented in the code to solve the periodic HF and KS equations are reported in Table 2.1.

Table 2.1. Exchange-Correlation Functionals available in the CRYSTAL code.

Type	**Name**	**Exchange**		**Correlation**	
LDA	SVWN	Slater	[139]	VWN	[140]
	SPWLSD	Slater	[139]	PWLSD	[141]
	SPZ	Slater	[139]	PZ	[92]
GGA	PBE	PBE	[88]	PBE	[88]
	PW91	PW91	[87]	PW91	[87]
	PBEsol	PBEsol	[142]	PBEsol	[142]
	SOGGA	SOGGA	[143]	PBE	[88]
	WC	WC	[144]	PBE	[88]
Hybrid	B3LYP	B/HF	[59]	LYP	[60]
	PBE0	PBE/HF	[88]	PBE	[88]
	B1WC	WC/HF	[144]	PW91	[87]

Unlike other common solid state *ab-initio* codes, *e.g.* VASP [145], CASTEP [146], ABINIT [147] and CPMD [148] which employ either plane waves (PW) as basis set in combination with atomic pseudo-potentials to screen the core electrons or projected-augmented waves, CRYSTAL performs all-electron calculations adopting a linear combination of atom-centred Gaussian-type orbitals (GTO). The crystalline orbitals, ψ_i(r;k) (CO), are treated as linear combinations of Bloch functions, ϕ_μ(r;k) (BF):

$$\psi_i(\mathrm{r};\mathrm{k}) = \sum_{\mu} a_{\mu j}(\mathrm{k})\,\phi_\mu(\mathrm{r};\mathrm{k}) \tag{2.21}$$

and the Bloch functions are defined in terms of local functions, indicated as atomic orbitals (AO), that are expressed as linear combination of a certain number of GTOs usually used in standard molecular quantum chemistry

codes. Each atom A is therefore represented by p_A GTOs, each resulting from a "contraction" of M_{iA} Gaussian primitives of angular momentum components l,m centred in R_A:

$$\chi_{iA}(r_A) = \sum_{j=1}^{M_{iA}} c_{iA,j} N^{l,m}(\alpha_{iA,j}) X^{l,m}(r_A) \exp[-\alpha_{iA,j} r_A^2] \quad (2.22)$$

where $r_A = r - R_A$, $X^{l,m}$ are real solid harmonics, $N^{l,m}$ normalization coefficients and $c_{iA,j}$ and $\alpha_{iA,j}$ are known as *coefficients* and *exponents* of GTOs, respectively.

The choice of using GTO functions has some advantages and drawbacks. The main advantage is the possibility of exploiting the experience gained in the preparation of these sets from molecular quantum chemistry and the extremely efficient algorithms available for performing one- and two-electron GTO-integrals. A limited number of functions is required for a good description of the COs and not only 3-dimensional crystals, but also structures periodic in 2- (slabs), 1- (polymers) and 0- (molecules) dimensions are treated with the same approach without any need of artificial replication of the subunits and avoiding spurious effects due to artificial replicated images. From a technical perspective, moreover, exact HF exchange as well as hybrid functionals are standard in GTO-based solid state computer codes such as CRYSTAL, whereas, in contrast, their implementation in codes using PW is still limited and problematic because of the delocalized nature of PW basis sets. The most serious drawback is the incompleteness of the basis set. In contrast with the PW sets that, in principle, are complete and whose quality is determined by a single parameter (the energy cutoff), there is no mathematically exact procedure to achieve convergence with respect to the basis set using AO functions. In fact, the simple addition of more AOs may eventually result in pseudo-overcompleteness (*i.e.*, linear dependencies among basis functions). Moreover, since AO functions depend upon which atoms are present and their relative positions, they suffer from incomplete basis set errors on forces (also known as Pulay forces [149]) and from basis set superposition errors on energy (BSSE, see Sec. 2.1.5.5).

Among the main features of the CRYSTAL code, we cite the most exploited ones in this work:

- Full geometry optimization through the use of analytic gradients of the energy with respect to both lattice parameters and atomic positions [150,151, 152]. It is also possible to perform volume constrained geometry optimization.

In all cases, the symmetry of the system is fully exploited with substantial time savings.

- Calculation of vibrational frequencies at k = 0 (Γ) [153] and the corresponding infrared intensities [154], in the harmonic approximation; anharmonic correction for the stretching mode of X-H bonds [155] (see Sec. 2.1.5.4).
- Fermi contact and dipolar hyperfine coupling constants evaluation (see Sec. 2.1.5.3). It should be noticed that however no relativistic corrections for core electrons are yet implemented in CRYSTAL (see EPR parameters for Cu-doped ZnO in Sec. 4.3.2).

In the most recent version [69,70], the CRYSTAL code is connected to CRYSCOR, a post-HF code which allows the calculation of the correction to the energy and to the density matrix of the crystalline system at the local MP2 level, the lowest order of perturbation theory [156].

In the following we report some computational details used for all the calculations presented in this work using the CRYSTAL code.

Computational Details. Cut-off limits in the evaluation of Coulomb and exchange series appearing in the Self Consistent Field (SCF) equation for periodic systems were set to 10^{-7} for Coulomb overlap tolerance, 10^{-7} for Coulomb penetration tolerance, 10^{-7} for exchange overlap tolerance, 10^{-7} for exchange pseudo-overlap in the direct space, and 10^{-14} for exchange pseudo-overlap in the reciprocal space [70]. The condition for the SCF convergence was set to 10^{-6} a.u. on the total energy difference between two subsequent cycles.

The gradients with respect to atomic coordinates and lattice parameters are evaluated analytically. The equilibrium structure is determined by using a quasi-Newton algorithm with a Broyden-Fletcher-Goldfarb-Shanno (BFGS) Hessian updating scheme [157]. Convergence in the geometry optimization process is tested on the root-mean-square (rms) and the absolute value of the largest component of both the gradients and nuclear displacements. For all atoms, the thresholds for the maximum and the rms forces have been set to 0.000450 and 0.000300 a.u., and those for the maximum and the rms atomic displacements to 0.001800 and 0.001200 a.u., respectively.

2.1.4.2 GAUSSIAN Code

The GAUSSIAN code [158] is based on Gaussian basis sets and is the most widely used program for isolated molecules, and it provides a cluster approach to model solids. Its main advantages are the high flexibility in the choice of basis sets, effective core potentials, density functionals, and the availability of excellent geometry optimizers and initial guesses for the self-consistent-field iterations. Moreover, it supports analytic Hessians [159] for all functionals, even meta and hybrid meta functionals.

In the present work GAUSSIAN code has been used to model nitrogen point defects in bulk MgO (see Chapters 8 and 9) in the framework of the cluster approach. A cluster is a representative portion of a given material, made of a limited number of atoms, that is cut out from the ideal infinite crystal. The system is treated as a sort of "molecule" and even though this procedure appears less rigorous than the periodic approach, it is justified by the localized nature of the defect under investigation, described in infinite dilution condition that is precluded to the periodic approach. However, cutting out the cluster from the extended solid results in a number of non-physical effects. In the case of an ionic oxide, *e.g.* MgO, the main problem is the description of the long-range electrostatic potential (the Madelung potential). The latter is usually reproduced by means of a finite array of point charges (PCs) located in lattice positions, whose values are the nominal charges of the ions. However, this approach is affected by two main drawbacks. From one side the anions at the edge of the quantum-mechanical cluster experience a non-physical polarization due to presence of nearby positive point charges and on the other side no long-range polarization induced by the defect or adsorbate, especially if charged or polarized, is taken into account. The first drawback can be overcome by replacing positive point charges at the interface with quantum-mechanical cluster with effective core potentials (ECPs), which simulate the exchange repulsion, preventing non-physical polarization [160]. On the other side, an approximate way to describe the long-range polarization induced by the defect is based on the shell model [161], a classical model of a polarizable ion consisting in two point charges, a positive one for the core and a negative one for the shell, coupled by a harmonic potential. The displacement of the shell relative to the core simulates the polarization of a classical ion in an electric field. P. V. Sushko and A. L. Shluger [162] implemented the shell model in the GUESS code interfaced with the GAUSSIAN code.

2.1.5 Computationally Investigated Material Properties

The theoretical results presented in this work concern the study of bulk and surface properties of metal oxides. In particular the study is structured in two main areas of research: doping and surface reactivity. Doping by point defects or higher dopant concentration has been analyzed in terms of effects on the electronic (*i.e*. band-gap shift and transition energy levels, see Sec. 2.1.5.1) and magnetic properties (*i.e*. magnetic interaction and EPR parameters, see Sec. 2.1.5.3). The relative stability of the various defects has been compared on the basis of their formation energy (see Sec. 2.1.5.2) at different experimental conditions (*i.e*. oxygen chemical potential) and system conductivity (*i.e*. Fermi level values). The surface reactivity has been studied in terms of vibrational frequencies (see Sec. 2.1.5.4) and molecules binding energy (see Sec. 2.1.5.5). Most of the properties reported has been compared to experiments. In the present section a general overview of some of these properties is provided focusing on the problems that motivated our computational choices.

2.1.5.1 Electronic Properties

Band Gap. One of the most important properties defining the electronic structure of a system is the band gap. Usually it is distinguished in fundamental and optical gap. The fundamental gap corresponds to the difference between the first ionization potential I_P and the first electron affinity E_A and it can be measured, for example, by photoemission spectroscopy. The optical gap is defined as the difference between the energies of the lowest excited many-particle state and the ground state, and it can be evaluated, for example, by determining the optical absorption spectrum. So far we focused on time-independent, static DFT, that is inherently a ground state theory and, in principle, cannot make predictions about excited states. However, especially for a solid with periodic boundary conditions, it is common practice to approximate the fundamental gap to the Kohn-Sham gap in a ground-state theoretical framework. In fact, for a N-electron system I_P and E_A are related to the N-th and (N+1)-th Kohn-Sham eigenvalues via Eq. (2.23) [163]:

$$\begin{aligned} I_P(N) &= -\mathrm{e}_N(N-\delta) \\ E_A(N) &= -\mathrm{e}_{N+1}(N+\delta) \end{aligned} \tag{2.23}$$

where δ is the infinitesimal decrement/increment of the integer particle number N. In other words, I_P can be equated with the highest occupied Kohn-Sham eigenvalue e_N (N–δ) for a system approaching the integer particle number from below, whereas E_A can be equated with the lowest infinitesimally occupied eigenvalue e_{N+1} (N+δ) for a system approaching the integer particle number from above. The latter value differs from that obtained for the lowest unoccupied eigenvalue e_{N+1} (N–δ) of a system approaching the integer particle number from below by exactly the derivative discontinuity in E_{xc}, Δ_{xc} (see Sec. 2.1.3). A standard Kohn-Sham calculation is known to be equivalent to approaching the integer particle number from below [164], therefore the fundamental gap can be evaluated by Eq. (2.24):

$$I_P - E_A = e_{N+1} - e_N + \Delta_{xc} \tag{2.24}$$

Since LDA and GGA do not possess a derivative discontinuity, they yield a Kohn-Sham gap that underestimates the fundamental one, often considerably [165]. Hybrid functionals partially overcome this limitation because they use orbital-specific potentials and therefore, the above derivative discontinuity argument does not directly apply. However the performance of hybrid functionals with respect to the fundamental gap often strongly depends on the type of hybrid functional used. For example, the PBE0 tends to overestimate band gaps for semiconductors and underestimate them for insulators, the HSE works significantly better for small- and medium-gap solids but it still underestimates the gap of large-gap insulators [122]. Finally, even if fundamental gaps are not part of the training set of the B3LYP functional, its predicted band gap energies are within 10% at most of experimental values for a wide range of solids [166].

The optical gap, defined as the excitation of one electron in the presence of the other $N-1$ electrons, is an excite-state property and should be correctly described in the framework of time-dependent DFT (TD-DFT). However, since the optical gap is smaller than the fundamental one by the exciton binding energy [167] and in many solids this difference is within 0.1 eV, in ground-state DFT it is common practice to estimate the optical gap in first approximation using hybrid functionals. The optical gap, E_g, has been therefore calculated within the one-particle picture as difference of the highest occupied Kohn-Sham eigenvalue e_N (N) and the lowest unoccupied Kohn-Sham eigenvalue e_{N+1} (N). A thorough investigation of dispersion of the

energy of band edges in the *k*-space must be provided in order to identify the correct minimum gap. The degree of quantitative agreement with experimental values depends strongly on both the hybrid functionals used and the chemical nature of the systems studied. For the three oxides considered in this work (ZnO, ZrO_2, MgO) the experimental band gaps are well reproduced by the hybrid B3LYP and this evidence justifies the choice of this functional as a reliable tool to gain insight into the details of the electronic structure of the doped systems.

Transition Energy Levels. Point defects and impurities affect significantly the electronic properties of semiconductor materials. They are classified as deep or shallow depending on they introduce levels within the band gap or near the band edges, respectively. These levels involve transitions between different charge states of the centre and to compare electronic structure calculations with their experimental detection one should go beyond the single-particle Kohn–Sham eigenvalues approach. A better approximation of electronic transitions involving charge state variations of defects or impurities can be achieved by means of transition energy levels computation [66,67,68]. The relative stability of the various charge states is determined by the *formation energy*:

$$E_{form-D,q}(E_F,\mu) = \left[E_{D,q} - E_H\right] + q\cdot\left[E_v + E_F\right] + \sum n_i\mu_i \qquad (2.25)$$

where D is the defect; q is the dimensionless charge state of the defect (*e.g.* +2,+1,0,–1,–2), $E_{D,q}$ and E_H are the total energies of the host+defect and the host-only supercells, respectively, E_v is the bulk valence band maximum, E_F is the Fermi level referenced to the bulk valence band maximum, n_i is the number of added ($n_i > 0$) or removed ($n_i < 0$) atoms to create the defect, and μ_i is the chemical potential of the defect species. It is noteworthy to point that the formation energy in Eq. (2.25) is computed as a total electronic DFT energies difference neglecting all entropy and volume effects. This assumption has been corroborated by the evidence that vibrational contributions to the entropy cancel to a large extent and that the influence of volume changes are even smaller [168].

The value of the Fermi level where charge states q and q' are equal in formation energy defines the transition level $\varepsilon(q/q')$,

$$E_{form-D,q}(E_F = \varepsilon(q/q'), \mu) = E_{form-D,q'}(E_F = \varepsilon(q/q'), \mu) \quad (2.26)$$

From Eq. (2.25) it follows that:

$$[E_{D,q} - E_H] + q \cdot [E_v + \varepsilon(q/q')] + \sum n_i \mu_i = [E_{D,q'} - E_H] + q' \cdot [E_v + \varepsilon(q/q')] + \sum n_i \mu_i \quad (2.27)$$

thus:

$$\varepsilon(q/q') = \frac{E_{D,q'} - E_{D,q}}{q - q'} - E_v \quad (2.28)$$

We can distinguish two cases: i) one negative charge (electron, e^-) is added to the system or ii) a positive charge (hole, h^+) is added to the system. Here q' corresponds always to a defect with one electron more, (q + 1e^-): for example this corresponds to a transition from a neutral A^0 to a negatively charged defect A^-, $\varepsilon(0/-1)$, or from a positively charged defect A^+ to the neutral variant A^0, $\varepsilon(+1/0)$, or vice versa. Double charge transitions can be derived from single charge transitions [for example $\varepsilon(+2/0)$ from $\varepsilon(+1/0)$ and $\varepsilon(+2/+1)$] given that the slope of the formation energy curves, as a function of the Fermi level, is known to be equal to q (see Eq. (2.25)).

In the expression of $\varepsilon(q/q')$ in Eq. (2.28) the difference in total energy between the charge state q and the charge state q' is present. This term cannot be easily computed with the present computational setup. In fact, the total energies of charged systems have no physical meaning in the CRYSTAL code [69,70] because of the interaction with the balancing background of charge. This interaction cannot be evaluated in a straightforward way, therefore one must find a way to circumvent the problem. A previously reported B3LYP study [169] on ZnO defects estimated differences in total energy by differences in single-particle energy eigenvalues. This, however, is a very crude approximation. Here we use the theorem by Janak [72] stating that:

$$E_{D,q'} - E_{D,q} = \int_0^1 \mathrm{e}_{h+1}(N + n)\,dn \quad (2.29)$$

where e_{h+1} (N) is the Kohn–Sham eigenvalue of the lowest unoccupied state for the q charge state defect [h+1 = Highest Occupied Molecular Orbital (HOMO)+1 or Lowest Unoccupied Molecular Orbital (LUMO)] and n is the portion of electron added. Instead of calculating the eigenvalues for all values of n between 0 and 1, Eq. (2.29) is simplified according to the mean value

theorem for integrals to

$$E_{D,q'} - E_{D,q} = \frac{\varepsilon_{h+1}(N) + \varepsilon_{h+1}(N+1)}{2} \tag{2.30}$$

Thus, the total energy differences associated to vertical transitions are evaluated from the shift of the Kohn–Sham eigenvalues following the charge addition. This approximation was found to give accurate results for hybrid functionals [170,171]. Note that ε_{h+1} (N+1) is the Kohn-Sham eigenvalue of the highest occupied state (HOMO) for the q' charge state defect. The zero energy reference is set at the top of the valence band, E_v = 0. In the case of spin-polarized calculations the relevant spin-orbital eigenvalue is considered [*e.g.* for neutral doublet states as for H_i or N_s, we considered the alpha component for (+1/0) transition and the beta component for (0/–1) transition, respectively (see Secs. 3.3.1 and 5.4.3)].

With the approach just described optical transition levels, $\varepsilon^{opt}(q/q')$, have been computed at fixed atomic positions (vertical transitions). Thermodynamic transition levels are derived from optical transition levels according to the following equation [66,172]:

$$\varepsilon^{therm}(q/q') = \varepsilon^{opt}(q/q') \pm E_{rel} \tag{2.31}$$

where E_{rel} is the relaxation energy in absolute value, as computed from total energy difference between the charged state (*e.g.*, +1 or –1) in its relaxed configuration and in the neutral relaxed configuration (Franck-Condon shift) [173].

Thermodynamic transition levels have been also computed by extending the Janak's theorem to charged states in their relaxed geometry (adiabatic transitions). The agreement with the approach at Eq. (2.31) is very good (within 0.05 eV) except when the lattice relaxation is large [for example in the case of the doubly charged oxygen vacancy in ZnO (see Sec. 3.3.3)].

The computed optical and thermodynamic transition levels are then inserted in the band gap of the material with reference to the top of the valence band E_v (see Fig. 2.2). The accuracy of this procedure is related to the fact that the experimental band gap value is excellently reproduced by the hybrid functional used (*e.g.*, for ZnO: 3.44 eV [174] experiment vs 3.38 eV theory).

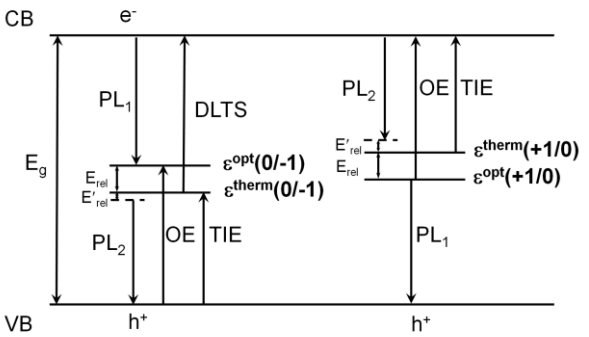

Figure 2.2. Schematic representation of electronic transitions in doped or defective semiconductors and of the spectroscopic techniques which can measure these transitions. The ↑ arrows indicate an electron excitation, the ↓ arrows indicate an electron decay. $\varepsilon^{\text{therm}}$ and ε^{opt} are defined with respect to the VB maximum for (0/–1) and (+1/0) charge state transitions. For the meaning of E'_{rel} and PL_2 transitions see Fig. 2.3. E_{rel} corresponds to $\varepsilon^{\text{therm}} - \varepsilon^{\text{opt}}$ in absolute value.

The real meaning of transition levels is made explicit by considering the experimental spectroscopic techniques producing a comparable observable. Figure 2.2 summarizes how the transition levels can be related to experimental data for $(q/q') = (0/-1)$ and (+1/0) cases. The charge transition experienced by the defect during the experiment can be either $q \rightarrow q'$ or $q' \rightarrow q$. For example, thermodynamic transition levels can be evaluated in deep-level transient spectroscopy (DLTS) experiments, in the case of deep centres, or as thermal ionization energy, *e.g.* estimated by means of high-resolution electron energy loss spectroscopy (HREELS) in the case of shallow defects (see Cu-doped ZnO in Sec. 4.3.1).

On the contrary, the optical levels are vertical transitions according to the Frank–Condon principle and can be observed with optical excitation or photoluminescence (PL) spectroscopies. PL_1 type emissions (see Figs. 2.2 and 2.3) are associated to the vertical decay of one electron (a) from the conduction band (CB) into the neutral defect state, $\text{A}^0 + \text{e}^-_{\text{CB}} \rightarrow \text{A}^-$ (0/–1) transition, or (b) from the defect state to the valence band (VB), $\text{A}^0 \rightarrow \text{A}^+ + \text{e}^-_{\text{VB}}$ (+1/0) transition, always in the minimum energy configuration of A^0.

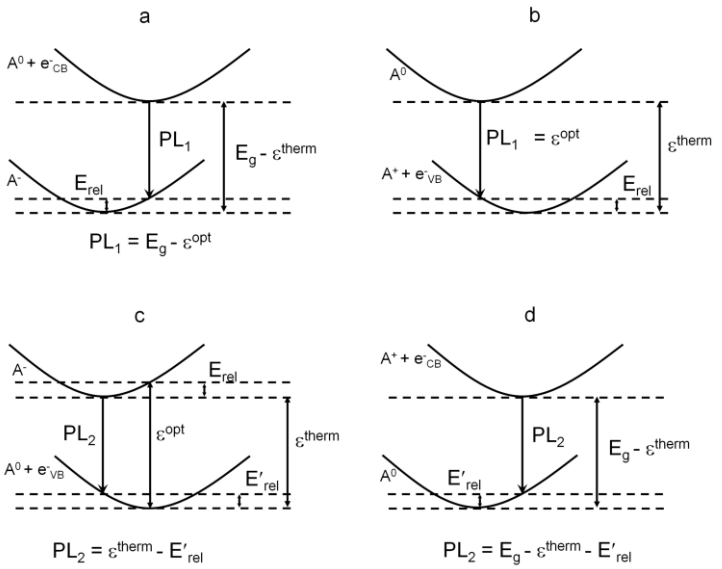

Figure 2.3. Schematic representation of photoluminescence processes and of the corresponding transition levels, see also Fig. 2.2. (a) PL_1 transition for the (0/–1) case; (b) PL_1 transition for the (+1/0) case; (c) PL_2 transition for the (0/–1) case (note that the transition is smaller than ε^{therm}, as reported in Fig. 2.2, by E'_{rel}); (d) PL_2 transition for the (+1/0) case (note that the transition is smaller than E_g–ε^{therm}, as reported in Fig. 2.2, by E'_{rel}). E'_{rel} is the energy gain associated to the relaxation in the neutral A^0 configuration; E_g is the energy gap.

Photoluminescence can also occur as the consequence of a more complex path. An electron can be excited in the CB, then can decay non-radiatively into a defect state with formation of the A^- centre. PL_2 corresponds to the decay of one electron from the minimum configuration of the negatively charged defect to the valence band, $A^- \rightarrow A^0 + e^-_{VB}$ (0/–1) transition. PL_2 can also correspond to the vertical decay of one CB electron into the positively charged defect, $A^+ + e^-_{CB} \rightarrow A^0$ (+1/0) transition, in the minimum energy configuration of A^+ (see Fig. 2.3). In particular, we want to note that in the case of the (0/–1) transition, PL_2 is the emission resulting from the recombination of the excited electron, temporarily trapped at the defect (A^-), with a hole in the valence band. If the decay process $A^- \rightarrow A^0 + e^-_{VB}$ is very fast, there is no time for A^- to relax into its minimum, the emission takes place in the A^0 minimum atomic configuration, and PL_2 corresponds to ε^{opt}, see Fig. 2.3. For longer residence times of the electron at the A^- defect and for higher temperatures, the defect has the time to relax in its minimum energy configuration. In this case the

emission PL_2 corresponds to $\varepsilon^{therm} - E'_{rel}$, as shown in Fig. 2.3. Thus, the PL_2 emission from A^- can be in the energy window $\varepsilon^{therm} - E'_{rel} < PL_2 < \varepsilon^{opt}$, which accounts for the commonly observed large width of the emission peak.

Of course, the spectroscopic observation of the transitions indicated in Fig. 2.2 is purely hypothetical. Most probably only some of these transitions will be effectively registered.

Some further corrections have been made to the formation energy of the defect centres:

1) The potential alignment correction [67], which allows to compare bulk and defect calculations, was obtained by aligning, for example, the Zn 1s core level states for ZnO (Zr 1s core level states for ZrO_2) in the supercell containing a given defect with those of the bulk.

2) Errors due to spurious electrostatic interactions in the finite-sized cells were corrected using the scheme proposed by Leslie and Gillan [175] and by Makov and Payne [176], valid for localized defects in the gap and not for shallow donors for the reasons described by Oba *et al.* [177], using the multipole correction,

$$\Delta E_{MP} = (1 + f)\frac{q^2 \alpha_M}{2\varepsilon L} \tag{2.32}$$

where α_M is the supercell lattice-dependent Madelung constant, ε is the static dielectric constant of the host (*e.g.*, for ZnO experimental value = 8.15 [178], for *t*–ZrO_2 experimental value = 39.8 [179]), L is the average distance between two charged defects, and f is a proportionality factor accounting for the L^{-3} term (–0.35 evaluated by Lany and Zunger [67]); α_M/L has been determined as the electrostatic potential created by a charge at the defect position in the supercell model, in a balancing background of charge, repeated with the periodic boundary conditions.

3) No band-filling and band hybridization correction for shallow donors [67,68] were made for the following reasons: (i) the B3LYP band gap value is consistent with experiment, therefore the position of CB minimum is expected to be correct; (ii) the present approach is not based on total energies but on single-particle eigenvalues at Γ point, and therefore there is no spurious band dispersion. Of course, this is valid under the assumption that Γ eigenvalue corresponds to the infinitely diluted limit.

2.1.5.2 Thermodynamics

A reliable and thorough description of the energetics of point defects is a paramount requirement of computational science to provide a valuable comparison with experiments and to predict new materials and properties. A constrained equilibrium with the gas phase reactants is a common assumption that constitutes the basis for an "*ab-initio, atomistic thermodynamics*" approach [180,181]. Formation energies $E_{form\text{-}D,q}$ (see Eq. (2.25)) are computed in order to identify the lowest-energy atomic structure for a given condition of thermodynamic reservoirs, *i.e.* for certain chemical potentials μ_i of the surrounding gas phase. The chemical potentials depend on the experimental growth conditions and in principle they can be varied without bounds. However, since they are subjected to the equilibrium condition with bulk metal oxide MeO, they are constrained to precise range of values. The upper bounds for μ_O and μ_{Me} are half molecular oxygen total energy, $\frac{1}{2}E^{tot}_{O_2}$, and the bulk metal total energy, E^{bulk}_{Me}, at which the condensation of oxygen atoms and the metal precipitation start, respectively. In addition if we consider the following equation

$$\mu_{Me} + \mu_O = E^{tot}_{MeO} \tag{2.33}$$

where E^{tot}_{MeO} is the total energy of the bulk MeO unit, only one of the two chemical potentials is independent and in addition to Eq (2.33) we introduce lower bounds for the chemical potentials. The upper limit of μ_O will correspond to a lower limit of μ_{Me} (oxygen-rich/metal-poor conditions) and vice versa (oxygen-poor/metal-rich conditions):

$$\mu^{\min}_{Me} = E^{tot}_{MeO} - \tfrac{1}{2}E^{tot}_{O_2}, \quad \mu^{\min}_{O} = E^{tot}_{MeO} - E^{bulk}_{Me} \tag{2.34}$$

The total energy of MeO, E^{tot}_{MeO}, can also be expressed in terms of the formation energy:

$$E_{form}[\mathrm{MeO}] = E^{tot}_{MeO} - E^{bulk}_{Me} - \tfrac{1}{2}E^{tot}_{O_2} \tag{2.35}$$

If we use the upper bounds as zero point of energy and relate the oxygen chemical potential to the total energy of the isolated O_2 molecule, we obtain

$$\Delta\mu'_O = \mu_O - \tfrac{1}{2}E_{O_2} \tag{2.36}$$

and the allowed range for $\Delta\mu'_O$ is given by

$$E_{form}[\mathrm{MeO}] \le \Delta\mu'_O \le 0, \quad \text{with} \quad \Delta\mu'_{\mathrm{Me}} = E_{form}[\mathrm{MeO}] - \Delta\mu'_O \tag{2.37}$$

However, this approximation is correct only in the assumption that other equilibria which involve the system are not established. In the case, for example, we want to investigate the doping with a metal Me′, we have to consider also the possibility of precipitation of the metal Me′ and the formation of other oxides (*e.g.*, Me′O, Me′$_2$O) at varying oxygen concentration (see results for Cu-doped ZnO in Sec. 4.3.6). Therefore, in addition to Eq. (2.37), we have to consider the following system of disequations,

$$\begin{cases} \Delta\mu'_{Me'} \le 0 \\ 2\Delta\mu'_{Me'} + \Delta\mu'_O \le E_{form}^{Me'_2O} \\ \Delta\mu'_{Me'} + \Delta\mu'_O \le E_{form}^{Me'O} \end{cases} \tag{2.38}$$

and solving them, we obtain the values for $\Delta\mu'_{Me'}$ in different ranges of $\Delta\mu'_O$ (see results for Cu-doped ZnO in Sec. 4.3.6).

The total energies in Eq. (2.25) and provided by DFT calculations are however referred to a zero-temperature and zero-pressure state and in order to bridge the *pressure gap* [182] with the experimental conditions, we consider the chemical potentials μ_i of the gas molecules involved in the doping mechanism as a function of temperature and pressure. In an ideal-gas-phase reservoir [168], the oxygen chemical potential is defined as

$$\Delta\mu'_O(T, p_{O_2}) = \mu_O(T, p^\circ) + \frac{1}{2}k_B T \ln\left(\frac{p_{O_2}}{p^\circ}\right) \tag{2.39}$$

where the standard oxygen chemical potential $\mu_O(T, p^\circ)$ is easily obtained from enthalpy and entropy changes taken from thermochemical tables at p° = 1 atm [183]. This formalism enables one to compare the relative stabilities of impurities as a function of the gas-reservoir chemical potential and to construct a (T,p) diagram of stability regions of different defect species.

Besides the analysis of formation energy in terms of chemical potentials, it is also possible to analyze the relative stability in terms of the Fermi level E_F of the system. The Fermi level can be considered as the electron chemical

potential and can be varied from the top of the valence band to the bottom of the conduction band. Only the portion of the curves relative to the most stable charge state at a certain Fermi level will be considered. The slope of the curve identifies the charge state: positive slope corresponds to $q = +1$, no slope $q = 0$, and negative slope $q = -1$. The equilibrium concentration of defect D in charge state q is provided by the Boltzmann factor $\exp(-E_{form\text{-}D,q}/k_BT)$.

In conclusion, *ab initio* atomistic thermodynamics provides a connection between the microscopic and macroscopic regimes and allows one to predict the preferred structure of a material as a function of environmental conditions and the regions of enhanced catalytic activity. The most severe limitations come from the fact that only a limited number of structures can be considered and therefore a careful structural sampling is strictly required.

2.1.5.3 Magnetic Properties

Ferromagnetism. The theoretical description of magnetic systems based on DFT requires methods which go beyond the standard LDA or GGA approximations and must include some treatment of the self-interaction problem (see Sec. 2.1.3). This problem is very severe in the case of ferromagnetism in insulators or semiconductors induced by doping. In fact, there are basically two routes for the appearance of ferromagnetism in these systems. In the first case, an atom of lower valency (*e.g.* N) replaces an anion (*i.e.* O) in the compound, thus reducing the number of *sp* electrons in the valence band. This may result in a shift of E_F to higher energies so that E_F crosses the minority spin band, with the appearance of metallic character for one spin subsystem (the minority spin), while a forbidden band (band gap) is still present for the opposite spin subsystem (the majority spin) [184]. This is the physical picture that emerges when high dopant concentrations are considered; DFT calculations without inclusion of the self-interaction correction strongly favour this physical picture [45,184,185,186]. The second physical mechanism is that the impurity atom is basically isolated and introduces localized spin-polarized states above the top of the valence band. In this case is the short-range exchange interaction that can produce a ferromagnetic ordering. Not surprisingly, DFT studies performed by correcting for the self-interaction favour this second kind of situation, but then room-temperature ferromagnetism is more difficult to establish [187,188]. It is only for relatively high defect concentrations that the localized states form an

extended band, and one converges to a magnetic half-metal. Some of the theoretical studies on induced magnetism in nonmagnetic oxides have considered large concentrations of defect centres, up to 25% [184,189]. Not all experimental approaches may be able to incorporate such a large amount of cation vacancies or of non-metal impurities without changing the structure or giving rise to phase segregation. On the other hand, in order to achieve a ferromagnetic ordering, the distance between the various magnetic centres cannot exceed a given value that has been estimated in approximately four nearest neighbours [45]. This implies a minimum concentration of about 5% of defects to establish magnetic percolation on a fcc lattice [45].

However, these theoretical predictions largely depend on the level of theory used. In this respect, one of the most efficient ways to include the self-interaction correction is to use hybrid functionals where a portion of exact Hartree–Fock exchange is mixed in with the DFT exchange. This is the method adopted here. In this work, in particular, magnetic interactions have been considered by evaluating the total energy differences of ferromagnetic (FM) and antiferromagnetic (AFM) states for diluted defect concentration ($\Delta E = E^{AFM} - E^{FM}$). Different geometrical configurations and distances between magnetic defects have been investigated (see Cu-doped ZnO, Sec. 4.3.4).

EPR Parameters. Electron Paramagnetic Resonance (EPR) spectroscopy is one of the most powerful tool for investigating paramagnetic species. It is based on the interaction of electromagnetic radiation with magnetic momenta arising from electrons. Two main interactions involve the unpaired electron and determine the features of the experimental spectra: (a) the hyperfine interaction and (b) the spin-orbit coupling. The former is the magnetic interaction of the electron with nuclei of nonzero nuclear spin which determines the multiline structure of the spectrum (hyperfine structure). The spin-orbit coupling is defined as the interaction of the electron spin S with the electron orbital angular momentum L, and it causes the dependence of the resonance on the orientation of the radical in the external magnetic field.

EPR spectroscopy is intimately related to quantum chemistry, since it provides an experimental means to measure the wave function of the unpaired electron(s). Moreover it is sensitive to very small amounts of paramagnetic centres and this makes it preferred respect to less sensitive techniques such as X-ray photoemission spectroscopy (XPS) . For a complete characterization of the defect, however, a comparison with computed spin properties and

parameters such as the hyperfine coupling constants is necessary. In this context for the calculation of the EPR parameters the use of a hybrid functional is recommended by the fact that recent work has shown the tendency of standard DFT approaches (LDA and GGA) to delocalize electrons and holes resulting, sometimes, in an incorrect description of paramagnetic centres [61,190]. This problem, due to the self-interaction in standard DFT, is partly removed by the use of hybrid functionals where the exact Hartree-Fock (HF) exchange is mixed in with the DFT exchange (see Sec. 2.1.3). In the following, the computational approach to calculate EPR parameters is briefly reported.

The hyperfine interactions of the unpaired electron spin *S* with the nonzero nuclear spin *I* have been calculated by the evaluation of the hyperfine matrix *A* in the hyperfine spin-Hamiltonian, $H_{hfc} = S \cdot A \cdot I$ [191]. The components of *A* can be represented as

$$A = \begin{bmatrix} A_1 & 0 & 0 \\ 0 & A_2 & 0 \\ 0 & 0 & A_3 \end{bmatrix} = a_{iso} U + \begin{bmatrix} T_1 & 0 & 0 \\ 0 & T_2 & 0 \\ 0 & 0 & T_3 \end{bmatrix} \tag{2.40}$$

where U is the unit matrix. The isotropic part, a_{iso}, of each coupling constant is related to the spin density at the nucleus (the Fermi contact term) while the T_n elements constitute the dipolar part of the hyperfine matrix *A*.

For nuclear spins $I > ½$, most notably ^{14}N and ^{2}H, the nuclear transitions are also affected by the quadrupole interaction, which is the interaction between the quadrupole moment of the nucleus and the electric field gradient at that nucleus caused by all electrons. Analysis of the nuclear quadrupole coupling constants gives local information of the electric field gradient near the nuclear spin. The quadrupolar parameters for the paramagnetic species, *e.g.* nitrogen N, (see Sec. 5.3.2.3) have been calculated from the computed electric field gradient (EFG): the nuclear quadrupole coupling constant $\left(\frac{eQ(N)}{h}\right)$ and the asymmetric parameter $\left(\eta = \frac{V_{xx}(N) - V_{yy}(N)}{V_{zz}(N)}\right)$. Here, $eQ(N)$ is the electric quadrupole moment of the N nucleus, *h* is Planck's constant, and V_{ii} are the eigenvalues of the traceless EFG tensor at the position of N nucleus. The principal axis system for the EFG tensor is chosen such that $V_{zz}(N) > V_{yy}(N) > V_{xx}(N)$, whereby $0 < \eta < 1$. (The electric quadrupole moment for N is taken

from Ref. [192] in units of barns: 0.02044).

The description of g values in terms of electronic structure parameters requires to account for various magnetic contributions and to work with sufficiently accurate eigenfunctions. Spin-orbit interaction can be either accounted for self-consistently or treated as a perturbation. In the latter case, the g_{ij} elements of the g tensor can be expressed in terms of deviation from the free electron g_e value according to Eq. (2.41),

$$g_{ij} = g_e \delta_{ij} + 2\lambda \sum_{n=0} \frac{\langle 0|L_i|n\rangle\langle 0|L_j|n\rangle}{E_n - E_0} \tag{2.41}$$

where δ_{ij} is the Kronecker delta ($\delta = 0$ for $i \neq j$ and $\delta = 1$ for $i = j$), L_i and L_j are the components of the orbital angular momentum operator, 0 represents the ground state and n the different excited states and E_0 and E_n are the energies of the ground state and the excited states, respectively [191]. Here we use the scheme proposed by Neese [193] and implemented in the code GAUSSIAN03 [158] where the g tensor is evaluated as a mixed second derivative property with respect to the applied field and the electron magnetic moment.

2.1.5.4 Vibrational frequencies

Vibrational frequencies, referred to the Γ point and within harmonic approximation, were calculated on the optimized geometry by diagonalising the mass-weighed Hessian matrix W_{ij}

$$W_{ij}(\Gamma) = \sum_G \frac{H_{ij}^{0G}}{\sqrt{M_i M_j}} \tag{2.42}$$

where H_{ij}^{OG} is the Hessian matrix of second derivatives of the electron-nuclear repulsion energy E evaluated at equilibrium, with respect to the displacement coordinates u_i and u_j of atom A in cell 0 and of atom B in cell G, respectively:

$$\sum_G H_{ij}^{0G} = \sum_G \left[\frac{\partial^2 E}{\partial u_i^0 \partial u_j^G} \right]_0, \quad i = 1,...,3N; \quad j = 1,...,3N \tag{2.43}$$

The Hessian matrix is obtained by numerical differentiation of analytical first derivatives $v_j = \partial E / \partial u_j$ using a difference quotient or “two point” formula [70,153]:

$$h(x) = \frac{[v_j(x + u_i) - v_j(x)]}{u_i} \tag{2.44}$$

with a step u_i = 0.001Å.

The computed frequencies were analysed through the J-ICE program [194] and scaled for the factors obtained by the ratio between the experimental and the theoretical values for the molecule considered (see Sec. 6.4).

Vibrational normal modes that involve H atoms, and in particular X–H stretching modes, can be largely affected by anharmonicity. The procedure adopted in this work to compute the anharmonicity of X–H stretching modes, reported and validated in several previous works [155,195,196], assumes that the X–H distance is treated as a pure normal coordinate decoupled with respect to all other modes. While this assumption is fully justified for an isolated OH vibration, *e.g.* in brucite [195], silica or zeolite [155], this is not allowed for molecules as NH_3, CH_4 or H_2O with all the stretching modes coupled. For this reason NH_x modes in Sec. 6.4 are scaled in respect to the free NH_3 molecule while the stretching mode of the surface hydroxyl group OH coming from the partial dissociation of adsorbates is calculated including anharmonic contributions. A sixth order polynomial fit is used to interpolate the total energy values for a set of OH values around the equilibrium (–0.2/+0.3 Å). The one-dimensional nuclear Schrödinger equation is solved using the program ANHARM developed by P. Ugliengo [197] and provides the three lowest eigenvalues E_0, E_1 and E_2 that are then used to compute the fundamental anharmonic frequency $\omega_{01} = E_1 - E_0$, the first overtone $\omega_{02} = E_2 - E_0$ and anharmonic constant $\omega_e x_e = (2\omega_{01} - \omega_{02})/2$.

2.1.5.5 Binding Energies

The binding energy, is defined as the total (electronic) energy difference, per unit cell and per adsorbate molecule, between surface+adsorbate (*SA*) and the clean surface (*S*) and free molecule (*A*):

$$E_b(SA) = E_{SA}(SA) - E_S(S) - E_A(A) \tag{2.45}$$

where the subscripts indicate the optimized geometry used. Since we used a local basis set, the results are known to be affected by the basis set superposition error (BSSE) that was taken into account and corrected using the counterpoise correction method, E_b^{CP} [198]:

$$E_b^{CP}(SA) = E_{\text{int}}^{CP}(SA) - E_{surf}^{CP}(S) - E_{ads}^{CP}(A) \tag{2.46}$$

with the interaction correction term $E_{\text{int}}^{CP}(SA)$ and the isolated surface $E_{surf}^{CP}(S)$ and adsorbate correction terms $E_{ads}^{CP}(A)$ defined as:

$$\begin{aligned} E_{\text{int}}^{CP}(SA) &= E_{SA}^{SA}(SA) - E_{SA}^{SA}(A) - E_{SA}^{SA}(S), \\ E_{surf}^{CP}(S) &= E_{SA}^{S}(S) - E_{S}^{S}(S), \\ E_{ads}^{CP}(A) &= E_{SA}^{A}(A) - E_{A}^{A}(A) \end{aligned} \tag{2.47}$$

where the superscripts indicate the basis set functions used.

In order to get a more realistic comparison with the experimental adsorption enthalpy ΔH_{exp} obtained from TDS experiments, we considered also the corrections to enthalpy to obtain the adsorption enthalpy ΔH_{calc}. The latter was obtained by adding the zero-point energy (*ZPE*) and the thermal energy (*TE*) contributions. The *TE* term for NH_3 adsorption on ZnO $(10\bar{1}0)$ surface was calculated at T = 298 K that is close to the TDS peak at 280 K for the full-monolayer desorption (see Sec. 6.4). It is defined as $TE = E_{\text{trans}}(T) + E_{\text{rot}}(T) + E_{\text{vib}}(T) + RT$ for the molecule in the gas phase and as $TE = E_{\text{vib}}(T)$ for the solid (ZnO with and without the adsorbate) where $E_{\text{trans}}(T)$, $E_{\text{rot}}(T)$, and $E_{\text{vib}}(T)$ are the translational, rotational, and vibrational contributions, respectively, and RT was added for the molecule to account for the PV term (assuming ideal gas approximation) [199].

2.2 Experimental Methods

2.2.1 CW and Pulsed EPR

This Section is aimed at providing a short introduction to the experimental techniques of EPR spectroscopy employed in this work. For a detailed overview we refer the reader to some fundamental text-books [191,200,201] and review articles [202,203].

The classical continuous wave (CW) EPR spectroscopy is by far the most commonly used electron magnetic resonance technique. In a normal CWEPR experiment, the sample is irradiated with a fixed frequency and a given interval of magnetic field is swept to look for the condition of the magnetic resonance described by Eq. (2.48).

$$h\upsilon = g\mu_B B \tag{2.48}$$

where h is the Planck constant, ν the microwave frequency, μ_B the Bohr magneton, B the magnetic field, and g the effective g value. A CWEPR spectrum is therefore a diagram where microwave absorption (or more frequently its first derivative) is reported as a function of the magnetic field swept in the experiment.

When anisotropies of the g tensor give rise to considerable complexity, as in the case of the radical anion N_2^- in bulk MgO (see Sec. 9.3), an excellent tool, commonly used, is the multifrequency approach. This approach is based on the fact that the magnetic field separation ΔB between two lines due to anisotropy of the g tensor varies linearly with the microwave frequency according to Eq. (2.49) which is directly derived from Eq. (2.48).

$$\Delta B = \frac{h\nu}{\mu_B}\left(\frac{1}{g_1} - \frac{1}{g_2}\right) \tag{2.49}$$

The use of a high-frequency mode, for instance, instead of a classical X-band mode, increases, for a given paramagnetic centre, the magnetic field separation of the various g components. Moreover, the hyperfine line separation, arising from the interaction between the nuclear spin and the unpaired electron, is not affected. Therefore, if X-band spectra (using a frequency of about 9.5 GHz) show very complex overlapping hyperfine structures, they can be better resolved by running a high-frequency spectrum. The most commonly used high-frequency bands are the Q-band at about 35 GHz and the W band at about 94 GHz (see Sec. 9.3).

An advanced EPR technique is the pulsed EPR spectroscopy that combines the sensitivity and the selectivity of EPR spectroscopy, with time resolution associated with pulsed methodology. In pulsed EPR, or Electron Spin Echo (ESE)-detected EPR, a $\pi/2$ pulse is applied, which turns the magnetization **M** from z into the xy plane (see Fig. 2.4b). After the pulse, **M** then starts to precess around the magnetic field direction. Since the field felt by each electron is slightly different, the electron spins on some centres precess quicker than others, and dephasing of the macroscopic magnetization occurs, known as ‘‘free induction decay’’ (FID) (see Fig. 2.4c). Then, a second π pulse is applied at a time τ after the first pulse by which all electron spins are rotated by π into the xy plane (see Fig. 2.4d). The effect is that the fast-

precessing spins are now put back the slower-precessing spins and they have to catch up. The spins then continue to precess, and all spins are in phase again at a time τ after the second pulse and the macroscopic magnetization that occurs can be detected and is called electron spin echo (ESE) (see Fig.2.4e). The most famous and common pulse sequence is $\pi/2 - \tau - \pi - \tau -$ echo and is known as Hahn echo sequence [204]. The microwave frequency is fixed while the magnetic field is swept, and the amplitude of the echo signal is monitored. Only when the resonance condition of Eq. (2.48) is fulfilled an echo becomes visible.

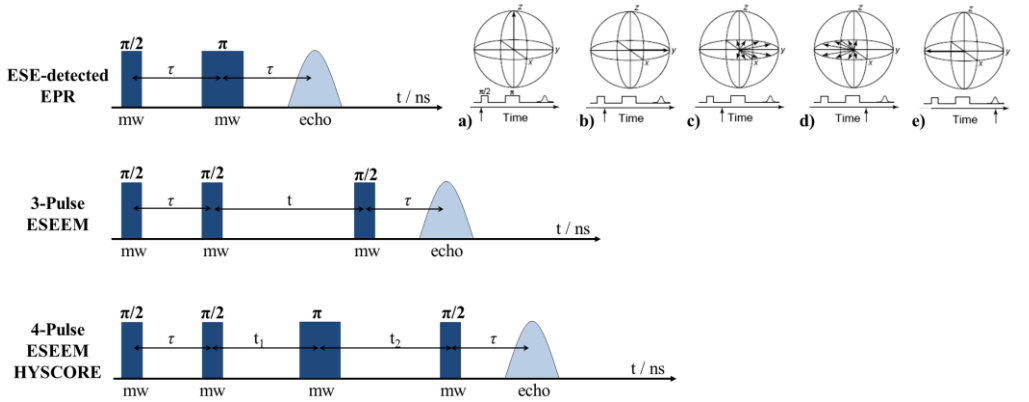

Figure 2.4. Most commonly used pulsed EPR techniques and relative pulse sequences. For the two-Pulse sequence it is reported also the evolution of the **M** vector in the *xy* plane [from a) to e)].

From ESE-detected EPR experiments, electronic *g* values can be obtained with high accuracy. However, if one wants to elucidate the nuclear hyperfine and quadrupole coupling constants, sometimes more complicated pulse sequences are needed. In particular, two powerful methods are the Spin Echo Envelope Modulation (ESEEM) spectroscopy and the hyperfine sublevel correlation spectroscopy (HYSCORE) that is the two-dimensional analogue of ESEEM (see Fig. 2.4). They are especially suited when the nuclear transition frequencies are close to 0 MHz. Above 5 MHz it is usually employed the electron nuclear double resonance (ENDOR) method [201] that is a hybrid NMR/EPR method in which both microwave and radiofrequency pulses are used to flip the electron and nuclear spins, respectively. The pulse sequences for ESEEM and HYSCORE experiments, instead, only involve microwave pulses and they are non-selective with respect to the nuclear spin state, that

means that the microwave pulses are able to flip the electron and the nuclear spin at the same time. A coherent superposition of nuclear spin states is created by the application of the microwave pulse and it evolves during the time intervals between successive pulses. The coherences are larger for the nearby nuclei whose nuclear magnetic moment has a large magnetic dipole–dipole interaction with the unpaired electron. Because of these coherences, echo modulations will be visible when the time between the two pulses is increased stepwise and the ESE signal is monitored. The ESEEM spectrum is the frequency spectrum obtained from the Fourier transform of the modulations and it provides the nuclear-spin transition frequencies and allows one to interpret the hyperfine interactions. For nuclear spins $I > ½$, the nuclear transitions are also affected by the quadrupole interaction, and the analysis of the spectra allows elucidation of nuclear quadrupole coupling constants (see Sec. 5.3.1). The ESEEM technique was pioneered by Rowan *et al.* [205] and is commonly used with either a $\pi/2 - \tau - \pi - \tau -$ echo sequence in which the time τ is swept, or a $\pi/2 - \tau - \pi/2 - T - \pi/2 - \tau -$ echo sequence in which the time T is swept (see Fig. 2.4). The four-pulse variant of ESEEM spectroscopy is called HYSCORE spectroscopy and it was pioneered by Höfer *et al.* [206]. It employs a $\pi/2 - \tau - \pi/2 - t_1 - \pi - t_2 - \pi/2 - \tau -$ echo sequence in which both the time intervals t_1 and t_2 are swept, thus giving rise to a two-dimensional modulation pattern (see Fig. 2.4). A spectrum similar to a two-dimensional NMR spectrum is obtained after a double Fourier transformation, and it allows one to correlate and group together nuclear frequencies that stem from the same nucleus. For this reason, HYSCORE technique is very useful when many nuclei contribute to the ESEEM spectrum.

Finally, a particularly efficient approach to enhance weak echo modulations till one order of magnitude is the use of matched or high-turning-angle (HTA) mw pulses for optimizing the generation and transfer of coherence. In Sec. 5.3.1 Matched HYSCORE experiments were employed to increase the amplitudes of combination peaks and to get information on the relative signs of hyperfine coupling constants.

Instruments. Continuous wave (CW) and pulse X band spectra [microwave (mw) frequency 9.76 GHz], reported in Chapters 5 and 9, have been recorded on a ELEXYS 580 Bruker spectrometer equipped with a liquid-helium cryostat from Oxford Inc (see Fig. 2.5). The magnetic field was measured with a Bruker ER035M NMR Gaussmeter.

The W-band CW-EPR spectra, reported in Chapter 9, were recorded using a

Bruker E600 spectrometer equipped with the standard TeraFlex probe-head with a TE_{011} cavity. Experiments were carried out at 40 and 10 K, using a Oxford ITC503S temperature controller.

The CW-EPR spectra were simulated using the EPRsim32 program [207]. The HYSCORE spectra were simulated using the ”saffron” routine built into the Easyspin package [208].

Figure 2.5. ELEXYS 580 Bruker spectrometer used in the group of Prof. Elio Giamello at the University of Turin.

2.2.2 HREELS and TDS Apparatus

2.2.2.1 HREELS

High Resolution Electron Energy Loss Spectroscopy (HREELS) analyzes the energy distribution and sometimes also the angular distribution of electrons, with a well-defined energy (usually $\leq$ 10 eV), scattered from a target. Three main inelastic excitation mechanisms are involved in HREELS: dipole scattering, impact scattering and negative ion resonance (NIR). Since 100 eV electron has a mean free path in a solid of about 1 nm that increases slowly with increasing energy, HREELS is a large surface sensitive technique, suitable to investigate vibrational and electronic surface excitations (plasmons, HOMO–LUMO excitations) of solids or adsorbed molecules on surface. It is usually employed to analyze chemical bonding and adsorption geometry of adsorbates, in order to prove the reaction mechanism by identifying the

intermediates. By comparison with infrared spectroscopy, the most common vibrational spectroscopy, HREELS has a relative poor energy resolution (usually 4 meV = 32 cm^{-1}; the best one obtained is 0.6 meV = 5 cm^{-1} for CO on W(110)) [209] but it has a high detection sensitivity and a wider energy window of vibration (normally from 5 to 500 meV = 40–4000 cm^{-1} in comparison with 800–4000 cm^{-1} by IR).

HREELS is a standard method for metals while for metal oxides it is severely affected by experimental difficulties such as charging problems. In fact, HREELS is based on the solution of Laplace equation for the potential and this is dramatically complicated by the presence of space charge $\rho(r,\vartheta,z)\frac{(\Delta r)^2}{\varepsilon_0}$, which usually only occurs in dielectric media because in a conductive medium the charge tends to be rapidly neutralized or screened. To overcome these charging problems for insulating oxides, a special model system, namely ultrathin oxide films grown epitaxially on metal surfaces, has been introduced.

In HREELS only vibrations with dynamic transition dipole moment are IR-active. Moreover, because of the high electron mobility, metals have an additional selection rule in comparison with oxide systems: the metal-surface selection rule. The electrons in metals are able to screen centres of charge in electric fields and to respond fully to variations in their magnitude and positions, at least at the frequencies with which we are concerned (those of interatomic vibrations). For this reason only those vibrational modes with a component of dynamic dipole moment perpendicular to the surface can be observed (usually these modes belong to the totally symmetric representation of the system point group).

Besides charging problems, the second major problem concerning metal oxides is the presence of intense optical Fuchs-Kliewer phonons [210]. Although the losses caused by the excitation of these phonons provide useful information about the stoichiometry and the structure of oxide surfaces, their intensity is so strong that they make the other energy losses extremely difficult to detect. Surface phonons are always present in each system since they are lattice vibrations but for metals they are less intense for two reasons: (i) monoelemental systems do not exhibit dipole transitions so that the intensity is lower because the selection rules are not respected; (ii) in metals or oxides with little band gap (*e.g.* RuO_2) dipole vibrational transitions are compensated by electron transitions because of transition times (electron transition time $\tau \sim$

10^{-15} s << vibrational transition time ν ~ 10^{-12} s). To overcome the effect of surface phonons there are two solutions:

1. Acquisition of spectra using high primary electron energies and off-specular analysis in the impact scattering regime;
2. Fourier deconvolution of combined losses [211].

A recent new application of HREELS concerns the measure of small ionization energies of shallow donor defects [212]. The broadening of the quasi-elastic peak Δ (given by $\Delta_{tot}^2 = \Delta_{app}^2 + \Delta^2$, where Δ_{app} denotes the apparatus broadening, [212]) depends in fact on the density of free charge carriers n_c and on the sample temperature:

$$\Delta^2 = \frac{C}{4}\pi^2\omega_{sp}^2\left[\frac{2}{e^{\hbar\varpi_{sp}/k_BT}-1}+1\right]\cos\alpha \qquad (2.50)$$

with $C = \frac{4}{\pi}\frac{1}{\varepsilon+1}\frac{1}{\cos^2\alpha}\frac{1}{ka_0}$, $\omega_{sp} = \varpi_p/\sqrt{1+\varepsilon}$, and $\varpi_p = \sqrt{n_c e^2/m^*\varepsilon_0}$, with ε the relative dielectric constant (*e.g.*, 4.6 for ZnO, [213]), k the wave vector of the incident electron, a_0 the Bohr radius, m* the effective mass of electrons (*e.g.*, 0.19 m_e for ZnO, [214]), ε_0 the vacuum dielectric constant, k_B the Boltzmann constant, ω_{sp} and ω_p the surface and bulk plasmon frequencies, respectively and α the electron angle of incidence (55°). For a shallow defect, the charge carrier density n_c depends on the temperature, *e.g.* copper interstitials act as shallow donors with small ionization energies in ZnO and therefore a low temperature increment is sufficient to promote electrons in the CB (see Cu-doped ZnO in Sec. 4.3.1). For a *n*-type semiconductor, the CB charge density n_c can be calculated from Eq. (2.51) [215,216]:

$$\ln n_c = \frac{1}{2}\ln\left(\frac{N_d N_{c,0}}{2}\right) - \frac{\varepsilon_d}{2k_BT} + \frac{3}{4}\ln T \qquad (2.51)$$

where N_d is the density of donor atoms, $N_{c,0}$ defines the effective conduction band density of states and corresponds to $N_{c,0} = \left(\frac{m^* k_B}{2\pi\hbar^2}\right)^{3/2}$, ε_d denotes the donor state ionization energy. If we insert the expression for n_c in (2.51) into (2.50), and we plot Δ^2 as a function of T, we can experimentally evaluate the donor state ionization energy ε_d by means of a nonlinear least squares regression analysis. This value can be then compared with the calculated thermodynamic transition level of the model defect (see Cu-doped ZnO in Sec.

4.3.1).

2.2.2.2 TDS

Thermal Desorption Spectroscopy (TDS) belongs to the wide class of Temperature Programmed Desorption (TPD) techniques and it is one of the most important methods for the determination of kinetic and thermodynamic parameters of desorption processes or decomposition reactions. TDS is generally used to detect the chemistry of adsorbed molecules on well-defined single crystal surfaces in UHV conditions. The surface is heated resistively by a generally linear heating rate $\beta(t) = dT / dt$, and monitored by a thermocouple. An electron ionization quadrupole mass spectrometer (EI-MS) is used to detect the vaporized particles. The MS detector is covered by a shield, with a small aperture that is positioned close to the surface (~1mm) to avoid detecting gases not evolved by the surface. Since the slow heating rate induces thermal decomposition of large molecules before desorption, if TDS is used for identification of adsorbed molecules it is limited to small molecules.

The main information derivable from TDS analysis is the evaluation of the kinetic parameters: the reaction order, n, the activation energy for desorption, E_d, and the pre-exponential factor, ν_n. These parameters are correlated with the desorption rate, r_{des}, by the Arrhenius-type equation, called Polanyi-Wigner equation:

$$r_{des} = -\frac{d\Theta}{dt} = K_n \Theta^n = \nu_n \cdot \exp\left(-\frac{E_d}{RT}\right) \cdot \Theta^n \qquad (2.52)$$

where Θ is the surface coverage, defined as the ratio between the number of adsorbed particles and the number of adsorption sites available at surface.

A preliminary condition for the validity of the Polanyi-Wigner equation is that the desorption signal must be proportional to r_{des}. This requirement is achieved if re-adsorption of desorbed particles on the sample is avoided by the use of a constant and sufficiently high pumping speed in UHV conditions. Moreover, for the application of the Polanyi-Wigner equation it is necessary one rate-limiting step of the desorption process.

Two analysis types are available: qualitative and quantitative analyses.

Qualitative or shape analysis provides a rough evaluation of the number of stable adsorbed phases and the desorption order. The latter can be estimated by using different initial coverages, Θ_0. Zeroth-order desorption (n = 0) is

spontaneous and generally shows a blue shift of desorption rate maximum temperature (T_{max}) by increasing Θ_0; first order desorption (n = 1) entails the desorption of intact species or their decomposition products and usually exhibits a constant T_{max} and an asymmetric shape; second order desorption (n = 2) involves recombination followed by desorption and shows a red shift of T_{max} and symmetric shape of desorption spectra with increasing coverages. However, if lateral interactions between adsorbate particles are present, the desorption parameters become coverage-dependent [$E_d(\Theta)$, $\nu_n(\Theta)$] and the interpretation becomes more difficult if not impossible. The lateral interactions involve adsorbed particles, adsorbate-induced changes in the surface and different types of adsorption sites. Other qualitative methods employ an index to evaluate the desorption order (*e.g.* shape index [217], skewness index [218]).

Several quantitative methods exist for the evaluation of the kinetic parameters n, E_d and ν_n [219,220,221,222,223]. They may be divided in two groups: (a) integral methods which relate kinetic parameters with peak characteristics like half-width $W_{1/2}$ and T_{max} but they are valid just if parameters are not coverage-dependent; (b) differential techniques that plot r_{des} versus 1/T from different TPD spectra and evaluate E_d and ν_n from slope and intercept, respectively.

The most important integral analyses are Redhead's peak maximum method [224] and Chan-Aris-Weinberg (CAW) approach [218].

The differential approach involves the construction of an Arrhenius plot based on Polanyi-Wigner equation in the form:

$$\ln\left(\frac{r_{des}}{\Theta^n}\right) = \ln \nu_n - \frac{E_d}{RT} \tag{2.53}$$

If E_d and ν_n are coverage-independent they are estimated from the slope and the intercept of $\ln\left(\frac{r_{des}}{\Theta^n}\right)$ versus 1/T, respectively.

A reliable differential method for the evaluation of $E_d(\Theta_0)$ and $\nu_n(\Theta_0)$ over the entire coverage range was also proposed [225,226]. It is based on the construction of an Arrhenius plot from several TDS experiments conducted at different Θ_0 [225] and/or β [226] (the heating rate must vary over two orders of magnitude to achieve reasonable range of temperature and rate for the plot).

Instruments. All the experiments were carried out in an ultra-high vacuum

(UHV) apparatus (see Fig. 2.6) consisting of two chambers, separated by a valve. The upper chamber has a base pressure of 5×10^{-11} mbar and since it is used for the preparation of the sample, it is also called preparation chamber. It is equipped with an Argon ion sputter gun for cleaning sample surface, a low energy electron diffraction (LEED) optic and a mass spectrometer (Pfeiffer, Prisma) that is differentially pumped with an ion getter pump during thermal desorption spectroscopy (TDS) experiments. The lower chamber has a base vacuum of 2×10^{-11} mbar and it holds a high-resolution electron energy loss (HREEL) spectrometer (Delta 0.5, SPECS, Germany). HREEL spectrometer operates with a straight-through resolution close to 1 meV (8.065 cm^{-1}) and with an incident angle of electron beam fixed at 55° with respect to the sample surface normal. Energy losses in either specular (reflective angle of 55°) or off-specular directions can be detected by a rotatable analyzer.

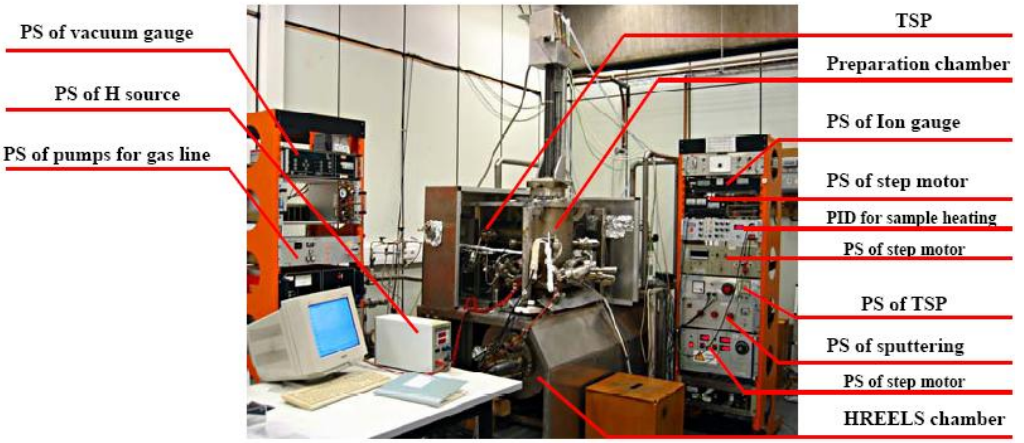

Figure 2.6. HREELS apparatus used in the group of Dr. Yuemin Wang at the Ruhr Universität Bochum. Note: PS indicate power supply. Courteously reproduced from Ref. [227].

The UHV conditions are achieved thanks to a vacuum apparatus consisting of a turbomolecular pump with large pumping speed (300 l/s) and an oil-free fore vacuum system based on a small turbomolecular pump combined with a membrane pump. HREELS chamber is usually pumped only by an ion getter pump. Moreover, a titanium sublimation pump (TSP) is placed in both chambers.

The single crystal sample (2 mm × 5 mm × 7 mm) is mounted on a Ta plate (thickness, 0.5 mm) by specifically designed thin Ta foils, with the

thermocouple contacting the sample on the lateral side. Gases are dosed by backfilling the chamber through different leak valves that connect the preparation chamber with gas bottles and exposures are given in units of Langmuir (1 L=$1.33 \cdot 10^{-6}$ mbar·s).

2.2.3 UHV-FTIRS

Fourier transform infrared spectroscopy (FTIRS) is one of the most powerful surface analytical techniques. Its main success is related to the study of vibrations of adsorbed species on metal surfaces. In particular, it has been successfully applied to obtain a number of informations about the chemical nature of adsorbate species, the coordination symmetry, the degree of unsaturated sites, the intermediate species formed via a certain reaction, the presence and the nature of Lewis and Brønsted acid sites [228,229,230,231, 232]. Unfortunately, its application to metal oxide surfaces is instead severely affected by several experimental difficulties and IR investigations on well-characterized surfaces of oxide single crystals are very scarce in literature. These limitations are especially related to the significantly smaller IR bands intensity of adsorbates on oxide single crystals than those observed for the same adsorbates on metal surfaces because of the absence of image dipoles. Kattner and Hoffmann [233] estimated a decrease of the signal-to-noise (S/N) ratio of the optical properties of oxides by one to two orders of magnitude relative to metals. Furthermore, there are severe problems in IR investigations of powder samples because of air contaminants in IR spectrometer and also on sample, resulting in the reaction of adsorbed molecules with pre-adsorbed species on powder surface, such as hydroxyl groups or carbon containing species. However, a new ultrahigh vacuum (UHV) infrared spectroscopy apparatus [234] (see Fig. 2.7), designed for the spectroscopic characterization of oxides, single crystals as well as powders, has allowed the group of Dr. Y. Wang (Ruhr University of Bochum) to partially overcome these limitations and to provide a deep understanding of a number of systems [235,236,237,238,239,240]. The innovative design of the apparatus (see Fig. 2.7) allows carrying out both reflection-absorption IR spectroscopy experiments at grazing incidence on well-defined oxide single crystal surfaces and FTIR transmission measurements for powder particles. Furthermore high-quality IR data with high sensitivity and stability are guaranteed by the presence of a completely evacuated optical path that avoids background

signals from gas phase H_2O, CO_2, and other species.

Instruments. An innovative ultra-high vacuum–Fourier transform infrared spectroscopy (UHV-FTIRS) apparatus (see Fig. 2.7) that combines a state-of-the-art vacuum IR spectrometer (Bruker, VERTEX 80v) with a novel UHV system (PREVAC) has been used to study ammonia adsorption on ZnO nanoparticles (see Chapter 6). The VERTEX 80v is a latest generation, high-resolution vacuum FTIR spectrometer with an actively aligned UltraScan interferometer, providing a standard optical resolution of better than 0.2 cm^{-1}. The detector chamber is equipped with two detectors: a liquid nitrogen cooled mercury-cadmium-telluride (MCT) detector and a room temperature DTGS detector, used to collect IR signals from reflection and transmission measurements, respectively. The UHV system (PREVAC) consists of four components: load-lock, distribution, measurement (FTIR), and magazine chambers with a base pressure of 1 x 10^{-8} mbar, 1 x 10^{-10} mbar, 2 x 10^{-10} mbar and 1 x 10^{-10} mbar, respectively. For additional details we refer the reader to Ref. [234].

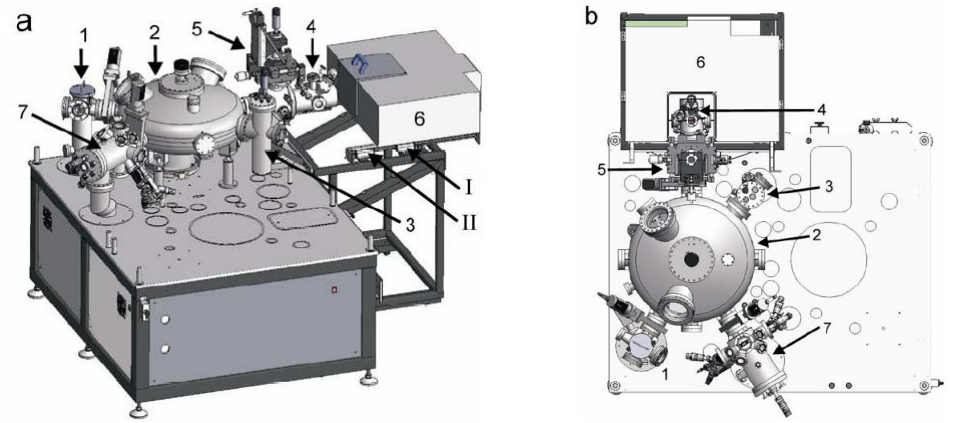

Figure 2.7. The UHV-FTIRS apparatus, used in the group of Dr. Yuemin Wang at the Ruhr Universität Bochum, in (a) perspective view and (b) top view. The labelled components are: 1) load-lock, 2) distribution, 3) magazine, (4) measurement (FTIR) chambers, 5) sample manipulator, 6) vacuum FTIR spectrometer, 7) preparation chamber. I and II represent two slides, permitting to move the spectrometer to two different positions. Courteously reproduced from Ref. [241].

PART II

ZINC OXIDE

Background

Zinc oxide is a wide gap semiconductor (3.44 eV at 2 K [174]) that has been attracting an increasing attention in the scientific community since the last decade because of its promising applications in optoelectronics and spintronics [242,243,244,245].

Zinc oxide crystallizes in the hexagonal wurtzite-type structure with lattice parameters a = 3.24 Å and c = 5.21 Å and space group $P6_3mc$ or C_{6v} [246]. Zn atoms are tetrahedrally coordinated to four O atoms (and vice versa) and the Zn d-electrons hybridize with the O p-electrons (see Fig. II.1). In Figure I the projected density of states clearly shows that the bottom of the conduction band is formed essentially from the 4s states of Zn^{2+} and the top of the valence band from the 2p states of O_2^-. The cubic zinc blende-type structure can be stabilized by epitaxial growth of ZnO on suitable cubic substrates while a transition to the rocksalt phase can be achieved at a pressure of ~9 GPa [247,248].

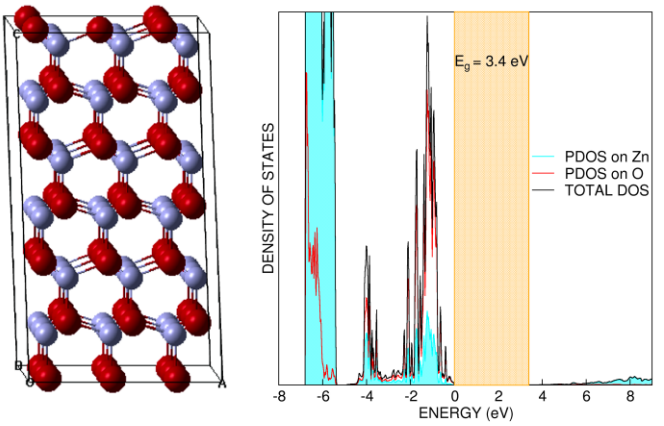

Figure II.1. (Left side) Wurtzite ZnO lattice structure where large dark red spheres and small light grey spheres represent O and Zn atoms, respectively. (Right side) Total and projected (on Zn and O atoms) B3LYP densities of states for bulk ZnO.

The wurtzite structure is the same as GaN to which ZnO provides therefore a close match for optoelectronic devices [249]. In particular, the availability of high-quality ZnO bulk single crystal and the amenability to wet chemical etching, that favor the device design and lower the fabrication costs, pointed ZnO as an alternative to GaN in optoelectronics. Furthermore, ZnO has a large exciton binding energy (~60 meV, cf. ~25 meV for GaN [174,250]) that allows intense near-band-edge excitonic emission at room and higher temperatures and makes ZnO a strong candidate for solid-state white lighting [251]. The possibility to grow epitaxial layers, quantum wells, nanorods and quantum dots has recently allowed the use of ZnO-based materials for blue/UV optoelectronic devices, like light emitting and laser diodes and as transparent conducting oxide (TCO) layers for transparent electrodes in flat panel displays and solar cells.

The use of ZnO in almost all the above applications has been, however, severely hindered by the lack of control over its electrical conductivity. ZnO crystals show almost always a *n*-type conductivity after synthesis that has been widely debated in the scientific community [13,30,31,242,243,244,245]. For a long time the unintentional conductivity has been attributed to intrinsic defects, like oxygen vacancies or zinc interstitials but this hypothesis has been recently excluded by density functional calculations and optically detected electron paramagnetic resonance experiments [30]. The most plausible cause of the *n*-type conductivity is at the moment the incorporation of shallow donor impurities, specifically hydrogen, that is nearly ubiquitous in all processes of preparation [24,252,253]. Interstitial H, that commonly has an amphoteric behaviour in semiconductors, acts only as shallow donor in ZnO but because of its high mobility, it appears unlikely to be the responsible of the *n*-type conductivity. However, recently it has been demonstrated that H can be captured in an oxygen void where it behaves still as a shallow donor and can therefore explain the high stability of the *n*-type conductivity [252].

The major issue concerning ZnO-research is the achieving of a stable, reliable and reproducible *p*-type doping. In photocatalysis *p*-type doping of ZnO is necessary to reduce the wide band-gap exploiting the visible light (like for N-doped TiO_2 [254]). In optoelectronic devices (TTFT, LED, OLED) *p*-type doping is the key prerequisite for the production of *p*-*n* homojunctions (today only the more expensive *n*-ZnO/*p*-GaN and *n*-ZnO/*p*-SiC heterojunctions are available [255]). The *p*-type doping is severely hampered

by a series of limitations, first of all the tendency toward the *n*-type conductivity and the presence of compensating donor centres (*e.g.* oxygen vacancies and zinc interstitials). Furthermore, there are very few candidate shallow acceptors in ZnO and some of them, like alkali metals (*i.e.* Li, Na, K) behave also as shallow donors if they enter the lattice in an interstitial void [30,31]. Metals of IB-column (*i.e.* Cu, Ag, Au) are deep acceptors in the cation sites and the elements of V-column (*i.e.* P, As, Sb) are deep acceptor in the anion sites [30,31]. The most promising candidate as a shallow acceptor has been indicated to be nitrogen substitutional to oxygen, because of the similar ionic radius and electronegativity. Although some works [256,257] have claimed the achieving of stable *p*-type conductivity upon nitrogen doping, no reproducible homogeneous *p*-*n* junctions followed and a thorough understanding of the nitrogen defects in ZnO is still missing.

Zinc oxide has been emerging also as a promising candidate for spintronics applications [13]. The introduction of spin carriers in ZnO by means of a dilute controlled doping is expected to open the way to new magnetic, electronic and optical functionalities of the material. In particular, the transition metal (TM) doped ZnO represents a valuable material for diluted magnetic semiconducting oxide (DMSO) to be used, for example, in electrically controlled magnetic sensors, spin light-emitting diodes (spin-LEDs) and spin field effect transistors (spin-FETs) [13,258]. Achievement of room temperature (RT) ferromagnetism by Mn and Cu doping, avoiding unwanted secondary ferromagnetic phases due to metal clustering, is the final goal of nowadays experimental efforts [13]. Few theoretical studies [51,52] have already inspired some experimental work, although initial expectations were not fulfilled by actual results [259,260,261]. In diluted magnetic semiconductors (DMSs), *p*-type doping with light elements has been also investigated to avoid the problems connected with precipitation of metal clusters in the case of TM dopants [262].

Finally, zinc oxide finds several industrial applications as heterogeneous catalyst thanks to the chemical properties of its surfaces [244]. In particular, ZnO plays a crucial role in the production of methanol, the third most important chemical product of chemical industry. ZnO substrate has been observed to promote small Cu particles as active catalyst but the atomistic mechanism is still under investigation [263]. For this reason most of the works concerning adsorbates on ZnO surfaces is focused on molecules relevant for methanol production from synthesis gas (H_2, CO, CO_2), either as products, or intermediates (*e.g.*, formiate) [244, 264,265,266].

ZnO crystals are dominated by four low Miller index surfaces: the nonpolar

$(10\bar{1}0)$ and $(11\bar{2}0)$ surfaces and the polar zinc-terminated (0001) and oxygen-terminated $(000\bar{1})$ surfaces (see Fig. II.2).

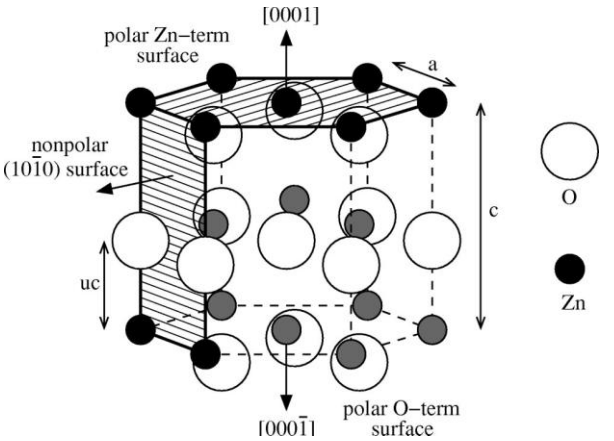

Figure II.2. Schematic representation of wurtzite structure of ZnO with the low Miller index surfaces: the nonpolar mixed-terminated $(10\bar{1}0)$ surface and the polar zinc-terminated (0001) and oxygen-terminated $(000\bar{1})$ surfaces. Courteously reproduced from Ref. [267].

The mixed-terminated $(10\bar{1}0)$ surface is the energetically most favourable one and the most abundant in polycrystalline ZnO samples. The absence of the electrostatic instability made this the surface of choice for a great number of theoretical works on this surface [268,269,270,271]. On the opposite, the electrostatic instability of the polar surfaces severely limited their theoretical characterization [272]. These surfaces belong to the class of the so-called Tasker-type3 surfaces [273] and are formed by alternating layers of oppositely charged ions (see Fig. II.2). The sequence of ions creates a dipole moment perpendicular to the surface which diverges with slab thickness and with sample size [274]. Therefore, in principle, polar surfaces of very small oxide particles could be stable, but, for macroscopic samples, the electrostatic instability becomes so large that either the electronic or geometric structure of the surface has to change [244,272]. However, these stabilization mechanisms differ for different oxides and for the various polar surfaces. For ZnO such mechanisms are still very controversial and highly debated in literature [244].

CHAPTER 3

Donor Defects*

Abstract

A hybrid density functional study based on a periodic approach with localized atomic orbital basis functions has been performed in order to compute the optical and thermodynamic transition levels between different charge states of defects impurities in bulk ZnO. The theoretical approach presented in Sec. 2.1.5.1 allows the accurate computation of transition levels starting from single particle Kohn-Sham eigenvalues. The results are compared to previous theoretical findings and with available experimental data for a variety of defects ranging from oxygen vacancies, zinc interstitials, and hydrogen impurities. We find that H and Zn impurities give rise to shallow levels and the oxygen vacancy is stable only in the neutral, V_O^0, and doubly charged, V_O^{2+}, variants.

* The results described in this Chapter have been reported in: F. Gallino, G. Pacchioni, C. Di Valentin, *J. Chem. Phys.*, **2010**, 133, 144512.

3.1 Introduction

Both native and extrinsic defects have been deeply investigated as recently reviewed by Janotti *et al.* [30] and McCluskey *et al.* [31], with a particular focus on shallow acceptor species since they are expected to induce the desired but still not practicable *p*-type conductivity. Known acceptor impurities are Li, Cu, and Zn vacancies, which are, however, deep impurity states and do not contribute to *p*-type conductivity [242,275]. Shallow donor species such as interstitial hydrogen and zinc are suggested to be responsible of the *n*-type conductivity of as-prepared ZnO samples. DFT calculations have played an important role to gain insight into this fundamental and crucial issue [24,67,177,252,276,277], through the investigation of the electronic structure and energetics of a large number of possible defects.

The computational characterization of both donor and acceptor defects requires the accurate description of the details of the band structure and the correct evaluation of charge states transition energy levels (see Sec. 2.1.5.1). It is common practice to discuss the energy levels introduced in the gap by defect centres using the single-particle Kohn-Sham eigenvalues. This approach, however, is not well justified if electronic transitions are involved, whereas transition levels between different charge states are a better approximation (see Sec. 2.1.5.1). As far as the band gap problem is concerned, hybrid exchange-correlation functionals represent a practical, although not perfect, solution, having positive effects on both the reliability of the computed defects energetics and spin localization (see Sec. 2.1.5.1). Various forms of hybrid functionals have been used in this context, going from the popular B3LYP [59,60] approach [278] to the PBE0 [116,279] and to the more recent HSE06 functionals [118,119,120,121,122,280]. Considering the specific object of this work, bulk ZnO, a study of native defects and interstitial hydrogen has been performed at the HSE06 level of theory using the VASP code [177].

In the present study the B3LYP functional is used in combination with a localized atomic orbitals basis-set approach for periodic calculations, as implemented in the CRYSTAL06 code [71], to investigate defects in ZnO. We will show below that the B3LYP functional reproduces the experimental band gap of bulk ZnO which is an excellent starting point for determining the position of donors and acceptors levels in the band gap of the material. One of the major values of the work, however, is that we present an approach to

compute defect transition levels using the CRYSTAL code (see Sec. 2.1.5.1). This periodic code has played a major role in the community of solid state and surface chemistry in describing bonding at surfaces with the language of chemistry, the language of orbitals, and in showing the importance of hybrid functionals to treat a number of problems in solids [61]. However, a direct use of CRYSTAL to determine defects transition levels is not possible at the moment because of the problems connected to the meaning of the total energy for charged supercells. We have circumvented this problem by making use of the Janak's theorem which states that the total energy of two systems differing for their charge state can be deduced from the corresponding Kohn-Sham eigenvalues. This new approach is applied and validated for the case of ZnO for which other periodic pseudopotential-planewave calculations and experimental data exist. ZnO is thus an excellent benchmark system to check the validity of the present approach opening the possibility to study charge transition levels of defects in solids using the CRYSTAL code and classical hybrid functionals.

We have analyzed the following defects: hydrogen interstitial and substitutional (to O), zinc interstitial and oxygen vacancy.

3.2 Computational Details

All-electron spin-polarized calculations were performed within the linear combination of atomic orbitals (LCAO) approach, as implemented in CRYSTAL06 package [71]. The hybrid B3LYP functional [59,60] has been used and the all-electron Gaussian-type basis sets adopted are an 8-411(d1) [281] for oxygen, 8-64111(d411) [282] for zinc, 7-311(d1) [283] for nitrogen and 311(p1) [284] for hydrogen.

108- and 192-atom supercells, obtained by expansion matrices 3 x 3 x 3 and 4 x 4 x 3, have been used for simulating the bulk ZnO (wurtzite, space group $P6_3mc$). The bulk lattice parameters have been optimized for stoichiometric ZnO: a = 3.278 Å, c = 5.287 Å. The supercell size effect was checked for one case (interstitial H) with a 400-atom model (5 x 5 x 4). For this latter calculation we used the massive-parallel version of the CRYSTAL06 code.

The reciprocal space is sampled according to a regular sublattice with a shrinking factor (input IS) equal to 2 (for both supercells) corresponding to 4-8 *k*-points in the sampling of the irreducible Brillouin zone [71].

The densities of states (DOS) have been computed with a 3 x 3 x 3 *k*-point

mesh (6 or 14 *k*-points according to *k*-point symmetry). The zero point of orbital energy is set to the top of VB. The Kohn-Sham eigenvalues were computed on each *k*-point of the mesh but only those at Γ are discussed because of the direct band gap of ZnO. For additional details about the computational parameters used in this work we refer the reader to Sec. 2.1.4.1.

Estimates of the positions of the transition levels for the various defects considered in the work have been obtained using the approach described in Sec. 2.1.5.1.

3.3 Results and Discussion

We have considered two intrinsic (interstitial zinc, Zn_i, and oxygen vacancy, V_O) and two extrinsic defects (interstitial hydrogen, H_i, and substitutional hydrogen to O, H_O), see Fig. 3.1. We first present the shallow donor species (H_i, H_O and Zn_i), then the deep donor species (V_O).

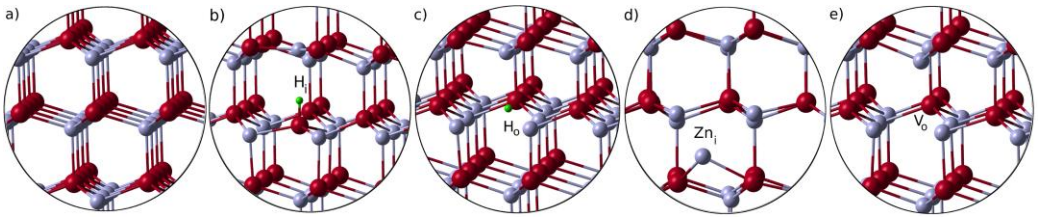

Figure 3.1. Structural models of (a) stoichiometric bulk ZnO, (b) interstitial hydrogen, H_i, (c) substitutional hydrogen to O, H_O, (d) interstitial Zn in an octahedral void, Zn_i, (e) oxygen vacancy, V_O. Zn, O and H are represented by grey, red and green spheres, respectively.

The optical, $\varepsilon^{opt}(q/q')$, and thermodynamic, $\varepsilon^{therm}(q/q')$, transition levels for all defect centres considered in this work are reported in Table 3.1.

Table 3.1. Transition levels for all defect centres considered in this work (in eV).

Defect	Supercell	Transition (q/q')	$\varepsilon^{opt}(q/q')$	$\varepsilon^{therm}(q/q')$	E_{rel}[a]
$\mathbf{H_i}$	400	(+1/0)	3.28	3.33	0.05
$\mathbf{H_O}$	192	(+1/0)	3.36	3.39	0.03
$\mathbf{Zn_i}$	192	(+1/0)	2.78	3.22	0.44
		(+2/+1)	2.92	3.29	0.37
		(+2/0)	2.85	3.26	/
$\mathbf{V_O}$	108	(+1/0)	0.86	1.81	0.95
		(+2/+1)	1.61	2.69	1.08
		(+2/0)	1.24	2.25	/

[a] Relaxation energy of the defect centre in the charged state in absolute value as defined in Eq. (2.31).

3.3.1 Hydrogen Impurities

The shallow donor character of H impurities in ZnO is well established and supported by unambiguous experimental evidences [212,253]. The ionization energy associated with these donor levels is about 25 meV by EELS temperature dependence experiments [212], 35 meV by EPR studies [285], and 51 meV by electrical conductivity measurements [286]. Accurate DFT studies, based on periodic pseudopotential planewave calculations, have recently shown that H impurities are indeed shallow donors [177]. Therefore, this system represents an excellent test case to validate our computational approach (see Sec. 2.1.5.1).

We have placed one H atom in the supercell in both interstitial (H_i, bound to a lattice O atom) and substitutional to O (H_O) sites. The supercell size effect on the shallow donor character of the defect states has been evaluated in the case of H_i by performing calculations with 108-, 192- and 400-atom supercells. The H atom binds to an O ion of the lattice (distance of 0.981–0.968 Å), locating itself along the crystallographic *c*-axis, thus in an intermediate position between the O and the axial Zn ions. The charge density associated to the unpaired electron introduced by the additional H atom is spread over various sites, but the largest component is on the O and Zn ions, where H was inserted. The electronic state introduced by the H-impurity is commonly described as a perturbed host state (PHS) [67], whose nature is clearly evident when comparing the band structure of bulk stoichiometric ZnO with H-doped

ZnO as in Figure 3.2.

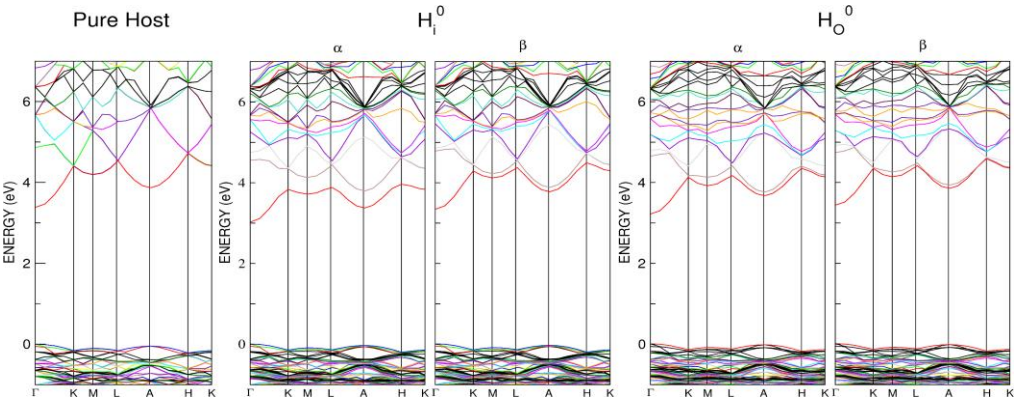

Figure 3.2. Band structure of H_i and H_O defects in ZnO (192-atom supercell). On the left, the band structure of the pure bulk ZnO is reported as reference.

The original state associated to the bottom of the CB becomes occupied in the H_i-doped system and is only slightly deformed and slightly lower in energy. The larger the supercell used, the smaller the perturbation of this state, which indicates that in the infinitely diluted limit this state is really very weakly perturbed and, therefore, can be described as a very shallow donor.

To provide a quantitative support to these considerations, the optical transition level $\varepsilon^{opt}(+1/0)$ has been computed for the various supercell sizes: the value goes from 0.38 eV below the bottom of the CB for the 108-atom model to 0.21 eV for the 192-atom model to 0.10 eV for the 400-atom model. This transition level corresponds to the vertical ionization energy of the donor state. The trend clearly indicates that by increasing the size of the supercell, the shallow nature of the donor state becomes more pronounced.

The thermodynamic transition level, $\varepsilon^{therm}(+1/0)$, is 0.06 eV below the bottom of the CB for 400-atom supercell. This transition level corresponds to the energy required to thermally excite the electron from the shallow donor state to the conduction band.

For the 192-atom supercell we have also considered the possibility of H going substitutional to O (H_O), since recent calculations indicate this as a potential model species [287]. Our calculations confirm the shallow donor character of this defect with $\varepsilon^{therm}(+1/0)$ at the CB minimum.

Only a qualitative comparison with previous reports is possible. A LDA+U

plane-wave study reported that the thermodynamic transition level falls above the bottom of the CB making the H_i^0 centre always higher in energy than H_i^+; this means that H_i^0 is a donor state at any Fermi level position. However, these results are affected by the band gap correction which, for LDA+U method, is rather severe [252]. A hybrid functional plane-wave DFT study states that the thermodynamic transition level $\varepsilon^{therm}(+1/0)$ of H_i is located at the CB minimum, which can be translated in a negligible energy value which is not reported explicitly [177]. It is relevant to stress that while we are discussing the results which include spin-polarization, the other mentioned results have been obtained at a non-spin-polarized level. In principle, spin-polarization could favour localized states and this could be the origin of the small discrepancy in the transition levels values. However, all methods indicate that the H impurity in ZnO is a shallow donor species in perfect agreement with the experimental findings.

3.3.2 Interstitial Zn: Zn_i

The interstitial zinc species, extensively investigated, is an intrinsic donor defect in ZnO [30,31]. There is an experimental indication based on electron irradiation that shallow donor states at 30 meV below CB minimum could be associated to Zn interstitials [288]. In principle, the sublattices of oxygen and zinc ions offer two different voids for interstitial atoms: a tetrahedral and an octahedral cavity where the first nearest neighbors are three ions not belonging to the sublattice (*i.e.*, three oxygen ions in the case of the zinc sublattice). It has been reported that, given the large size of zinc, the octahedral interstice is 0.9 eV more stable than the tetrahedral one [252]; therefore, we have only considered the octahedral Zn_i in the zinc sublattice. The lattice relaxations are very small, leading to Zn_i–O bond lengths of 2.07 Å for neutral Zn_i (2.02 Å for Zn_i^+ and 2.00 Å for Zn_i^{2+}). The distances between Zn_i and the six nearest Zn ions are 2.44–2.59 Å and increase by ~1% by removing one or two electrons.

Zn_i is reported to be a shallow donor, with its 3d states well below the O 2p VB and the occupied 4s state highly mixed with the CB [177]. The size of the supercell and the consequent concentration of defects may have a stronger effect on the evaluation of the transition levels than in the case of the H impurity. As it is appreciable from the band structure in Figure 3.3 and from the electron density plot (not reported), the impurity state is rather localized for Zn_i^0 and for Zn_i^+ (α-state). The transition levels are: $\varepsilon^{therm}(+2/+1) = 0.23$ eV

and $\varepsilon^{therm}(+1/0)$ = 0.36 eV with respect to the bottom of the CB (108-atom model). These values are larger than for a typical shallow donor. Increasing the supercell size to 192 atoms, $\varepsilon^{therm}(+2/+1)$ decreases to 0.09 eV and $\varepsilon^{therm}(+1/0)$ becomes 0.16 eV, again with respect to the CB minimum. Thus, the supercell size does affect the results suggesting that even larger supercell would be required to obtain a higher accuracy. The double charge transition has been evaluated to be $\varepsilon^{therm}(+2/0)$ = 0.13 from CB minimum for the larger model. Previous LDA+U studies reported the thermodynamic transition levels of Zn_i above the CB minimum for (+2/+1) and (+1/0) transitions [252]. Hybrid functional methods with plane-wave basis set report a tiny transition level about 0.1 eV below the bottom of the CB [177] in perfect agreement with our results.

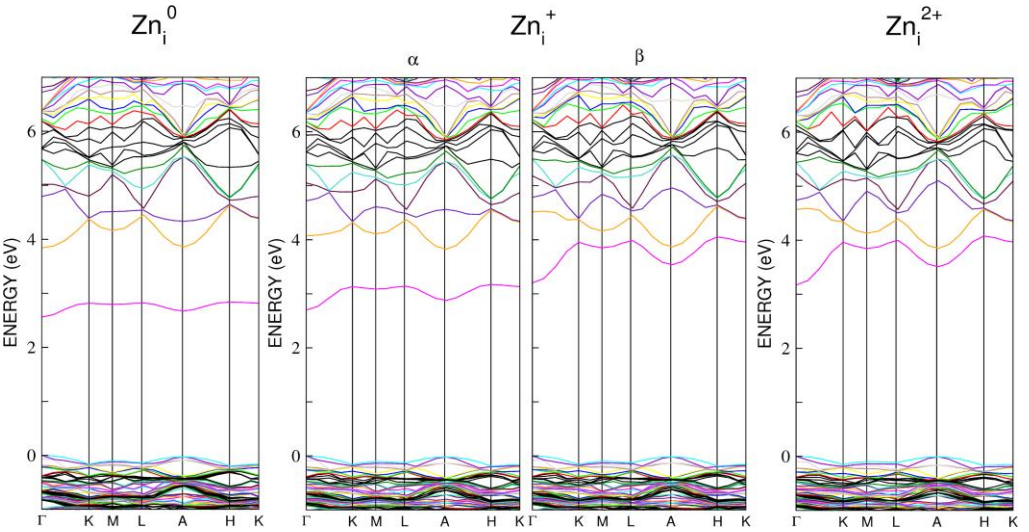

Figure 3.3. Band structure of Zn_i defect in ZnO in various charge states (192-atom supercell).

3.3.3 Oxygen Vacancy: V_O

The oxygen vacancy is probably the most studied and the most controversial native defect in ZnO [67,30,31]. For a long time it has been considered responsible for the unintentional *n*-type conductivity in the material and classified as a shallow donor species, always ionized and identified by the EPR feature with g_{av}~1.96 [289,290,291,292]. This assignment was proven to be incorrect. Experiments and calculations showed that the signal at g~1.96 is

typical of a conduction band electron, coulombically attracted by the ionized donor centre in a "hydrogenic effective mass state" [24,253] and also observed for H-, Al-, Ga-, In- doped ZnO [285,293]. The paramagnetic Vo^{+} species was identified for the first time by Smith and Vehse [294] by EPR for a high energy electron irradiated single crystal with an axial *g*-tensor of $g_{\|}$=1.9948 and $g_{\perp}$=1.9963. Quantum mechanical calculations [67,177,276,295] have shown that the oxygen vacancy creates well localized electronic levels in the band gap, behaves like a deep donor with negative U character so that the V_O^{+} species is thermodynamically unstable and can only be observed under irradiation (photoexcitation). These findings have been taken as the proof that the oxygen vacancies cannot be responsible for the unintentional *n*-type conductivity of ZnO.

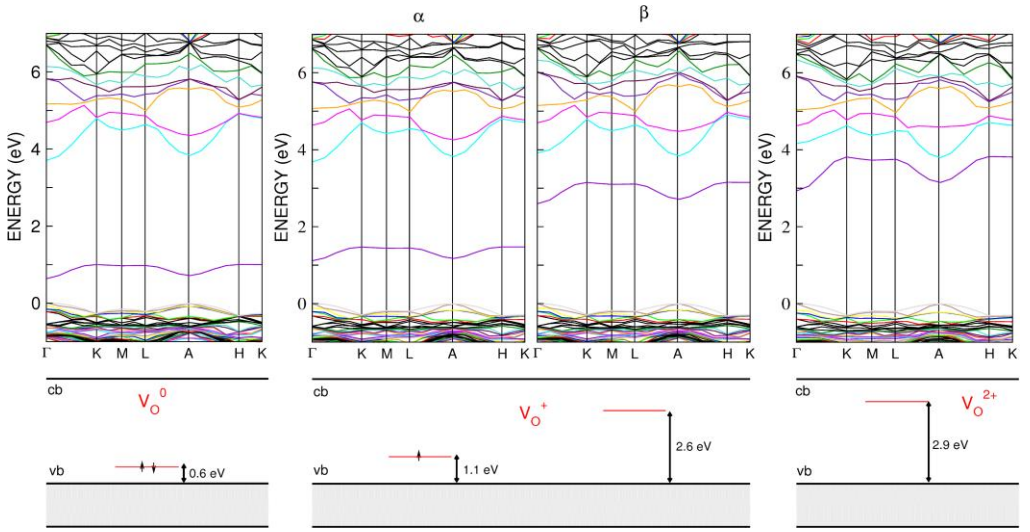

Figure 3.4. Band structure of V_O defect in ZnO in various charge states (108-atom supercell). In the bottom scheme the Kohn–Sham eigenvalues at Γ point are reported.

Our results are consistent with this model. The neutral V_O induces a moderate lattice relaxation with a displacement of the four nearest Zn ions toward the vacancy with a Zn–O bond elongation of about 7.5%. The singlet configuration is 2.9 eV more stable than the triplet one and creates a full occupied and a well localized electronic state 0.6 eV above the top of the VB (Fig. 3.4). The electron density plot clearly shows that this defect level has a strong Zn character (not reported). The ionization of V_O to give V_O^{+} and V_O^{2+} induces a large outward relaxation of the zinc ions by about 5.5% and 21.5%

for V_O^+ and V_O^{2+}, respectively. As observed by Janotti and Van de Walle [276], the large lattice relaxation for the double charged vacancy significantly reduces its formation energy, favoring the negative-U character of V_O. In fact, on the basis of the computed thermodynamic transition levels, $\varepsilon^{therm}(+1/0)$ = 1.81 eV and $\varepsilon^{therm}(+2/+1)$ = 2.69 eV, we find that the V_O^+ state is always thermodynamically unstable for any value of the Fermi level. Below a Fermi level of 1.81 eV the most stable species is V_O^{2+}, above a Fermi level of 2.69 eV the most stable species is V_O^0. The transition level $\varepsilon^{therm}(+2/0)$ is computed to be 2.25, in excellent agreement with the values obtained by plane-wave calculations [67,177,276] in the range of 1.9–2.4 eV.

Another open issue concerns the oxygen vacancy formation energy. Janotti and Van de Walle [252] and Lee *et al*. [295] reported a very high formation energy (ΔH~4 eV) for V_O at O-poor/Zn-rich conditions and consequently they excluded the presence of V_O in the material. In contrast, Lany and Zunger [277] and Oba *et al*. [177] predicted a very low formation energy (ΔH~1 eV) that would favor high concentrations of the defect in bulk ZnO. We have determined the formation energy of V_O in ZnO with respect to ½ O_2 as 3.5 eV. For low oxygen chemical potentials the formation energy decreases considerably and in the limit of oxygen poor conditions it becomes even slightly negative, –0.3 eV. However, one should notice that such a low oxygen chemical potential corresponds to an O_2 partial pressure of about 10^{-27} atm, which has no physical meaning.

Finally, the green luminescence of ZnO (~2.45 eV) has been reported as an evidence of the presence of V_O in bulk ZnO. We are able to evaluate the excitation and emission energy in the photoluminescence process (see computational approach in Sec. 2.1.5.1). The excitation energy (exp. 3.1 eV) is estimated as $E_g - \varepsilon^{opt}(+1/0)$ = 2.53 eV ($V_O \rightarrow V_O^+ + e^-_{CB}$). The emission is the consequence of the excited electron recombination with the hole at the defect level (PL_2, see Figs. 2.3d and 3.5), for (+1/0) = 0.80 eV and for (+2/+1) = 0.20 eV or at the top of the valence band (PL_1, see Figs. 2.3b and 3.5), $\varepsilon^{opt}(+1/0)$ = 0.86 eV, $\varepsilon^{opt}(+2/+1)$ = 1.61 eV, and $\varepsilon^{opt}(+2/0)$ = 1.24 eV. On the basis of these computed energy values for possible emissions involving the oxygen vacancy defect centre, we tentatively assign the observed photoluminescence (~2.45 eV) to the (+1/+2) transition $V_O^+ \rightarrow V_O^{2+} + e^-_{VB}$ [*i.e.* $\varepsilon^{opt}(+2/+1)$ = 1.61 eV] which presents the best agreement, in line with previous works [276].

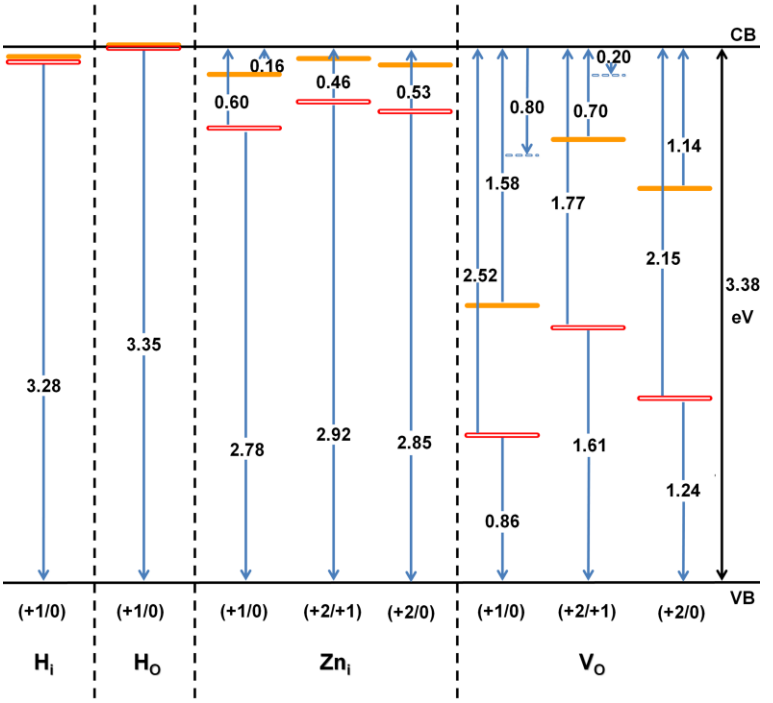

Figure 3.5. Thermodynamic and optical transition levels (eV) in the band gap of ZnO for various dopants and defects centres. Solid orange line = ε^{therm}, hollow red line = ε^{opt}, dotted line PL_2 transitions (see also Figs. 2.2 and 2.3). Results for 192-atom supercell, except for H_i and V_O centres which have been obtained with a 400-atom and 108-atom supercell, respectively. Values smaller than 0.15 eV are not reported.

3.4 Conclusions

In this work we have calculated the optical ε^{opt} and thermodynamic ε^{therm} transition levels of defects in different charge states in ZnO. So far this has been possible only within plane-wave DFT approaches. Here we used a periodic DFT approach with an atomic orbital basis set and a hybrid exchange-correlation functional (in particular the popular B3LYP functional). For the calculations we used the CRYSTAL06 code. The problem with this code is the calculation of the total energy of charged supercells, an aspect which is essential in order to go beyond the single-particle Kohn–Sham eigenvalues for the evaluation of the charge trapping ability of a given defect. The problem has been overcome by making use of the Janak's theorem, which shows that the

total energy difference between two charge states of a given defect can be obtained from the Kohn–Sham eigenvalues of the system with N and N+1 electrons. Using this approach and other corrections, we have been able to calculate the optical and thermodynamic transition levels of the following defects: hydrogen interstitial and substitutional to O positions, interstitial Zn and oxygen vacancy.

Hydrogen is confirmed to produce very shallow states in the gap of ZnO. At the highest level of calculation, using a supercell of 400 atoms, we find that the thermodynamic transition level $\varepsilon^{\text{therm}}(+1/0)$ is 100 meV below the bottom of the conduction band (with a computed band gap of 3.38 eV to be compared with the experimental value of 3.44 eV). Experimentally, the transition level of the H-impurity is between 25 and 51 meV below the conduction band. The agreement, given the size of the band gap and the intrinsic accuracy of the computational method, can be considered as very satisfactory. This, together with the results for other defects, fully validates the procedure followed for the calculation of the transition levels.

Finally, in Figure 3.5 and Table 3.1, we summarize all the transition levels, optical and thermodynamic, for the defects considered. This corresponds to the outcome of the calculations of the spectroscopic transitions described schematically in Fig. 2.2. This could be useful for the interpretation of past and future experimental measurements on these systems.

CHAPTER 4

Copper Doping[†]

Abstract

A combined experimental and first principles study of Cu defects in bulk ZnO is presented. Cu particles are epitaxially deposited on the polar O–ZnO($000\bar{1}$) surface at RT. Upon heating, a broadening of the quasi-elastic peak in high resolution electron energy loss spectra is observed, corresponding to an electronic doping effect of Cu atoms in bulk ZnO with an ionization energy of 88 meV. Cu impurities in ZnO, although commonly acting as acceptors, are presently observed to induce shallow donor states. We assign these to interstitial Cu species on the basis of a hybrid density functional study. In our calculations we also analyze copper substitutional to zinc, Cu_s, in terms of transition energy levels and hyperfine coupling constants with reference to available spectroscopic data. We investigate the potential magnetic interaction between copper species, their interaction with oxygen vacancies and the possibility of copper clustering. The relative stability of the various copper impurities considered in this study is finally compared on the basis of their formation energy at different oxygen chemical potentials and Fermi level values.

[†] The results described in this Chapter have been reported in: H. Qiu, F. Gallino, C. Di Valentin, Y. Wang, *Phys. Rev. Lett.*, **2011**, 106, 066401; F. Gallino, C. Di Valentin, *J. Chem. Phys.*, **2011**, 134, 144506.

4.1 Introduction

The perspective of preparing a ZnO-based material combining both magnetic and semiconducting properties has prompted an intense research activity aimed at identifying a valuable and reliable transition metal dopant, in a so-called diluted magnetic semiconducting oxide with room temperature (RT) ferromagnetic properties [13,51,258,296,297,298]. Elements like Mn and Cu, that do not present secondary ferromagnetic phases due to partial clustering, are highly preferred. In addition, the Cu/ZnO system has been largely used as an excellent catalyst for the industrial methanol synthesis. However, key questions on the microscopic mechanism of the reaction are still open and the incorporation of Cu atoms into ZnO may play a role in determining the catalytic activity of Cu/ZnO [264,299].

Cu doping of ZnO has been previously achieved by either pulsed-laser ablation or high temperature diffusion (T > 1000 °C), resulting in Cu ions substituting lattice Zn ions [261,300]. Several studies based on photoluminescence experiments [301,302], electrical measurements [303,304] and on GGA+U calculations [305] have reported a deep acceptor state with the transition energy level (0/–1) high in the band gap. In this Chapter we present a comprehensive overview investigation of copper doping in ZnO and we address several specific issues which are still under debate in the literature. First of all we perform a combined experimental and theoretical study on a Cu-ZnO system prepared by Cu deposition on ZnO single crystal surfaces. The HREELS data reveal that Cu can diffuse into bulk ZnO by a mild thermal treatment yielding an unusual donor state in ZnO. Theoretical modelling suggests that the shallow donor state results from the formation of interstitial Cu^{+} ions in ZnO. Copper impurities are also investigated as well-established electron acceptors [31] and acceptor and donor properties are discussed in terms of thermodynamic and optical transition levels. Then the controversial relative stability of ferromagnetic (FM) and antiferromagnetic (AFM) phases [306,307,308,309,310,311] for substitutional Cu to lattice Zn atoms is analyzed. Finally, the possibility of interaction with oxygen vacancies [308,309] and of copper clustering [307,309,310] in bulk ZnO matrix is explored. The stability of all these diverse species has been compared on the basis of their formation energy, as a function of the Fermi level and of the oxygen chemical potential, which determines whether the system is in an oxidizing or reducing environment (see Sec. 2.1.5.2).

4.2 Experimental and Computational Details

4.2.1 Experimental Section

All experiments were carried out in a HREELS system, as described in Sec. 2.2.2. In short, the O–ZnO($000\bar{1}$) sample was prepared by repeated cycles of Ar ion sputtering and subsequent annealing at 850 K for 10 min. The Cu evaporator used in this work is a home-made setup with an electronic beam heating. The film thickness is measured by a quartz crystal with an experimental error of about 10%. The broadening (Δ) of the quasi-elastic peak in HREELS is derived according to the formula by $\Delta_{tot}^2 = \Delta_{app}^2 + \Delta^2$, where Δ_{app} denotes the apparatus broadening [212].

4.2.2 Computational Methods

The calculations have been performed within spin-polarized DFT, using the hybrid B3LYP functional [59,60]. The Kohn–Sham orbitals were expanded in Gaussian type orbitals, as implemented in CRYSTAL06 package [71] (the all-electron basis sets are O 8-411(d1) [281], Zn 8-64111(d411) [282] and Cu 8-6411(d41) [312]). In some cases results have been refined by performing single point calculations with a larger basis set 8-64111(d41) [313] for copper. The bulk wurtzite ZnO has been modeled by a 192-atom supercell [4 x 4 x 3] with optimized bulk lattice parameters: a = 3.278 Å, c = 5.287 Å. The copper impurity has been inserted: i) substitutional (s) to Zn atoms: $Zn_{1-x}Cu_xO$ (Cu_s, Cu_sCu_s) and $Zn_{1-x}Cu_xZn_yO$ (Cu_sZn_i); ii) interstitial (i): $ZnCu_yO$ (Cu_i); iii) in the presence of oxygen vacancies (V_O): $Zn_{1-x}Cu_xO_{1-x}$ (Cu_sV_O); and iv) both interstitial and substitutional to Zn atoms: $Zn_{1-x}Cu_{x+y}O$ (Cu_sCu_i, Cu_s2Cu_i). The copper atomic concentration has been varied in the range x+y = 0.0104 ÷ 0.0312 for the various defects considered [x = 0.0104 (Cu_s, Cu_sV_O, Cu_sCu_i, Cu_s2Cu_i), x = 0.0208 (Cu_sCu_s), y = 0.0104 (Cu_i, Cu_sZn_i, Cu_sCu_i), y = 0.0208 (Cu_s2Cu_i)].

The reciprocal space was sampled in a 2 x 2 x 2 k-point mesh corresponding to 4 ÷ 8 k-points of the irreducible Brillouin zone [71]. The densities of states (DOS) were computed with a 3 x 3 x 3 k-point mesh. The Kohn-Sham eigenvalues were computed on each k-point but only those at Γ are discussed because of the direct band gap of ZnO. The zero point of orbital

energy was set to the top of VB. Additional details about the computational parameters used in this work can be found in Sec. 2.1.4.1.

We refer to Secs. 2.1.5.1, 2.1.5.2 and 2.1.5.3 for the detailed description of the theoretical approach to compute transition energy levels (ε), formation energies (E_{form}) and hyperfine coupling constants for the interaction of the unpaired electron spin with the nuclear spin of the ^{63}Cu nuclide, respectively. Thermodynamic transition levels ($\varepsilon^{\text{therm}}$) of defects in bulk materials can be directly compared to donor levels ionization energies, as determined with the experimental approach of this and previous work [212].

4.3 Results and Discussion

4.3.1 Shallow Donor Sates Induced by In-Diffused Cu in ZnO

Experiments. The polar O–ZnO($000\bar{1}$) surface is electrostatically unstable because of uncompensated surface charges and exhibits a complex surface structure [244]. The HREEL spectrum of the clean O–ZnO surface is characterized by intense Fuchs-Kliewer phonons at 68, 135 and 201 meV (see Fig. 4.1) [314].

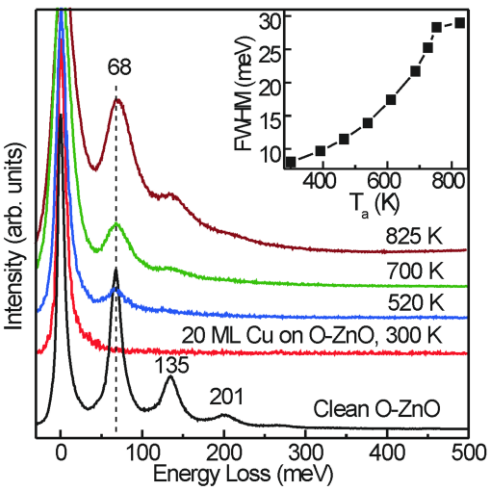

Figure 4.1. HREEL spectra obtained after 20 ML Cu deposition on the clean O-ZnO($000\bar{1}$) surface at 300 K and then annealing to the indicated temperatures. The inset shows the FWHM value of the quasi-elastic peak as a function of annealing temperature T_a. All spectra were recorded at room temperature in specular geometry with the primary electron energy of 10 eV and incident angle of 55º with respect to the surface normal.

After deposition of Cu up to 20 ML at RT, the surface phonons are fully screened by Cu layer. They reappear and increase in intensity with annealing the sample to higher temperatures. Upon heating to 825 K, the spectrum of Cu/O–ZnO becomes comparable with that of the clean O–ZnO (see Fig. 4.1). We can first rule out the possibility of Cu desorption from the surface, as confirmed by the corresponding thermal desorption spectroscopy data (not reported). The present HREELS results could be attributed to the aggregation of Cu particles on ZnO($000\bar{1}$) and/or diffusion into bulk ZnO. Importantly, the reappearance of the Fuchs-Kliewer phonons is accompanied by a dramatic increase of the full width at half maximum (FWHM) value of the quasi-elastic peak in HREELS (see inset of Fig. 4.1). Obviously, this significant peak broadening cannot be explained by the aggregation of Cu clusters on O–ZnO, but, according to similar observations on H/O-ZnO [212], it originates from the excitation of low-energy plasmons, which is related to an electronic doping effect of Cu defects formed via diffusion into bulk ZnO. This assignment is further evidenced by additional experiments discussed below.

For doped semiconductors, the broadening (Δ) of the quasi-elastic signal in HREELS depends on the density of free charge carriers and the sample temperature [315]. For comparison, we carried out temperature-dependent experiments on differently treated Cu/O-ZnO samples. Figure 4.2 presents the results of Δ (Δ^2) as a function of temperature below 300 K.

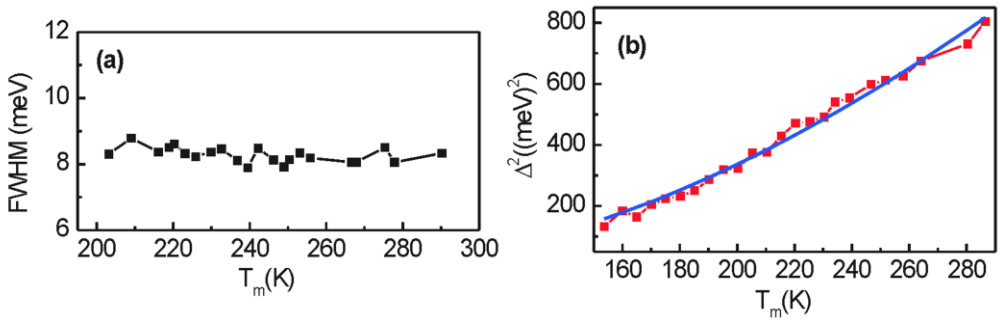

Figure 4.2. (a) The broadening (FWHM, Δ) of the quasi-elastic peak in HREELS as a function of the measurement temperature T_m for the clean O-ZnO($000\bar{1}$) surface deposited with 20 ML of Cu at 120 K without further heating treatment. (b) The value of Δ^2 as a function of the measurement temperature T_m for the Cu/O-ZnO sample prepared by 20 ML Cu deposition at RT followed by annealing to 825 K and then cooling down to 120 K. The solid curve in (b) is the result of a non-linear least squares fit, which gives an ionization energy of 88 meV.

For the sample freshly prepared by deposition of 20 ML Cu at 120 K without additional heating treatment, the FWHM is nearly constant with a slight deviation within the experimental error, indicating no formation of shallow donor states, thus confirming that Cu atoms do not diffuse into bulk ZnO below RT. In contrast, for the Cu/O–ZnO sample obtained after first annealing to 825 K and then cooling down to low temperatures, the value of Δ^2 exhibits a continuous increase with raising the measurement temperature T_m (see Fig 4.2b). This finding provides another experimental evidence for the electronic doping effect of Cu species incorporated in bulk ZnO.

On the basis of the formula for temperature-dependent conduction band (CB) charge density *n* and the broadening Δ as described in Eqs. (2.50 and 2.51), we can further estimate the corresponding ionization energy. The solid curve in Figure 4.2b presents the result of Δ^2 as a function of temperature calculated by a nonlinear least square fit, yielding an ionization energy of 88 meV. This rather small value corresponds to the formation of shallow donor states created by the incorporation of Cu atoms in bulk ZnO, which is not simple to rationalize since all Cu related species in ZnO have been reported in the literature as deep acceptors with ionization energies always larger than 2 eV [301,302,303,304]. Note that a deep acceptor state would not lead to an apparent quasi-elastic peak broadening in HREELS. In order to understand the origin of the low ionization state, we have carried out a DFT investigation by means of the hybrid density functional B3LYP, which reproduces with excellent accuracy the bulk ZnO band gap (exp. 3.44 eV [174] vs theo. 3.38 eV).

Theory. Copper doping of ZnO is commonly viewed as Cu substitution of one lattice Zn^{2+} ion (Cu_s) and it has been largely studied in literature. From an experimental point of view, copper doping of zinc oxide single crystal has been easily achieved by pulsed laser techniques [260,261], ion implantation [302,316], flux methods [304,317] and high temperature treatments [300,318]. In particular, in a recent work based on the emission channeling technique [316] it has been demonstrated that ~70% of Cu atoms are substitutional to zinc with rms displacements of 0.16–0.17 Å from the original lattice site. Copper is in a 2+ formal oxidation state, Cu_s^{2+}, replacing a Zn^{2+} lattice ion and the overall system is thus charge neutral. The presence of a hole in the Cu_s^{2+} 3*d* shell (see Fig. 4.3a) causes a Jahn-Teller distortion of the tetrahedral

coordination sphere with a shortened axial Cu–O distance from 2.00 to 1.90 Å. The unpaired electron is highly localized on a Cu d_{z^2} -orbital pointing toward the closest oxygen (see Fig. 4.3a). All the Cu 3d states are localized inside the VB, except for the unoccupied beta spin component, 2.7 eV above the VB top (see Fig. 4.3a).

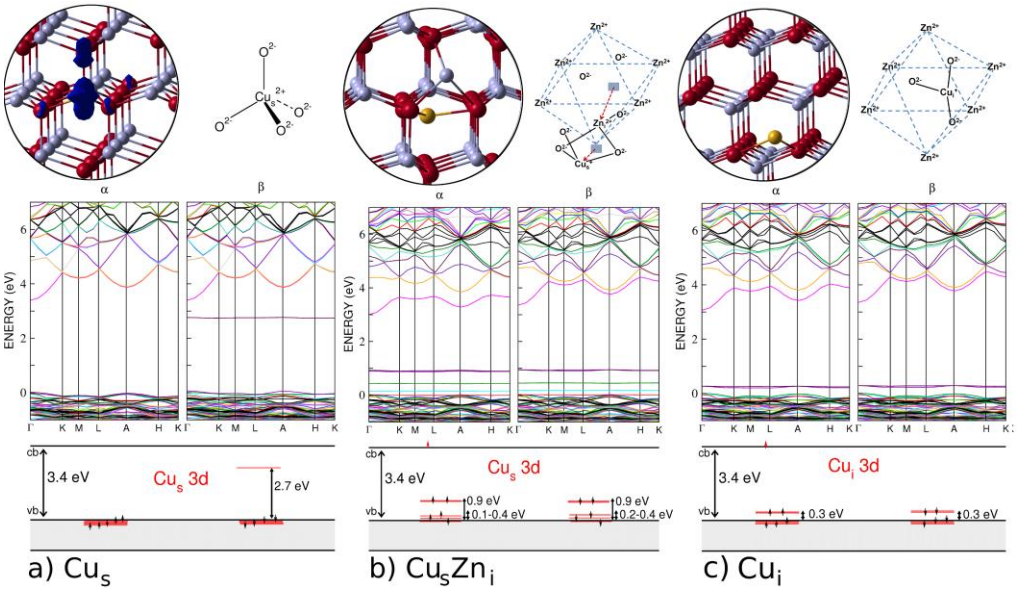

Figure 4.3. Upper panel: spin density plot and schematic structure of the (a) Cu_s species in bulk ZnO. Ball and stick and schematic representations of the (b) Cu_sZn_i and (c) Cu_i species in bulk ZnO. Zn, O and Cu are represented by grey, red and yellow spheres, respectively. Lower panel: band structures for the various models together with a schematic representation of the Cu d states in the band gap of the material (from Kohn-Sham eigenvalues in Γ). The red arrow represents the unpaired electron delocalized in the CB for Cu_sZn_i and Cu_i.

The Cu_s^{2+} species has been previously studied and identified as a deep acceptor [305,307,319]. The addition of an extra electron fills up the Cu 3*d* shell (Cu_s^{+}) and induces a considerable outward relaxation of the nearest O atoms by 4% ÷ 9% restoring the original zinc tetrahedral coordination. The corresponding relaxation energy, E_{rel}, is 0.58 eV and the Cu 3d states are lifted up in the band gap and splitted by the crystal field in *e* and t_2 components. Further addition of a second extra electron does not cause significant distortion of the system but only a tiny distortion of the bottom of CB in a commonly described perturbed host state (PHS) [67], where the electron is delocalized.

The corresponding (0/–1) and (–1/–2) transition energy levels computed with the present computational setup (0.91 and 0.12 eV below the CB bottom, respectively) are consistent with the experimental data and a recent GGA+U study [305]. While Cu_s^{2+} is a good acceptor that can easily capture electrons from any shallow donors present in the bulk [(0/–1) charge transition], Cu_s^{+} is a very poor acceptor [(–1/–2) charge transition]. Concluding, a stoichiometric excess of donors with respect to Cu_s^{2+} acceptor species can result in a residual *n*-type conductivity.

The question is the following: which type of donors could be present? A generally recognized double electron shallow donor is interstitial zinc (Zn_i) in ZnO. Since Cu_s is a single electron compensating acceptor, if one Cu atom kicks out one Zn atom from its lattice position, forming a Cu_s and a Zn_i species, we expect an extra electron stabilized at the CB bottom which could be responsible of a *n*-type conductivity. Thus, we investigated the co-presence of these defects (Cu_sZn_i) in a nearby (2.4 Å) or far apart (10.0 Å) configuration. The Cu_s and Zn_i species prefer to be in close contact (by 1.5 eV) as a consequence of a significant lattice rearrangement. Cu and Zn atoms share the same lattice site in a so-called split-interstitial configuration (see Fig. 4.3b). The electronic structure of the system is very similar to that observed for Cu_s^{+}. This indicates that only the first electron from the Zn impurity has been transferred to the Cu_s while the second lies in a PHS. The system is a shallow donor with thermodynamic transition level $\varepsilon^{therm}(+1/0)$ computed to be 113 meV from the CB minimum (see Fig. 4.4).

Cu atoms may also occupy interstitial voids in ZnO (Cu_i). Since for Zn_i the octahedral cavity was found to be 0.9 eV more stable [252], we assume a similar situation for Cu_i (see Fig. 4.3c). Similar structural relaxations are observed for Cu_i and Zn_i, with almost identical distances to O [2.07 Å (see Sec. 3.3.2)] and to the nearest Zn ions [2.44–2.59 Å (see Sec. 3.3.2), 2.42–2.50 Å respectively]. Differently from Zn_i, a double electron shallow donor, Cu_i is expected to behave as a single electron shallow donor, which is confirmed by the present calculations. The thermodynamic transition level $\varepsilon^{therm}(+1/0)$ for Cu_i defect centre is computed to be 126 meV from CB minimum which is, as for the case of Cu_sZn_i (113 meV), in rather good agreement with the experimentally determined 88 meV (see Fig. 4.4).

We have identified one deep acceptor (Cu_s) and two shallow donor species (Cu_sZn_i and Cu_i) with computed donor ionization energies in good agreement with the experimental value. The stability of these species is now compared at the oxygen-poor limit (further details are in Sec. 2.1.5.2 and 4.3.6). Formation

energies are reported as a function of the Fermi level (E_F) ranging from the top of the VB to the bottom of the CB. While absolute values of formation energies are dependent on the choice of reference compounds, relative values are not. We observe that the Cu_sZn_i species is always less stable than the Cu_i species by 0.75 eV. The most stable species at low Fermi level values (E_F < 1.80 eV) is Cu_i (in particular Cu_i^+), while at high Fermi level values (E_F > 1.80 eV) it is Cu_s. These results mean that Cu_i is always a better donor species than Cu_sZn_i and is the predominant defect for a broad range of E_F. Only for an electron rich system, which is not the present case, an acceptor species such as Cu_s becomes favored.

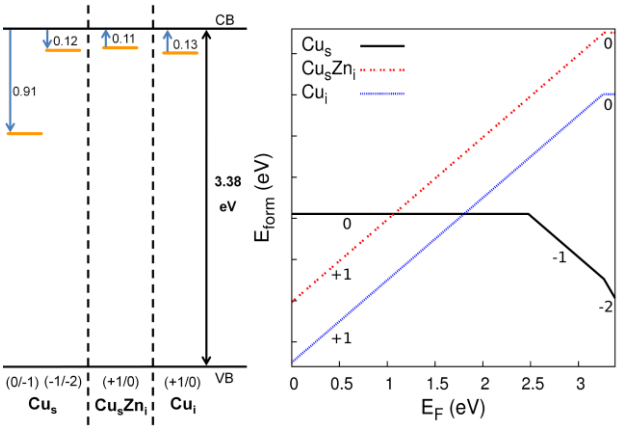

Figure 4.4. Left panel: thermodynamic transition levels (eV) in the band gap of ZnO for Cu acceptor (↓) and donor (↑) species in bulk ZnO. Right panel: formation energy of Cu defects as a function of the Fermi level at the oxygen poor limit. The slope corresponds to the charge state of the defect considered. Tick marks unit on *y* axis is 0.5 eV.

In conclusion, based on the very good agreement of the experimental ionization energy of 88 meV with the computed $\varepsilon^{therm}(+1/0)$ value of 126 meV and the thermodynamic analysis, reported in Figure 4.4, we propose the shallow donor species to be Cu_i in bulk ZnO.

4.3.2 Comparison with Spectroscopic Data

Photoluminescence. Cu_s^{2+} is reported to be an acceptor species, responsible of the typical green luminescence in ZnO with a zero-phonon doublet at 2.86 eV, analyzed by the pioneering work of R. Dingle [301]. This emission was

attributed to the transition from an excited Cu_s^+ $3d^{10}4s^0$ state [A^-] to the Cu_s^{2+} $3d^9 4s^0$ state [A^0] and its corresponding acceptor transition level (0/–1), in the semiconductor terminology, was estimated at 0.17 eV [304] and 0.19 eV [303] below the conduction band (CB) by electrical measurements [31]. The discrepancy in the position of the state as obtained by luminescence and electrical measurements is a consequence of a large Stoke shift in the former case.

The transition levels (0/–1) for Cu_s^{2+} computed in the present work with the hybrid functional B3LYP are consistent with the experimental data (see Table 4.1), and a recent work by Lany and Zunger [305] using a GGA+U method and applying a hole-state correction for the Zn and Cu d states. The green luminescence centred at 2.86 eV corresponds to the PL_2 transition (see Sec. 2.1.5.1 and Figs. 2.2 and 2.3 for details) where the excited electron decays from the defect A^- (Cu_s^+) to the valence band according to the Franck–Condon principle. Depending on the residence time of the electron at the Cu_s^+ defect, the emission peak should range from [$\varepsilon^{therm}(0/-1) - E'_{rel}$] to $\varepsilon^{opt}(0/-1)$ [320], computed from 1.96 eV to 3.06 eV respectively, in good agreement with the experimental peak at 2.86 eV. Previous theoretical works based on LDA and GGA calculations reported transition levels closer to the VB (0.7 [319] and 0.98 [307] eV, respectively) that were erroneously interpreted as the origin of the green luminescence according to a PL_1 type transition with the excited electron recombining at the defect level (see Sec. 2.1.5.1 and Figs. 2.2 and 2.3 for details). These calculations are severely affected by the band-gap error and the self-interaction problem, two well-known shortcomings of standard DFT methods.

Table 4.1. Optical and thermodynamic transition levels for some selected Cu defects considered in this work (in eV).

Defect	Transition	$\varepsilon(q/q')^{therm}$	$\varepsilon(q/q')^{opt}$	E_{rel}
$\mathbf{Cu_s}$	(0/–1)	2.48	3.06	0.58
$\mathbf{Cu_i}$	(+1/0)	3.26	3.20	0.06
$\mathbf{Cu_sZn_i}$	(+1/0)	3.27	3.13	0.14
$\mathbf{Cu_s2Cu_i}$	(+1/0)	3.30	3.27	0.03
$\mathbf{Cu_sV_O}$	(+1/0)	2.27	1.12	1.15

EPR Properties. Being substitutional copper to zinc a paramagnetic species in ZnO (Cu_s^{2+} $3d^9 4s^0$), it has been investigated by several groups with the EPR

spectroscopy. The continuous wave (CW) EPR spectrum of Cu_s^{2+} in a single crystal ZnO was first reported by Dietz *et al.* [317] and consists of a $S = ½$ species with axial symmetry, interacting with a single Cu nucleus resulting in a well-resolved hyperfine pattern due to the two copper isotopes (^{63}Cu, $I = 3/2$, 69.2% abundant and ^{65}Cu, $I = 3/2$, 30.8% abundant). The interpretation of the large *g* shifts and hyperfine coupling constants, (see Table 4.2), much debated in literature [317,321,322,323,324,325,326], is still an open question. In particular two main currents of thought can be identified. From one side Dietz *et al.* [317] proposed a model of interpretation of *g*-shifts involving a considerable covalency with the 3d hole spending 40% of its time on neighboring oxygens. The major criticism to this theory is related to the anomalously large overlap integral between the 3d and oxygen orbitals [322], in contrast with the experimentally estimated 90% ionic character of ZnO [327]. From the other side, Bates [323] drew the attention to the possible hybridization of the $3d^9$ ground state with the $3d^8 4p^1$ excited state. According to this hypothesis, the hole is estimated to spend 67.5% and 7.5% of its time in the 3d and 4p orbitals, respectively, which would also explain the large hyperfine coupling constants.

Here, we present for the first time the *ab initio* computation of hyperfine coupling constants for the model of substitutional copper in ZnO (see Fig. 4.1a).

Table 4.2. Spin Hamiltonian parameters for $^{63}Cu_s^{2+}$. All values are in MHz.

	A_1	A_2	A_3	a_{iso}	T_1	T_2	T_3	*spin*
Exp. [317][(a)]	± 584.60	∓ 692.52	∓ 692.52	∓ 266.81	±851.41	∓ 425.71	∓ 425.71	/
Exp. [321]	± 593.59	∓ 683.53	∓ 683.53	∓ 257.82	±851.41	∓ 425.71	∓ 425.71	/
(b)	+449.60	-359.17	-359.17	-89.58	+539.18	-269.59	-269.59	0.74
(c)	+333.15	-485.92	-485.92	-212.90	+546.05	-273.02	-273.02	0.74

[a] We propose a different decomposition of the *A* tensor into the a_{iso} and *T* components than what reported in the experimental Ref. [317] in agreement with the interpretation of Bates [323] and Zheng *et al.* [324].
[b] Cu basis set from Ref. [313].
[c] Fully decontracted Cu basis set from Ref. [313].

In the most stable electronic configuration, described in Figure 4.1a, the unpaired electron lies mostly in a d_{z^2} state, as a consequence of the trigonal distortion along the *c*-axis with a shorter Cu–O bond. The spin density on the Cu atom is 0.74 while 0.15 is on the axial O, according to a Mulliken analysis. The hyperfine coupling constants have been obtained after complete

decontraction of the Cu basis-set to increase the flexibility of the core s-functions (see Table 4.2). The isotropic component is in rather good agreement with the experimental value. The negative value of the a_{iso} indicates that the unpaired spin density is of the minority spin character (beta) since g_N for Cu is positive. This can be explained by an exchange interaction of the spin density more distant from the nucleus, leaving the minority spin density in the region near the nucleus. The dipolar tensor T is axial, as experimentally observed. The quantitative agreement is in this case less satisfactory. The discrepancy is most probably due to the spin–orbit contribution which has not been included in the present calculations. This is found to be essential for the quantitative reproduction of experimental values in the case of transition metal compounds and in particular for Cu^{2+} complexes [328,329]. Although largely underestimated, the computed dipolar components make up the major part of the hyperfine coupling constants, in line with the fact that the unpaired electron lies mostly in a *d* orbital.

4.3.3 Magnetic Properties: Cu_sCu_s

The magnetic properties resulting from Cu-doping of ZnO have been intensively investigated [306,307,308,309,310,311] with the final goal of achieving a suitable ferromagnetic material for spintronic applications. The experimental evidences are controversial and ferromagnetism has been so far reported for both conductive *p*-type [260,261] or *n*-type [330] and insulating [331,332] samples. An accurate description of the direct exchange coupling of Cu ions is important to clarify Cu-doped ZnO magnetic properties, and eventually to predict potentially interesting combinations with co-dopant elements for RT-ferromagnetism. Hybrid exchange-correlation functionals are precious tools since LDA and GGA approaches often fail to describe, even qualitatively, strongly localized unpaired charge carriers, due to the spurious delocalization deriving from the incorrect description of the self-interaction [53,333,334]. This problem can be overcome by adding a percentage of exact Hartree–Fock exchange, as in hybrid functionals, or using an on-site potential and requiring the linear dependence of total energy on the electron occupation, also known as generalized Koopmans' condition [305]. In this work we use the hybrid B3LYP functional, as implemented in the CRYSTAL06 code, that has been successfully used to describe the magnetic properties of a wide variety of solids [333,335,336,337].

We have considered only first and third next-neighbours Cu_s since the magnetic interactions are reported to decrease as r^{-t}, with r the distance between the Cu ions and t varying between 11 and 15 [338]. Two configurations are examined, with the Cu ions lying in the *xy*-plane (perpendicular to the *c*-axis) or along the *z*-axis (equivalent to the *c*-axis, see Fig. 4.5) and with Cu–Cu distance of 3.34 Å (next-neighbours) and 5.27 Å (the third next-neighbours), respectively. The atomic positions are fully relaxed for each configurations and then they are kept fixed for the calculation of ferromagnetic (FM) and antiferromagnetic (AFM) states. The energy differences, $\Delta E = E^{AFM} - E^{FM}$, accounting only for the different magnetic interactions, are negligible, +3 meV and +1 meV for *xy*-plane and *z*-axis configurations, respectively. The unpaired electrons in both structural configurations and in both magnetic states are largely localized in a *d* state of the Cu ions with a small delocalization on one next-neighbouring O ion (see Fig. 4.5).

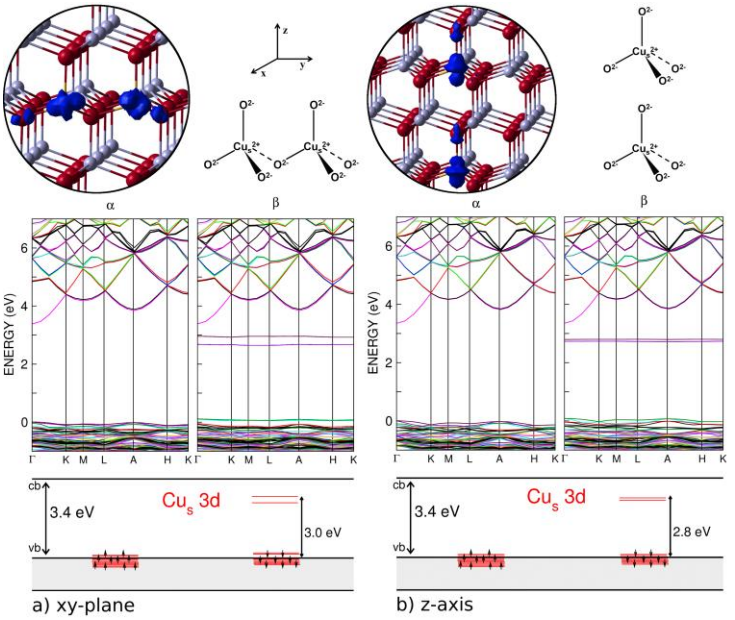

Figure 4.5. Upper panel: spin density plots and schematic structures of the Cu_sCu_s species in bulk ZnO for the FM states in the a) *xy*-plane configuration and b) *z*-axis configuration. Zn, O and Cu are represented by grey, red and yellow spheres, respectively. Lower panel: band structures for the two models in the FM state together with a schematic representation of the electronic structure (from Kohn–Sham eigenvalues in Γ).

In the lower panels of Figure 4.5 a schematic representation of the electronic structure is reported showing that the Cu *d* states in the FM state of both structural configurations are localized in the proximity of the VB top with the two unoccupied beta spin components (one for each Cu_s) lying high in the band gap of ZnO. The atomic spin density from the Mulliken analysis on the two Cu species is 0.74 e, indicating a high spin localization. Comparison of total energies of *z*-axis and *xy*-plane configurations in the FM magnetic states (FM) shows that the most stable species is the *z*-axis one by 8 meV.

Table 4.3. Total energy difference $\Delta E = E^{AFM} - E^{FM}$ (in meV) for *xy*-plane (next-neighbours) and *z*-axis (the third next-neighbours) configurations with different functionals and supercell-size models, as reported in literature.

	DFT method	**N° atoms**	**ΔE**	
			***xy*-plane**	***z*-axis**
This work	B3LYP	192	+3	+1
Ref. [339]	LDA	32	~+90	~+10
Ref. [339]	LDA+U	32	~+25	~0
Ref. [307]	GGA	72	~+130	~+10
Ref. [308]	GGA	32	+129	/
		48	+120	/
		72	+130	/
		108	+160	/
Ref. [308]	GGA+U	72	~+30	/
Ref. [310]	B3LYP	32	–669	+13

In Table 4.3 total energy differences from previous works for comparison with the present hybrid functional results are reported. It is evident that for the *z*-axis configuration, where the two Cu ions are further apart, the FM and AFM solutions are basically degenerate or very close in energy for all methods. For the *xy*-plane configuration with two next neighbouring Cu ions, apart from a small supercell B3LYP calculation which is totally off with respect to the other values, it is possible to observe that LDA and GGA functionals overestimate the relative stability of the FM solution, while LDA+U [339], GGA+U [308] and present B3LYP calculations are in closer agreement with a tiny or negligible energy difference. Note that the supercell models used for these three calculations are rather different which may

account for the slight differences in energy (LDA+U:32 vs GGA+U:72 vs B3LYP:192 atoms). This short overview of the data is fully consistent with the LDA and GGA poor performances when describing localized unpaired electrons as discussed above. The larger and spurious delocalization intrinsic of LDA and GGA methods is the probable reason for the overestimated magnetic interaction between the two Cu centres occupying the next-neighbouring sites (FM vs AFM for *xy*-plane, see Table 4.3).

Concluding, the B3LYP results from this work indicate that Cu_s impurities in ZnO do not present any direct magnetic interaction and would be magnetically disordered at room temperature. The observed RT-ferromagnetism [260,261,330,331,332] of Cu-doped ZnO might be induced by Cu_s interaction with other magnetically active impurities [332,340]. However, this analysis goes beyond the purpose of the present study and will be the object of future work.

4.3.4 Copper Clustering: Cu_sCu_i, Cu_s2Cu_i

Cu_sCu_i. Larger concentrations of Cu species in bulk ZnO may lead to more complex systems where both substititutional and interstitial copper species are present. These systems may present some interesting or unexpected electronic properties. For example, a substitutional and nearby interstitial copper pair (Cu_sCu_i), after full structural relaxation, are found to actually share an original Zn lattice position. Thus the two copper species are perfectly equivalent and cannot be distinguished into a substitutional and interstitial copper anymore (see Fig. 4.6a). This final configuration is obtained starting from a copper atom both in a tetrahedral or an octahedral void. Both species hold a Cu^+ formal oxidation state since the original shallow donor Cu_i species donates the high lying electron to the original deep acceptor Cu_s species. This results in a close shell configuration as represented schematically in the lower panel of Figure 4.6a. The nearby Cu_sCu_i pair is largely favoured (1.1 eV) with respect to the non-interacting Cu_s and Cu_i species, far apart in the supercell model, even though the compensating electron transfer is analogously observed.

Cu_s2Cu_i. A second interstitial copper species in the presence of a Cu_sCu_i pair (Cu_s2Cu_i, see Fig. 4.6b) re-establishes a donor character of the overall system [$\varepsilon^{therm}(+1/0)$ = 0.08 eV from CB minimum], with a single unpaired electron in a perturbed host state (see the schematic representation of the

electronic structure in Fig. 4.6b). The second Cu_i is almost unperturbed in the original interstitial position both if close to or far apart from the Cu_sCu_i fragment. The former configuration is favored by 0.5 eV indicating a tendency of Cu species to cluster, as we will discuss below (see Sec. 4.3.6).

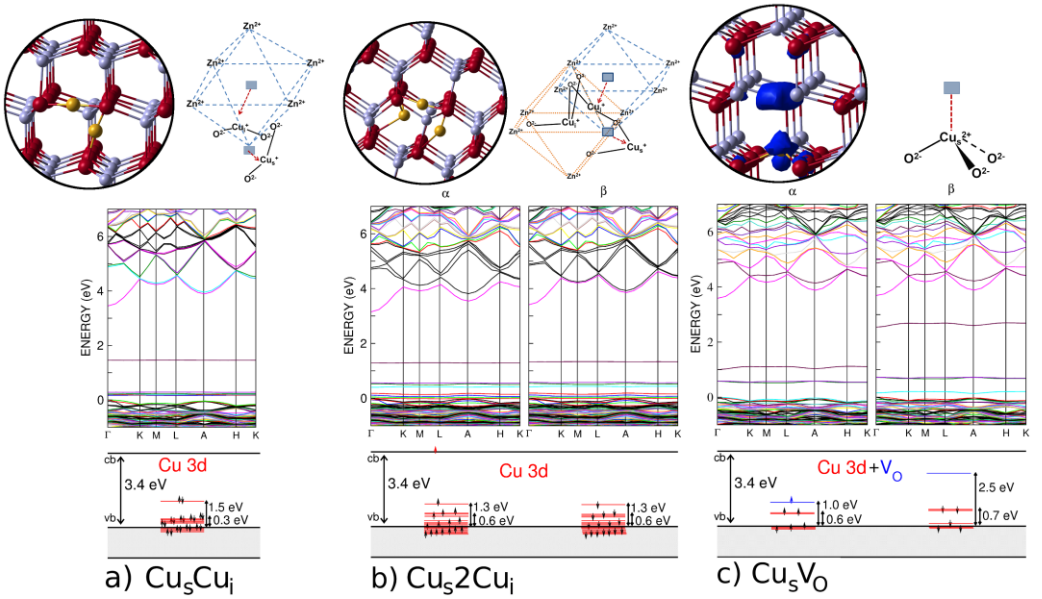

Figure 4.6. Upper panel: ball and stick and schematic structures of the a) Cu_sCu_i and b) Cu_s2Cu_i species in bulk ZnO. Spin density plot and schematic structure of the c) Cu_sV_O species in bulk ZnO. Zn, O and Cu are represented by grey, red and yellow spheres, respectively. Lower panel: band structures together with a schematic representation of the electronic structure (from Kohn-Sham eigenvalues in Γ). Red and blue arrows represent the unpaired electron delocalized in the CB for b) and the unpaired electron localized in the V_O for c), respectively.

4.3.5 Interaction with Oxygen Vacancies: Cu_sV_O

Some recent theoretical works [308,309,339,341] analyzed the potential interaction between transition metal dopants and oxygen vacancies, V_O, in ZnO. Oxygen-poor conditions favor oxygen vacancies formation which are double donor defects [342] (see Sec. 3.3.3). We have investigated the interplay of a single neutral V_O with a nearby (in both axial and equatorial positions) or a distant substitutional copper species (Cu_s). The situation with copper substituting one of the nearest zinc atoms around the vacancy is about 0.4 eV

more stable (see Fig. 4.6c).

Partial charge transfer from the vacancy to the metal is observed when the two impurities are in direct contact, with the unpaired electron still partially localized in a Cu 3d_{z^2} state (0.3 e from the Mulliken spin population analysis), as shown by the spin density plot in Figure 4.6c. The partial spin localization on Cu is true for the vacancy in both axial (reported in the figure) and equatorial positions with respect to the Cu ion. The V_O state is commonly a doubly occupied state [30], however, in the presence of an axial neighboring Cu ion, it is mixed with the Cu d_{z^2} state, as proved by the projected density of states (not reported) and, most importantly, it becomes singly occupied (see the schematic representation of the electronic structure in the bottom panel of Fig. 4.6c). This system (Cu_sV_O), with an unpaired electron in V_O, is still a rather deep donor with $\varepsilon^{therm}(+1/0)$ = 2.27 eV from VB (see Table 4.1). We wish to note that these calculations could not be performed in the presence of ghost functions on the vacancy site because of technical problems related to the vicinity of the Cu ion. The absence of ghost functions may induce an enhanced and spurious mixing of the V_O state with the Cu *d* states.

When the two impurities are far apart in the supercell model (about 10 Å) there is no electron transfer from the vacancy to the copper ion (0.74 e on Cu from Mulliken spin population analysis).

4.3.6 Relative Stability of Cu Species

Finally, the energetics for the various copper defects which have been investigated in this study and presented in the previous sections is compared. The relative stability is discussed in terms of formation energy, E_{form}, and analyzed as a function of (a) the Fermi level of the system, E_F, (see Fig. 4.7) and (b) the oxygen chemical potential, μ_O (see Fig. 4.8). We take μ_O = ½ $\mu(O_2)$ + $\Delta\mu_O'$ with $\Delta\mu_O'$ ranging from –3.78 to 0 eV where the value of $\Delta\mu_O'$ = 0 corresponds to the oxygen rich limit at which oxygen condensation will occur, whereas $\Delta\mu_O'$ = –3.78 is the calculated formation energy of wurtzite ZnO (to be compared with the experimental heat of formation of –3.63 eV [343]). We refer the reader to Sec. 2.1.5.2 for exhaustive details.

(a) We first focus the attention on the dependence of the relative stability of the various defect species with the Fermi level of the system and fix the oxygen chemical potential at the oxygen poor [μ_O = ½ $\mu(O_2)$ – 3.78 eV, Fig.

4.7 left panel] and at the oxygen rich [μ_O = ½ $\mu(O_2)$, Fig. 4.7 right panel] limits. The range of Fermi level considered goes from the top of the valence band to the bottom of the conduction band. Only the portion of the curves relative to the most stable charge state at a certain Fermi level is reported.

At oxygen poor conditions (Fig. 4.7 left panel), Cu_i is predominant for a wide range of Fermi level values, confirming the facility to obtain *n*-type conductivity in ZnO. Interstitial copper species are even more stable by few tenths of an eV when a donor-acceptor copper pair (Cu_s2Cu_i) is present in the neighbourhood, indicating a tendency of copper defects to cluster in bulk ZnO. Cu-doping is therefore experimentally expected to produce inhomogeneously doped regions as reported by Sudakar *et al.* [344] and calculated by Huang *et al.* [307]. Going towards higher Fermi levels (E_F > 2.18 eV), *i.e.* for electron rich systems, the Cu_s becomes thermodynamically the most stable species. At oxygen rich conditions, the situation changes drastically with Cu_s becoming the most stable copper defect at any Fermi level (Fig. 4.7 right panel).

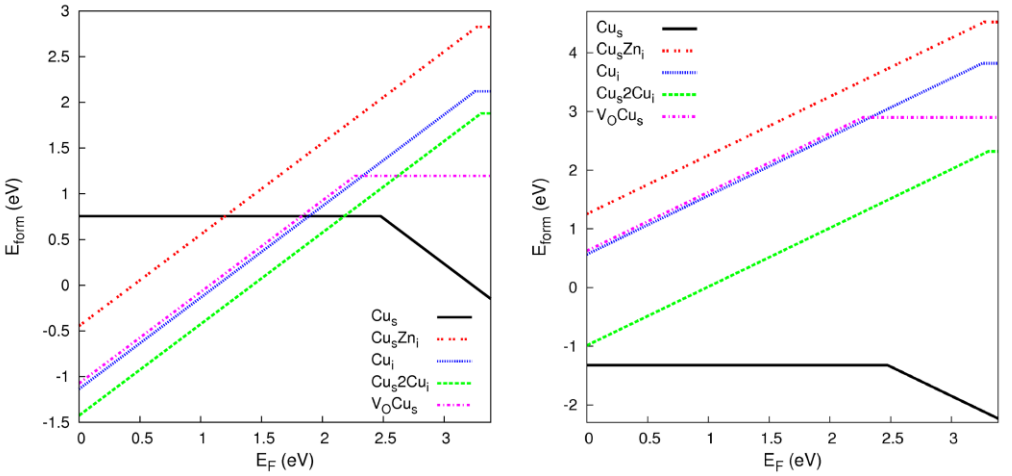

Figure 4.7. Formation energy of Cu defects as a function of the Fermi level (left panel) at the oxygen poor limit ($\Delta\mu'_O$ = –3.78, $\Delta\mu'_{Zn}$ = 0, $\Delta\mu'_{Cu}$ = 0) and (right panel) at the oxygen rich limit ($\Delta\mu'_O$ = 0, $\Delta\mu'_{Zn}$ = –3.78, $\Delta\mu'_{Cu}$ = –1.70). The slope corresponds to the charge state of the defect considered.

(b) The dependence of the formation energy for the most stable charge states at the zero Fermi level (E_F = 0) of all the Cu-doped models considered in this work is now analyzed. In Figure 4.8 we report the formation energies as a function of $\Delta\mu'_O$. In order to take into account the equilibria with the copper

oxides (Cu_2O and CuO) and zinc oxide (ZnO) formation for increasing oxygen concentration or for less negative $\Delta\mu'_O$, we consider the following system of equations (see Sec. 2.1.5.2 for more details):

$$\begin{cases} \Delta\mu'_{Cu} \le 0 \\ 2\Delta\mu'_{Cu} + \Delta\mu'_{O} \le E_{form}^{Cu_2O} \text{ (calc. } -2.08,\ \text{exp. } -1.75) \\ \Delta\mu'_{Cu} + \Delta\mu'_{O} \le E_{form}^{CuO} \text{ (calc. } -1.70,\ \text{exp. } -1.64) \end{cases} \quad (4.1)$$

where formation energies $E_{form}^{Cu_2O}$ and E_{form}^{CuO} of the oxides have been computed with the same computational setup as for all the other calculations and are in good agreement with the experimental heats of formation [178]. Solving the system of disequations above, we obtained the following values for $\Delta\mu'_{Cu}$ in different ranges of $\Delta\mu'_O$:

$\Delta\mu'_{Cu} = 0$ in the range $-3.78 \le \Delta\mu'_O \le -2.08$ (4.2)

$\Delta\mu'_{Cu} = (-2.08 - \Delta\mu'_O)/2$ in the range $-2.08 \le \Delta\mu'_O \le -1.32$ (4.3)

$\Delta\mu'_{Cu} = (-1.70 - \Delta\mu'_O)$ in the range $-1.32 \le \Delta\mu'_O \le 0$ (4.4)

and $\Delta\mu'_{Zn} = (-3.78 - \Delta\mu'_O)$ for all the range of $\Delta\mu'_O$ (4.5)

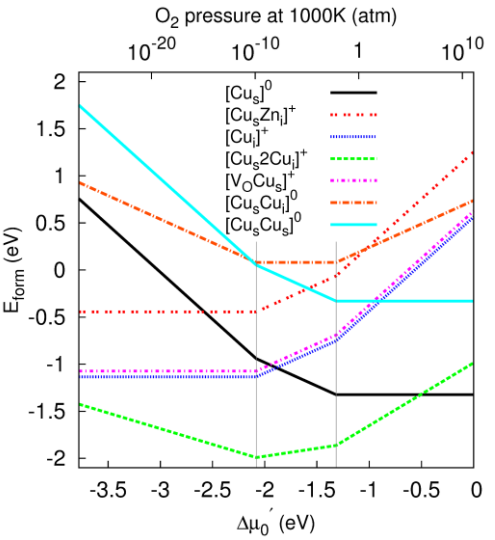

Figure 4.8. Formation energy of Cu defects as a function of delta oxygen chemical potential $\Delta\mu'_O$ at the zero Fermi level (E_F = 0). Note that there are three regions in function of the predominant equilibrium, *i.e.* Cu metal, Cu_2O and CuO, see text for details.

From the graph in Figure 4.8 we observe that the clustering of copper species is energetically favored for a large range of oxygen chemical potential, especially at oxygen poor conditions. Interstitial copper is also preferred at oxygen poor conditions although it may compete with substitutional copper in the presence of oxygen vacancies. This was not obvious and has the meaning that forcing an interstitial additional copper atom in the lattice costs approximately as substituting a zinc atom and removing an oxygen atom altogether. We also learn that interstitial copper (Cu_i) is thermodynamically preferred to interstitial zinc (Cu_sZn_i), *i.e.* a copper atom cannot push a zinc atom from its lattice position into an interstitial site. Finally, the substitutional copper species becomes favoured at oxygen rich conditions, as expected.

4.4 Conclusions

The purpose of this work was to provide an overview on copper doped bulk ZnO based on hybrid exchange-correlation functional calculations. Copper has been investigated in a variety of sites and concentrations, also in the presence of intrinsic defects such as oxygen vacancies. Computed properties have been compared to experimental data. In particular, the present HREELS data demonstrates that Cu particles deposited on the O–ZnO($000\bar{1}$) surface can diffuse into bulk ZnO by thermal treatment at temperature higher than RT. Cu, commonly reported as an acceptor species in bulk ZnO, is presently found to induce a shallow donor state, leading to a dramatic quasi-elastic peak broadening in the HREEL spectra. A temperature-dependent analysis of the broadening gives an ionization energy of 88 meV. Based on the very good agreement of this value with the computed thermodynamic transition energy levels, we propose the shallow donor species to be interstitial Cu in bulk ZnO. Substitutional copper is confirmed to be a deep acceptor species and the hyperfine coupling constants with ^{63}Cu nucleus are computed for the first time and prove a negative Fermi contact term of the isotropic component and large values for the dipolar component. Ferromagnetic and antiferromagnetic spin configurations have been compared in different structural configurations for substitutional (to Zn) copper species and with previously reported data in literature. Although the ferromagnetic is found to be the true ground state within our computational setup, the energy difference with respect to the

antiferromagnetic state is so tiny that magnetic order for this type of system can be excluded. The presence of a higher concentration of copper impurities is found to favour copper clustering. Intrinsic defects such as oxygen vacancies may spontaneously transfer one electron to substitutional copper species. The thermodynamic analysis of the relative stability of the various copper impurities considered in this work indicates that interstitial copper is favoured for a large range of oxygen chemical potentials. Substitutional copper is preferred at oxygen rich conditions. For higher concentration of copper in ZnO copper clustering is preferred and reduces the cost of doping.

CHAPTER 5

Nitrogen Doping[‡]

Abstract

Nitrogen doping is investigated by a combined computational and experimental study on polycrystalline and single crystal ZnO. Electron paramagnetic resonance (EPR) experiments, in conjunction with density functional theory (DFT) calculations, provide a detailed description of defective centres produced upon nitrogen doping of polycrystalline ZnO. Two distinct paramagnetic species are formed upon annealing of ZnO nanoparticles in ammonia atmosphere, which are characterized by the interaction of the unpaired electron with one and two N nuclei. The monomeric defect, on the basis of quantum chemical calculations, is assigned to a nitrogen ion substituting a lattice oxygen ion. Nitrogen doping is achieved on ZnO $(10\bar{1}0)$ surface upon ammonia sputtering. The crucial role of the subsequent oxidation treatment to get rid of residual hydrogen impurities is investigated through thermal desorption spectroscopy (TDS). HREELS experiments provide the optical transition energies of nitrogen defects. Finally, the computation of transition energy levels proves that nitrogen acts as deep acceptor species in ZnO disappointing the hopes to achieve *p*-type conductivity through nitrogen-doping.

[‡] The results described in this Chapter have been reported in: F. Gallino, C. Di Valentin, G. Pacchioni, M. Chiesa, E. Giamello, *J. Mater. Chem.*, **2010**, 20, 689; F. Gallino, L. Jin, H. Noei, C. Di Valentin, Y. Wang, *in preparation*; F. Gallino, G. Pacchioni, C. Di Valentin, *J. Chem. Phys.*, **2011**, 133, 144512.

5.1 Introduction

Nitrogen is emerging as an important doping element in different semiconducting oxides. In the case of TiO_2, it is one of the most promising candidates in the development of effective photocatalysts capable of operating efficiently under solar energy irradiation [254,345,346]. In the case of ZnO, the incorporation of N atoms in the oxide lattice has been regarded as the most promising way to achieve *p*-type doping of this material, which is fundamental for opto-electronic as well as photochemical applications [31,257,347,348]. Different groups have observed shallow acceptor levels with hole-binding energies of only 100-200 meV after N-doping of ZnO thin films and bulk crystals [31,242,348,349,350]. However N-doping is still a controversial matter and it remains an open issue until an atomistic description of nitrogen incorporation and of its bulk species is achieved. Just a multidisciplinary approach may provide a full understanding of the doping mechanism. On the theoretical side, earlier calculations for nitrogen impurities substituting for oxygen (N_s) based on standard density functional theory (DFT) methods (LDA and GGA) yielded a value of ~0.4 eV for the acceptor ionization energy [351,352]. However, the local density or generalized approximations to DFT are severely affected by underestimation of band gaps and by an incorrect delocalization of defect levels resulting in the tendency of overestimating shallow acceptor states [190,305,353]. In this work we use a hybrid exchange-correlation functional, in particular the popular B3LYP [59,60], that well reproduces the experimental gap and partially improves the spin localization.

So far, N impurities in ZnO have been obtained by direct synthesis with chemical vapour deposition (CVD) methods in N_2O or NH_3 atmospheres [354], by mechanochemical methods [355,356] or by post-synthesis treatments with NH_3 at high temperature [357]. The first nitrogen EPR signal in ZnO was reported by Carlos *et al.* [358] and assigned to a substitutional N atom replacing an oxygen anion in the ZnO lattice. Detailed single crystal studies have followed, *e.g.* by the group of Halliburton, and paramagnetic species associated to N^- and N_2^- impurity states have been proposed [359,360]. Complex centres containing N and Zn interstitials have also been reported by optically detected magnetic resonance [361]. In the case of polycrystalline samples, however, even though some reports are available in the literature [355,362], there are scant details about the EPR characteristics of N dopants incorporated in ZnO powders. Polycrystalline materials offer the advantage of

being easy to produce and provide the opportunity to tune the optical and electronic properties by confinement of the electronic wave function over nanometer sized particles [363].

In the first part of this Chapter, we report a CW and pulsed EPR study in conjunction with DFT calculations aimed to characterize nitrogen defective centres produced upon annealing in NH_3 atmosphere of polycrystalline ZnO. We observe two distinct paramagnetic species that are characterized by the interaction of the unpaired electron with one and two N nuclei and we focus our attention on the nature and properties of the monomeric N species. Electron spin echo (ESE) detected EPR and HYSCORE experiments allow us to access a detailed characterization of the hyperfine and quadrupolar tensors of the defect. Irradiation experiments carried out at 4 K at 450 nm wavelength show that the EPR intensity of the monomeric species increases under irradiation in accordance with the data reported by Halliburton and co-workers [359,360] for N acceptors in single crystals of ZnO. Periodic hybrid DFT calculations provide a detailed investigations of all the possible models of nitrogen insertion, their corresponding electronic structures and relative thermodynamic stabilities. On the basis of these calculations, in good agreement with the EPR data, the main nitrogen species is assigned to a N atom replacing a lattice oxygen.

So far, however, an atomistic overview of the doping process of nitrogen insertion is still missing. In order to achieve a full insight of this mechanism, in the second part of this Chapter we afford a "surface science" approach [364]. In particular, we investigate a model system, the ZnO $(10\bar{1}0)$ surface under ultrahigh vacuum (UHV) conditions, which makes it possible to address specific problems that are unapproachable on polycrystalline samples. At first we provide a detailed thermal desorption spectroscopy (TDS) study that shows the effectiveness of nitrogen doping achieved upon NH_3 sputtering and the fundamental role of post-treatment oxidation. Nitrogen bulk species are then investigated through high-resolution electron energy loss spectroscopy (HREELS) measurements with a 66 eV electron primary energy. This technique describes the optical transitions induced by the defective states within the material gap that are directly comparable with the transition energy levels calculated through the computational method presented in Sec. 2.1.5.1. By means of the comparison between experimental and computed data and referring to other recent hybrid functional studies [365,366], it is demonstrated that nitrogen acts as a deep acceptor species in ZnO disappointing the hopes to

achieve *p*-type conductivity through nitrogen-doping.

5.2 Experimental and Computational Details

5.2.1 Powder Sample Preparation and EPR Techniques

Nitrogen doped ZnO powders were synthesized starting from commercial ZnO nanosized powders (Sigma-Aldrich *nanopowder*, < 100 nm *particle size*, *surface area* 15–25 m^2g^{-1}). The powder was heated in $^{14}NH_3$ or $^{15}NH_3$ gas following the procedure proposed by Pfisterer *et al*. [362] with a final oxidation at 500 °C for 1 h in an oxygen atmosphere (pressure 40 mbar).

CW and pulsed EPR experiments were performed at 5 K with a repetition rate of 1 kHz. Electron-spin-echo (ESE) detected EPR experiments were carried out with the pulse sequence: $\pi/2 - \tau - \pi - \tau -$ echo, with mw pulse lengths $t_{\pi/2}$ = 16 ns and t_π = 32 ns and a τ value of 200 ns. Hyperfine sublevel correlation (HYSCORE) experiments [206] were carried out with the pulse sequence $\pi/2 - \tau - \pi/2 - t_1 - \pi - t_2 - \pi/2 - \tau -$ echo with mw pulse lengths $t_{\pi/2}$ = 16 ns and t_π = 32 ns. The time intervals t_1 and t_2 were varied in steps of 8 ns starting from 96 ns to 3288 ns. Three different τ values were chosen (τ = 132 ns, 228 ns and 252 ns). An eight-step phase cycle was used to eliminate unwanted echoes. *Matched* HYSCORE *experiments* [367] were carried out with the sequence $\pi/2 - \tau -$ (HTA) $- t_1 - \pi - t_2 -$ (HTA) $- \tau -$ echo. The amplitude of the microwave field of the matching pulses was 31.2 MHz. The optimal length of the high turning angle (HTA) pulse was experimentally determined with a 2D three-pulse experiment where the pulse length of the second and third pulses were increased in steps of 8 ns starting from 8 ns. The optimal HTA pulse length was found to be 104 ns. The time traces of the HYSCORE spectra were baseline corrected with a third-order polynomial, apodized with a Hamming window and zero filled. After two-dimensional Fourier transformation, the absolute value spectra were calculated. The spectra were added for the different τ values in order to eliminate blind-spot effects.

For more details on CW and pulsed EPR experiments we remind the reader to Sec. 2.2.1.

5.2.2 Single Crystal Sample Preparation, TDS and HREELS Techniques

High resolution electron energy loss spectroscopy (HREELS), thermal

desorption spectroscopy (TDS), and low energy electron diffraction (LEED) experiments were carried out in an UHV apparatus consisting of two chambers separated by a valve and described in Sec. 2.2.2. In all experiments the ZnO $(10\bar{1}0)$ sample was cleaned by repeated cycles of sputtering (1keV Ar^+, 30 min) and annealing in O_2 (1 x 10^{-6} mbar, 850 K, 2 min) and in UHV (850 K, 5 min). Typically, about two sputtering cycles with annealing in UHV were followed by one cycle with annealing in O_2 [239,240] (for more details see Sec. 2.2.2). The surface cleanness was checked by LEED and HREELS. The exposures are given in units of Langmuir (L) (1L = 1.33×10^6 mbar×s).

Since the UHV apparatus could not allow the drastic conditions of the doping procedure proposed by Pfisterer *et al*. [362], we achieved nitrogen doping by sputtering the sample in ammonia atmosphere (beam voltage: 2keV; ammonia dosing: 4500L) at 650 K. The sputtering gases were $^{14}NH_3$ and $^{15}ND_3$ and a subsequent oxidation treatment (4500L) followed at different temperatures. The doping effectiveness was then checked through TDS with a heating rate of 1.5 $K \cdot s^{-1}$. HREELS experiments were performed with impinging electrons with a primary energy of 66 eV.

5.2.3 Computational Details

Spin-polarized calculations were performed using the hybrid B3LYP [59,60] as implemented in the CRYSTAL06 code [71]. The all-electron basis-sets were: O 8-411(d1) [281], Zn 8-64111(d411) [282], N 7-311(d1) [283]. We considered a supercell of 108 atoms, obtained by an expansion matrix 3 x 3 x 3. The bulk lattice parameters have been optimized for bulk stoichiometric ZnO: a = 3.2781 Å, c = 5.2876 Å. A 2 x 2 x 2 k-point mesh was used for the structural optimizations (6 or 8 k-points according to k-point symmetry) and a 3 x 3 x 3 k-point mesh (10 or 14 k-points according to k-point symmetry) was used to calculate the densities of states (DOS). The Kohn–Sham eigenvalues were computed on each k-point but only those at Γ are discussed in the text because of the direct band gap. For additional details about the computational parameters used in this work we refer the reader to Sec. 2.1.4.1.

A detailed description of the computational method to calculate hyperfine and quadrupolar parameters can be found in Sec. 2.1.5.3. Details on the computation of transition energy levels and formation energies are provided in Secs. 2.1.5.1 and 2.1.5.2, respectively. The supercell size effect was checked with a 192-atom supercell model (4 x 4 x 3).

5.3 ZnO Powder

5.3.1 EPR Results

The as received ZnO powders display an EPR spectrum characterized by a slightly asymmetric line with g_{av} = 1.959 (see Fig. 5.1a). This signal, widely reported in the literature [368], is always present in native ZnO and is attributed to shallow donor impurities. No sign of any hyperfine interaction is detectable for this signal.

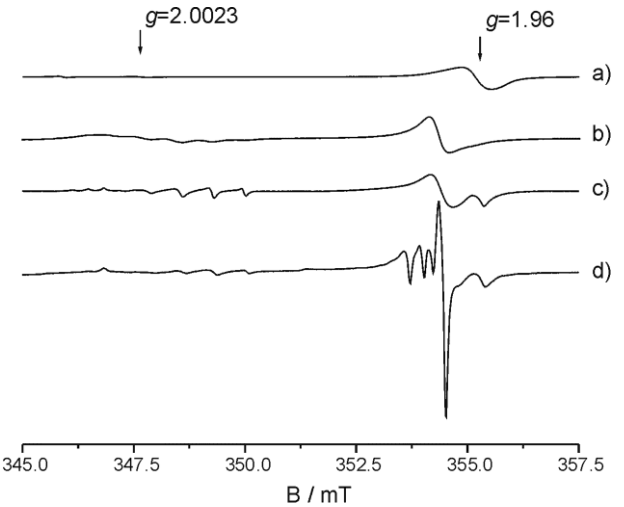

Figure 5.1. CW EPR spectra of a) ZnO starting material, spectrum recorded at 77 K; b) N-doped ZnO, spectrum recorded at 77 K; c) N-doped ZnO, spectrum recorded at 20 K; d) N-doped ZnO, spectrum recorded at 4 K.

After treating with ammonia, the sample develops a pale yellow color and a new spectrum is observed at 77 K, Figure 5.1b. In the high field region of the spectrum a new signal emerges at g = 1.963, while the characteristic signal at g = 1.959 of the as prepared material is no longer detected. In the low field portion of the spectrum, centred at about the free electron g value a complex and unresolved multiline signal is also observed. By cooling the sample to 20 K (see Fig. 5.1c) the linewidth of this signal sharpens considerably and a well resolved powder pattern is observed, which can be interpreted as arising from an S = 1/2 centre interacting with two equivalent N nuclei (I = 1). A similar

signal was observed in "red" ZnO containing large amounts of nitrogen [369] and its features correspond to the molecular nitrogen acceptor centres ("N_2^-") reported by Halliburton and co-workers [360]. The spin-Hamiltonian parameters for this centre are reported in Table 5.1. By further cooling the sample to 4 K the complex multiline pattern, due to the molecular nitrogen acceptors, decreases in intensity, while the EPR signal in the high field region changes considerably and a set of well resolved lines appears.

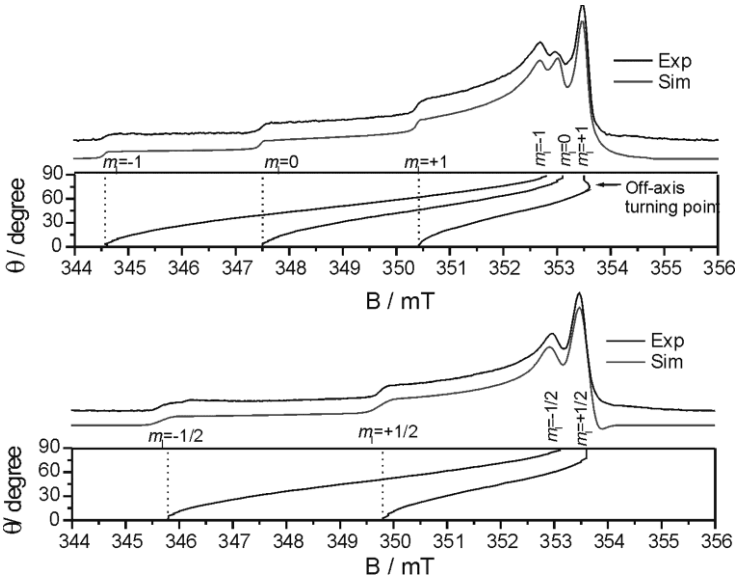

Figure 5.2. ESE detected EPR spectra of ^{14}N (top) and ^{15}N (bottom). Both spectra were recorded at 4 K with the following pulse sequence: $\pi/2 - \tau - \pi$ – echo, with a mw $\pi/2$ length t_p = 80 ns and pulse interval τ = 300 ns.

In order to better characterize the new EPR spectrum, electron spin echo (ESE) detected EPR experiments have been performed. No spin echo signals are observed above 9 K, while a pronounced echo is detected at 4 K. Figure 5.2 shows two-pulse echo detected EPR spectra of ^{14}N and ^{15}N doped ZnO. The advantage of the echo detected EPR technique in this case is that overlapping species can be separated owing to the difference in their relaxation times. In particular, no trace of the complex multiline spectrum observed at g = 2.00 in the CW spectrum is detected in the field swept echo experiment, which indicates that this species is characterized by very fast relaxation times which, even at 4 K, exceed the dead time of the instrument

(about 100 ns). This fact may be attributed to fast kinetic effects, which are presently under investigation in the laboratory of the group of Prof. E. Giamello (University of Turin) by means of specific high field EPR experiments. The nature of this signal has been discussed by Garces *et al.* [360] in the case of N–doped ZnO single crystals and attributed to molecular nitrogen acceptors. The CW EPR spectrum observed at 20 K (see Fig. 5.1c) does not, at present, allow us to provide any better characterization for this centre. In the following section we will thus concentrate on the monomeric N impurity.

The spectrum in Figure 5.2 (top) corresponds to the absorption powder pattern of the CW experiment and shows the typical powder absorption pattern expected for an $S = 1/2$ species with axial symmetry interacting with a single ^{14}N ($I = 1$) nucleus. The simulation was carried out assuming the following spin Hamiltonian

$$H = \beta_e \mathrm{B}^{\mathrm{T}} g S + \sum_i S^{\mathrm{T}} A_i I_i \tag{5.1}$$

with virtually axial $\boldsymbol{g}$ and $\boldsymbol{A}$ tensors ($g_z = 1.9947$, $g_{x,y} = 1.9630$; $A_z = 81.3$ MHz, $A_{x,y} = 8.6$ MHz). This assignment is further confirmed by isotopic substitution using ^{15}N ($I = 1/2$). The simulation of the ^{15}N spectrum was obtained using the same set of spin-Hamiltonian parameters deduced from the simulation of the ^{14}N spectrum [see Fig. 5.2 (top)], accounting for the different nuclear spin, and scaling the hyperfine coupling constants according to the ratio of the nuclear magnetic moments of the two isotopes (^{14}N/^{15}N = 0.26099/0.14325 = 1.82). The spin-Hamiltonian parameters deduced from the simulation are reported in Table 5.1.

Table 5.1. Spin-Hamiltonian parameters for the experimentally observed N species.

Species	$g_\perp$	$g_\parallel$	A_x/MHz	A_y/MHz	A_z/MHz	$\lvert e^2qQ/h\rvert$/MHz	η
N	1.9630	1.9947	±8.6(±0.3)	±8.6(±0.3)	∓ 81.3(±0.8)	5.3±0.2	0.2±0.05
N–N	1.9935	2.0037	|20.08|	|20.08|	|10.10|		

Analysis of the powder spectral pattern reveals that the intense feature at high field is due to an off-axis turning point, as revealed by the spectral road maps, and not to a second species. It should be noted that in the ESE spectra shown in Figure 5.2 the intense feature due to shallow donors at $g = 1.959$ does not show up due to the fast relaxation times of these defects.

It is important to note that the echo signal reported in Figure 5.2 shows a marked increase in intensity under irradiation with $\lambda > 400$ nm. This effect is similar to that observed in the case of N doped TiO_2 [345] and can be understood assuming the presence of diamagnetic precursors, which become paramagnetic upon radiation-induced excitation.

In order to further characterize the N centre, HYSCORE experiments were carried out (see Sec. 2.2.1). HYSCORE is a two-dimensional experiment where correlation of nuclear frequencies in one electron spin (m_S) manifold to nuclear frequencies in the other manifold is created by means of a mixing π pulse. The HYSCORE spectrum of a $S = 1/2$, $I = 1$ disordered system is usually dominated by the cross peaks between the double quantum (dq) frequencies

$$\nu_{\mathrm{dq}}^{\alpha,\beta} = 2\sqrt{\left(\frac{a}{2} \pm \nu_I\right)^2 + K^2(3+\eta^2)} \tag{5.2}$$

where a is the hyperfine coupling at a given observer position while $K = e^2qQ/4I(2I–1)h$ is the quadrupolar coupling constant and η the so called asymmetry parameter. K and η are related to the principal values Q_x, Q_y and Q_z of the traceless $\boldsymbol{Q}$ tensor by the following relations: $Q_x = –K(1 – \eta)$, $Q_y = –K(1 + \eta)$ and $Q_z = 2K$.

The standard HYSCORE spectrum (not reported) recorded at observer position $B_0 = 353.2$ mT (corresponding to the $g_\perp$ position) shows a pair of elongated ridges running along the antidiagonal and two intense correlation peaks in the (– , +) quadrant at (–11.4, +7.5) and (–7.5, +11.4) MHz. The two peaks are separated by approximately $4\nu_N$ (where ν_N is the nitrogen Zeeman frequency) and, based on Eq. (5.2), they can be associated with the dq transitions of a strongly coupled nitrogen nucleus (*i.e.* $A/2 > \nu_N$). From the first order equation for the dq nuclear frequencies, a value of about 9 MHz can be estimated for the hyperfine coupling at this observer position, which corresponds to the value found from the simulation of the ESE spectrum.

A far better spectral resolution is obtained by the use of matched HYSCORE as shown in Figure 5.3a. The dq transitions at (–11.4, +7.5) and (–7.5, +11.4) MHz are still the dominating features, however a number of correlation ridges are now visible in the spectrum. Moving the observer position toward lower field resulted in an a dramatic decrease of the intensity of the spectrum and no signal could be observed with either standard or matched variants of HYSCORE close to the $g_\parallel$ position. This is consistent with

a coupling constant of the order of 80 MHz, which falls out of the detection window.

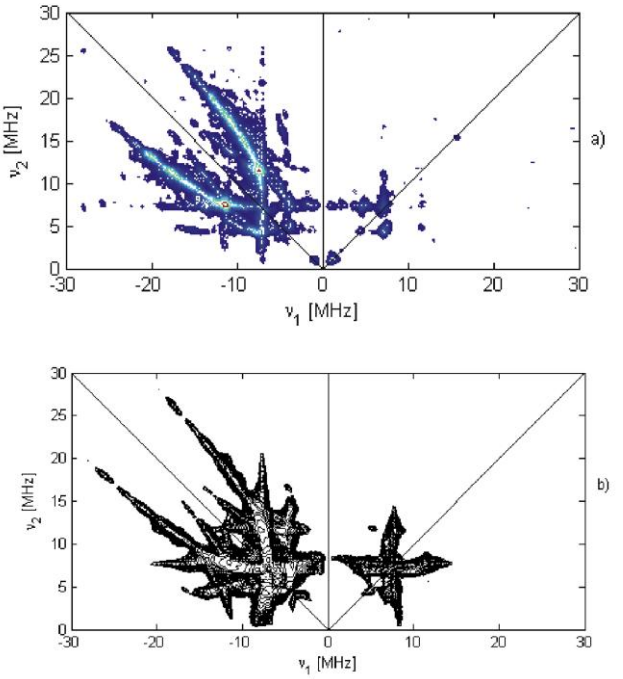

Figure 3 a) An experimental matched HYSCORE spectrum of N-doped ZnO (HTA = 104 ns). Three τ values (τ = 132 ns, 228 ns and 252 ns) are added together; b) computer simulation of the spectrum.

Computer simulation of the spectrum was performed using the values deduced from the simulation of the ESE spectrum as starting parameters and taking into account the quadrupole coupling. The effect of a sizeable quadrupole coupling is to distort the lineshape of single quantum ($-m_I$, m_I) transitions due to second order effects, while it determines the first order correlation patterns of all other transitions. The best fit was obtained with a nuclear-quadrupole coupling constant e^2qQ/h = 5.3 MHz and an asymmetry parameter η = 0.2. It is interesting to compare the quadrupole coupling constant obtained from the simulation with parameters determined for ammonium and nitrate salts in the solid state. In particular, large variations for the quadrupole coupling have been reported for the NH_4^+ ion in the range 0 (NH_4Cl) to 1.2 (ethylendiamine dihydrochloride) MHz, while e^2qQ/h values

ranging between 0.5 and 0.75 MHz have been reported for nitrates [370]. An analysis of the quadrupolar interaction can be helpful in determining the charge state of the defect and will be addressed in light of the results coming from the DFT calculations.

The relative orientation of the hyperfine and nuclear quadrupole interaction was tested with the simulation and the two tensors were found to be coincident.

The simulation of the matched HYSCORE spectrum allows us to refine the spin-Hamiltonian parameters deduced from the simulation of the ESE spectrum and, more importantly, to obtain the quadrupolar tensor for N defects. Moreover, the HYSCORE spectrum, even though it does not lead to the absolute signs of the hyperfine tensor elements, allows the establishment of their relative signs, as reported in Table 5.1.

The experimental $^{N}\boldsymbol{A}$ can be decomposed in the usual way into the isotropic Fermi contact term $^{N}a_{iso}$ and the anisotropic traceless dipolar term $^{N}\boldsymbol{T} = (-T,-T, 2T)$:

$$^{N}A = {}^{N}a_{iso}\,1 + {}^{N}T \tag{5.3}$$

with

$$^{N}a_{iso} = \frac{8\pi}{3} g_e \beta_e g_k \beta_n \left|\psi_{(0)}\right|^2 \tag{5.4}$$

and

$$^{N}T = g_e \beta_e g_k \beta_n \frac{1}{\left\langle r^3 \right\rangle_{2p}} \times \left[-\frac{2}{5}, -\frac{2}{5}, \frac{4}{5}\right] \tag{5.5}$$

The isotropic pseudo-contact interaction $P\langle g\rangle$ and dipolar through space term could be neglected here as they are insignificant. Further analysis of hyperfine structure is possible only if the signs of the $^{N}\boldsymbol{A}$ tensor components are known. For this we use the results from the HYSCORE simulation. Since the nuclear magnetic moment of ^{14}N is positive ($g_N > 0$), the sign of the dipolar hyperfine constants was taken to be positive leading to a positive a_{iso} (this choice is in agreement with DFT calculations, *vide infra*), thus the decomposed $^{N}\boldsymbol{A}$ tensor assumes the form:

$$^{N}A/h = \begin{vmatrix} -8.6 & & \\ & -8.6 & \\ & & +81.3 \end{vmatrix} \text{MHz} = 21.4 + \begin{vmatrix} -30.0 & & \\ & -30.0 & \\ & & +59.9 \end{vmatrix} \text{MHz} \tag{5.6}$$

The extracted ${}^{N}a_{iso}$ and ${}^{N}T$ components may be compared with the corresponding atomic values for assessment of the spin density repartition on the N 2s and 2p orbitals. Introducing the appropriate numerical values [371] yields ${}^{N}\rho_{2s} = {}^{N}a_{iso} / {}^{N}A^{o}_{iso}$ = 21.4 MHz/1540 MHz = 0.014 and ${}^{N}\rho_{2p} = {}^{K}T/{}^{K}T^{o}$ = 30 MHz/46.26 MHz = 0.65; from this qualitative analysis one can deduce that in total, the unpaired electron spin density ${}^{N}\rho_{total} = {}^{N}\rho_{2s} + {}^{N}\rho_{2p}$ = 0.66 is consistent with the unpaired electron being localized in a p orbital of the N atom, whereby some degree of s-p hybridization is indicated by positive spin density in the N 2s orbital.

In summary our experimental results show that:

1) Nitrogen atoms are incorporated in the host ZnO crystal as a consequence of annealing treatment in a NH_3 atmosphere, leading to two distinct paramagnetic centres.

2) The paramagnetic centres are constituted by a dimeric species characterized by exceedingly fast relaxation times (not discussed in this work) and a monomeric species, whose EPR spectrum becomes resolved at T < 6 K. The species is photoactive and the EPR spectral intensity increases under irradiation with $\lambda > 400$ nm.

3) ESE spectra, in conjunction with matched HYSCORE experiments, allow us to determine the spin-Hamiltonian parameters for this species, which clearly indicate that the unpaired electron is localized in the nitrogen 2p orbitals. Based on the reports by Carlos [358] and Halliburton [359] this species may be described in terms of a N^{2-} ion with electronic configuration $2s^2p^5$. Such a configuration corresponds to the localization of a positive hole on a nitride (N^{3-}) ion. We should remark however that the observed *g* factor ($g_{\perp} < g_{||} < g_e$) is somewhat unexpected for a trapped hole centre, even though in the case of ZnO a broad range of values have been reported for these defects. Positive *g* shifts (*i.e.* $g > g_e$) have been reported in the case of acceptor centres in ZnO [372] or P and As impurity centres in ZnSe [373]. On the other hand Hausmann and Schallenberger [374] reported two defects in ZnO characterized by negative *g* shift, which were attributed to O^- ions in different interstitial sites. The negative experimental *g* shift would fit with an electron donor centre. Considering that the unpaired electron is shown by the hyperfine coupling to be unambiguously localized on the N atom, an electron donor centre would result in a $2s^2\ 2p^1$ electronic configuration, corresponding to a N^{2+} ion, which seems rather unrealistic from the chemical point of view. In an

effort to clarify the nature of the N impurity we have performed DFT calculations on different atomistic models considering three possibilities for the nitrogen insertion, namely substitutional for the oxygen, interstitial and substitutional for the Zn. The results are reported in the following sections.

5.3.2 Theoretical Results

5.3.2.1 Models and Electronic Structure

Several possible modes of insertion of N in the bulk of ZnO have been considered in this work: a) substitutional to O, b) interstitial, and c) substitutional to Zn. One N atom has been inserted in the 108-atom supercell, leading to a concentration of *ca*. 1%, consistent with the experimentally estimated value.

We start from the substitutional to O species (N_s). Two possible isomers have been identified which differ for the orientation of the singly occupied *p*-state: parallel or perpendicular to the crystal *c*-axis. Since a parallel orientation of the spin to the *c*-axis was established for the N doping species in a single crystal ZnO sample [358,359], we have restricted the discussion to the corresponding isomer which is also the most stable (by 0.05 eV).

There is only a very tiny structural rearrangement after doping, which results in slightly elongated N–Zn bonds with respect to the O–Zn bonds in pure ZnO. The impurity states associated to the substitutional nitrogen are basically N 2p states very close to the top of the valence band with some small contribution from lattice oxygens, as evident from the projection of the density of states (PDOS) of the N atom, Figure 5.4. Correspondingly, the band structure presents rather flat N defect states (see Fig. 5.5) and the spin density plot looks like a N 2p function along the *c*-axis (see Fig. 5.4). We note that the three highest states are highly localized 2p orbitals on nitrogen. The energy difference between the highest N impurity state and the top of the O 2p valence band is 0.30 for the α (up) component and 0.40 eV for the β (down) component.

Nitrogen may enter the ZnO lattice in an interstitial position by two possible paths, either through the octahedral (N_{iOct}) or the tetrahedral (N_{iTet}) void, which leads to two interstitial species, the octahedral one being more favoured by 0.61 eV; the two interstitials present very similar electronic structural features. For this reason we will limit the discussion to the N_{iOct} results. The interstitial N species are lattice species since the N atom is

inserted in between a lattice O and two adjacent Zn ions, resulting in a twisted $(Zn)_2N–O(Zn)_2$ fragment as shown in Figure 5.4. The N–O distance is 1.38–1.39 Å. The defects states associated with this N species are more detached from the O 2p valence band. There are two π*-type states located at 0.97 eV, 0.52 eV (spin up component) and one π*-type state at 1.27 eV (spin down component) above the top of the valence band (see Fig. 5.5). The spin density plot (see Fig. 5.4) indicates an asymmetric distribution on the N–O atoms which can be quantitatively evaluated from the Mulliken spin population analysis with a 0.88 e on N and a 0.12 e on O.

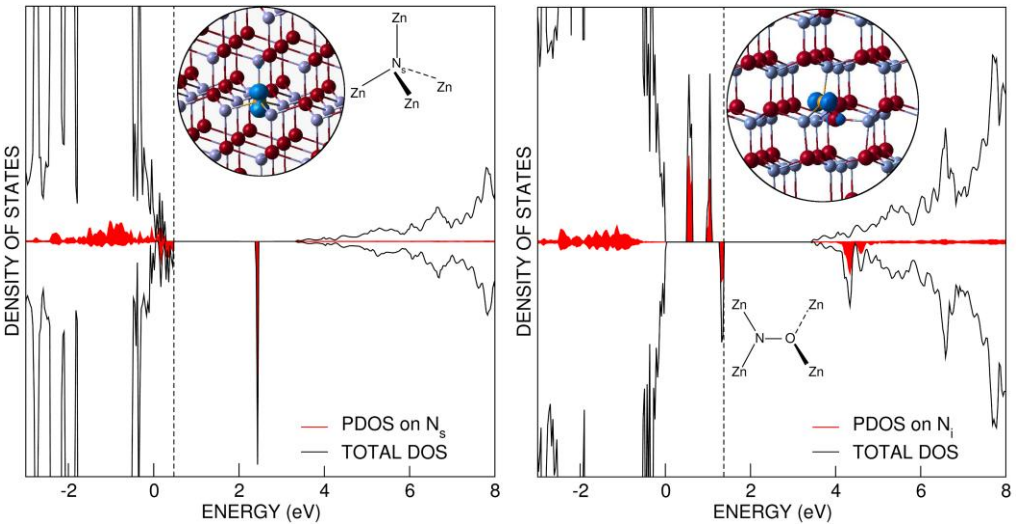

Figure 5.4. Total and projected (on N ion) B3LYP densities of states for the N_s (left panel) and N_{iOct} (right panel) species. The zero energy value is set at the top of the O 2p band. The dotted line indicates the Fermi energy. Insets: spin density plots and schematic structure of the defect centre. Zn, O and N are represented by grey, red and yellow spheres, respectively.

The substitution of a lattice Zn ion (N_{Zn}) with N has not been successful. The insertion of N in the Zn vacancy causes a reorganization of the lattice resulting in the formation of a neutral NO species (with the oxygen atom coming from the lattice) weakly bound to the lattice ions and inserted in the void left by the missing ZnO unit; the N–O bond length is 1.22 Å. This process would eventually be energetically very costly. The electronic structure of these species is essentially that of a neutral NO molecule with a singly occupied molecular π* state and the second orthogonal π* state empty.

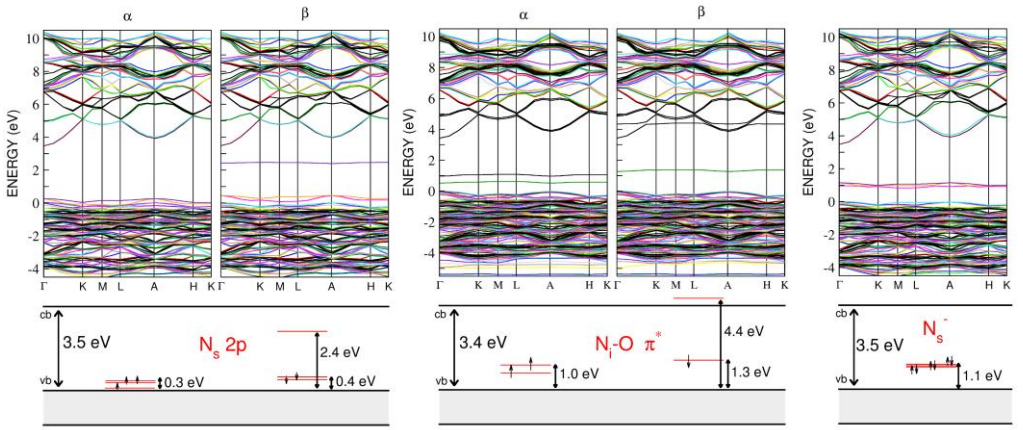

Figure 5.5. B3LYP electronic band structures together with a schematic representation of the electronic structure (from Kohn–Sham eigenvalues in Γ) for the N_s (left panel), N_{iOct} (centre panel) and N_s^- (right panel) species.

5.3.2.2 Thermodynamics

The relative stabilities of the various models considered have been compared by analyzing the formation energy of the defects as a function of the oxygen chemical potential, μ_O, a parameter characterizing the oxygen environment during synthesis (see Sec. 2.1.5.2).

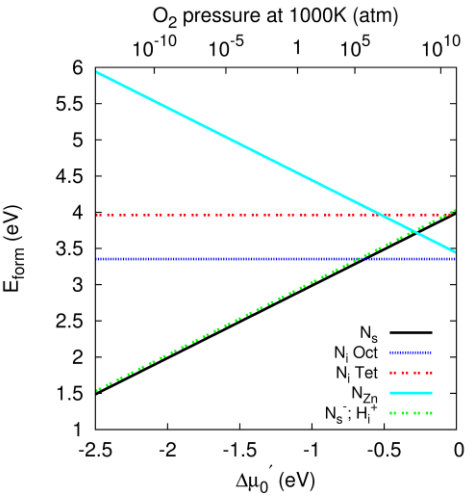

Figure 5.6. The stability diagram for the various species as a function of oxygen chemical potential or O_2 partial pressure.

In Figure 5.6 the formation energies, E_{form}, are plotted as a function of $\Delta\mu'_O$, according to Eq. (2.25) and in order to translate the range of oxygen chemical potential considered into a more usual measure of oxygen concentration, we converted $\Delta\mu'_O$ into oxygen pressure at a fixed temperature of 1000 K (top *x*-axis) [see Sec. 2.1.5.2 and Eq. (2.39)], the typical annealing temperature used for N-doped ZnO. It must be noted that values of oxygen chemical potential below 2 eV correspond to oxygen partial pressures which cannot be reached experimentally. For nitrogen, we used a fixed value of the chemical potential μ_N, and we took the value at which the formation energy of N_2 is zero: $\mu_N = ½ \mu(N_2)$.

From the diagram in Figure 5.6, it is evident that the substitutional N_s species is more stable in a wide range of oxygen chemical potentials from very oxygen-poor conditions to rather high oxygen partial pressures.

5.3.2.3 Computed EPR Properties

The comparison of experimental and computed EPR properties, hyperfine coupling constants and quadrupole interaction terms, provides deeper insight into the proposed model species and allows a clear assignment of the experimental features (see Table 5.2).

The computed hyperfine coupling constants (a_{iso} and dipolar tensor $\boldsymbol{T}$) of the N_s species fit the experimental data extremely well: 19.6 MHz against 21.4 MHz for the a_{iso} and 62.0, –31.0, –31.0 MHz against 59.9, –30.0, –30.0 MHz for the dipolar tensor, Table 5.2. For the interstitial species (N_{iOct} and N_{iTet}) the agreement is poorer both for the a_{iso} and the dipolar tensor ($\boldsymbol{T}$), see Table 5.2 (notice that in general the dipolar part is reproduced with high accuracy at this level of theory). The hyperfine coupling constants computed for the N_{Zn} species, which actually leads to isolated NO species in ZnO are rather far from the experimental data.

The Mulliken spin density on the N atom is found to range from 0.75 for N_s to 0.88 for N_{iOct}. The value for N_s is in good agreement with the experimentally estimated value of 0.66 reported above. Important insights are derived from computed quadrupole coupling constants. Analysis of Table 5.2 shows that e^2qQ/h is rather close for the different species and in line with the experimental value, with the exception of the N_{Zn} species. This provides further evidence that this species is unrealistic. On the other hand, the

asymmetry parameter η appears to be very sensitive to the local coordination of the N atom as already observed in the case of molecular systems [375]. We found, in fact, that the two interstitial species are characterized by rather large η values, which are incompatible with the experimental HYSCORE spectrum. The N_s substitutional species is found to be perfectly axial ($\eta = 0$), as expected from the symmetry of the defect. This is in line with the small η value (0.2) extracted from the simulation of the HYSCORE spectrum. The discrepancy between the calculated and experimental values can be explained by local distortions in the polycrystalline systems, which can affect the electric field gradient of the defect.

Table 5.2. Spin-Hamiltonian parameters for the monoatomic N species in ZnO (in MHz).

	A_{zz}	A_{yy}	A_{xx}	a_{iso}	T_{zz}	T_{xx}	T_{yy}	$\frac{e^2qQ}{h}$	η
Exp.[a]	81.3	8.6	8.6	21.4	59.9	–30.0	–30.0	|5.3|	0.2
$\mathbf{N_s}$	82.1	11.4	11.4	19.6	62.0	–31.0	–31.0	+6.1	0.00
$\mathbf{N_{iOct}}$	104.2	7.0	4.7	30.8	73.4	–37.9	–35.5	–6.1	0.58
$\mathbf{N_{iTet}}$	98.1	10.6	8.6	26.3	71.8	–36.9	–34.9	–6.0	0.55
$\mathbf{N_{Zn}}$	107.1	21.2	14.8	23.7	83.4	–44.9	–38.5	–3.3	0.80

[a] The experimental values are derived from the data reported in Table 5.1.

The comparison of theoretical with experimental EPR parameters together with the thermodynamic analysis reported in the previous paragraph indicate that among the considered species only the N substitutional to oxygen can account for the experimental EPR spectrum.

5.3.2.4 Interaction with Shallow Donors

Since pristine ZnO samples are characterized by the presence of shallow donors, as discussed above, we have analyzed the possibility that these donors interact with the monomeric N-species. In order to model this situation we have introduced a H atom in the supercell (H-interstitials are considered to be one of the most common shallow donors, see [212] and Sec. 3.3.1) together with a N atom in substitutional position to O (N_s). After full structural relaxation we observed that the extra electron introduced by the H atom has dissociated from the proton and was transferred to the N species which

behaves as a good electron trap: (N_s^-, H_i^+). As a consequence, the N–Zn distances shrink by about 0.4–1.1 Å. This electron transfer quenches the paramagnetic N-centre which transforms into a diamagnetic N_s^- species. A similar process occurs in N doped TiO_2: the N impurities interact with oxygen vacancies and act as trapping centres for electrons in shallow donor states [345,376]. A N_s^- species can also be obtained by simply adding an extra electron to the supercell model (charged supercell calculation balanced by the introduction of a background of charge). This second model does not require the presence of any impurity and is representative of the presence of free extra electrons in the sample. The resulting electronic structure (see Fig. 5.5) is essentially identical to that obtained for the N_s, H co-doped system:

$$N_s^{\bullet} + e^- (\text{from shallow donor}) \rightarrow N_s^- \tag{5.7}$$

The doubly occupied nitrogen impurity states are shifted upward with respect to those of the paramagnetic N_s species by about 0.7–0.8 eV, due to the increased Coulombic repulsion (see Fig. 5.5). The resulting diamagnetic species is clearly invisible to EPR spectroscopy. Consistent with the experimental finding that upon irradiation (λ > 400 nm) at 4 K the EPR intensity of the monomeric N_s species increases, we propose that excitation of one electron from the N_s^- diamagnetic precursor leads to formation of the $N_s^{\bullet}$ species:

$$N_s^- + h\nu (\text{vis}) \rightarrow N_s^{\bullet} + 1\,e^- (\text{excited}) \tag{5.8}$$

Again, this behaviour of the doping centres is very similar to what was observed for the N-doped TiO_2 samples upon visible light irradiation, where the intensity of the EPR signal is found to reversely oscillate between two given values when switching the irradiation lamp on and off [345].

The stability of the N_s^- species has been theoretically investigated by comparing the formation energy of the (N_s^-; H_i^+) pair as a function of the oxygen chemical potential to the curves discussed in the previous paragraph for the paramagnetic monoatomic species N_s and N_i (see Fig. 5.6). The stability of this pair is essentially identical to that computed for the N_s species resulting in the superposition of the two curves. In other words, the energy associated to the processes of formation of the two species is of the same entity (values at $\Delta\mu'_O$ = 0) as well as the dependence with respect to the

oxygen chemical potential (slope of the curve).

5.4 ZnO Single Crystal

5.4.1 TDS Results

The nitrogen doping process has then been investigated on the non-polar ZnO $(10\bar{1}0)$ surface. Since the drastic experimental conditions used to achieve nitrogen doping on the polycrystalline sample cannot be reached in our UHV-apparatus (see Sec. 2.2.2), a milder doping process was adopted. In particular, the single crystal was sputtered with NH_3 gas (beam voltage: 2 keV; ammonia dosing: 4500 L) at 650 K.

The effectiveness of nitrogen doping has been evaluated by means of thermal desorption spectroscopy (TDS). Since the molecular ion NH_3^+ has the same ratio mass to charge m/e (17) of the OH^+ ion, coming from the cracking pattern of water and with an intensity of 20% with respect to the molecular ion H_2O^+, we used $^{15}ND_3$ as nitrogen source to avoid any overlap. The obtained TDS spectra for deuterium molecule, water, nitrogen molecule and ammonia are reported in Figure 5.7.

After $^{15}ND_3$ sputtering new features appear at high temperatures respect to $^{15}ND_3$ exposed surface (see Fig. 5.7). A broad and complex desorption band for $^{15}ND_3$ is observed in the range 450-1000 K, with a maximum peak around 650 K (see Fig. 5.7d). Two TDS features for water desorption are visible at 650 K and 850 K (see Fig. 5.7b) and an intense D_2 desorption peak appears above 700 K (see Fig. 5.7a).

Since NH_3 adsorbed on the clean and sputtered ZnO $(10\bar{1}0)$ surface has been proved to completely desorb at 400 K and 600 K, respectively, (see Chapter 6) the feature observed in the range 450-1000 K is due to bulk ammonia. Two hypotheses of mechanism may be proposed to explain this broad desorption band. First of all, we have to consider the presence of different available sites for incorporation of $^{15}ND_3$ in bulk sample (tetrahedral or octahedral voids, O or Zn lattice vacancies). $^{15}ND_3$ has different energy barriers to diffusion, stabilities and bond strengths according to its bulk site: it can behave as molecular species and be easily desorbed or it can be strongly incorporated in the lattice and hardly removable. Therefore, according to the kind of bulk species, $^{15}ND_3$ diffusion to the surface or $^{15}ND_3$ decomposition with subsequent diffusion of atomic D and atomic ^{15}N to the surface (maybe

with different energy barriers) can be the rate determining step in the thermal desorption process. Moreover, while the water desorption already observed in the range 300-650 K for the $^{15}ND_3$ exposure of the surface is due to molecularly adsorbed water and OH species desorption, the two peaks at 650 K and 850 K are strictly correlated with ammonia decomposition/diffusion to the surface. If $^{15}ND_3$ is totally or partially decomposed in D and ^{15}N or $^{15}ND_x$ species, the hydrogen diffuses to the surface and in part it desorbs like D_2 and partially it comes in contact with 3-fold coordinated O atoms (O_{cus}), triggering water desorption. On the other hand, if $^{15}ND_3$ diffuses to the surface, there it may desorb or be oxidized by O_{cus} and subsequently it may desorb like $^{15}N_2$ or ^{15}NO. In both these hypotheses water desorption is expected and since we observed two peaks (see Fig. 5.7b), we may suppose they have different nature.

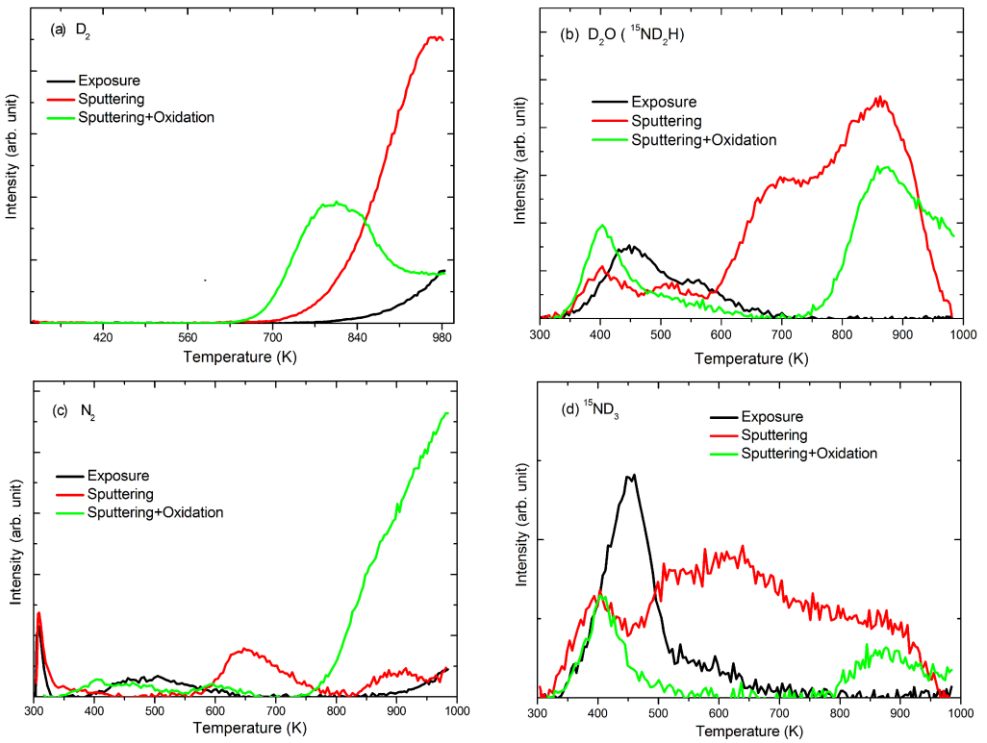

Figure 5.7. Comparison of TDS spectra for $^{15}ND_3$ exposure, $^{15}ND_3$ sputtering and sputtering followed by oxidation (700 K for 10 min) on the stoichiometric ZnO $(10\bar{1}0)$ surface. The data are for the following species: (a) D_2 (m/e 4), (b) D_2O (m/e 20) overlapped with $^{15}ND_2H$, (c) $^{15}N_2$ (m/e 30) and (d) $^{15}ND_3$ (m/e 21). The heating rate was 1.5 $K \cdot s^{-1}$.

The analysis of $^{15}N_2$ and D_2 desorption features (see Fig. 5.7 a,c) may shed a light on the two models proposed, decomposition and diffusion. Both these spectra show two features, one at 650 K and the other above 750 K but the intensity ratio is opposite: for $^{15}N_2$ the 650 K feature is the predominant one (see Fig. 5.7c); for the D_2 the 650 K peak is almost negligible with respect to the signal above 750 K (see Fig. 5.7a). For the decomposition model we expect the evolution of a large amount of D_2 and water (D_2O) and almost absence of $^{15}ND_3$ desorption. Instead, for the diffusion model we expect desorption peaks for $^{15}ND_3$ and for the species formed by the oxidation process, D_2O, $^{15}N_2$ and ^{15}NO. Actually the two desorption processes observed at 650 K and above 750 K show different species distribution. At 650 K the main species is water but it is less intense with respect to the feature above 750 K and two maxima are observed for $^{15}ND_3$ and $^{15}N_2$ desorption. Above 750 K D_2 is the most abundant species followed by water, while $^{15}ND_3$ and $^{15}N_2$ have very low intensity. According to these observations the 650 K desorption spectra fit better with the diffusion model, while the desorption above 750 K is better described by the decomposition model.

We can summarize that upon ammonia sputtering of ZnO $(10\bar{1}0)$ surface we have obtained the insertion of $^{15}ND_x$ species in bulk ZnO, with different thermodynamic stabilities according to their positions in the lattice. At 650 K and above 750 K we observe two water desorption features of different nature and we have tentatively assigned them to a diffusion-decomposition two steps mechanism and to subsequent steps in thermal decomposition of bulk $^{15}ND_3$, respectively.

An additional observation is noteworthy. If the decomposition of $^{15}ND_3$ is complete, at so high temperature (~950 K) all ^{15}N atoms are expected to diffuse to the surface and then to be desorbed especially as $^{15}N_2$. However only a very little amount of $^{15}N_2$ is observed in TDS spectra after sputtering. Therefore we oxidized the sample at 700 K for 10 minutes and we observed a dramatically increase of the $^{15}N_2$ desorption peak (see Fig. 5.7c). In literature, oxidation post-treatment process is described to be fundamental and to trigger the activation of bulk nitrogen species to atomic nitrogen, substitutional to an oxygen lattice [377]. The larger amount of total nitrogen desorbed after oxidation can be explained only supposing that, in the sputtered sample, the heating is not able to completely decompose bulk $^{15}ND_x$ to atomic nitrogen. Oxygen acts as catalyst, diffuses in the lattice and decreases the energy barrier

for the N–D bond breaking reaction. As reported by Jokela *et al.* [378] N–H complexes are stable up to ~950 K and this may imply that 700 K is not sufficient to decompose $^{15}ND_x$ bulk species. The energy cost for a complete decomposition of $^{15}ND_3$ is too high for this temperature range, unless O_2 is used as oxidizing catalyst.

According to this model, upon oxidation we suppose to decompose all $^{15}ND_x$ species in the bulk and consequently to remove the hydrogen, D_2, whose desorption takes place at lower temperature than oxidation temperature (700 K). However, the second water feature above 750 K is still present and with the same intensity with respect to the sputtered sample (see Fig. 5.7b). Also D_2 desorption is observed even if less intense (see Fig. 5.7a). This observation may be explained considering the sample depth and the O_2 diffusion. Oxygen molecules may be unable to diffuse in all the sample, shallow layers and deep layers, at that oxidation conditions (temperature and time). In the deepest layers some $^{15}ND_x$ may be still present and by heating the sample they are partially decomposed with diffusion of D atoms on the surface and consequently desorption of D_2 and water. This hypothesis takes also into account the lower D_2 signal but to provide a clear proof to our hypothesis, more experimental evidences are needed.

In this context, we have investigated in deeper details the oxidation process. In Figure 5.8 the TDS spectra obtained for different oxidation time are reported. We used NH_3 as sputtering gas instead of $^{15}ND_3$ since we are interested only in the desorption features for hydrogen and nitrogen molecules (see Fig. 5.8). The H_2 feature almost disappears after 30 minutes while the water desorption decreases but it is observable even after 60 minutes. The N_2 desorption peak starts to decrease after 60 minutes. These evidences confirm the fundamental role played by oxidation in getting rid of the excess of hydrogen that is achieved already for 30 minutes of oxidation at 700 K. A residual amount of hydrogen however is still present in these conditions and recombines with surface oxygen and desorbs as water. Longer time of oxidation, *e.g.* 60 minutes, causes partial removal of nitrogen itself. Even in this case, therefore, the diffusion of oxygen molecules in the deep layers of the crystal breaking all the residual N–H bonds, favoured by longer times of oxidation, must be balanced with the over-oxidation of NH_x species in the shallow layers. In this context we can assess that 30 minutes of oxidation at 700 K is the best operative compromise.

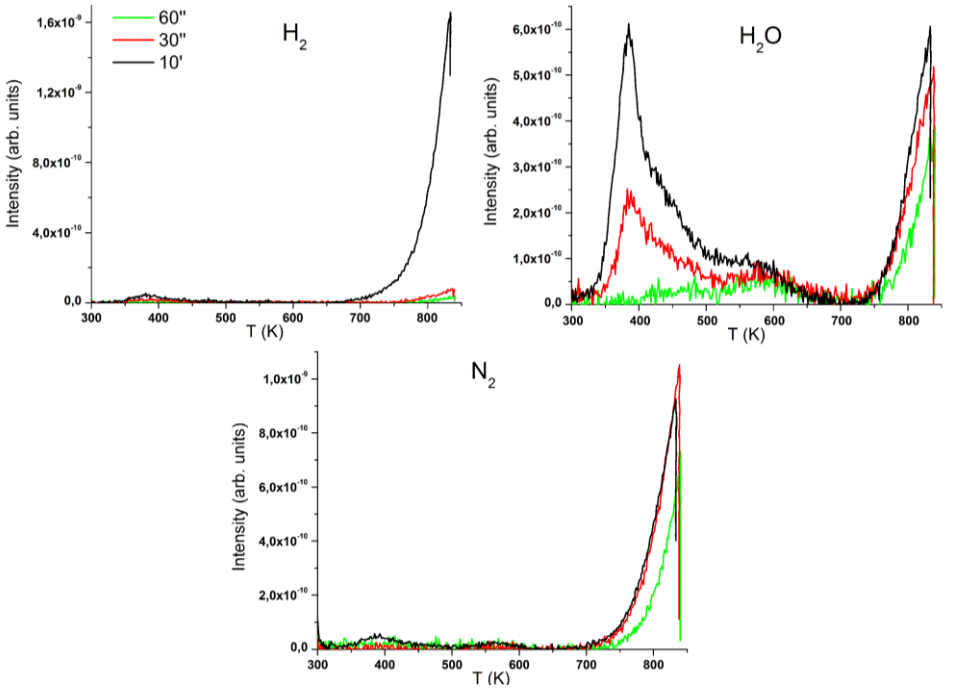

Figure 5.8. TDS spectra for NH_3 sputtering followed by oxidation (700 K) for different time: 10, 30 and 60 min. The data are for the following species: (left top) H_2 (m/e 2), (right top) H_2O (m/e 18), (bottom) N_2 (m/e 14). The heating rate was 1.5 $K \cdot s^{-1}$.

Finally, in order to corroborate our hypotheses we repeated TDS experiments with NH_3 (see Fig. 5.9). The spectra are very similar to those observed for $^{15}ND_3$ experiments. To avoid NH_{3-x} desorption at low temperature the samples were flashed at 750 K before TDS experiments and this pre-treatment induces some differences especially for the sputtered sample. The hydrogen desorption is reduced at high temperature and new N_2 and N features are observed (see Fig. 5.9 a,c,d). However, spectral evidences are consistent with our model. Oxidation confirms its fundamental role in the activation of bulk nitrogen by catalyzing the decomposition of NH_3. The oxidation conditions are not sufficient to get rid of the water desorption feature above 750 K. Flashing the sample at 750 K improves the thermal decomposition of NH_3 for sputtered sample, as we can appreciate by the increasing of N_2 desorption (see Fig. 5.9c) but it improves also the oxidation of NH_3 since the water feature is significantly less intense than that for sputtered sample. Moreover it is appreciable a 30 K shift to high temperature in water desorption for oxidized sample (see Fig. 5.9b). This evidence may be

explained by thinking that, since the oxidation of bulk NH_x species in the shallow layers is complete for oxidized sample, higher temperatures are needed to decompose NH_x species in deep layers. For the sputtered sample the water desorption starts at lower temperature because of the decomposition of NH_x species in the shallow layers.

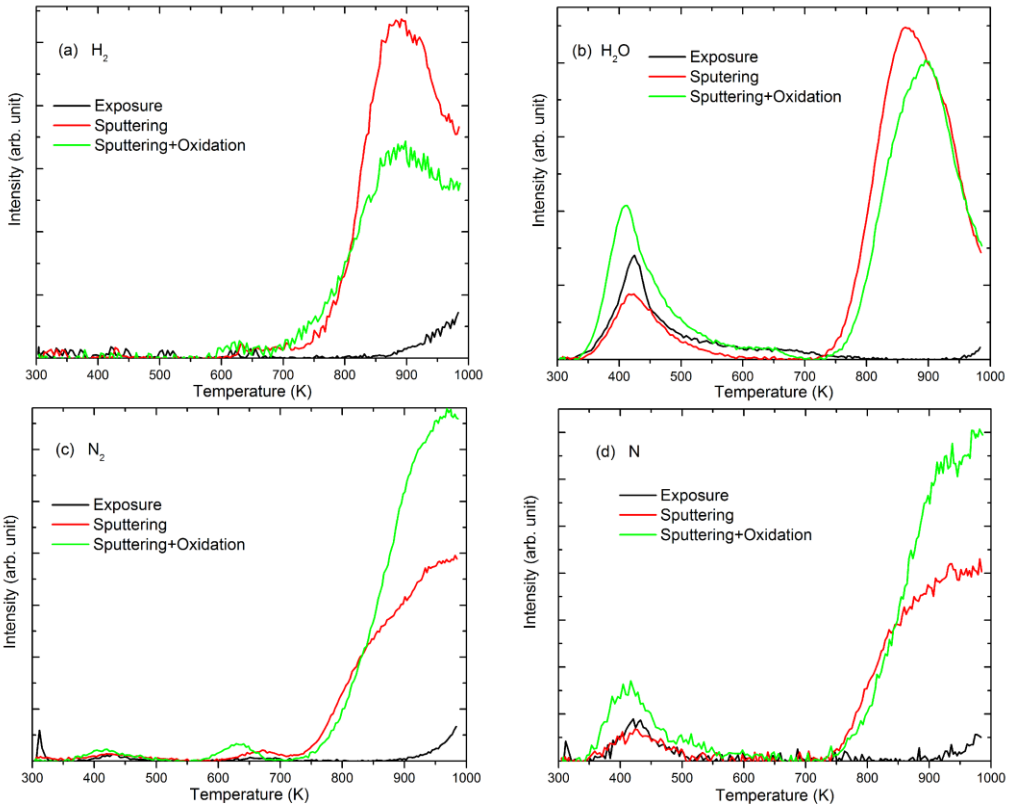

Figure 5.9. Comparison of TDS spectra for NH_3 exposure at room temperature, NH_3 sputtering and sputtering followed by oxidation (700 K for 10 min) on the stoichiometric ZnO $(10\bar{1}0)$ surface. The sputtered sample and the sputtered and oxidized sample were flashed at 750 K before TDS experiments. The data are for the following species: (a) H_2 (m/e 2), (b) H_2O (m/e 18), (c) N_2 (m/e 28), (d) N (m/e 14). The heating rate was 1.5 $K \cdot s^{-1}$.

5.4.2 HREELS Results

In order to investigate the defect states of the nitrogen species inserted in the bulk single crystal, we perform HREELS measurements.

The commonly used 10 eV electron incident energy in HREELS experiments does not allow to investigate bulk species since it monitors only the 0-500 meV loss energy peaks region, typical of adsorbate species. To get informations on electronic transitions of nitrogen impurities, we used an electron incident energy of 66 eV and the recorded spectra are reported in Figure 5.10.

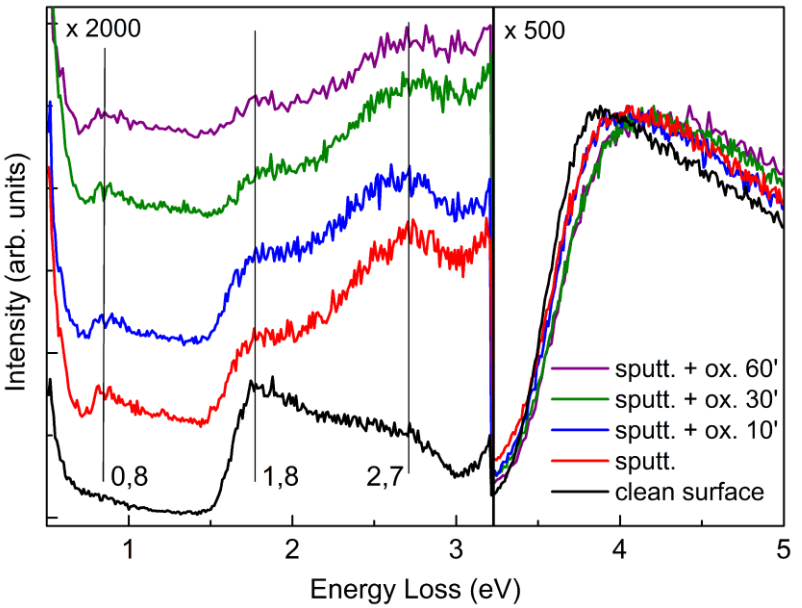

Figure 5.10. HREEL spectra recorded for the stoichiometric clean ZnO $(10\bar{1}0)$ surface and after sputtering followed by oxidation at 700 K for 10, 30 and 60 minutes. Before HREELS measurement the sample was flashed at 650 K to remove eventually adsorbed species after treatment. All spectra were recorded at RT in specular geometry with an incidence angle of 55° with respect to the surface normal and with a primary energy of 66 eV.

First of all, we observe for all the spectra a well-reproduced band gap of 3.4 eV as expected for ZnO. In the intra-band-gap region where no peaks are expected for the pure sample, a broad loss signal is however present for the clean surface, centred at 1.8 eV. After sputtering two new features appear at 0.8 and 2.7 eV that are therefore related to the insertion of NH_x species in ZnO bulk (see Fig. 5.10). In order to get more insights, we oxidized the sample for different time (10, 30 and 60 minutes). While the 0.8 eV loss peak is almost unaffected by the oxidation, the 2.7 eV loss peak decreases in intensity for

increasing oxidation time. On the basis of these evidences and of the above TDS results about the effects of oxidation on nitrogen species, we tentatively assign the 0.8 eV signal to an isolated nitrogen species and the 2.7 eV peak to a NH_x species that is gradually decomposed at increasing the oxidation time. The electron energy loss peaks can be directly compared to the calculated optical transition levels and therefore ab-initio DFT models can provide an atomistic evidence to corroborate these assignments.

5.4.3 Transition Energy Levels

So far, in Sec. 5.3.2.1 nitrogen species are shown to be rather deep acceptors but the analysis has been limited to the single-particle Kohn-Sham eigenvalues. A better description of their electronic properties is provided by the calculation of the transition energy levels that describe the energy cost for the transitions between different defect charge states (see Sec. 2.1.5.1). As mentioned in Sec. 2.1.3, the use of a hybrid exchange-correlation functional allows to partially overcome the well-known limitations of LDA and GGA functionals in describing localized defect states (see Sec. 2.1.3). Another method, recently proposed by S. Lany and A. Zunger [305], to get rid of standard DFT functionals shortcomings is the use of a Hubbard U term and of an onsite hole-state potential, V_{hs}.

Using the method reported in Sec. 2.1.5.1, we calculated the transition energy levels for the substitutional nitrogen to lattice oxygen, N_s, identified in polycrystalline ZnO sample in Sec. 5.3. In particular, we considered two transitions, as reported in Eq. (5.9): from the charged state to the neutral one (forward direction) and from the neutral state to the charged one (backward direction).

$$N_s^- \rightleftharpoons N_s^0 + e^- \tag{5.9}$$

where the electron e^- can be in the valence band or in the conduction band (see figure in Table 5.3). In Eq. (2.28) the transition level $\varepsilon(q/q')$ describes, by definition, a transition from the q charge state to the q' charge state where $q' = q + 1e^-$. In Figures 2.2 and 2.3 the thermodynamic and optical transition levels $\varepsilon(0/-1)$ represent the excitation of an electron from the valence band to the unoccupied acceptor state of A^0, forming the negatively charged defect A^- ($A^0 + e_{VB}^- \rightarrow A^-$). In particular, the optical transition $\varepsilon^{opt}(0/-1)$ is computed at the

fixed atomic positions of the relaxed neutral defect A^0 (vertical transitions). The opposite excitation ($A^- \rightarrow A^0 + e_{CB}^-$) that corresponds to the forward direction in Eq. (5.9) was not considered in Sec. 2.1.5.1. Only the emission transition ($A^- \rightarrow A^0 + e_{VB}^-$) was taken into account (see PL_2 in Figs. 2.2 and 2.3). In Table 5.3 we report also the optical excitation from A^- to A^0 that conventionally we called $\varepsilon^{opt}(-1/0)$ and we calculated at the fixed atomic positions of the relaxed negatively charged defect A^-. We stress that this is not an acceptor but a donor transition. The computed transition levels are reported in Table 5.3 and compared with the values from two recent studies [365,366] using the hybrid HSE functional [118,119,120,121,122] and the onsite hole-state potential, V_{hs}, together with a GGA+U approach [305].

Table 5.3. Transition levels for nitrogen substitutional to oxygen, N_s, in bulk ZnO (in eV).

Ref.	DFT Method	N° Atoms	$\varepsilon^{opt}(-1/0)$	$\varepsilon^{opt}(0/-1)$	$\varepsilon^{therm}(0/-1)$	E_{rel} [a]
this work	B3LYP	192	2.46	2.16	1.47	0.69
[366]	HSE (α=0.25)	72	-	2.28	1.44	0.84
[365]	HSE (α=0.36)	72	2.4	~1.7	1.3	~0.3
[366]	HSE (α=0.38)	72	-	-	2.10	-
[366]	GGA+U +V_{hs}	72	2.59	2.47	1.62	0.85

[a] Relaxation energy of the defect centre in the charged state in absolute value as defined in Eq. (2.31).

Hollow red line = $\varepsilon^{opt}(0/-1)$, hollow violet line = $\varepsilon^{opt}(-1/0)$ (see text for details and also Figs. 2.2 and 2.3).

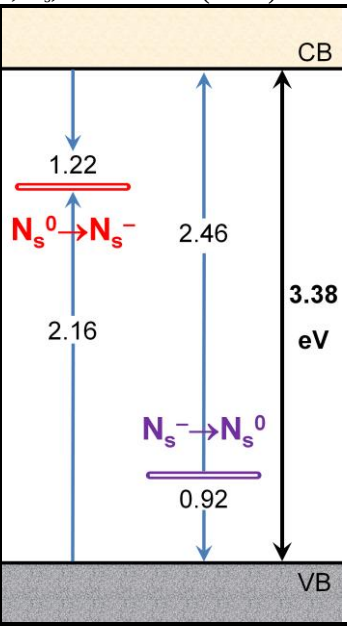

First of all, we observe a good agreement of our data with the values obtained with the HSE functional using the standard $\alpha = 0.25$ and with the GGA+U calculation employing the additional onsite potential V_{hs} [305]. The modest discrepancies may be assigned to the different evaluation of the relaxation energy (E_{rel}) with different supercells. The comparison with the HSE functional, where the α value is optimized to better fit the experimental gap ($\alpha = 0.36$ [365] and $\alpha = 0.38$ [366]) is less satisfactory. Note that the set of

results are not even consistent between the two almost identical approaches. Furthermore, the value of E_{rel}~0.3 as reported in Ref. [365] appears unrealistically too low.

Thus, on the basis of our and previously reported data, we conclude that N_s in ZnO is a deep acceptor species. The acceptor transition level $\varepsilon^{opt}(0/-1)$ is well-detached from the valence band and the original hopes of achieving *p*-type conductivity upon nitrogen-doping are completely disregarded.

However, the computed values are actually in rather bad agreement with the data presented in the HREELS measurements on N-doped ZnO $(10\bar{1}0)$ surface. This discrepancy is currently under investigation in our research groups and new theoretical models are tested in order to understand the electron energy loss peaks reported in Figure 5.10.

5.5 Conclusions

Nitrogen doping has been investigated through a combined and multidisciplinary study on both polycrystalline and single crystal samples. Nitrogen impurities have been introduced in polycrystalline ZnO upon annealing under ammonia atmosphere. The resulting material shows a pale yellow colour and exhibits a series of distinct EPR spectra, two of which are due to nitrogen-containing paramagnetic defects, namely a monomeric and a dimeric species. In this work we concentrated on the nature of the monomeric species. HYSCORE experiments allowed the obtainment of both the hyperfine and quadrupole coupling tensors, which clearly indicate that the unpaired electron is localized in the 2p orbitals of a nitrogen atom. Different modes of insertion of nitrogen in the bulk of ZnO have been tested by means of quantum mechanical calculations in order to achieve a quantitative understanding of the electronic defect structure and a detailed microscopic structure model for this defect. Interstitial, substitutional to O and substitutional to Zn nitrogen species have been considered. The relative stabilities of the various models have been compared by analyzing the formation energy of the defects as a function of the oxygen chemical potential, resulting in a larger thermodynamic stability for the substitutional species to oxygen. Computed EPR properties for this species are in good agreement with the experimental data indicating that the experimental EPR spectrum is consistent with a nitrogen ion substituting a lattice oxygen ion.

Nitrogen doping is also investigated on the ZnO $(10\bar{1}0)$ surface where the insertion of nitrogen impurities upon ammonia sputtering has been proved through TDS spectra. A post-sputtering oxidation treatment has been demonstrated to be crucial in breaking residual nitrogen-hydrogen bonds in the deep sample layers. The optimal operative conditions for oxidation have been shown to be 30 minutes at 700 K. The optical transition levels of nitrogen species have been then investigated through HREEL spectroscopy. Two main electron energy losses have been observed at 0.8 eV and 2.7 eV and they have been attributed to an isolated nitrogen species and to a NH_x species on the basis of their behaviour for increasing oxidation time. These levels are compared with the calculated optical transition energy levels for the N_s species. Even though the very deep acceptor levels computed for N_s allow us to exclude nitrogen-doping as a viable route to achieve *p*-type conductivity in ZnO, their bad agreement with the HREELS data leaves some open issues. In particular, the HREELS peak observed at 0.8 eV is still unexplained together with the unexpected negative *g* shift for the nitrogen monomeric species identified in the polycrystalline sample.

In view of these limitations the assignment of nitrogen impurities to nitrogen ions substituting lattice oxygen ions in ZnO should be considered as tentative. Other theoretical models are currently under investigation in order to shed a light on these still open issues.

CHAPTER 6

Ammonia Adsorption on ZnO $(10\bar{1}0)$ Surface[§]

Abstract

The reactivity of ZnO surfaces towards ammonia has been investigated in a combined experimental and computational study. Different coverages and samples (*i.e.* powder and single crystal) have been addressed. While at low coverage ammonia adsorbs molecularly, for the full monolayer coverage it is found to form an ordered adlayer with (2 x 1) periodicity presenting alternating molecular NH_3 and singly deprotonated NH_2 moieties adsorbed on cationic sites. The adsorption enthalpy has been observed to decrease with the coverage and this proves that the repulsive interactions between adsorbates are higher than attractive electrostatic interactions (*i.e.*, hydrogen bonds). Therefore repulsive interactions are probably the driving force for partial NH_3 dissociation at full coverage.

[§] The results described in this Chapter have been reported in: H. Noei, F. Gallino, L. Jin, C. Di Valentin, Y. Wang, *J. Am. Chem. Soc., submitted.*

6.1 Introduction

The interaction of ammonia with metal oxide surfaces is of great importance from the viewpoint of industrial chemistry. NH_3 is used as a probe molecule to differentiate Lewis acid sites from Brønsted acid sites on catalysts such as alumina, silica, MgO, ZnO, and TiO_2 [379,380,381,382]. In a generally accepted model for ammonia adsorption on the metal-oxide surfaces, an ammonia molecule acts as a strong Lewis base and adsorbs preferentially at Lewis acid sites, *i.e.* metal-ion sites, through the σ-type interaction between the N-localized $3a_1$ molecular orbital (MO) and the unoccupied orbitals of the metal ions [383,384,385]. However, adsorption of NH-containing molecules is a particularly challenging case with regard to the structures and geometries formed after adsorption.

The recent progress in surface science is the result of an increasingly consolidated combination of advanced experimental techniques and state-of-art *ab initio* computational methods [244]. Two of the most powerful surface analytical instruments are the Fourier transform infrared spectroscopy (FTIRS) and the high-resolution electron energy loss spectroscopy (HREELS). These techniques have been successfully applied on metal surfaces to obtain a series of information about the chemical nature of adsorbate species, the coordination symmetry, the degree of unsaturated sites, the intermediate species formed via a certain reaction, the presence and the nature of Lewis and Brønsted acid sites [228,229,235,236,237,238]. However, HREELS investigations on metal oxide single crystals are very scarce, because of the intense optical Fuchs–Kliewer phonons [210,314] together with the charging problems commonly encountered for insulating substrates, which severely limited the application of HREELS for single crystal studies [386,387,388]. Also, IR investigations of powder samples present serious problems because of air contaminants in the IR spectrometer and in contact with the sample, resulting in the reaction of adsorbed molecules with pre-adsorbed species on the powder surface, such as hydroxyl groups or carbon containing species.

These strong limitations have been overcome in the group of Y. Wang (Ruhr Univerity of Bochum, Germany) by designing an ultrahigh vacuum (UHV) FTIRS apparatus (see Sec. 2.2.3) in combination with a standard HREEL spectrometer, which allows to obtain high-quality IR data for molecular species adsorbed on oxide surfaces (both single crystals and powder particles). With this approach it was recently gained a deep understanding of a

number of systems [235,236,237,238,239,240]. In particular, water [238,389, 390] and methanol [237] adsorbed on the nonpolar ZnO $(10\bar{1}0)$ surface have been investigated. The ZnO $(10\bar{1}0)$ surface is the main cleavage plane of ZnO and one of the better-understood oxide surfaces [267], being a good candidate for fundamental studies of the adsorption of small molecules. In these studies, high quality vibrational data were obtained by HREELS which allows direct identification also of adsorbate species formed on ZnO powder surfaces by comparison with IR data. The water and methanol adsorptions at low temperature and high coverage have been observed to result in a monolayer of adsorbates with a (2 x 1) periodicity which consists of an equal fraction of undissociated and singly deprotonated molecules (hydroxyl and methoxy species, respectively). While the dissociation of water is expected and observed for most oxides [238,391], it is really surprising to observe a similar geometrical arrangement of adsorbates for the more complex case of methanol. In fact, although the phase is similar, it has been demonstrated that the driving force for the formation of the (2 x 1) periodicity is different: hydrogen-bonding mediated attractive interaction in the case of adsorbed water molecules and steric repulsion of the methanol/methoxy species in the case of methanol molecules [237].

Ammonia is a stronger Brønsted acid than water and methanol (pK_a^{NH3}: 9.3, pK_a^{H2O}: 14.0, pK_a^{CH3OH}: 15.5, [178]), therefore we may expect a similar dissociative adsorption, possibly even at low coverage. However, even though partially decomposed ammonia has been reported on Zn-terminated (0001) surface [392,393], Ozawa *et al.* [394,395] observed that ammonia adsorbs only molecularly, up to saturation coverage on mixed-terminated $(10\bar{1}0)$ surface at room temperature (RT). That study was based on photoelectron spectroscopy (PES), near-edge X-ray absorption fine structure spectroscopy (NEXAFS), X-ray photoelectron spectroscopy (XPS) and ultraviolet photoelectron spectroscopy (UPS). Partial dissociation was reported to start at the anneal temperature of 350 K in competition with the desorption reaction that is complete at 625-650 K. This experimental evidence has been confirmed by a number of theoretical works [385,396,397,398] that predicted only molecularly adsorbed ammonia stable on ZnO $(10\bar{1}0)$ surface. These computational studies considered only isolated NH_3 molecules and, thus, a systematic investigation of ammonia adsorption at different coverages is still lacking.

In this Chapter, we present a combined experimental and computational

work on the NH_3 adsorption on ZnO surfaces. Different coverages and different temperature ranges for both a ZnO $(10\bar{1}0)$ single crystal and ZnO powder surfaces have been considered. The vibrational frequencies of adsorbates were determined by means of HREELS and UHV-FTIR spectroscopy. Through thermal desorption spectroscopy (TDS) we have been able to estimate the adsorption enthalpy for multilayer, monolayer and submonolayer situations. The periodic density functional study has been performed with the hybrid B3LYP functional [59,60] and has investigated three different coverage regimes.

The motivation of this study is two-fold. On one side, the chemical reactivity of the well-known ZnO $(10\bar{1}0)$ surface is investigated for oxygen-free molecules and can be related to the recent findings for water and methanol adsorption in order to provide a predictive tool for the adsorption of small molecules based on their chemical properties and their steric hindrance. On the other side, a comprehensive and atomistic picture of NH_3 adsorption on ZnO may be fundamental to improve the design of ZnO-based ammonia gas sensors [399,400] and to shed a light on the N-doping process of ZnO. So far, nitrogen impurities in ZnO have been obtained by post-synthesis treatments at high temperature only in NH_3 atmosphere [357] (see Chapter 5). A detailed description of NH_3 adsorption on the surface would provide in this sense a better understanding of the activation process for nitrogen bulk diffusion and doping.

6.2 Experimental and Computational Details

6.2.1 Experimental Section

The polycrystalline sample used in this study was NanoTek ZnO (provided by Nanophase Technologies; purity: >99%). It was prepared by physical vapor synthesis based on the oxidation of vaporized metallic Zn, followed by condensation of ZnO. After heating at 723 K for 4 h, its specific surface area, determined by BET analysis of N_2 physisorption, amounted to 14 m^2/g. Ultra high vacuum–Fourier transform infrared spectroscopy (UHV-FTIRS) experiments on the ZnO nanoparticles were performed in an UHV apparatus described in Sec. 2.2.3. The ZnO powder sample was first pressed into a stainless steel grid and then mounted on a sample holder, which was specifically designed for the FTIR transmission measurements under UHV

conditions. The base pressure in the measurement chamber was 2×10^{-10} mbar. The optical path inside the IR spectrometer and the space between the spectrometer and the UHV chamber were also evacuated to avoid atmospheric moisture adsorption, thus resulting in a high sensitivity and long-term stability. The ZnO nanoparticles were cleaned in the UHV chamber by heating to 850 K to remove all adsorbed species such as carbon-containing contaminants and hydroxyl groups. Prior to each exposure, a spectrum of the clean ZnO nanoparticles was recorded to be used as a background reference. We exposed the sample to NH_3 by backfilling the measurement chamber through a leak valve. The exposures are given in units of Langmuir (L) ($1L = 1.33 \times 10^{6}$ mbar×s). All UHV-FTIR spectra were collected with 1024 scans at a resolution of 4 cm^{-1} in transmission mode [234,238].

High resolution electron energy loss spectroscopy (HREELS), thermal desorption spectroscopy (TDS), and low energy electron diffraction (LEED) experiments were carried out in an UHV apparatus consisting of two chambers separated by a valve and described in Sec. 2.2.2. In all experiments the ZnO $(10\bar{1}0)$ sample was cleaned by repeated cycles of sputtering (1keV Ar^+, 30 min) and annealing in O_2 (1×10^{-6} mbar, 850 K, 2 min) and in UHV (850 K, 5 min). Typically, about two sputtering cycles with annealing in UHV were followed by one cycle with annealing in O_2 [239,240]. The surface cleanness was checked by LEED and HREELS (for more details see Sec. 2.2.2).

6.2.2 Computational Methods

Periodic density functional theory (DFT) calculations were carried out with the CRYSTAL09 package [69,70]. The exchange-correlation contributions to the total energy were treated using the hybrid B3LYP functional [59,60] with 20% of exact Hartree-Fock exchange that has shown a better agreement with experiments in calculated geometries and vibration frequencies than other functionals (*e.g.* LDA and GGA [155, 401]) (see Sec. 2.1.5.4). In particular, B3LYP does not provide the overestimated H bond strength in OH groups and the related red shift of the OH stretching affecting most of the other functionals [402,403].

The all-electron Gaussian-type basis sets adopted were 8-411(d1) [281] for oxygen, 8-64111(d41) [404] for zinc, 7-311(d1) [283] for nitrogen and 311(p1) [284] for hydrogen. The condition for SCF convergence was set to 10^{-6} and 10^{-10} hartree during geometry optimization and frequency calculation,

respectively. The reciprocal space was sampled by a 2 x 2 x 2 k-point mesh corresponding to 4 k-points of the irreducible Brillouin zone [70]. Additional details about the computational parameters used in this work can be found in Sec. 2.1.4.1.

The mixed-terminated ZnO $(10\bar{1}0)$ surface is non-polar and consists of ZnO dimers rows separated by trenches along the crystallographic $[1\bar{2}10]$-direction. It has been modelled by slab with 2D periodic boundary conditions and a (4 x 2) surface unit cell. A noteworthy advantage of CRYSTAL09 package is the absence of repetition of the slab along the *z*-direction that avoids artificial electrostatic interactions across the vacuum region affecting other codes. The theoretical optimized bulk lattice parameters of a = 3.278 Å, c = 5.288 Å, and u = 0.3796 used for the lateral extension of the slab are in good agreement with the experimental values of a = 3.250 Å, c = 5.207 Å, and u = 0.3825 [405,406]. The atoms of the upper half of the supercell together with the adsorbed molecules were fully relaxed by minimizing the atomic forces, whereas the atoms in the bottom half were kept frozen. The slab thickness was set to eight instead of six ZnO layers to include additional relaxation energy.

We refer to Secs. 2.1.5.4, 2.1.5.5 for the detailed description of the theoretical approach to compute the vibrational frequencies and the binding energy of the adsorbed molecules. For NH_x species only harmonic frequencies referred to the Γ point were calculated on the optimized geometry without correction for anharmonicity for the reasons discussed in Sec. 2.1.5.4. They are scaled for the following factors obtained by the ratio between the experimental and the theoretical values for NH_3 molecule: 0.957 for symmetric deformation or wagging mode (δ_s), 0.981 for asymmetric deformation or scissoring mode (δ_a), 0.968 symmetric stretching (ν_s) and 0.962 for asymmetric stretching (ν_a). On the opposite, the stretching mode of the surface hydroxyl group OH coming from the partial dissociation of adsorbates is calculated including anharmonic contributions (see Sec. 2.1.5.4). Finally, the binding energy was corrected for vibrational contributions to get a value of adsorption energy ΔH_{calc} comparable with what is obtained from TDS data (see Sec. 2.1.5.5).

6.3 Results

6.3.1 Interaction of NH_3 with Clean ZnO Nanoparticles

Figure 6.1 presents UHV-FTIR spectra recorded after NH_3 adsorption on the clean ZnO nanoparticles at 100 K and after the sample was heated to higher temperatures. Prior to the exposure to NH_3, the sample was heated to 850 K and then cooled to 100 K in a UHV chamber, in which the readsorption of CO_2 or other species from the residual gas in the course of experiments is negligible. As a result, no IR bands are observed in the corresponding spectrum (see Fig. 6.1A), revealing the presence of the clean, adsorbate-free ZnO surfaces.

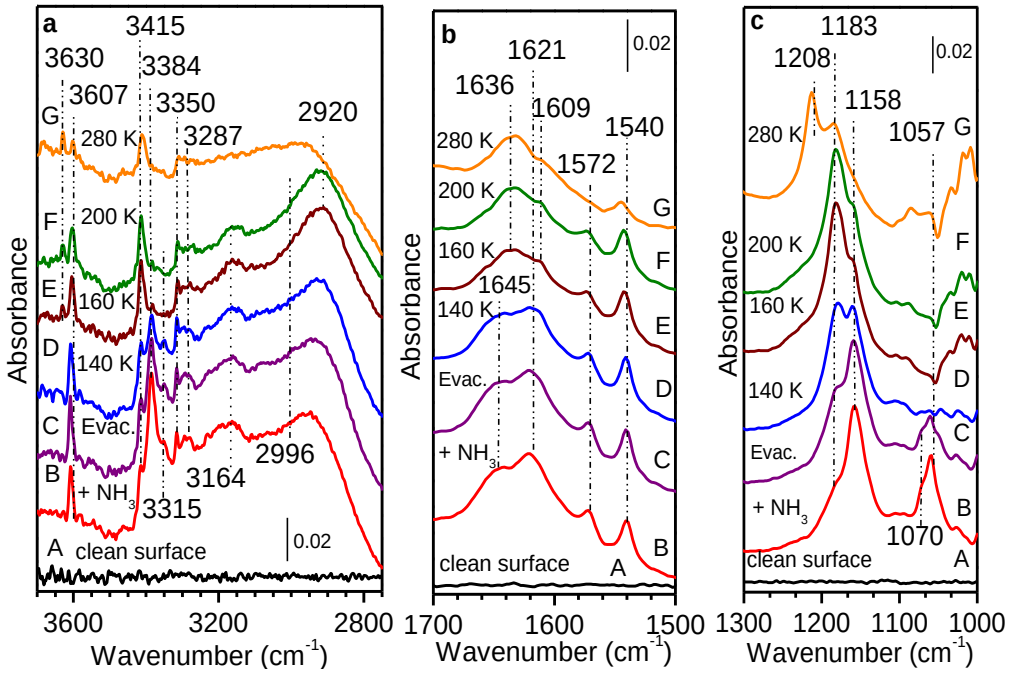

Figure 6.1. UHV-FTIR spectra obtained after exposing the clean ZnO nanoparticles to 1 x 10^{-4} mbar NH_3 at 100 K in an UHV chamber and further heating to the indicated temperatures; (A) clean surface, (B) exposure to NH_3: (1 x 10^{-4} mbar), (C) storing in UHV at 100 K for 30 min., heated to: (D) 140 K, (F) 160 K, (F) 200 K, (G) 280 K.

Exposing the clean ZnO samples to NH_3 leads to the appearance of a number of IR bands, shown in different ranges at around 3650-2800 cm^{-1}, 1700-1500 cm^{-1} and 1300-1000 cm^{-1}. When a pressure of 1 x 10^{-4} mbar of NH_3

is achieved, eight IR bands appear in the range of 3650-2800 cm^{-1} at around 3607, 3415, 3384, 3315, 3350, 3287, 3164, and 2996 cm^{-1} (see Fig. 6.1a-B). In the range of 1700-1500 cm^{-1}, the IR spectrum shows four intense bands located at 1645, 1621, 1572, and 1540 cm^{-1} (see Fig. 6.1b-B). Finally, at low frequency range of 1300-1000 cm^{-1}, two main IR bands appeared at 1158 and 1057 cm^{-1} in company with two shoulders at 1183 and 1070 cm^{-1}, respectively (see Fig. 6.1c-B). After the NH_3-treated sample in the UHV chamber (1×10^{-10} mbar) was stored at 100 K, nearly no change has been observed in IR spectrum (see Fig. 6.1C,a-c).

In order to get more insight into the interaction of NH_3 with the ZnO particles, IR spectra were recorded after the sample was heated to higher temperatures. The corresponding data are displayed in Figure 6.1 D-G. We focus separately on different frequency regime containing the fingerprint IR bands for chemisorbed species resulting from NH_3 adsorption and dissociation on ZnO powders. (1) IR regime 3650-2800 cm^{-1} (see Fig. 6.1a, D-G): with increasing temperatures, the main bands at 3607, 3384, 3315, and 3287 cm^{-1} decrease in intensity. The band at 3384 disappears completely at 160 K, while the bands at 3287, 3607, and 3315 cm^{-1} are still observable at 280 K. Simultaneously, the relatively weak band (shoulder) at 3415 cm^{-1} increases and reaches its highest intensity at 280 K. Furthermore, by heating to 160 K (see Fig. 6.1a-E) a new band appears in the hydroxyl region at 3630 cm^{-1} and slightly increases in intensity during the heating of the ZnO sample to 280 K, while the frequency remains nearly unchanged. Finally, the broad band at 2996 cm^{-1} shifts to 2920 cm^{-1} at higher temperatures. (2) IR regime 1700-1500 cm^{-1} (see Fig. 6.1b): with increasing temperatures, the main bands at 1645 and 1540 cm^{-1} decrease in intensity until they disappear completely at 160 K (see Fig. 6.1b-E); simultaneously, two new bands appear at 1636 and 1609 cm^{-1} and increase in intensity at higher temperatures. The IR band at 1621 cm^{-1} disappears at 250 K. The IR feature at 1572 cm^{-1} first remains unchanged upon heating to 200 K but disappears at high temperature as 280 K. (3) IR regime 1300-1000 cm^{-1} (see Fig. 6.1c): the IR spectra change dramatically in this region with increasing temperatures. The main bands at 1158, 1057 cm^{-1} together with the shoulder at 1070 cm^{-1} decrease significantly in intensity. The band at 1057 cm^{-1} with the shoulder at 1070 cm^{-1} disappears completely at 160 K (see Fig. 6.1c-E), while the shoulder at 1183 cm^{-1} grows in intensity. The band at 1158 cm^{-1} disappears at 280 K and, simultaneously, a new band appears at 1208 cm^{-1}.

Considering Figure 6.1 it is evident that there is a large difference in IR

bands at 100 K and 160 K. Hence, to support clearly the assignment of the observed IR bands to NH_3-related adsorbate species at elevated temperatures, the ZnO sample was further exposed to NH_3 at 150 K and subsequently heated to the indicated temperatures. The corresponding UHV-FTIR spectra are reported in Figure 6.2 in three frequency ranges: 3650-3100 cm^{-1}, 1700-1500 cm^{-1} and 1300-1000 cm^{-1}.

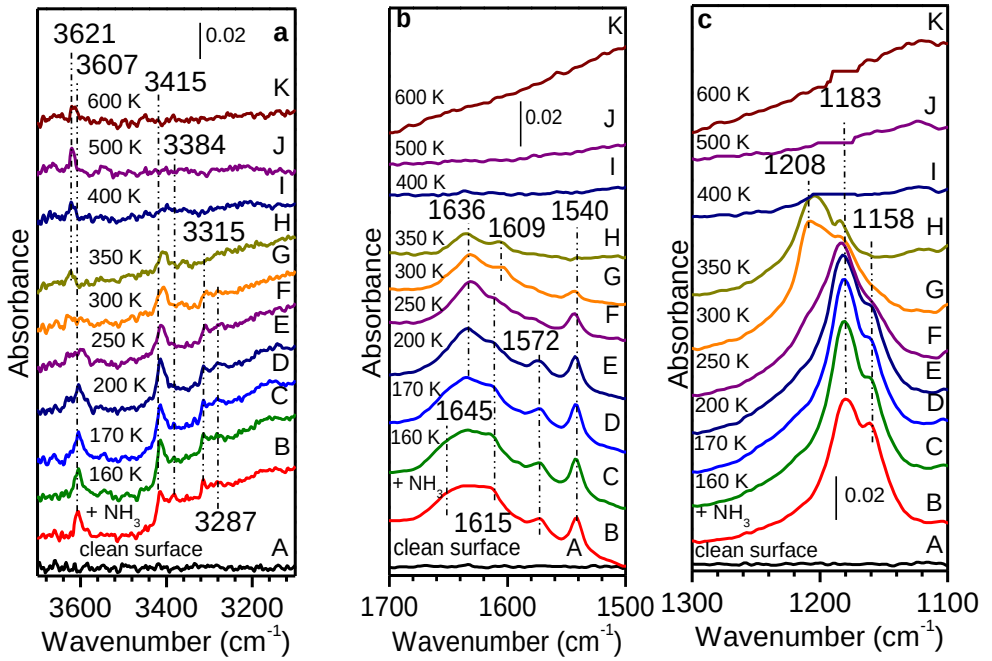

Figure 6.2. UHV-FTIR spectra obtained after exposing the clean ZnO nanoparticles to 1 x 10^{-4} mbar NH_3 at 150 K in an UHV chamber and further heating to the indicated temperatures; (A) clean surface, (B) exposure to NH_3 (1 x 10^{-4} mbar), heated to: (C) 160 K, (D) 170 K, (F) 200 K, (F) 250 K, (G) 300 K, (H) 350 K, (I) 400 K, (J) 500 K, (K) 600 K.

The maximum intensity of the IR bands are recorded at the pressure 1 x 10^{-4} mbar of NH_3 (see Fig. 6.2a-c;B). (1) In the IR regime 3650-3100 cm^{-1} a series of bands appears at 3607, 3415, 3384, 3315, and 3287 cm^{-1} (see Fig. 6.2B;a). After annealing the sample to the indicated temperatures, the band at 3384 cm^{-1} disappears at 160 K, while the bands at 3607, 3315, and 3287 cm^{-1} decrease in intensity at higher temperatures and are totally removed at 350 K. Simultaneously, a relatively weak band (shoulder) appears at 3621 cm^{-1}, which increases in intensity with heating and reaches to its maximum at 500 K. At

last, the band at 3415 cm^{-1} disappears at 400 K. (2) In the IR regime 1700-1500 cm^{-1} (see Fig. 6.2b-B) five bands are detected at 1645, 1615 (previously observed at 1621 at 100 K), 1572, and 1540 cm^{-1}. With annealing to higher temperatures the IR band at 1645 cm^{-1} disappears at 160 K and a new band arises at 1636 cm^{-1}, which is stable up to 400 K. The other two bands at 1615 and 1572 cm^{-1} decrease in intensity until they disappear completely at around 250 K (see Fig. 6.2b-G) and a new band appears at 1609 cm^{-1}, in agreement with Figure 6.1. This band disappears together with the band at 1540 cm^{-1} at 400 K (see Fig. 6.2b-I). (3) The IR spectrum in the regime of 1300-1000 cm^{-1} (see Fig. 6.2c-B) shows two main bands at 1183 and 1158 cm^{-1} at 150 K. The band at 1158 cm^{-1} decreases significantly in intensity during heating and disappears at around 350 K, while the band at 1183 cm^{-1} remains stable until 400 K. Also, a new shoulder emerges at 250 K around 1208 cm^{-1} and disappears at 400 K (see Fig. 6.2c-I).

To get more insight into different coverage of NH_3 on ZnO nanoparticles, the clean sample was further exposed to NH_3 at 300 K. Figure 6.3 shows NH_3 on clean ZnO sample at 300 K with a significant decrease in the number of IR bands. The corresponding UHV-FTIR spectra show several IR bands at 3621, 3600 (3607 cm^{-1} at 100 and 150 K), 3422 (3415 cm^{-1} at 100 and 150 K), 3399, 3309 (3315 cm^{-1} at 100 and 150 K), 3287, 1632 (1636 cm^{-1} at 100 and 150 K), 1609, 1540, 1208 and 1183 cm^{-1} (see Fig. 6.3B in a-c). The lower intensity and large shifts of IR bands at room temperature compared with those bands observed at low temperature are due to the coverage difference of NH_3 at different temperatures. Interestingly, IR spectra of the NH_3 adsorbed on ZnO change after evacuation at 300 K. The bands at 3309, 3287, 1540, and 1183 cm^{-1} diminish significantly in intensity (see Fig. 6.3C,a-c). The bands at 3309, 3287, and 1540 cm^{-1} disappear at 350 K (see Fig. 6.3 a and b; C), while the band at 1183 cm^{-1} remains stable until 450 K together with the band at 1208 cm^{-1} (see Fig. 6.3c-C). With increasing temperature, the bands at 3600, 3422, and 3399 cm^{-1} decrease largely in intensity and disappear at 400 K (see Fig. 6.3a-F); simultaneously, the band at 3621 cm^{-1} increases in intensity and remains stable till 800 K (see Fig. 6.3a). With increasing temperatures, the main bands at 1632 and 1609 cm^{-1} decrease in intensity until they disappear completely at 430 K (see Fig. 6.3b).

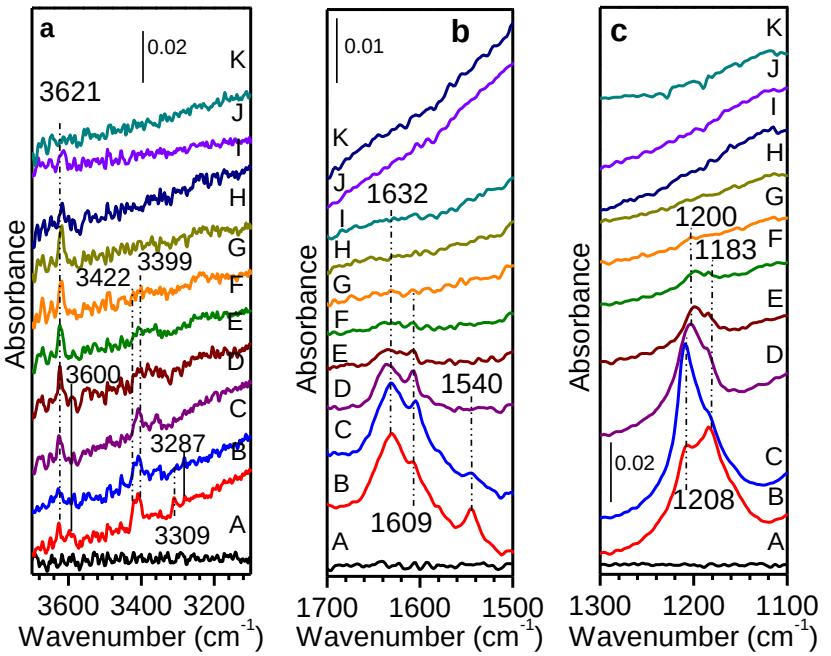

Figure 6.3. UHV-FTIR spectra obtained after exposing the clean ZnO nanoparticles to 5 x 10^{-4} mbar NH_3 at 300 K in an UHV chamber and further heating to the indicated temperatures; (A) clean surface, (B) exposure to NH_3 (1 x 10^{-4} mbar), (C) storing in UHV at 100 K for 30 min., heated to: (D) 350 K, (E) 400 K, (F) 430 K, (G) 450 K, (H) 480 K, (I) 500 K, (J) 750 K, (K) 800 K.

6.3.2 TDS and HREELS data on ZnO (10 $\bar{1}$ 0) single crystal surfaces

Figure 6.4 shows the TDS data of ammonia (mass 17) recorded after exposing the mixed-terminated ZnO (10 $\bar{1}$ 0) surface to different amounts of NH_3 at 100 K. Four desorption peaks of NH_3 are observed at 400, 280, 175, and 140 K, indicating the presence of four adsorbate states referred as α_1, α_2, β, and γ. The peak at 175K, identified as β state, is not saturated and slightly shifts from 175 K to 180 K with increasing NH_3 exposure (see inset Fig. 6.4). This evidence is characteristic of zero-order desorption kinetics and is related to the presence of multilayer of NH_3 species weakly bound to the surface. The α_2 and α_1 phases, corresponding to the dominant desorption peak at 280 K and to the broad feature centred at 400 K, are indicative of full-monolayer and sub-monolayer NH_3 desorption on ZnO (10 $\bar{1}$ 0) surface, respectively. Finally, the low-temperature γ phase shows a desorption peak at 140 K, which is clearly

lower than the temperature for multilayer NH_3 desorption and can be tentatively associated to NH_3 weakly bound to surface oxygen sites via N-H···O hydrogen bonds.

Assuming a pre-exponential of 10^{13} s^{-1} and first-order kinetics, the activation energies for the adsorption of ammonia from the two main states, α_2 and α_1, are estimated to amount to 0.77 eV (74 kJ/mol), and 1.08 (104 kJ/mol), respectively (note that the heating rate in the conventional TDS experiment was 1.0 K/s).

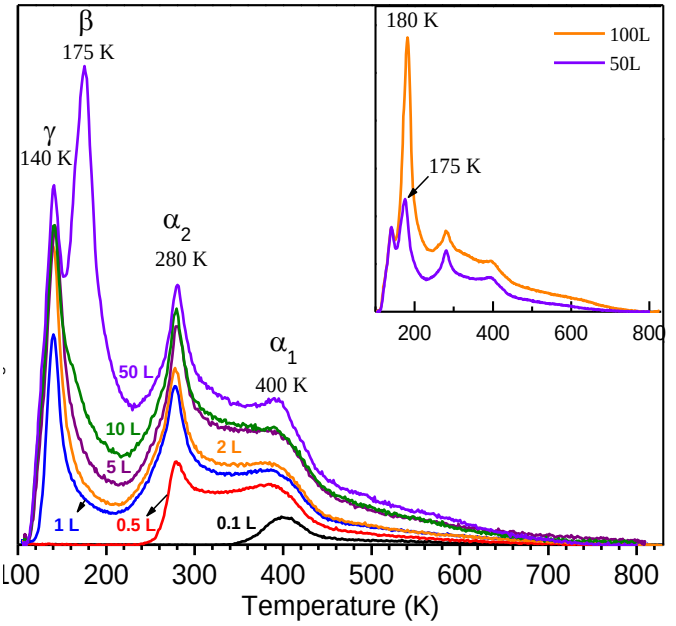

Figure 6.4. TDS spectra of ammonia (mass 17) for various NH_3 exposures on ZnO($10\bar{1}0$) at 100 K. The heating rate was 1 K/s.

An unambiguous identification of the surface NH_3 species is provided by HREELS. Figure 6.5 displays the HREEL spectra recorded after exposing the clean ZnO ($10\bar{1}0$) surface to 100 L of NH_3 at 100 K and subsequently heating to the indicated temperatures. The EELS spectrum for the clean mixed-terminated ZnO ($10\bar{1}0$) surface shown in Fig. 6.5A, is dominated by the intense primary Fuchs-Kliewer phonon mode at 549 cm^{-1} and its overtones [314]. The latter are successfully removed by Fourier deconvolution and the

spectrum of clean sample has been recorded (see Fig. 6.5B). After the exposure of ZnO (10 $\bar{1}$ 0) surface to 100L of NH_3 at 100K, a number of new bands appears at 394, 1060, 1160, 1183, 1208, 1540, 1609, 1645, 3407, and 3607 cm^{-1} (see Fig. 6.5C-F). For additional information, the sample was heated to elevated temperatures after exposure to NH_3 at 100 K. Upon heating the vibrational bands decrease largely in intensity and the bands at 1060, 1540, 1645, and 3607 cm^{-1} disappear at 300 K, accompanied by desorption of α_2 state in TDS at 280 K, while the peak at 1609 cm^{-1} remains stable at 300 K, in a very good agreement with the molecular NH_3 desorption at 400 K in TDS.

The observed frequencies are reported in Table 6.1 and assigned to the corresponding vibrational modes according to the comparison with IR and computational data.

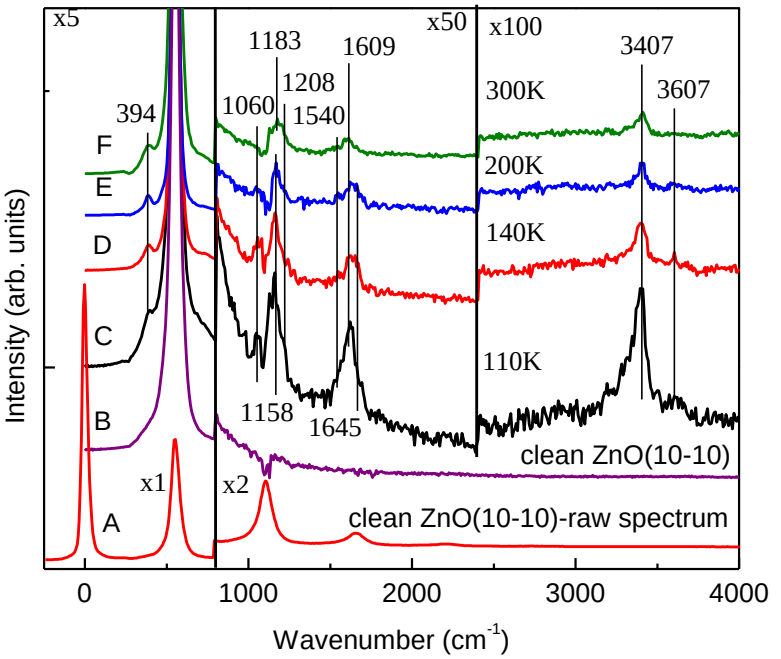

Figure 6.5. HREELS data recorded after exposing the ZnO(10 $\bar{1}$ 0) surface (curves A,B) to 100 L of NH_3 at 100 K and subsequent annealing to the indicated temperatures (curves C-F). All spectra are reported after Fourier deconvolution except the raw spectrum for the clean surface (curve A). The surface phonon at 549 cm^{-1} is not completely removed by the Fourier deconvolution. The spectra were recorded in specular direction with an incidence angle of 55° and with a primary electron energy of 10 eV.

6.3.3 Theoretical Results

Ammonia adsorption on the non-polar ZnO $(10\bar{1}0)$ surface has been investigated for different coverages. In particular, we considered one, four and eight molecules per unit cell corresponding to 0.25, 0.50 and 1.00 monolayer (ML). A (4 x 2) surface unit cell has been used since up to eight molecules can be considered on the surface. This approach enhances the degrees of freedom of the system lifting the constraint of equivalent molecules for translational symmetry resulting from smaller unit cells. Zn and O surface atoms are three-fold coordinated and have been demonstrated to act as Lewis acid and base sites, respectively [240]. However, it has been found that, for isolated molecules, both water [389] and methanol [237] adsorb molecularly on the non-polar ZnO $(10\bar{1}0)$ surface. Only for higher coverages water [390] and methanol [237] partially dissociate forming surface hydroxyl groups because of favourable hydrogen bonds formation.

A single adsorbed ammonia molecule on the (4 x 2) model surface can be considered as non-interacting with its periodic images since they are separated by 13.1 and 10.6 Å in the $[1\bar{2}10]$- and [0001]-direction, respectively. A systematic investigation of the most stable adsorption mode has been obtained by considering ten different initial geometries of one NH_3 molecule above the surface. Both undissociated and dissociated structures have been analysed in a monodentate configuration on a Zn surface atom (see Fig. 6.6a-c) and in a bridging position between two ZnO dimers along the $[1\bar{2}10]$-direction (see Fig. 6.6d). The most representative optimized geometries are reported in Figure 6.6. As expected and already reported in previous calculations [385,396,397,398], the molecular adsorption is highly preferred. In particular in the most stable configuration, as shown in Figure 6.6a, the N atom coordinates via its lone electron pair to a surface Zn^{2+} cation and one H atom forms a hydrogen bond across the trench to a surface O^{2-} anion. The calculated binding energy is 1.01 eV and the angle between the surface normal and the N–Zn axis is evaluated ~35° in good agreement with experiments [394]. The crucial role played by the hydrogen bond in NH_3 adsorption is evinced in Figure 6.6b where the same geometry with the NH_3 180° rotated is 0.16 eV lower in energy since the previous 1.82 Å O–H distance became 2.58 Å for this new configuration.

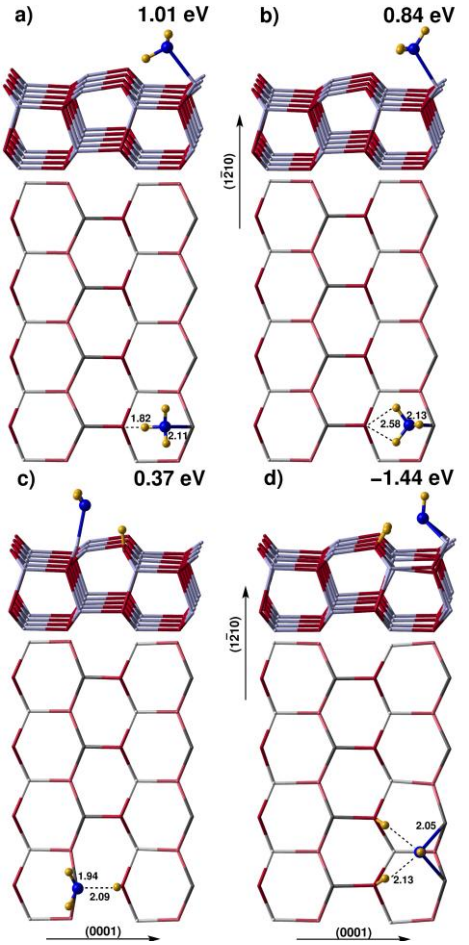

Figure 6.6. Front (upper part) and top (lower part) views of the main adsorption configurations and corresponding binding energies of isolated NH_3 molecules (0.25 ML) adsorbed on the ZnO $(10\bar{1}0)$ surface. In the front views Zn and O atoms are represented by gray and black sticks, respectively. In the top views Zn and O atoms are depicted by gray and black sticks in the first surface layer and in white and light gray sticks in the second surface layer, respectively. N and H atoms are drawn by large dark gray and small light gray spheres. The dash lines represent the H bonds between OH groups and N atoms and their distance is reported in Å such as the Zn-N one. The d) configuration with a negative binding energy is a metastable structure that is reported only to appreciate the energy cost of removing a second H atom. The binding energies are corrected for BSSE error.

The dissociation of the adsorbed molecule with the transfer of the H atom across the trench to the surface O^{2-} anion is not stable and spontaneously

recombines leading to the configuration in Figure 6.6a. On the contrary, the transfer of the H atom to the neighbouring dimer across the trench (not reported) results in a highly distorted and metastable geometrical arrangement, 1.15 eV lower in energy respect to Figure 6.6a. The only stable dissociated structure, reported in Figure 6.6c, is achieved by transferring the H atom to the O^{2-} anion of the ZnO dimer adsorption site. However this configuration is highly energetically demanding since it implies the rupture of the Zn–O dimer bond. No stable bridging adsorption structures were found because they generally evolve into the on top arrangements except for the configuration in Figure 6.6d with a double dissociated NH_3 molecule that nevertheless is 2.45 eV less stable than the molecular adsorption.

The coverage dependence of NH_3 adsorption on ZnO $(10\bar{1}0)$ surface was studied by performing geometry optimizations for different periodic arrangements of increasing amount of adsorbed molecules. In Figure 6.7 and 6.8 the most significant configurations for half and full coverages, respectively, are reported. The corresponding binding energies per molecule decrease significantly with increasing ammonia concentration and this is in contrast to what observed for water [389] and methanol [237]. To better understand the issue, we considered the interaction of two adsorbed molecules in neighbouring sites (not reported) in the most stable molecular configuration of Figure 6.6a. Both along the [0001]- and the $[1\bar{2}10]$-directions the binding energy decreases of 0.04 eV and 0.10 eV, respectively. This observation may be rationalized by supposing the steric repulsion between adsorbates much higher in energy than the electrostatic interactions between H atoms and N atoms of different molecules. Actually this is what was observed for a full methanol monolayer where the steric repulsion cost between the methyl groups was energetically higher than the gain arising from hydrogen bonds interaction [237]. In the case of molecularly adsorbed ammonia, the steric repulsion is not as high as for methanol, but, since the nitrogen atom is four-fold coordinated, there is no lone-pair available for H-bonds so that the interaction between NH_3 molecules can be only repulsive. In this sense the energy cost to couple two molecules will be higher or lower depending on the distance between adsorbates: 5.28 Å and 3.70 Å along the [0001]- and the $[1\bar{2}10]$-directions, respectively. For half coverage the molecular adsorption is still the most stable one as can be observed in Figure 6.7.

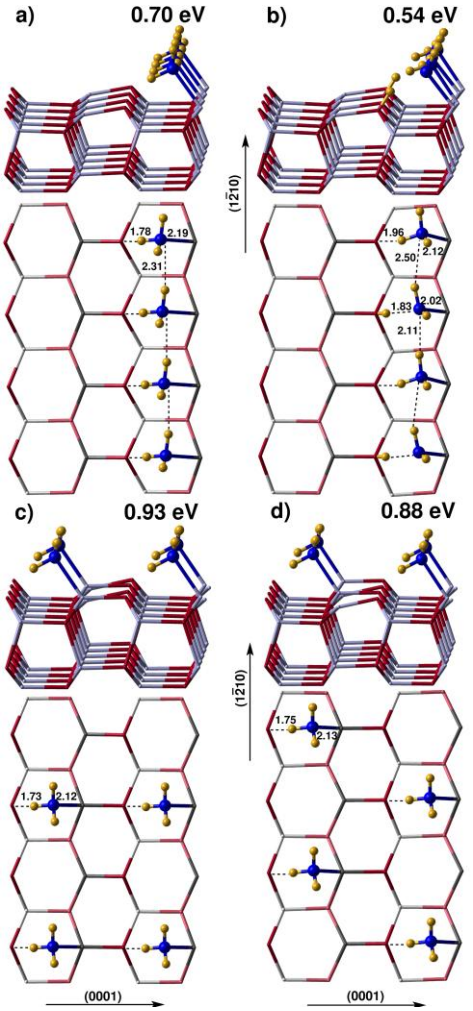

Figure 6.7: Front (upper part) and top (lower part) views of the main adsorption configurations and corresponding binding energies of half NH_3 coverage (0.50 ML) on the ZnO $(10\bar{1}0)$ surface. In the front views Zn and O atoms are represented by gray and black sticks, respectively. In the top views Zn and O atoms are depicted by gray and black sticks in the first surface layer and in white and light gray sticks in the second surface layer, respectively. N and H atoms are drawn by large dark gray and small light gray spheres. The dash lines represent the H bonds between OH groups and N atoms, and between neighbouring NH_3 molecules and their distance is reported in Å such as the Zn-N one. The binding energies are corrected for BSSE error.

In particular, the energetically most preferred geometry is a (2 x 1) surface superstructure with ammonia arranged along the [0001]-direction as reported

in Figure 6.7c. This molecules array is 0.23 eV and 0.05 eV more stable than a column of adsorbates along the $[1\bar{2}10]$-direction and than a (2 x 2) surface superstructure as depicted in Figure 6.7a and Figure 6.7d, respectively. Even if no full-dissociated configurations were found, a stable structure with half molecules dissociated and alternatively arranged along the $[1\bar{2}10]$-direction, as represented in Figure 6.7b, was observed 0.39 eV lower in energy than the undissociated adsorption. A column of full-dissociated molecules spontaneously evolve to the geometry of Figure 6.7b while the transfer of H atoms from ammonia rows along the [0001]-direction across the trench to the surface O^{2-} anions is not stable and spontaneously recombine to the configurations in Figure 6.7c and Figure 6.7d. In this sense the NH_3 dissociation seems to be favoured by increasing steric repulsion. For a low hindrance the energy cost of breaking a N–H bond is higher than the energy gain obtained from the creation of the hydrogen bonds. For higher steric repulsion the dissociation becomes more convenient than the molecular adsorption. Therefore the main difference between water, methanol and ammonia adsorption on ZnO $(10\bar{1}0)$ surface is the peculiar interaction governing the adsorption: attractive hydrogen bonds for water and methanol and steric repulsion for ammonia. This different behaviour can be rationalized considering the presence of free lone electron pairs on the O atoms of water and methanol and their absence on the N atom of ammonia.

However, surprisingly when the coverage is increased to a full monolayer, the most stable configuration for ammonia adsorption is a half-dissociated (2 x 1) surface superstructure, represented in Figure 6.8c. This geometrical arrangement is 0.05 eV more stable than the undissociated configuration of Figure 6.8a and is the analogue to the configuration observed for water [389] and methanol [237] monolayers. We can therefore conclude that also ammonia adsorption on ZnO $(10\bar{1}0)$ surface is found to induce the formation of hydroxyl surface groups for a full monolayer. For this coverage also a full-dissociated configuration is found stable (see Fig. 6.8b) even if 0.21 eV lower in energy than the half-dissociated one. Finally a tendency to prefer homogeneous rows of adsorbates is confirmed by the significantly lower binding energy of the half-dissociated NH_3 (2 x 2) surface superstructure of Figure 6.8d.

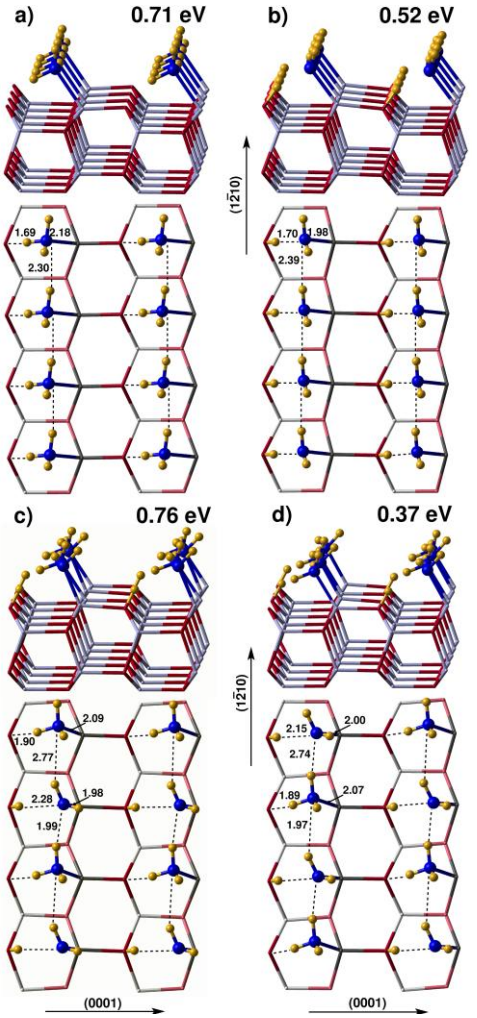

Figure 6.8. Front (upper part) and top (lower part) views of the main adsorption configurations and corresponding binding energies of full NH_3 coverage (1.00 ML) on the ZnO $(10\bar{1}0)$ surface. In the front views Zn and O atoms are represented by gray and black sticks, respectively. In the top views Zn and O atoms are depicted by gray and black sticks in the first surface layer and in white and light gray sticks in the second surface layer, respectively. N and H atoms are drawn by large dark gray and small light gray spheres. The dash lines represent the H bonds between OH groups and N atoms, and between neighbouring NH_x molecules and their distance are reported in Å such as the Zn-N one. The binding energies are corrected for BSSE error.

Finally, in Tables 6.1 and 6.2 the calculated frequencies in harmonic approximation are reported for the most stable structures for one ammonia

monolayer, the half-dissociated configuration of Fig. 6.8c, and for low coverage, the molecularly adsorbed isolated molecule of Fig. 6.6a.

Table 6.1. Experimental and calculated vibrational frequencies (in cm^{-1}) for ammonia full monolayer coverage. The geometrical configuration used for the frequency calculations is the half-dissociated and the undisocciated monolayer reported in Figure 6.8c and Figure 6.8a, respectively.

High Coverage: Full Monolayer

Species	Vibrational Mode	Experiment		Theory	
		IR powder	HREELS $(10\bar{1}0)$ ZnO	Half-dissociated	Undissociated
NH_3	$\nu_{Zn\text{-}N}$	-	394	379	287
	δ_s	1158 1183	1158 1183	1219	1220
	δ_a	1621 (1615) 1645	1609 1645	1599 1682	1597 1678
	ν_s	2996	-	3032	3375
	ν_a	3415	3407	3404	3458
NH_2	$\nu_{Zn\text{-}N}$	-	-	480	-
	δ	1540	1540	1513	-
	ν_s	3287	-	3324	-
	ν_a	3315 (3309)	-	3374	-
OH	ν	3607	3607	3627	-

Table 6.2. Experimental and calculated vibrational frequencies (in cm^{-1}) for ammonia low coverage. The geometrical configuration used for the frequency calculations is the molecularly isolated molecule reported in Figure 6.6a.

Low Coverage: Isolated Molecule

Species	Vibrational Mode	Experiment		Theory
		IR powder	HREELS $(10\bar{1}0)$ ZnO	
NH_3	$\nu_{Zn\text{-}N}$	-	394	360
	δ_s	1208	1208	1213
	δ_a	1609 1636	1609 1645	1603 1655
	ν_s	2920	-	2966
	ν_a	3399 3422	3407	3358 3427

A detailed discussion of these values with a comparison with experimental results is provided in the following session.

6.4 Discussion

On the basis of the measured and computed vibrational and thermal stability data of NH_3 on ZnO powders and single crystal ZnO $(10\bar{1}0)$, we can provide a consistent assignment of the IR bands observed on the ZnO surfaces (see Tables 6.1 and 6.2). In Figure 6.1, two IR bands at the lower wavenumbers of 1057 and 1070 cm^{-1} are related to the NH_3 weakly bound to surface O sites via NH---O hydrogen bonds on ZnO surface, and they are removed completely at 140 K (see Fig. 6.1D), as confirmed by the TDS peak at 140 K (γ state). The band at 1057 cm^{-1} is also observed by HREELS on the ZnO $(10\bar{1}0)$ surface and disappears at 140 K, together with the bands at 1621 and 1645 cm^{-1} (see Fig. 6.5 C and D). The intense IR/HREELS band at 1158 cm^{-1} in Figure 6.1c and Figure 6.4C decreases largely in intensity and totally disappears at 280 K, in line with the TDS peak in α_2 state (see Fig. 6.4). The band at 1158 cm^{-1} is attributed to the symmetry bending vibrations (δ_s) and the bands at 1645 and 1621(1615) cm^{-1} are assigned to the asymmetry bending vibrations (δ_a) of high coverage (full monolayer) NH_3 on ZnO $(10\bar{1}0)$ surface. The asymmetry bands of NH_3 shift to 1609 and 1636 cm^{-1} at half monolayer (low coverage) of NH_3 on ZnO surface at higher temperatures than 280 K. The absence of the bands at 1057, 1070, and 1158 cm^{-1} in IR spectra of ZnO powders at room temperature provides further evidence for our assignment.

In Figure 6.1c one IR band at 1183 $cm^{-1}$is present which decreases largely in intensity by heating to 280 K and simultaneously a new band appears at 1208 cm^{-1}. The decrease of the 1183 cm^{-1} band is along with the decrease of the bands at 1540, 3287, 3315 cm^{-1}, which are characteristic for NH_2 species. The HREELS data also demonstrate that the band at 1183 cm^{-1} decreases, while the 1208 cm^{-1} band increases in intensity. The removal of the IR band at 1183 cm^{-1} corresponds to desorption of α_2 state at 280 K in the TDS data. At this temperature the half monolayer of NH_3 releases from the surface, and at submonolayer no indication of further partial NH_3 dissociation on ZnO $(10\bar{1}0)$ surface is observed. This results in diminishment of the NH_2-related bands at 1540, 3287, 3315 cm^{-1}. Based on this conclusion, the band at 1183 cm^{-1} is assigned to the symmetry bending vibration δ_s of NH_3 coadsorbed with NH_2,

while the band at 1208 cm^{-1} is attributed to the symmetry bending vibration δ_s of isolated NH_3 species on ZnO $(10\bar{1}0)$ (see Fig. 6.1 c).

These assignments are corroborated by the frequency calculation (see Tables 6.1 and 6.2). In particular we observe a good agreement with the experimental values for both high and low coverage. It is noteworthy to observe that there is no significant difference in the low frequency region between the half-dissociated and undissociated configurations and therefore they are not decisive in proving partial dissociation of ammonia on ZnO surface. Finally, the experimental observation of two IR bands for δ_s mode, while only one value is expected from theory, confirms the presence of heterogeneous regions with different coverages at low temperature.

The band at 1540 cm^{-1} (see Fig. 6.1b) increases largely in intensity with rising the dose of NH_3 at 100 K together with the bands at 3287 and 3315 cm^{-1}, and decreases in intensity by heating ZnO to elevated temperatures (see Fig. 6.1). Thanks to the good agreement with the computed values for the half-dissociated configuration (see Table 6.1), they are assigned to the bending (δ), symmetry stretching vibration (ν_s), and asymmetry stretching vibration (ν_a) of NH_2, respectively. However, the decisive proof of the partial dissociation of NH_3 at full monolayer on mixed-terminated ZnO $(10\bar{1}0)$ surface is provided by the formation of hydroxyl group at 3607 cm^{-1} in IR and HREEL spectra (see Fig. 6.1), which is assigned to the stretching vibration of OH (ν_{OH}). This value is in very good agreement with the calculated value of 3627 cm^{-1} that corresponds to an isolated OH, not involved in hydrogen bonding with the frontal N atom at 2.5 Å. For the half-dissociated model, we also found another configuration almost degenerated in energy where the OH group is closer to the N atom (2.3 Å) and therefore is interested in a hydrogen bond that dramatically shifts the ν_{OH} value to 3480 cm^{-1}. This observation highlights the high sensitivity of the OH vibration mode with respect to the small distance variations that results in different geometrical configurations, almost degenerated in energy but severely different in ν_{OH} values. The intensity of the band at 3607 cm^{-1} raises largely at higher dose of NH_3 and disappears/decreases at lower coverage of NH_3, indicating again the NH_3 dissociation on ZnO surface at high coverages (see Fig 6.1a). For ZnO powder samples, we have observed one additional band at 3621 cm^{-1} at 160 K and higher temperatures. Based on previous studies on hydroxyl groups on ZnO powder samples, this band is assigned to the stretching vibration of OH species on oxygen-terminated of ZnO $(000\bar{1})$ surface [238].

The intense IR band observed at 3384 cm^{-1} and disappeared at 160 K is assigned to the asymmetric stretching vibration of NH_3 at high coverage (multilayer). The broad band at 2996 cm^{-1} and the intense band at 3415 cm^{-1} (3422 cm^{-1} at 300 K), in excellent agreement with the HREELS feature at 3407 cm^{-1} and with the computed values 3032 and 3404 cm^{-1}, are attributed to the symmetry (ν_s) and asymmetry (ν_a) stretching vibrations of NH_3 species on mixed-terminated ZnO $(10\bar{1}0)$ surface at a full monolayer coverage. We must note that these bands, in particular the ν_s mode, are significantly blue-shifted in the case of the undissociated configuration (3375 and 3458 cm^{-1} vs 3032 and 3404 cm^{-1}, see Table 6.1), and allow us to exclude the presence of neighbouring NH_3 adsorbates. If all the surface is ammonia covered, half molecules are partially deprotonated. Finally, the band at 2996 cm^{-1} shifts to the lower frequency at 2920 cm^{-1} at low coverage of NH_3 at 160 K (see Fig. 6.1) in line to what is observed for computed frequency for the isolated molecule (from 3032 cm^{-1} to 2966 cm^{-1}, see Table 6.2).

The IR results of NH_3 adsorption at 150 K provide further evidence for the assignment of the IR and HREEL data. As shown in Fig. 6.2, the most significant bands at temperatures higher than 250 K are centred at 1208, 1609/1636, and 3415 cm^{-1} and can be assigned to the symmetry (δ_s) and asymmetry (δ_a) bending modes as well as the asymmetry (ν_a) stretching vibrations of low coverage of NH_3 on the ZnO $(10\bar{1}0)$ surface, respectively.

An unambiguous identification of the surface NH_3 species is provided by NH_3 adsorption on clean ZnO powder surfaces at room temperature. As shown in Figure 6.3, the band at 1158 cm^{-1}, which is assigned to the $\delta_s(NH_3)$ mode of the full-monolayer NH_3 on ZnO $(10\bar{1}0)$, is missing. The major IR band appears at 1183 cm^{-1} with a shoulder at 1208 cm^{-1}. They are assigned to the $\delta_s(NH_3)$ modes of NH_3 coadsorbed with NH_2 and isolated NH_3 species on ZnO $(10\bar{1}0)$, respectively. The 1183 cm^{-1} band largely decreases in intensity during evacuation at 300 K and simultaneously we have observed the growth of the band at 1208 cm^{-1} (see Fig. 6.3c). They disappear completely at 450 K. The second group of bands are observed at 1609/1636 (1632), 3399, and 3422 cm^{-1}. The former band is attributed to the $\delta_a(NH_3)$ and the other two bands at 3399, and 3422 cm^{-1} are assigned to the $\nu_a(NH_3)$ modes of molecularly adsorbed isolated NH_3 on ZnO surface. Interestingly, three weak bands are observed at 3309, 3281 and 3621 cm^{-1} and are assigned to the ν_s and ν_a vibrations of NH_2 species as well as the ν mode of OH group, respectively. This reveals a slight dissociation of NH_3 on ZnO powder samples at room

temperature. Furthermore, the OH band at 3621 cm^{-1} emerges at room temperature and disappears by heating up to 800 K. This feature is totally in agreement with previous data on ZnO powder and oxygen-terminated ZnO $(000\bar{1})$ surfaces. The 3621 cm^{-1} band is therefore assigned to the stretching vibration of hydroxyl group formed on the ZnO $(000\bar{1})$ surface.

HREELS spectra show one extra band at 394 cm^{-1}, assigned to the stretching vibration of ν(Zn-N) in excellent agreement with the computed value of 379 cm^{-1} for the half-dissociated configuration (see Table 6.1). Moreover, the comparison with the red-shifted ν(Zn-N) frequency of 287 cm^{-1} for the undissociated configuration provides an additional proof to exclude the presence of a full monolayer of undissociated ammonia.

Finally we analyse the binding energy reported in Table 6.3 for the low and half coverages, corresponding to the α_1 and α_2 phases of TDS data (see Fig. 6.4). The computed adsorption enthalpy ΔH_{calc} values of –0.99 and –0.78 eV are in excellent agreement with the experimental results. In particular we observe that the adsorption energy for high coverage decreases confirming that the repulsive interactions between adsorbates are higher than the attractive interactions coming from the increasing number of hydrogen bonds. The driving force for the partial ammonia dissociation is therefore the steric repulsion between molecules as it was previously observed for methanol [237].

Table 6.3. Calculated and experimental values of standard adsorption enthalpy of ammonia adsorption on ZnO $(10\bar{1}0)$ surface for high coverage (full monolayer, FM) and low coverage. All the values are in eV.

coverage	ΔE_{noCPC} [a]	BSSE	ΔE_{CPC} [b]	Δ(ZPE) [c]	Δ(TE) [d]	ΔH_{calc}	ΔH_{exp}
low	-1.27	+0.26	-1.01	+0.13	-0.12	-0.99	-1.08
FM	-1.03	+0.27	-0.76	+0.10	-0.12	-0.78	-0.77

[a] B3LYP binding energy not corrected for the counterpoise method
[b] Total B3LYP binding energy corrected for the counterpoise method
[c] Zero point energy contribution to enthalpy
[d] Thermal contribution to enthalpy at T = 298 K

6.5 Conclusions

Ammonia adsorption on ZnO $(10\bar{1}0)$ surface has been investigated for different coverages and samples (*i.e.*, powder and single crystal) through a combined experimental and computational study. The good agreement

between IR/HREELS vibrational bands and computed frequencies with a hybrid DFT approach has allowed an unambiguous assignment of adsorbate species.

At increasing the temperature, the coverage diminishes and various adsorption phases have been observed in the TDS spectra (see Fig. 6.4), which are called γ, β, α_2, and α_1. The latter corresponds to a submonolayer phase with isolated NH_3 molecules molecularly adsorbed on cation sites in a monodentate configuration and desorbing above 400 K. The adsorption enthalpy is about 1.0 eV and one hydrogen is involved in a hydrogen bond with the frontal oxygen ion (1.82 Å).

The molecular adsorption is preferred at increasing coverage till a fullmonolayer is achieved corresponding to the α_2 phase. The experimental observation of the stretching vibration of OH (ν_{OH}) at 3607 cm^{-1} and of the vibrational frequencies of NH_2 species, besides the shifted NH_3 frequencies, indicates a partial dissociation of NH_3 species at high coverage. This is corroborated by the DFT results that find, as the most stable configuration for the fullmonolayer, an ordered adlayer with a (2 x 1) periodicity where half of the ammonia molecules are singly deprotonated. The theoretical model is validated by a good agreement between the computed and measured frequencies. The hydroxyl group is observed to be isolated since, for small distance variations and involvement of hydrogen bonds, the ν_{OH} frequency dramatically changes. Although the half-dissociated model is the most stable one, the energy difference with respect to the full undissociated configuration is very small (only 0.05 eV). On the basis of the comparison between IR/HREELS and computed frequencies we would be tempted to exclude the presence of undissociated NH_3 domains. However, because of the tiny energy difference we must allow the possibility of having some coexisting domains of half-dissociated and undissociated adsorption mode on the ZnO $(10\bar{1}0)$ surface.

Our theoretical models are confirmed by the good concordance between the calculated adsorption enthalpies and TDS data. The observation of the enthalpy decrease, at increasing coverage, indicates that the repulsive interactions between adsorbates are higher than attractive electrostatic interactions (*i.e.*, hydrogen bonds). Therefore, repulsive interactions are probably the driving force for partial NH_3 dissociation at full coverage.

Finally, the high coverage phases β and γ are assigned to the desorption of a NH_3 multilayer and a NH_3 layer weakly bound to surface oxygen sites via

hydrogen bonds, respectively.

In conclusion, ammonia adsorbs molecularly on ZnO $(10\bar{1}0)$ surface at low coverage but at increasing coverage the repulsive interactions induce a partial dissociation of adsorbates forming an ordered adlayer with alternating NH_3 and NH_2 moieties. The latter is equivalent to what has been observed for methanol and oxygen even if in those cases the driving force was the attractive interaction coming from the increasing number of hydrogen bonds.

Ammonia is the only reagent able to provide nitrogen doping on ZnO sample in post-synthesis reactions (see Chapter 5). In the case of single crystals, nitrogen doping is achieved upon ammonia sputtering. In this study we have proved the reactivity of the clean ZnO $(10\bar{1}0)$ surface in promoting the partial dissociation of adsorbed ammonia molecules at low temperature. In order to get additional insight in the nitrogen doping mechanism we are currently investigating the ammonia adsorption on the sputtered ZnO $(10\bar{1}0)$ surface.

PART III

ZIRCONIUM DIOXIDE

Background

Zirconium dioxide shows a wide range of industrial applications that are strictly dependent on its crystalline phase. ZrO_2 can exist in at least five polymorphs [407,408]. At room temperature, only the baddeleyite structure, with a monoclinic $P2_1/c$ unit cell, is found which is stable up to around 1480 K, when it undergoes a first-order martensitic transition to a tetragonal phase ($P4_2/nmc$), further converted at 2650 K into the cubic fluorite phase ($Fm3m$) by a displacive transition (see Fig. III.1) [409]. Two additional orthorhombic *Pbca* and *Pnma* phases have also been observed above 3 and 20 GPa respectively [410,411]. The most stable monoclinic polymorph has no practical applications because of the crumbling of the ceramic components commonly observed during cooling from the tetragonal phase [412]. In contrast, the high temperature polymorphs (tetragonal and cubic) exhibit excellent mechanical (high fracture toughness and bulk modulus), thermal (low thermal conductivity, extremely refractory), chemical (chemically inert, corrosion resistant) and dielectric (static dielectric constants higher than 20 [179]) properties making ZrO_2 an excellent candidate for present and future technological devices.

Zirconium dioxide is currently used, for example, as a solid electrolyte in oxygen sensors [413] and solid oxide fuel cells operating at low temperatures [414], in thermal barrier coating applications [415], nuclear waste confinement [416], as a gate dielectric material in metal-oxide semiconductor devices (generally in combination with hafnium [417]), and as a catalytic support medium [418].

The room temperature stabilization of high symmetry polymorphs of ZrO_2 is commonly achieved either by transition metal doping or by preparation of nanocrystalline phases. So far, however, there is still no general consensus regarding the mechanisms governing the phase stabilization process [412,419,420,421]. In short, the tetragonal and the monoclinic structures can

be considered as distorted cubic structures. The 8-fold coordinated Zr atoms with O_h symmetry in c–ZrO_2 (see Fig. III.1, left panel) undergo a D_{2d} symmetry reduction, through a z-axis expansion of the unit cell in t–ZrO_2 (see Fig. III.1, central panel), while they become 7-fold coordinated in the m–ZrO_2 by elongation of one Zr–O (see Fig. III.1, right panel). The instability of high symmetry phases originates from the low ionic radii ratio (*e.g.* $R_{Zr^{4+}} / R_{O^{2-}} \approx 0.564$ in the fluorite structure) in the hard-spheres approximation for ionic compounds [422]. A lower ionic character favours structures with lower coordination numbers and this explains the higher thermodynamic stability of m–ZrO_2.

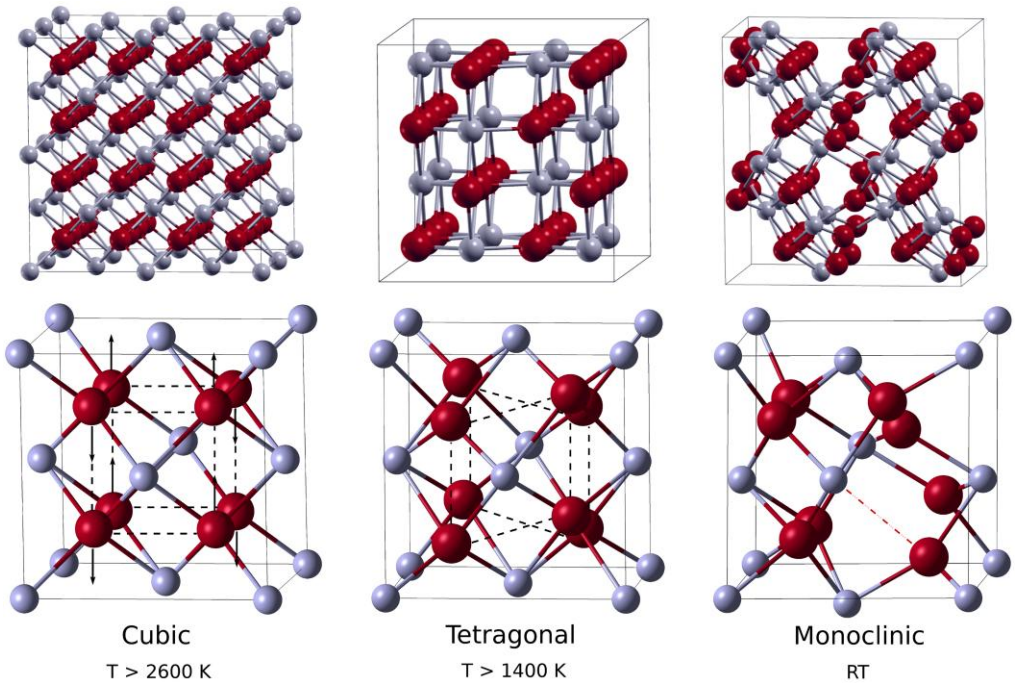

Figure III.1. Cubic, tetragonal and monoclinic ZrO_2 lattice structures with their relative temperature range of stability. In the upper panel polymorph cells are space-expanded to provide a better view of the three different phases. In the lower panel the cubic cell is taken as reference to show the deformation of the oxygen sublattice for t– and m–ZrO_2 (dashed lines and arrows). Large dark red spheres and small light grey spheres represent O and Zr atoms, respectively.

In this context, doping can favour the stabilization of high symmetry phases

essentially in two ways. On one side the substitution of Zr^{4+} with isovalent oversized (Ce^{4+}) and undersized (Ge^{4+}, Ti^{4+}) cations has been observed to stabilize *t*– and *c*–ZrO_2, relieving the internal lattice strain by the expansion of the cation network (in the case of oversized cations such as Ce^{4+}) or by the formation of a tetragonal scheelite like structure (in the case of undersized cations as Ge^{4+} or Ti^{4+} [423]). On the other side, doping with low valence cations (Y^{3+}, Gd^{3+}, Fe^{3+}, Ga^{3+}) induces a similar size-dependent internal stress effect and, moreover, favours the formation of oxygen vacancies, in order to achieve charge balance, which stabilize high symmetry polymorphs [419,423,424,425,426]. Finally, for nanocrystalline ZrO_2 other mechanisms of stabilization have been discussed which suppose the generation of excess of oxygen vacancies as a result of the nanoparticle size effect [412].

CHAPTER 7

Titanium Doping[**]

Abstract

It has been experimentally observed that Ti–doping of bulk ZrO_2 induces a large red-shift of the optical absorption edge of the material from 5.3 to 4.0 eV [Livraghi *et al*., *J. Phys. Chem. C,* **2010,** 114, 18553]. In this work, density functional calculations based on the hybrid functional B3LYP show that Ti dopants in the substitutional position to Zr in the tetragonal lattice cause the formation of an empty Ti 3d band about 0.5 eV below the bottom of the conduction band. The optical transition level $\varepsilon^{opt}(0/-1)$ from the topmost valence state to the lowest empty Ti impurity state is found at 4.9 eV in a direct band gap of 5.7 eV. The calculated shift is consistent with the experimental observation. The presence of Ti^{3+} species in Ti–doped ZrO_2, probed by means of electron paramagnetic resonance (EPR), is rationalized as the result of electron transfers from intrinsic defect states, such as oxygen vacancies, to substitutional Ti^{4+} centres.

[**] The results described in this Chapter have been reported in: F. Gallino, C. Di Valentin, G. Pacchioni, *Phys. Chem. Chem. Phys.*, **2011**, 13, 17667.

7.1 Introduction

Ti–doping of bulk ZrO_2 has been quite extensively investigated [420,427,428,429,430,431,432,433,434] during the last few years with the aim to improve the material properties. On one side Ti–doped ZrO_2 is considered as a promising candidate for advanced technological applications such as anode for solid oxide fuel cells [434] or high-*k* dielectric material for gate capacitors [427,428]. On the other side, TiO_2–ZrO_2 mixed oxides find application in heterogeneous catalysis for their surface acid-base properties, high thermal stability and strong mechanical strength [435]. Ti–doping significantly affects also the optical properties of ZrO_2, as recently reported by Livraghi *et al.* [432], inducing an increasing red shift of the optical band gap proportional to the Ti content, up to a limit of 1.3 eV for a molar fraction of 15% of TiO_2 in ZrO_2. Even if the large band-gap (E_g reduced from ~5.3 eV to ~4.0 eV) does not make it attractive for visible or solar light application, Ti–doped ZrO_2 represents a remarkable model system to investigate the role of the metal dopant (at low or increasingly larger concentrations, up to the limit of mixed oxides) in modifying the band structure of the material and interacting with other possible intrinsic impurities such as oxygen vacancies, V_O.

So far, we are not aware of any theoretical work investigating the electronic properties of Ti–doped ZrO_2. In this Chapter we provide a detailed study of Ti impurities in bulk ZrO_2 using the hybrid functional B3LYP [59,60] whose band gap value is in excellent agreement with the experimental one [436]. This is a basic requirement for determining the correct position of the defect or impurity levels. The experimentally observed red shift of the optical gap is investigated by varying the dopant concentration (from about 3% to 17%) in a tetragonal bulk model system, considering also the possibility of titanium clustering. Finally the interplay between Ti impurities and oxygen vacancy (V_O) species is analysed.

The Chapter is organized as follows. Section 7.2 provides details on the computational approach. In Section 7.3 we test our method on the bulk properties of stoichiometric ZrO_2 in its three main polymorphs (monoclinic, tetragonal and cubic) comparing different hybrid functionals. Section 7.4 focuses on Ti-doping, the modification of the material band gap and the interaction with V_O species. Section 7.5 summarizes our conclusions and presents an overview on the Ti-doping ZrO_2 system.

7.2 Computational Details

Spin-polarized periodic calculations were performed within the linear combination of atomic orbitals approach, as implemented in the CRYSTAL09 package [69,70]. The all-electron basis set adopted was the 8-411(d1) [281] for oxygen and the 8-6411(d41) [437] for titanium atoms. For zirconium we used the 311(d31) [438] valence electron basis set (PP) with the inner electrons described with an effective core potential by Hay and Wadt [439] not including the semicore 4s and 4p states. Two hybrid exchange-correlation functionals have been used, the popular B3LYP [59,60] with 20% of exact Hartree-Fock exchange and PBE0 [116] with 25% of exact exchange as determined from the perturbation theory.

The bulk lattice parameters have been optimized for pure ZrO_2 polymorphs: monoclinic, *m*–, tetragonal, *t*–, and cubic, *c*–ZrO_2. Ti–doping was simulated with a 108-atom supercell of bulk *t*–ZrO_2, obtained by the expansion matrix 3 x 3 x 2. The titanium impurity has been inserted substitutional (s) to Zr atoms or interstitial (i) at various concentrations, ranging from 1 to 6 atoms per supercell and corresponding to 2.7% – 16.7% of molar fraction.

The reciprocal space was sampled using Monkhorst-Pack [440] *k*-point grids with shrinking factors (4, 4, 4), (6, 6, 6) and (8, 8, 8) for the primitive cells of the monoclinic, tetragonal and cubic phases resulting in 30, 40 and 29 *k*-points in the irreducible Brillouin zone, respectively. A (4, 4, 4) set of shrinking factors was used for the 108-atom supercell, corresponding to 18–36 *k*-points of the irreducible Brillouin zone [70]. The densities of states (DOS) were computed with a 5 x 5 x 5 *k*-point mesh for the 108-atom supercell. The Kohn-Sham eigenvalues were computed on each *k*-point. We set the zero point of orbital energy at the top of the VB. For additional details about the computational parameters used in this work we refer the reader to Sec. 2.1.4.1.

7.3 Stoichiometric ZrO_2

As a preliminary step, we tested different functionals through the evaluation of bulk properties for the three low-pressure polymorphs of stoichiometric *m*–, *t*– and *c*–ZrO_2. The structural parameters *a*, *b*, *c* are reported in Table 7.1 and compared with experimental and computational literature data.

Table 7.1. Comparison of structural parameters of *m*-, *t*- and *c*-ZrO_2 and their relative energies (eV per ZrO_2 unit) obtained with B3LYP and PBE0 functionals from this work with previous theoretical and experimental data.[a]

		This work						
Phase		B3LYP	PBE0	LDA1	LDA2	GGA	PW1PW	Exp.
Monoclinic	a	5.246	5.187	5.102	5.086	5.192	5.212	5.151
	b	5.270	5.248	5.181	5.208	5.265	5.238	5.212
	c	5.405	5.326	5.264	5.226	5.358	5.367	5.317
	β	99.62	99.46	99.65	99.21	99.81	99.15	99.23
	E_m–E_t	–0.031	+0.019	–0.064	–0.05	–0.10	–0.030	–0.061
Tetragonal	a	3.642	3.608	3.565	3.563	3.628	3.611	3.592
	c	5.293	5.209	5.126	5.104	5.250	5.217	5.195
	d_{z_O}	0.052	0.045	0.044	0.042	0.049	0.048	0.057
	E_t–E_c	–0.074	–0.049	–0.049	–0.045	–0.07	–0.058	–0.057
Cubic	a	5.150	5.103	5.037	5.035	5.090	5.105	5.104/ 5.115

[a] Lattice parameters *a*, *b*, *c* are in Å and d_z is the displacement of the oxygen atom in *t*–ZrO_2 with respect to the position in the ideal *c*–phase in *c* units. Experimental relative energies (E_m–E_t and E_t–E_c) correspond to the enthalpy differences measured at the temperature of the phase transition [446]. Results from the present work are compared with those from previous studies: LDA plane-wave calculations where the Zr pseudopotential includes (LDA1 [409]) or not (LDA2 [443]) the semicore 4s and 4p states, GGA plane-wave calculations (GGA [444]) and hybrid functional PW1PW calculations within the localized basis set approach (PW1PW [445]). Room temperature data for the *m*–ZrO_2 are taken from Ref. [441] while values for the *t*– and *c*–ZrO_2 are obtained by extrapolation of $x \to 0$ in $(ZrO_2)_{1-x}(Y_2O_3)_x$ as reported in Ref. [442].

Room temperature data for lattice parameters of *m*–ZrO_2 are taken from Ref. [441] while those of *t*– and *c*–ZrO_2 are obtained for extrapolation to zero dopant concentration of the stabilized $(ZrO_2)_{1-x}(Y_2O_3)_x$ [442]. Since we are interested in the electronic structure of the system we choose to use a hybrid exchange-correlation functional because of the well-known poor performance of standard DFT approximations (LDA and GGA) in correctly describing band gap values and spin localization (see Sec. 2.1.5.1). In particular, we considered two different hybrid functionals, B3LYP and PBE0. We observe an excellent agreement (within 0.8% of error) with experimental values for the PBE0 functional and a slightly worse but still acceptable agreement (within 2% of error) for B3LYP. PBE0 provides the best lattice parameters also with respect to other theoretical methods, such as LDA and GGA (LDA1 [409], LDA2 [443], GGA [444]) in the planewave pseudopotential approach or the hybrid

PW1PW [445] with a localized basis set. However, PBE0 fails in reproducing the relative stability of the various phases (E_m–E_t and E_t–E_c), as experimentally determined at the temperature of the phase transition [446], while B3LYP gives the correct order (see Table 7.1). The computed energies do not contain thermal and entropic terms which may of course affect the stability order.

However, the most important property we are interested in is the band gap energy, E_g, since we want to investigate and compare the electronic structure of the pure and doped systems. We approximate it within the one-particle picture as the difference between the highest occupied and lowest unoccupied bands (see Sec. 2.1.5.1) and compare with the few experimental data available in literature (see Table 7.2).

Table 7.2. Comparison of band gap values (eV) of *m*–, *t*– and *c*–ZrO_2 obtained with B3LYP and PBE0 functionals from this work with previous theoretical and experimental data.[a]

			Monoclinic		Tetragonal		Cubic	
Experiments		VUV	5.83	/	5.78	/	6.1	/
		EELS	5.3	/	5.0	/	/	/
Theory	This work	B3LYP	5.61	(5.20)	5.70	(5.62)	5.50	(4.93)
		PBE0	6.09	(5.67)	6.20	(6.08)	6.03	(5.43)
		PW1PW	/	(5.49)	/	(5.83)	/	(5.01)
		LDA1	4.0	(3.6)	4.1	(4.0)	3.9	(3.3)
		LDA2	/	(3.12)	/	(4.10)	/	(3.25)
		LDA3+GW_0	/	(5.34)	/	(5.92)	/	(4.97)
		LDA4+GW_0	/	(5.6)	/	(5.9)	/	(5.3)

[a] Direct and minimum gap values are reported outside and inside brackets, respectively. Experimental values are obtained through ultraviolet spectroscopy in Y-doped ZrO_2 (VUV [447]) and by fitting electron energy loss spectroscopy data (EELS [409]). Previous theoretical results reported are: hybrid PW1PW functional calculations within the localized basis set approach (PW1PW [445]) LDA plane-wave calculations with pseudopotential for Zr including the semicore 4s and 4p states (LDA1 [409]), LDA plane-wave calculations (LDA1 [409] and LDA2 [443]), and many body perturbation theory corrections in the GW approximation including partial self-consistency in the calculation of the Green's function G with fixed screened Coulomb interaction W_0 (LDA3+GW_0 [421] and LDA4+GW_0 [448]).

The scarcity of experimental values is mainly due to the difficulty to obtain a pure and well-defined phases. For this reason in Table 7.2 we have only reported band gap values obtained from ultraviolet spectroscopy in Y-doped ZrO_2 [447] and by fitting the electron energy loss spectroscopy (EELS) data in the high energy region [409]. This is because Dash *et al.* [409] have recently

assigned the low energy gap observed in the EELS spectra at around 4 eV to defect states, probably oxygen vacancies. All the values obtained with other techniques (*e.g.* spectroscopic ellipsometry, SE, and X-ray photoemission spectroscopy, XPS), recently discussed also by Jiang *et al.* [421], are not reported because samples are generally thin amorphous or polycrystalline films. In Table 7.2 we also report band gap values from previous theoretical studies (PW1PW [445], LDA1 [409], LDA2 [443], LDA3+GW_0 [421] and LDA4+GW_0 [448]). The B3LYP results are in good agreement with previous hybrid functional PW1PW and GW_0 results. In particular, the order of the band gap $c– < m– < t–$ is reproduced. PBE0 values are constantly 0.5 eV higher than B3LYP. This discrepancy probably depends on the different fractions of Hartree-Fock exchange, rather than on the different approximations for the local part of the exchange and correlation functional (see Sec. 2.1.3).
On the basis of these results, we decided to perform the investigation of Ti–doped ZrO_2 by means of the B3LYP functional.

7.4 Ti-doped ZrO_2

Since X-ray diffraction data indicate that Ti–doped ZrO_2 is predominantly in the tetragonal phase [432], we have limited the investigation to the t–ZrO_2 polymorph. We note that the optical absorption edge red-shift of 1.3 eV is observed for a nominal Ti molar fraction of 0.15 [432]. This is a rather high concentration corresponding to 5–6 atoms in the 108-atom supercell model (0.14–0.17 molar fraction). In the following we start by discussing the diluted case with one Ti atom in the supercell model (~0.03 molar fraction) and then we increase the concentration up to a maximum of six Ti atoms per supercell model. Both Ti impurities in interstitial, Ti_i, or substitutional to lattice Zr, Ti_s, positions are considered.

7.4.1 Interstitial Ti (Ti_i)

Looking at the tetragonal as a distorted fluorite structure it is evident that the octahedral cavities are all empty (see lower panel of Fig. III.1) and can be filled with interstitial Ti atoms. In this way Ti has the same coordination of lattice Zr atoms, with four next-neighbour O ions at 2.15 Å and four second neighbour O atoms at 2.34 Å (see left panel of Fig. 7.1). This can be viewed

also as two intersecting tetrahedrons of O atoms, essentially similar to the coordination sphere of lattice Zr atoms in stoichiometric ZrO_2 where distances are 2.10 Å and 2.42 Å, respectively. Ti presents a $4s^2 3d^2$ valence shell. In a tetrahedral crystalline field (T_d), Ti 3d states split into *e* and t_2 states. In the case of the low spin electronic solution, two lower energy, fully occupied, Ti 3d (*e*) states are located in the middle of the band gap (~3.4 eV from the top of VB, see Fig. 7.1 left panel) with no electron transfer from Ti to lattice ions. The triplet (high) spin solution is 1.4 eV higher in energy than the singlet and results in the transfer of one electron from Ti to two next-nearest Zr^{4+} ions. On the basis of these results, it is unlikely that Ti_i could be responsible of the experimental 1.3 eV shift of the optical band gap. The Ti_i impurity states are occupied and, given their position in the gap, they would eventually give rise to additional absorption bands at higher wavelengths and not to a band edge shift as observed.

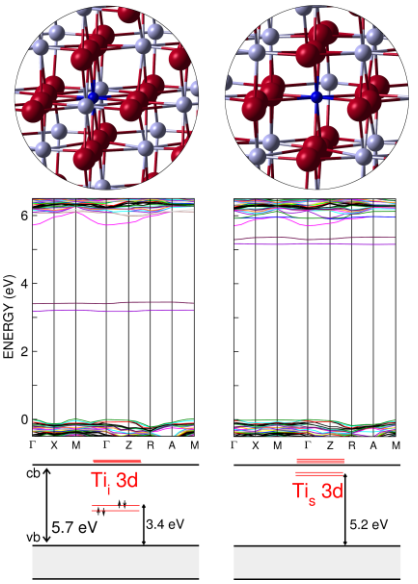

Figure 7.1. Upper panel: ball and stick representation of the Ti_i (left) and Ti_s (right) species in bulk ZrO_2. Zr, O and Ti are represented by small light grey, large dark red and small dark blue spheres, respectively. Lower panel: band structures together with a schematic representation of the Ti 3d states in the band gap of the material (from Kohn-Sham eigenvalues).

7.4.2 Substitutional Ti (Ti_s)

Ti is isovalent with Zr and when inserted in a lattice cation (Zr^{4+}) site all the valence electrons are formally transferred to the oxygen 2p VB. The relaxation is of opposite sign for first and second O neighbours. In particular the first shell relaxes about 9% inward while the second shell relaxes about 7% outward with respect to the Ti lattice position. Again, Ti is in a T_d crystalline field causing the Ti empty 3d levels to split into *e* and t_2 states which are close to and inside the CB, respectively (see right panel of Fig. 7.1). The single particle eigenvalues of the lower unoccupied Ti 3d states (*e*) are 0.4 eV from the conduction band minimum (CBM). In the case of Ti_s, it appears conceivable that for higher dopant concentrations an empty defect band forms close to CBM which may account for the experimental red shift of the optical absorption.

The relative stability of Ti_i and Ti_s defects has been analyzed in terms of formation energy E_{form}, as a function of the oxygen chemical potential, μ_O (see Sec. 2.1.5.2 for details). The substitutional Ti_s species results in the most stable defect for the whole range of oxygen chemical potentials (not reported). Therefore, from a thermodynamic point of view, Ti_s formation seems to be more likely for Ti–doped ZrO_2, in line with the observed variations in the optical spectrum.

7.4.3 Ti concentration effect on the electronic structure

In this Section we investigate the electronic structure modifications induced by a progressively increasing concentration of the Ti dopant. As mentioned before, Livraghi *et al.* [432] reported a 1.3 eV reduction of the optical band gap for a nominal Ti molar fraction of 0.15. However, considering a reaction yield lower than unity for the synthetic process, we can reasonably assume a dopant concentration of about 0.10–0.11, corresponding to four Ti atoms in a 108-atom supercell model.

If the four Ti atoms go interstitial, $4Ti_i$, 1/9 of octahedral voids are filled. In particular, we consider the geometrical configuration filling four adjacent octahedral cavities in the *xy* plane. The large steric hindrance results in a distorted tetrahedral coordination of the Ti atoms with distances from the oxygen ions in the range of 2.15–2.35 Å. Fully occupied Ti 3d states all lie in the middle of the band gap, 2.2 eV from CBM (not reported). As for the diluted case of Ti_i (see above), interstitial Ti atoms cannot account for an edge

shift of the ZrO_2 absorption band and therefore will not be further discussed.

Substitutional Ti species, Ti_s, have been investigated for increasing dopant concentrations from 2 to 4, 5 up to 6 atoms per supercell corresponding to 0.06, 0.11, 0.14, 0.17 molar fractions, respectively. In the 108-atom model there are 36 cation sites available for Ti-substitution, therefore the number of possible different geometrical configurations grows rapidly with dopant concentration. We first analyze the simplest case with two Ti_s species ($2Ti_s$).

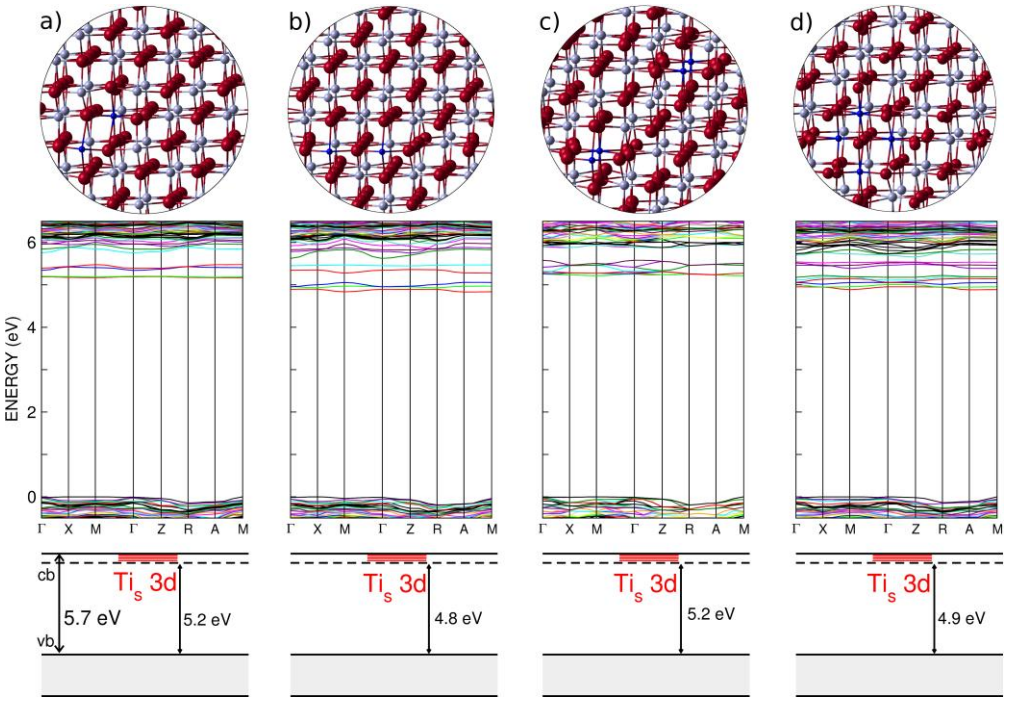

Figure 7.2. Upper panel: ball and stick representation of $2Ti_s$ (a and b) and $4Ti_s$ (c and d) defects in bulk ZrO_2 in different geometrical configurations (see text for details). Zr, O and Ti are represented by small light grey, large dark red and small dark blue spheres, respectively. Lower panel: band structures together with a schematic representation of the Ti_s 3d states in the band gap of the material (from Kohn-Sham eigenvalues). The dashed line emphasizes the possible red shift of the conduction band.

In Figure 7.2a and 7.2b the two most representative configurations for $2Ti_s$ are shown. One is the most stable configuration among those considered and consists of two Ti atoms separated by 3.81 Å along the (111) direction and sharing a common oxygen ion (see Fig. 7.2a). The band structure is essentially

identical to the diluted case with four 3d states (two *e* for each Ti atom) slightly mixed but highly localized at 5.2 eV from the valence band maximum (VBM). In the other configuration, the two Ti atoms are at a distance of 3.53 Å and share the same oxygen ion along the *xy* plane (see Fig. 7.2b). This geometry is less stable by 0.43 eV but shows a larger defect states overlap. The minimum gap between the Ti states and the VBM is calculated to be 4.8 eV.

To rationalize the different behaviour of these two configurations we further analyze the crystalline structure. Assuming the solid in a distorted fluorite structure, cations are in a distorted octahedral coordination sphere that consists of two different tetrahedra (one slightly closer than the other to the centre), that we call T_+ and T_-, according to the relative position of the apical vertex. T_+ and T_- alternate along the (111) direction, while chains of the same tetrahedron, either T_+ or T_-, expand along the *xy* plane. In the configuration of Figure 7.2a Ti atoms are in two different coordination tetrahedra, T_+ and T_-, and also the common O ion does not belong to the first coordination sphere. In contrast, the configuration in Figure 7.2b consists of two Ti atoms in the same *xy* plane sharing one O atom of the first coordination sphere. Here the lattice strain is probably higher and this is the reason for the lower stability of this configuration. However, the overlap of the $d_{x^2-y^2}$ orbitals is improved since the state lies in the same plane.

Our interpretation is corroborated by increasing the dopant concentration. For 4 Ti atoms in the supercell, the most stable geometrical configuration consists of two well separated Ti pairs (~8 Å) with Ti atoms in the same tetrahedron type and separated by 5.29 Å along the *z* axis corresponding to the tetragonal *c*-axis (see Fig. 7.2c). From the band structure we conclude that the Ti d states mixing is low because of the large distance. In contrast, considering four Ti_s all bound to the same O ion we observe an increased mixing of Ti 3d states resulting in the formation of a new small 3d band 0.8 eV below the CBM (see Fig. 7.2d). This result is consistent with the experimentally observed optical red shift of 1.3 eV. However, this second configuration with adjacent Ti_s dopants is 0.59 eV less stable probably due to a larger lattice strain.

An analogous behaviour is observed for 5 and 6 Ti atoms per supercell when at least some Ti atoms are close one to the other and in the same *xy* plane; in this case a new Ti 3d band at about 1.0 eV below CBM is formed. However, these configurations present always an energy cost associated with

the lattice strain.

A rigorous approach to compare electronic structure calculations with optical absorption spectra, should however include the computation of the transition energy levels. In Sec. 2.1.5.1 a detailed description of our new and original method to calculate transition energy levels using hybrid functionals and localized basis sets (as implemented in CRYSTAL code) is reported. In the context of this work, we consider only the optical transition level ε^{opt} since we are focusing on an optical excitation, where the relaxation contribution of the excited –1 charge state can be neglected. The optical transition level, $\varepsilon^{opt}(0/-1)$, for an isolated Ti_s is computed 4.9 eV from the VBM. In the KS approach the position of the defect level was estimated to be 5.2 eV from the VBM (see Fig. 7.1 right panel and Fig. 7.3). There is therefore a 0.3 eV energy difference between the two approaches. We expect a similar trend also for the higher concentrated models (4, 5, 6 Ti atoms per supercell). There are some technical difficulties in computing $\varepsilon^{opt}(0/-1)$ for cases where the defect states are actually forming a band. However, in a reasonable approximation, we can expect a similar 0.3 eV down-shift with respect to the KS level also for higher Ti concentrations. If we apply such a rigid correction for the $4Ti_s$ case (see Fig. 7.2c) the 5.2 eV value becomes 4.9 eV above the VBM, with a shift not far from the experiment [432].

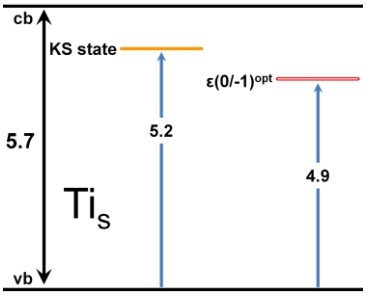

Figure 7.3. Schematic representation of the defect state position from Kohn-Sham eigenvalues and of the optical transition level $\varepsilon^{opt}(0/-1)$ calculated for Ti_s in bulk ZrO_2. We reported the direct gap in Γ. All values are in eV.

We can conclude that the optical band gap shift experimentally observed for Ti–doped ZrO_2 is rationalized by the present hybrid functional calculations showing the formation of a Ti 3d band. Optical transitions from the top of the VB to this new band are calculated to cost about 4.9 eV, which correlates with

the experimental red shift of the optical band gap from 5.3 to 4.0 eV.

7.4.4 Ti_s–V_O interaction

Oxygen vacancies, V_O, are one of the most common intrinsic defects in ZrO_2 and have been widely investigated by *ab initio* methods [428,429,436, 443,444,445,449,450]. In particular, they are responsible for the stability of the high symmetry polymorphs and their presence in *t*–ZrO_2 is highly likely.

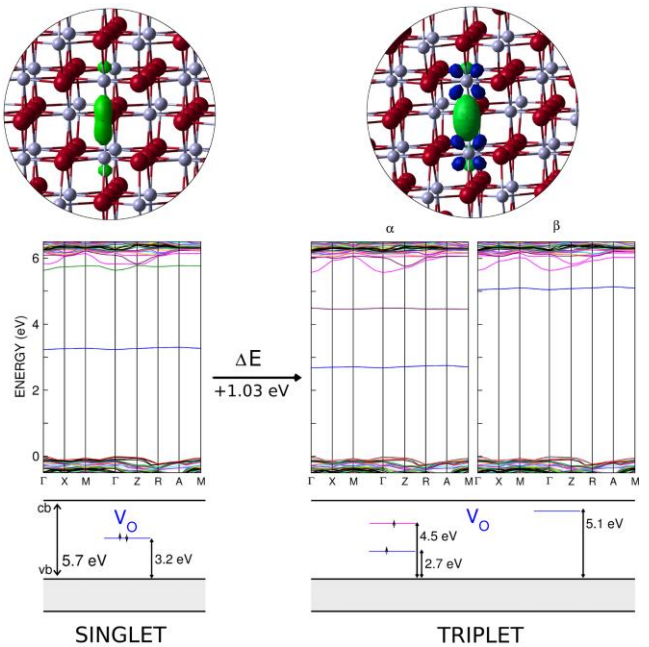

Figure 7.4. Upper panel: ball and stick representation of the V_O defect in the singlet (left) and triplet (right) state in bulk ZrO_2. Zr and O are represented by small light grey and large dark red spheres, respectively. The spin density plot is light green and dark blue on the vacancy site and Zr atoms, respectively. Lower panel: band structures together with a schematic representation of the V_O and Zr states in the band gap of the material (from Kohn-Sham eigenvalues).

Their interaction with Ti dopants may play a key role in reducing the doping energy cost [431], in increasing the resistive switching behaviour needed for resistive random access memories (RRAM) [429] or in enhancing the dielectric response for high-*k* dielectric applications [428]. In this context we are interested in studying the effects of the interplay between V_O and Ti_s

defects on the electronic properties. Livraghi *et al*. [432] observed the appearance of an EPR feature associated with Ti^{3+} species, besides the signal of the free electron trapped in a V_O void, after annealing the sample at 773 K under reducing conditions. This has been interpreted as the result of an electron transfer from a V_O to an empty 3d state of a Ti^{4+} ion. In the following we investigate it by means of theoretical modeling.

The isolated V_O centre in ZrO_2 is very similar to F centres in ionic crystals such as MgO and KCl with the extra electron density mostly localized on the vacancy site (see Fig. 7.4, left panel). The vacancy state appears as a distorted sphere because of tetragonal symmetry and induces a doubly occupied and highly localized single-particle level in the middle of the band gap, 3.2 eV above the VBM. This is consistent with previous reports for *c*–ZrO_2 [436,443,445,] and *m*–ZrO_2 [444,449], except for a larger relaxation of the four neighboring ions with inward and outward displacements of 11% and 12%, respectively. As a consequence of the distortion, two Zr–V_O distances of 1.86 and 2.71 Å can be observed. The F centre character is confirmed by the high energy cost of 1.03 eV to promote one electron to a near Zr ion in a triplet state (see right panel of Fig. 7.4).

As a next step both V_O and Ti_s species are introduced into the same supercell at a sufficiently large distance (5.45 Å). The singlet closed shell solution is simply the sum, with no modifications, of the electronic structures of the two isolated V_O and Ti_s species (see Fig. 7.5, left panel). No electron transfer is observed, and the doubly occupied V_O defect state is 3.4 eV above the VBM. However, promoting one electron to a Ti state (triplet solution) is a favorable process (–0.35 eV) (see Fig. 7.5, right panel), in contrast to what observed for the excitation of one electron on a Zr state, as discussed above. The majority spin component (α) KS state associated with V_O remains almost unperturbed (3.5 eV from VBM) while the minority spin component (β) is raised in energy (5.4 eV from VBM) (blue lines in Fig. 7.4 and Fig. 7.5). The second majority spin component, associated with Ti 3d levels, is only 3.0 eV from the VBM (red line in Fig. 7.5, right panel). This is different from the V_O centre in pure ZrO_2 in the triplet state, where only a tiny stabilization is observed for Zr^{3+} (red line in Fig. 7.4, right panel). The energy cost to form the oxygen vacancy is reduced from 6.2 eV in pure ZrO_2 to 5.7 eV in the Ti–doped one. On the basis of these results we can fully rationalize the experimental evidence of Ti^{3+} species formation in the presence of V_O and we predict an easier reduction of Ti–doped ZrO_2 by oxygen removal compared to the pure phase.

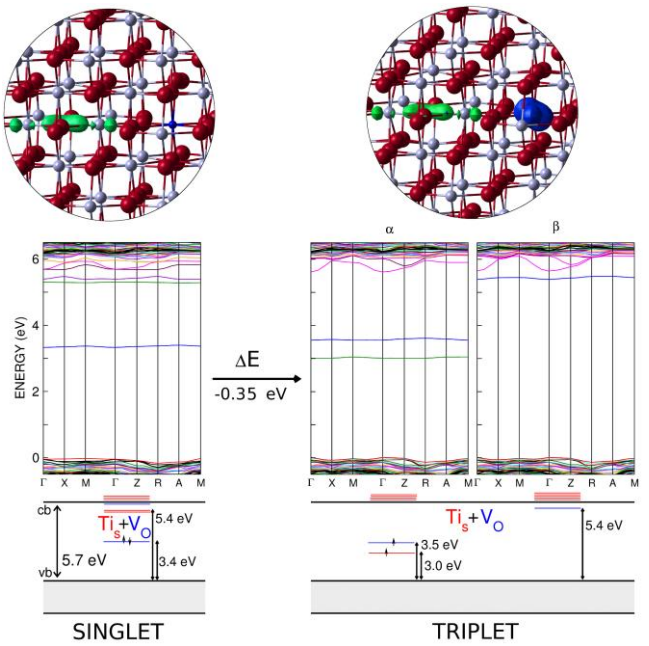

Figure 7.5. Upper panel: ball and stick representation of the V_O defect interacting with separated Ti_s species (5.45 Å) in the singlet (left) and the triplet (right) state in bulk ZrO_2. Zr, O and Ti are represented by small light grey, large dark red and small dark blue spheres, respectively. The spin density plot is light green and dark blue on the vacancy site and Ti atom, respectively. Lower panel: band structures together with a schematic representation of the V_O and Ti states in the band gap of the material (from Kohn-Sham eigenvalues).

7.5 Conclusions

Doping is a common way to modify band gaps of semiconductors and insulators. The dopant concentration is a key factor in determining the formation of localized or band impurity states. In the present study we have analyzed the effect of introducing an isovalent transition metal dopant (Ti) in bulk *t*–ZrO_2. This study has been triggered by the experimental observation of a large red-shift of the optical absorption edge from pure to Ti–doped ZrO_2 [432]. In particular, a nominal Ti concentration of 15% is found to induce a 1.3 eV red-shift.

On the basis of hybrid functional (B3LYP) calculations we observe that isolated impurities in substitutional and interstitial positions form localized

unoccupied or occupied states in the band gap, respectively. The empty states for Ti_s are just below the CBM (0.4 eV in a 5.7 eV computed band gap) while the occupied states for Ti_i are in the middle of the band gap (3.4 eV above the VBM). Higher concentrations of the dopant increase the number of states in the band gap. When the Ti_s impurities are very close in the lattice, separated by only one lattice O and lying in the same *xy* plane, there is a larger d-states mixing and therefore also a larger reduction of the occupied to empty states gap. However, configurations with the adjacent Ti species on the same *xy* plane are less stable, indicating that segregation of TiO_2 nano-phases is unfavorable and that diluted impurities are preferred.

In order to make direct comparison with the experimental optical absorption energies, we have computed optical transition levels which provide a more accurate estimation of the excitation energies than single particle KS eigenvalues. They are found to be about 0.3 eV lower than single-particle HOMO-LUMO energy differences (see Fig. 7.3). The computed optical absorption is estimated to be about 4.9 eV for a Ti dopant concentration comparable to the experimental one, in the most stable investigated configuration. There is a shift of about 0.8 eV with respect to the pure ZrO_2 computed optical direct band gap (5.7 eV) which is in broad agreement with the experimentally observed optical shift of 1.3 eV (from 5.3 to 4.0 eV, [432]). The discrepancy between experimental and computed values of the absorption shift may be due to excitonic effects which are not taken into account in the present approach.

Finally, in the presence of Ti impurities the energy cost to form an oxygen vacancy lowers from 6.2 eV to 5.7 eV, so that Ti doping is predicted to favor oxygen deficiency. This energy cost reduction is associated with the electron transfer from a doubly occupied vacancy state (F–type centre) to a Ti^{4+} centre with formation of a Ti^{3+} species. Such species have been actually detected by electron paramagnetic resonance (EPR) in the polycrystalline Ti–doped ZrO_2 samples [432].

To summarize, the hybrid functional study here reported has shown that Ti–doping of bulk ZrO_2 can largely modify its electronic structure by considerably reducing the optical absorption edge through formation of a Ti 3d band in the ZrO_2 band gap. Formation of Ti^{3+} centres also occurs as a result of internal electron transfers from intrinsic defects such as oxygen vacancies.

PART IV

MAGNESIUM OXIDE

Background

In the previous Chapters the importance of doping of wide-gap semiconductors, such as ZnO and ZrO_2, has emerged to be two-fold. On one side, dopants have been attracting a great interest because of the possibility of tuning the material electronic structure in order to achieve more efficient photoactive oxides under visible light [451,452] or blue/UV optoelectronic devices. In this context, Ti–doping was demonstrated to reduce the optical band gap of ZrO_2 by about 0.8 eV (see Chapter 7), while nitrogen and copper, two promising candidates as *p*-dopants of ZnO, were observed to induce only deep level states (see Chapters 4 and 5). On the other side, dopants often cause the formation of magnetic defect centres in the bulk, making these systems very appealing also in the field of spintronics with the possibility to obtain room temperature ferromagnetism. Several attempts have been made to achieve useful ferromagnetic order in oxide materials with transition metal (TM) or rare earth atoms [453]. However, due to the intrinsic magnetic behaviour of transition metals, it is difficult to discriminate magnetic properties induced in the doped material from those of other magnetic impurities.

A few years ago, Elfimov *et al.* [185] proposed to use classical non-magnetic oxides, such as CaO, with a significant concentration of cation vacancies (V_{Ca}) as potentially new materials with ferromagnetic ordering. The cation vacancy in alkaline-earth oxides has been studied in great detail in the past as one of the classical defects in ionic oxides [454,455]. It consists of a missing neutral alkaline-earth atom with formation of two O^- radical ions, located near the cavity. It has been predicted that with a concentration of a few percent of V_{Ca} centres, half-metallic ferromagnetism can result [185]. Shortly after, it was proposed by Kenmochi *et al.* [186] that B, C, or N impurities substituting the O ion in CaO could result in local moments in the 2p states of the doping elements and in room-temperature ferromagnetism. The specific

case of nitrogen substituting for oxygen in SrO has been considered both theoretically and experimentally by Elfimov *et al.* [189]. They concluded, based on X-ray absorption and N 1s core level X-ray photoemission spectra (XPS), that the source of magnetization is the N atom substitutional for O in the SrO lattice, and in particular the singly occupied N 2p orbital. These studies have stimulated an intense theoretical activity on both N–doped and cation deficient oxides [45,184,187,188,456].

In this context, magnesium oxide appears as an ideal case for studying the magnetic properties induced by defects. The simple face-centred cubic structure (*i.e.*, NaCl structure) and the small atomic number of the constituent elements, Mg and O, point in fact MgO as a particularly attractive model system for ionic oxides, thereby allowing the application of highly sophisticated computational techniques [457,458,459,460].

MgO also offers significant advantages over other oxides from an experimental point of view. It is a well-characterized crystalline ionic insulator and it can be easily prepared in a high purity form as single crystals, thin films or powders [461,462]. MgO can also be doped with selected extrinsic impurities, and by careful choice of the preparation method (*e.g.*, $Mg(OH)_2$ decomposition in vacuum at 530 K [463], sol-gel techniques [464], chemical vapour deposition [465]) it can be synthesized with a wide range of high surface areas (200-500 m^2g^{-1}). The microcrystals are well defined, with homogeneous size and regular shape despite the polycrystalline nature of the material and the facets generally expose the (100), (010) and (001) cristallographic planes [466].

CHAPTER 8

Nitrogen Doping[††]

Abstract

The nature of nitrogen doped MgO, N–MgO, is investigated by DFT calculations using both periodic supercells and embedded cluster models. The electronic structure and the spin properties, in particular the hyperfine coupling constants, of substitutional for O and interstitial N species are determined by using a hybrid exchange-correlation functional in order to account for the self-interaction problem in DFT. Both substitutional and interstitial N introduce magnetic impurities in bulk MgO and generate new energy levels at about 0.5–1.7 eV above the top of the MgO valence band. We have also considered the simultaneous presence of neutral magnesium vacancies (V_{Mg}) and neutral oxygen vacancies (V_O) in the material, and we found that a charge transfer can occur between the N–impurity states and these intrinsic defects. In particular, a substitutional nitrogen behaves as an electron donor in the presence of V_{Mg} and as an electron acceptor in the presence of V_O centres. The occurrence of the internal charge transfer may alter the magnetic properties of the material.

[††] The results described in this Chapter have been reported in: M. Pesci, F. Gallino, C. Di Valentin, G. Pacchioni, *J. Phys. Chem. C*, **2010**, 114, 1350.

8.1 Introduction

So far, the few evidences of induced ferromagnetism in MgO are referring to powder samples and have been attributed to the presence of Mg vacancies at the surface or at the interface of the MgO nanoparticles [467,468]. The estimated concentration of the defects, 3.4 x 10^{16} cm^{-3}, is two times larger than in bulk MgO. To the best of our knowledge, no example of induced ferromagnetism in N–doped MgO has been reported yet, but attempts are ongoing in several laboratories [469]. To optimize these efforts it is important to understand the fundamental characteristics of nitrogen doping from an atomistic point of view. For instance, it is generally assumed that the N–impurity enters in the MgO lattice in a substitutional for the O position, but, in general, one could expect also the formation of N interstitials. In the case of nitrogen doped TiO_2 interstitial nitrogen impurities have been unambiguously identified by means of combined EPR, XPS and theoretical modelling and associated to a specific photo-catalytic activity under visible light; in ZnO both isolated and molecular "N_2^-" acceptors have been identified [360] (see Chapter 5). The incorporation of nitrogen, in fact, may depend on the preparation method, wet chemistry, solid state synthesis, molecular beam epitaxy, *etc*. Another aspect that has not been investigated so far is the interplay between defects of a different nature in the material. For instance, in the case of C– or N–doped TiO_2, it has been shown that there is an exchange of electrons between defects that induce occupied states high in the gap (*i.e.*, the Ti^{3+} ions associated to O vacancies) and deep gap states induced by the C or N dopants [345,470]. The consequence is that magnetic N impurities in TiO_2 trap one electron from the Ti^{3+} ions and transform into diamagnetic N^- centres. As N introduces deep gap states in alkaline-earth oxides, this mechanism can take place also in these materials.

This Chapter reports the study of the electronic structure of N–doped MgO using both periodic supercell and embedded cluster calculations in order to simulate different dopant concentrations. We have considered substitutional and interstitial N species, their hyperfine coupling constants and their interplay with V_{Mg} and V_O centres, and the possible occurrence of charge exchange between the corresponding energy levels. The main purpose of this work is therefore the theoretical characterization of the electronic structure and spin properties of N–induced defects in MgO; the magnetic interaction of these centres and the magnetic ordering of the crystal are not discussed and are

subject of ongoing investigations.

8.2 Computational Details

For the calculations we have adopted two complementary strategies. First we have computed the properties of N–impurities in MgO by using a periodic supercell approach; then, we have studied the limit of extreme dilution of the defect by considering an embedded cluster model. In both cases, the calculations, which include spin polarization, have been performed using the hybrid B3LYP [59,60] functional.

The Kohn-Sham orbitals have been expanded in Gaussian Type Orbitals (GTO), as implemented in the CRYSTAL06 code [71] (the all-electron basis-sets are: Mg 8-511G [471], O 8-411(d1) [281]; N 7-311(d1) [283]). We considered three cubic supercells: $\sqrt{2}$ x $\sqrt{2}$ x $\sqrt{2}$ (16 atoms), $\sqrt{2}$ x $\sqrt{2}$ x 2 (32 atoms) and 2 x 2 x 2 (64 atoms). For the case of substitutional nitrogen, the stoichiometry is thus $MgO_{1-0.125}N_{0.125}$, $MgO_{1-0.0625}N_{0.0625}$, $MgO_{1-0.0312}N_{0.0312}$, respectively. The bulk lattice parameter (a = 4.239 Å) and the geometries of the defective systems have been fully optimized until the largest component of the ionic forces was less than 4.5×10^{-4} a.u. The reciprocal space is sampled according to a regular sublattice (k-points mesh) with a shrinking factor IS equal to 4 or 6, according to the supercell size. The MgO band gap in our approach, 6.9 eV, is underestimated by 12% with respect to the experimental one, 7.6–7.8 eV [472]. For additional details about the computational parameters used in the CRYSTAL code we refer the reader to Sec. 2.1.4.1. A detailed description of the computational method to calculate hyperfine coupling constants can be found in Sec. 2.1.5.3.

In the second approach the bulk of MgO is represented by a nanocluster containing about 1000 atoms. The central part, treated quantum-mechanically (QM), is surrounded by a region of 216 classical ions whose polarizability is described by a shell-model (SM) [161] (see Sec. 2.1.4.2). Cations in the SM region at the interface with the QM region are replaced by ions (hereafter, indicated as Mg*) on which a semi-local effective core pseudopotential (ECP) is centred, in order to reproduce the Pauli repulsion and avoid the non-physical polarization of QM interface anions. The whole QM cluster is thus $Mg_{14}O_{13}Mg^{*}_{24}$. Region I (QM and SM) is then surrounded by a large array of point charges (PC) in order to reproduce the long-range electrostatic potential.

This scheme is implemented in the GUESS code [473] interfaced with the GAUSSIAN03 code [158], and the total energy of the hybrid system is calculated as a sum of classical and QM contributions. All centres in the QM region and Mg* interface atoms have been allowed to move during the optimization, while only shells, not cores, have been relaxed in the SM region. The GTO basis sets used are 6-31G on Mg and 6-31G* on O and N. The estimated band gap with this cluster is 6.7 eV, that is slightly smaller than in the supercell approach.

8.3 Results and Discussion

8.3.1 Substitutional N Impurity (N_s)

The concentration of N impurities considered in the supercell approach is 3.1%, 6.2%, and 12.5% (supercells containing 64, 32, 16 atoms, respectively). These concentrations are from slightly below to well above, respectively, the minimum concentration (5%) that is expected to induce magnetic ordering [45]. The local properties of the N–substitutional impurity, however, are similar in the three supercells and only the results of the larger 64 atom supercell will be discussed in detail. When a lattice O^{2-} ion is replaced by nitrogen, one forms a $[N_s]^{2-}$ species with a hole in the 2p shell (see Fig. 8.1). The formal charge, –2, is consistent with that derived from the Mulliken population analysis, –2.2. The ground state is magnetic (doublet), and the unpaired electron resides in a 2p orbital (see Fig. 8.1). The spin population on N is 0.86, suggesting that the spin is largely localized on the impurity atom. The gap in N–MgO increases from 6.9 to 7.1 eV; the three occupied 2pα and the two occupied 2pβ levels are slightly above the top of the valence band, in an energy range from 0.5 to 0.8 eV (see Fig. 8.1). The empty 2pβ component is higher in the gap and lies at about 3.8 eV above the top of the valence band (see Fig. 8.1). Thus, N introduces deep states in the gap of MgO, and there is a splitting of about 3 eV between occupied and unoccupied states. The states are highly localized, and no band dispersion is observed; see Fig. 8.1 (the bandwidth is ~0.1 eV).

Replacing O with N is a thermodynamically unfavourable process. In fact, the cost of removing a neutral O atom from the MgO lattice, with formation of a V_O centre, is 10.6 eV; the energy gain when a N atom is filling the cavity is of 6.2 eV, so the final cost is 4.6 eV. Very similar formation energies are

computed with the 32 atom supercell or with the cluster model (4.2 and 4.5 eV, respectively). Also, the electronic structure is similar in the smaller supercell or in the embedded cluster, with the N 2p states slightly above the top of the valence band and a spin density on N close to 0.9. At the concentration of 6.2% of N impurities, the width of the N 2p minority spin band increases to 0.7 eV (from 0.1 eV at 3.1% N, Fig. 8.1) and the exchange splitting is reduced from 3.0 to 2.5 eV. If one considers the even higher concentration of 12.5% N impurities, the width of the minority spin band becomes 1.5 eV and the energy separation from the band formed by empty β states becomes only about 1 eV. Clearly, as the dopant concentration increases, one approaches the situation of a half-metal, but even with a 12.5% N concentration one is still far from this situation.

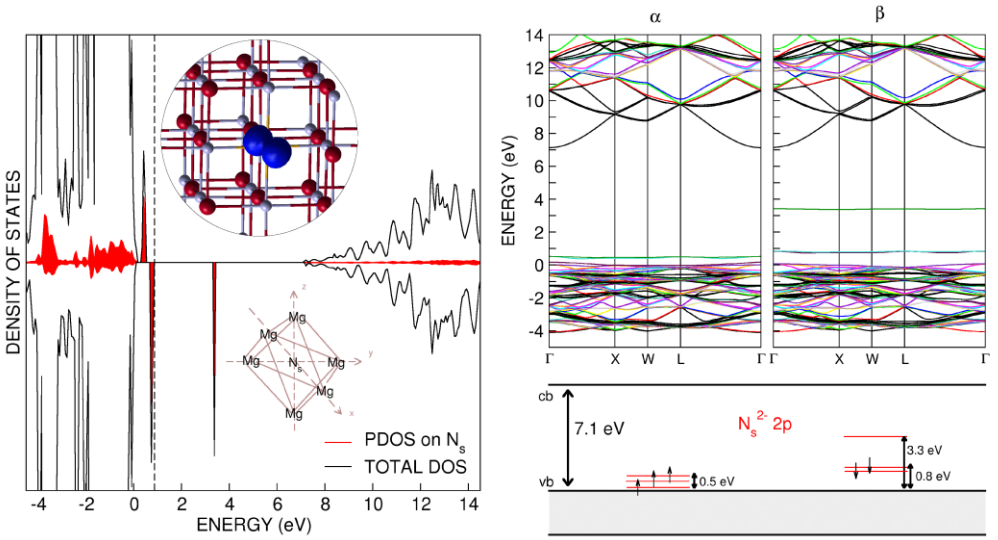

Figure 8.1. Electronic structure of a nitrogen substitutional impurity in bulk MgO, $[N_s]^{2-}$ (64 atoms supercell). Mg, O and N are represented by small light grey, large dark red and small yellow spheres, respectively. Left panel: projected density of states. Right panel: band structure for α (up) and β (down) electronic states. In the insets of the left panel, the spin density and the local environment of the defect are shown. The bottom of the right panel shows a schematic representation of the α and β N–induced states in the MgO gap.

There is one aspect, however, that differs in the three calculations, and this is the orientation of the singly occupied N 2p level. In the 64-atom supercell and in the cluster model, modelling low concentration of N impurities or the

limit of infinite dilution (no interaction with other magnetic defects), the singly occupied 2p orbital is oriented along the diagonal of the cube, pointing toward two second-neighbour Mg^{2+} cations (see Fig. 8.1). However, in the 32-atom supercell the singly occupied N 2p level is along the Mg–N–Mg axis and points directly toward the nearest-neighbour Mg^{2+} ions.

In Table 8.1 are reported the isotropic and dipolar components of the hyperfine coupling constants of the unpaired electron with the ^{14}N nucleus. First of all, we notice that the computed values are very similar in all models considered, small and large supercell, or embedded cluster (see Table 8.1). The a_{iso} is of about 11–14 G, while the dipolar term is dominant, as expected for an unpaired electron in a 2p type orbital. The superhyperfine interaction with neighbouring Mg or O ions (not shown) is very small, of the order of 0–2 G, and probably difficult to detect experimentally (also consider that the natural abundance of the magnetically active ^{25}Mg nucleus is only about 10%, while the coupling with ^{17}O is practically absent and can be observed only in isotopically enriched samples). This confirms that the spin is rather localized and that only the tails of the spin wave function extend beyond the N impurity.

Table 8.1. Hyperfine coupling constants (in G) of N substitutional for O, $[N_s]^{2-}$, and for N interstitial, $[N_iO]^{2-}$, in N–doped bulk MgO

	$\sqrt{2}x\sqrt{2}x2$ ($Mg_{16}O_{16}$)	2x2x2 ($Mg_{32}O_{32}$)	Cluster ($Mg_{14}O_{13}$)
		N substitutional $[N_s]^{2-}$	
a_{iso} (^{14}N)	13.7	13.6	10.8
B_1 (^{14}N)	-11.5	-11.9	-10.8
B_2 (^{14}N)	-11.8	-11.9	-10.8
B_3 (^{14}N)	23.3	23.8	21.6
		N interstitial $[N_iO]^{2-}$	
a_{iso} (^{14}N)	12.6	13.0	11.1
B_1 (^{14}N)	-11.1	-11.8	-10.6
B_2 (^{14}N)	-11.5	-11.3	-10.6
B_3 (^{14}N)	22.6	23.2	20.8
a_{iso} (^{17}O)	-12.4	-11.6	-11.7
B_1 (^{17}O)	16.1	15.2	14.4
B_2 (^{17}O)	16.5	15.3	14.3
B_3 (^{17}O)	-32.6	-30.5	-28.7

8.3.2 Interstitial N Impurity (N_i)

In all the studies reported so far, it has been assumed that N in N–doped MgO takes the position of a lattice O^{2-} ion (substitutional N, $[N_s]^{2-}$). However, we have seen above that the removal of one O and its replacement with a N atom has a considerable energy cost; it can occur preferentially when the preparation is done in oxygen-poor conditions, but is likely that, under oxygen-rich conditions, the N atoms will enter in the lattice in interstitial positions, without altering the Mg-to-O ratio. This is, indeed, what has been observed for other N–doped materials, like for instance N–TiO_2 [376,474] and N–ZnO (see Chapter 5).

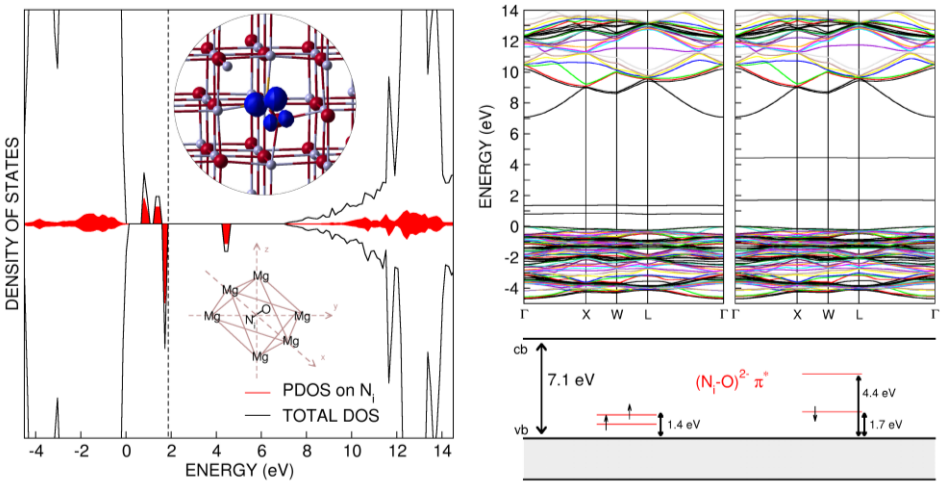

Figure 8.2. Electronic structure of a nitrogen interstitial impurity in bulk MgO, $[N_iO]^{2-}$ (64-atom supercell). Mg, O and N are represented by small light grey, large dark red and small yellow spheres, respectively. Left panel: projected density of states. Right panel: band structure for α (up) and β (down) electronic states. In the insets of the left panel, the spin density and the local environment of the defect are shown. The bottom of the right panel shows a schematic representation of the α and β N–induced states in the MgO gap.

We have considered this possibility by including a neutral N atom in an interstitial position of the regular MgO lattice and reoptimizing the structure. Independent of the starting point of the optimization and of the model used, cluster or supercell, the final structure shows the formation of a direct N–O bond and the appearance of a NO unit that takes the position of the O^{2-} ion in the lattice. In this formally $[N_iO]^{2-}$ unit, the N–O distance is 1.35 Å, slightly longer than in gas-phase NO, 1.15 Å. The NO unit is oriented along the

diagonal of the cube (see Fig. 8.2), and the unpaired electron occupies an orbital with π character distributed over both N and O atoms. The spin population for this π orbital is 0.73–0.76, depending on the model. The inclusion of the N atom induces a strain in the structure so that it is energetically unfavorable: the cost to add a gas-phase N atom to the MgO lattice varies from 2.1 to 2.8 eV, depending on the model. The distortion consists in a deformation of the cubic lattice around the NO unit, which is more pronounced for the case of a high concentration of N dopants.

The nature of the electronic states is reminiscent of that found for N–doped TiO_2 [474,475]. The occupied NO π*-like states are about 1.4–1.7 eV above the top of the MgO valence band, and the empty β component is in the midgap, 4.4 eV above the top of the valence band (see Fig. 8.2). With respect to substutional N, we notice that the states are higher in the gap (a feature found also in N–TiO_2 [475]) but the exchange splitting between α and β components is similar, about 3 eV. As for substitutional nitrogen, no band dispersion is observed (see Fig. 8.2), a sign of a strong localization.

The EPR properties of interstitial N are reported in Table 8.1. Here, we discuss the hyperfine interaction with both N and O nuclei of the defect centre because the unpaired electron is partly shared by these two atoms. However, an experimental detection of the O hyperfine splitting will be possible only in isotopically enriched MgO samples. Also in this case, the EPR properties are very similar for the three models considered (see Table 8.1). What is more surprising, however, is that the structure of the **A** tensor (a_{iso} and B components) for the $[N_iO]^{2-}$ unit are very similar to those computed for an isolated substitutional N (see Table 8.1). The a_{iso} value, in fact, is of 11–13 G, and B_1, B_2, and B_3 are nearly coincident with those of the $[N_s]^{2-}$ centre. This is precisely what has been found for the analogous defect centres in N–doped TiO_2 [474]. Unfortunately, due to the close similarity of the two signals, an experimental discrimination of $[N_s]^{2-}$ from $[N_iO]^{2-}$ based on the N-hyperfine coupling constants will be difficult, if not impossible. The problem could be solved by looking at the hyperfine interaction with the ^{17}O nucleus. In fact, the coupling with O is substantial, and results in appreciable values, in particular of the dipolar component B (see Table 8.1). Also, here the $a_{iso}(^{17}O)$ component is small, consistent with the fact that the unpaired electron resides in a level with π character.

All other coupling constants are small, again indicating the rather localized nature of the N–induced states.

8.3.3 Mg Vacancy and O Vacancy (V_{Mg}, V_O)

In the previous Sections 8.3.1 and 8.3.2, we have described the nature of the extrinsic defects connected to the incorporation of N atoms in the MgO lattice. Here, we briefly review the nature and electronic structure of two intrinsic defects, that are the Mg and the O vacancies. These defect centres have been discussed at length in the past [454,455,476,477], and therefore, we will only summarize their main features. The motivation for revisiting these two defects is two-fold: on one side, the cation vacancy has been proposed as one of the possible centres responsible for ferromagnetism in alkaline-earth oxides [45,185,456,467,468]; on the other side, the simultaneous presence of Mg or O vacancies and N impurities can result, at least in principle, in charge exchange between the different centres with alteration of their magnetic properties.

It is well-established that the Mg vacancy in MgO, V_{Mg}, corresponds to two holes located on the O ions around the vacancy [454,455]; the ground state is thus a triplet, exhibiting both a zero-field splitting and an axial *g*-tensor in EPR [478]. This defect centre has been studied in some detail both in the bulk and on the surface of MgO using a Hartree–Fock approach and periodic or embedded cluster models [479,480]. The lattice distortion induces a localization of the two holes on the O ions on the opposite site of the vacancy, with formation of two O^- radical ions [479]. The formation energy of the defect has been estimated to be very high and to be higher in the bulk than on the surface [479]. Therefore, migration of the V_{Mg} centres to the surface of MgO nanoparticles is expected to be thermodynamically favorable.

We have considered the electronic structure of the V_{Mg} centre in bulk MgO by using a supercell approach (64-atom supercell). The main difference with respect to the results reported by Baranek *et al*. [479] is that, here, we use a DFT approach with a hybrid functional. By removing a neutral Mg atom from the structure, we find two solutions where the two holes are either localized on two opposite sites of the vacancy, as found in Ref. [479], or localized on two adjacent O ions (see Fig. 8.3). The former solution is slightly preferred by 0.12 eV. The electronic structure is characterized by the presence of singly occupied O 2p states at the top of the valence band, while the corresponding empty β components are only 1.1 eV higher (see Fig. 8.3). This means that the V_{Mg} vacancy is an excellent electron trap and can easily transform into the

charged V_{Mg}^{-} centre that has been best characterized [481,482]. This is an important aspect since we have seen above that N atoms either in substitutional for O or in interstitial positions introduce occupied states in the gap at 0.5–1.7 eV above the top of the valence band (see Figs. 8.1 and 8.2). Being the empty states associated with the V_{Mg} centre lower in energy, it is conceivable that electrons can be transferred from the N–induced states to the O^{-} centres associated to the Mg vacancy with a global energy gain. This aspect will be considered explicitly in the next Section 8.3.4.

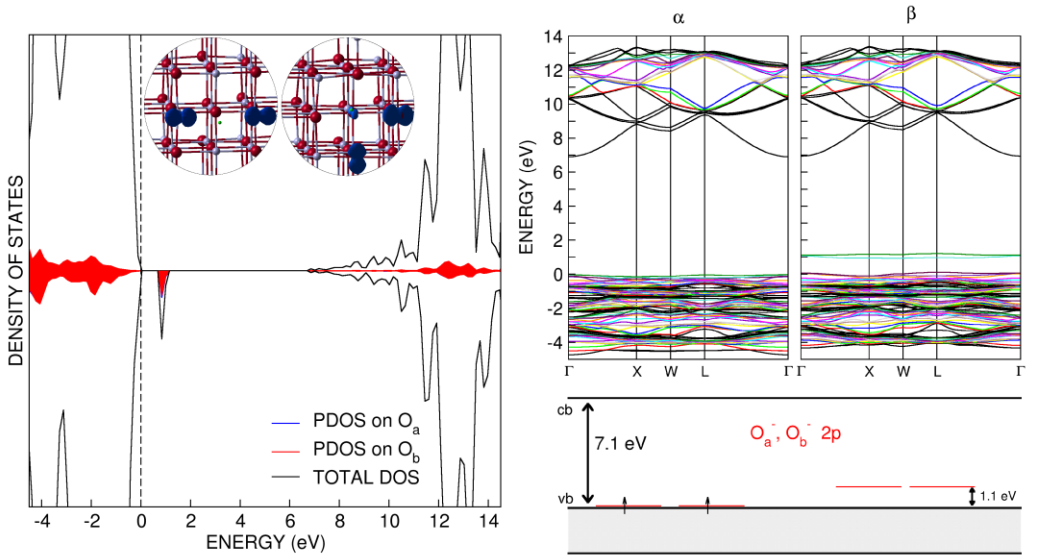

Figure 8.3. Electronic structure of a neutral magnesium vacancy in bulk MgO, V_{Mg} (64-atom supercell). Mg and O are represented by small light grey and large dark red spheres, respectively. Left panel: projected density of states. Right panel: band structure for α (up) and β (down) electronic states. In the inset of the left panel, the spin densities corresponding to two energetically close solutions are reported. In one case (preferred), one forms two O^{-} ions on the opposite sides of the cavity; in the other case, the two O^{-} ions are next neighbors. The bottom of the right panel shows a schematic representation of the α and β states in the MgO gap induced by a V_{Mg} centre.

The other MgO defect centre that has been fully characterized at both the theoretical and the experimental levels is the O vacancy, V_O, usually referred to as the F centre [476,477]. The literature on this centre is so abundant that we restrict here to the main features of the electronic structure. The removal of a neutral O from the ionic MgO lattice results in two extra electrons that are

trapped in the cavity left by the missing O atom. The relaxation around the defect is very small because the place of the O^{2-} ion is now taken by two electrons confined in the vacancy so that the crystal electrostatic potential is only moderately perturbed. The two electrons occupy a totally symmetric orbital that has no valence band nor conduction band character. In fact, the state lies in the mid of the gap of MgO. According to the supercell periodic calculations performed with the present approach, this energy level is 3.1 eV above the valence band. Thus, different from the V_{Mg} centre, the O vacancy introduces occupied levels that are high in the gap and, in principle, can transfer charge to the empty states of the N–induced defects.

8.3.4 Interplay between Mg and O Vacancies and N Impurities

In the previous Sections, we have considered the electronic structure and stability of individual native and induced defect centres in N–doped MgO. In this Section, we will consider the interaction between such defects, introducing a pair of defects in the same supercell and computing the final ground state structure. As an extrinsic defect, we have considered the substitutional N atom, $[N_s]^{2-}$, but the conclusions should apply in a similar way to the interstitial $[N_iO]^{2-}$ species. In the 64-atom supercell, we have included the $[N_s]^{2-}$ centre and created simultaneously an O or a Mg vacancy. The two point defects have been placed inside the supercell so as to reduce as much as possible their direct interaction. The total energy of the new system has then been evaluated after full geometry optimization.

When a Mg vacancy (corresponding to two O^- ions) and a $[N_s]^{2-}$ centre are present in the supercell, a net charge transfer occurs spontaneously:

$$\left[N_s\right]^{2-} + V_{Mg}^{0}(O^-;O^-) \rightarrow \left[N_s\right]^{-} + V_{Mg}^{-}(O^-;O^{2-}) \qquad (8.1)$$

In this process, one O^- species traps one electron and becomes a normal lattice O^{2-} ion, thus leaving only one O^- centre in the structure (V_{Mg}^-); the $[N_s]^{2-}$ loses one electron and transforms into $[N_s]^-$, a centre characterized by the presence of two holes in the N 2p levels (triplet). The $[N_s]^-$ states are lower in energy than in $[N_s]^{2-}$ and are positioned at the top and partially mixed with the valence band. The total spin multiplicity of the supercell is a quartet, with one spin localized on the O^- radical and two unpaired electrons localized on the N impurity. This solution is definitely the most stable one and suggests that, in

principle, the presence of V_{Mg} centres can interfere with that of $[N_s]^{2-}$ defects.

A similar situation arises when we consider the simultaneous presence of $[N_s]^{2-}$ and of neutral V_O centres, but now the charge transfer occurs spontaneously from the V_O defect to the N impurity. In fact, in the ground state, one of the two electrons of the V_O centre is transferred to the $[N_s]^{2-}$ defect with formation of a paramagnetic V_O^+ (F^+) and of a diamagnetic $[N_s]^{3-}$ defect:

$$\left[N_s\right]^{2-} + V_O^0(F^0) \rightarrow \left[N_s\right]^{3-} + V_O^+(F^+) \qquad (8.2)$$

The magnetic moment on the N atom is thus quenched, with possible alteration of the magnetic ordering in the material. The energy levels of $[N_s]^{3-}$ are shifted to higher energies (1.6 eV) compared with those of $[N_s]^{2-}$ (0.5–0.8 eV), while the state associated with the V_O^+ centre is stabilized and is found at 2.6 eV above the top of the valence band.

Of course, the fact that the charge transfer between defects of different kind is the thermodynamically most favoured solution does not necessarily imply that these processes play an important role in the material. First of all, although there is little doubt that the charge transfer leads to a more stable situation, the mechanism for the electron transport from one site to the other is not clear. In a semiconducting oxide like TiO_2, this can occur simply by thermal excitation of one electron from shallow Ti^{3+} states to the conduction band; in a wide gap material like MgO, this process may require high thermal energies and may not be accessible under normal conditions. The second important aspect is the abundance of the various defect centres, an aspect that largely depends on the preparation method. If the concentration of V_{Mg} or V_O centres is orders of magnitude smaller than that of the N atoms incorporated in the structure, the relevance of the charge transfer process is negligible. On the other hand, we have seen that the formation of N substitutional for O is probably easier when the preparation is done in oxygen-poor conditions. In this case, the concentration of O vacancies could be significant and interfere with the generation of N magnetic centres in the bulk of the oxide.

8.4 Conclusions

We have studied the electronic structure of N impurities in bulk MgO by

means of periodic and embedded cluster model DFT calculations with hybrid exchange-correlation functionals. We have considered both substitutional and interstitial N species; it is expected that substitutional N, $[N_s]^{2-}$, forms more easily under oxygen-poor conditions, while interstitial N, $[N_iO]^{2-}$, should be easier to form under oxygen-rich conditions. Interstitial N results in the formation of a strongly bound NO unit reminiscent of the species formed in the bulk of TiO_2 [474] and ZnO (see Section 5.3.2.1). In both cases, the resulting centres are magnetic, being characterized by the presence of a rather localized unpaired electron occupying a N 2p atomic orbital, $[N_s]^{2-}$, or a NO π-type molecular orbital, $[N_iO]^{2-}$. The hyperfine coupling constants for the two cases confirm the high degree of spin localization, an aspect that may disfavor the formation of a ferromagnetic order at room temperature. Unfortunately, the close similarity of the N hyperfine coupling constants may render a distinction of the two defect centres, based on EPR spectra only, quite difficult. A potentially useful technique that could help in the distinction is XPS, as it is known in analogous N–doped TiO_2 compounds that substitutional and interstitial nitrogen have different 2p XPS peaks.

We have also considered two classical defects in MgO, the Mg and O vacancies. If the preparation of the N–doped sample leads to a non-perfectly stoichiometric material, these centres could be present in significant concentrations. Because of the different position of the N–induced states in the MgO gap compared to those of the V_{Mg} or V_O centres, an electron exchange is possible with consequent thermodynamic stabilization. In particular, in the presence of V_{Mg}, a defect that corresponds to the formation of two O^- radical ions in the structure, the N impurity behaves as an electron donor and transfers charge to one of the O^- species that becomes diamagnetic, O^{2-}; two unpaired electrons remain on the substitutional N centre, $[N_s]^-$. When V_O centres are present, the N impurity behaves as an electron acceptor and traps one electron from V_O with formation of a diamagnetic $[N_s]^{3-}$ species and a paramagnetic V_O^+ defect.

On the basis of the present results, the possibility to obtain ferromagnetism in N–doped MgO seems problematic. The highly localized nature of the defects suggests, in fact, that relatively high concentrations of dopants are needed, a condition that could require specific synthetic methods.

CHAPTER 9

Trapped N_2^- Radical Anions[‡‡]

Abstract

Oxidation of magnesium nitride, Mg_3N_2, leads to segregated nitrogen impurities within the bulk of MgO. Electron paramagnetic resonance experiments in conjunction with quantum chemical calculations allow us to identify these paramagnetic centres as N_2^- radical anions trapped in anion vacancies in the bulk of MgO. The characteristics of the defect centre, derived from the spin Hamiltonian parameters, exhibit similarities but also some interesting differences with respect to the classical N_2^- species in KCl, a sort of prototype of molecular anions trapped in ionic crystals.

[‡‡] The results described in this Chapter have been reported in: F. Napoli, M. Chiesa, E. Giamello, M. Fittipaldi, C. Di Valentin, F. Gallino, G. Pacchioni, *J. Phys. Chem. C*, **2010**, 114, 5187.

9.1 Introduction

By virtue of its negative electron affinity, nitrogen forms temporary anion states upon interaction with excess electrons in the gas phase [483]. These transient-ions have been the object of numerous theoretical and experimental studies, which concur to the description of these systems in terms of short-living N_2^- ($^2\Pi_g$) doublet states [484,485]. These unstable anion states can be made thermodynamically favorable in the condensed phase by the effect of solvation and in particular by virtue of the Madelung potential in ionic crystals. As an example, N_2^- impurities have been reported in the case of irradiated azides and trapped at negative anion vacancies in different alkali halides [486,487,488,489]. In particular, the N_2^- species in KCl has been fully characterized by EPR spectroscopy long time ago, becoming soon a classical example of a molecular radical ion trapped in a solid [489]. The formation of N_2^- radical anions has also been reported to occur at the surface of "electron-rich" alkaline earth oxides [490] (MgO and CaO) via a direct surface-to-adsorbate electron transfer [491,492,493,494], however no reports are available on the identification of this radical anion in the bulk of alkaline earth oxides.

The present Chapter reports the EPR identification substantiated by DFT embedded cluster calculations of the N_2^- molecular anion in polycrystalline MgO obtained by oxidation of Mg_3N_2. Oxidation of metal nitrides is one way of incorporating nitrogen impurities in oxides, which has the advantage of easily tune the amount of incorporated nitrogen in the final oxide system. The identification of the paramagnetic N_2^- impurity is unambiguously obtained by means of X and W band CW-EPR and two pulse X band Echo detected EPR spectra, which are characterized by distinct hyperfine interactions due to two equivalent N atoms and a *g*-tensor typical of the $^2\Pi_{1/2}$ state of a 11–electron radical with $g_{yy} > g_{xx} > g_{zz}$; the only important shift from $g_e = 2.0023$ is observed for the g_{zz} component [495].

The motivation of this work is thus two-fold. On one side we report for the first time a thorough EPR characterization complemented by quantum chemical modelling of the N_2^- radical anion in MgO, which is of interest in order to contribute to the identification of the different species which can form during nitrogen incorporation in oxide insulators. On the other hand, comparison with the well-known case of the analogous N_2^- species in KCl, allows us to test in a rigorous way the reliability of *ab-initio* calculations of *g*-

tensors for paramagnetic centres in solids, a topic where the number of reported examples in the literature is still very limited.

9.2 Experimental and Computational Details

9.2.1 Experimental Section

Oxidation of Mg_3N_2 powders was carried out in air at 1073 K for 20 h. Powder X-Ray diffraction (XRD) patterns have been collected on a Philips 1830 XRD diffractometer using a Kα(Co) source and a X' Peret High-Score software for data handling.

Electron-spin-echo (ESE) detected EPR experiments were carried out with the pulse sequence: $\pi/2 - \tau - \pi - \tau -$ echo, with mw pulse lengths $t_{\pi/2}$ = 40 ns and t_π = 80 ns and a τ value of 200 ns. For more details on CW and pulsed EPR experiments we refer the reader to Sec. 2.2.1.

9.2.2 Computational Methods

For the calculations we used an embedded cluster model and the DFT approach (see Sec. 2.1.4.2). The quantum cluster consists of 19 O ions, 14 Mg ions and 30 Mg* ions represented by an effective core potential (ECP) with no valence electrons and basis functions associated. The Mg* ECPs provide a representation of the finite size of the Mg^{2+} ions and avoid spurious polarizations of the O^{2-} ions by the surrounding large set of about 8000 point charges (PC). The role of the PCs is to reproduce the Madelung potential of the ionic crystal (see Sec. 2.1.4.2). The central O^{2-} ion has been replaced by the trapped N_2^- dimer. Both orientations of the molecular axis, along the [100] or [110] directions, have been considered in the calculations. The positions of the dimer molecule and of the surrounding first and second neighbour ions have been optimized by keeping fixed the positions of the external Mg* ions.

For the calculations we have used the hybrid B3LYP [59,60] functional in combination with the 6-31+G* basis set for O and N atoms while the Mg^{2+} cations have been described by a 6-31G* basis set.

A detailed description of the computational method to calculate hyperfine coupling constants and the *g*-tensor can be found in Sec. 2.1.5.3.

9.3 Results and Discussion

Magnesium nitride can be converted to the corresponding oxide by high-temperature oxidation. The nitride to oxide conversion process can be monitored by means of XRD patterns as shown in Figure 9.1.

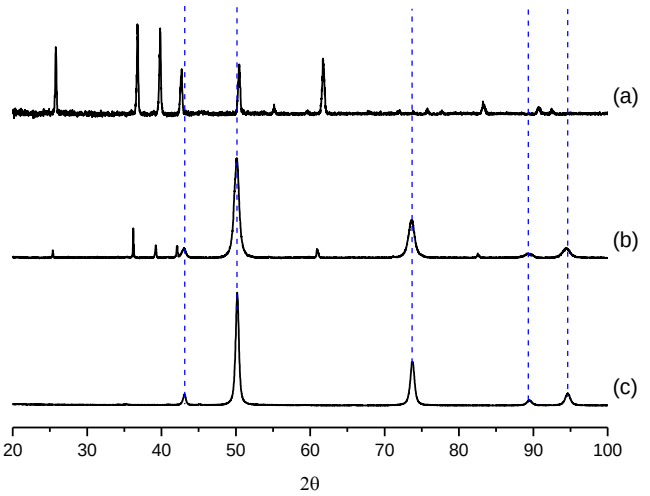

Figure 9.1. XRD patterns of (a) Mg_3N_2, (b) Mg_3N_2 oxidized at 873 K for 2 h, and (c) Mg_3N_2 oxidized at 1073 K for 20 h. Dashed lines indicate the MgO peak positions in the XRD pattern.

Upon treatment of the sample at 1073 K for 20 h the distinctive features of the Mg_3N_2 diffraction patterns are no longer observed and only peaks due to the MgO cubic structure are present in the XRD pattern. During the oxidation process, however, it is possible that nitrogen impurities remain trapped in the solid. This has been observed for example in the case of the oxidation of TiN to TiO_2 where XPS and EPR measurements led to the identification of substitutional or interstitial nitrogen impurities [496,497].

The EPR spectrum of the original magnesium nitride is shown in Figure 9.2a and is characterized by a narrow resonance line at g = 1.98 which is due to Cr^{3+} impurities contained in the sample. A small signal at g = 2 is also present which may be due to lattice defects. The spectrum of the oxidized sample (Fig. 9.2, spectra b and c) displays a completely different profile, characterized by a complex powder pattern dominated by five equally spaced hyperfine lines with relative intensities 1:2:3:2:1 as expected for an electron

interacting with two equivalent nuclei of spin one. We will show in the following that this spectrum is due to N_2^- radical anions trapped at oxygen vacancies. The narrow spectral line width provides indication that the species are isolated and non-interacting; this is in accord with the absence of modulations in the echo decay.

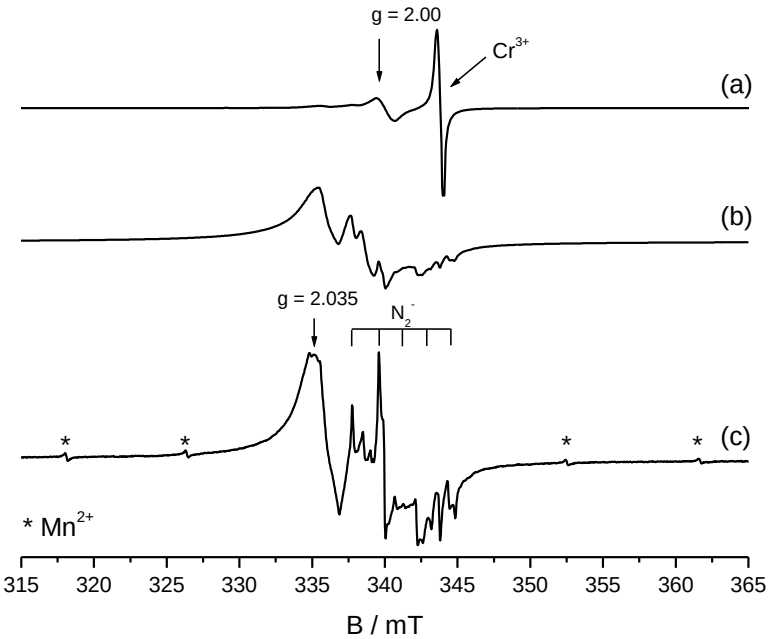

Figure 9.2 EPR spectra of (a) Mg_3N_2, (b) Mg_3N_2 oxidized at 873 K, and (c) Mg_3N_2 oxidized at 1073 K. Spectra were recorded a 77 K, 10 mW.

The CW-EPR spectrum is complicated by the presence of a number of spurious signals due to Mn^{2+} and Cr^{3+} impurities. Moreover a broad signal is also present at g = 2.035. In order to disentangle these overlapping signals, two pulse echo-detected EPR spectra have been recorded at 10 K. Under these circumstances species characterized by fast T_m are filtered off and only the N_2^- species is observed. In Figure 9.3 the echo-detected spectrum recorded at 40 K is shown as a first derivative together with the CW spectrum and the corresponding simulation.

The spectrum in Figure 9.3b was simulated using the following spin-Hamiltonian:

$$H = \mu_B BgS + SAI_a + SAI_b \tag{9.1}$$

The simulated spectrum was obtained using a single $S = 1/2$ species having rhombic $\boldsymbol{g}$ and $\boldsymbol{A}$ tensors, with two g values close to the free spin and one lower g value (1.983). These values are those expected for an 11-electron radical such as N_2^-.

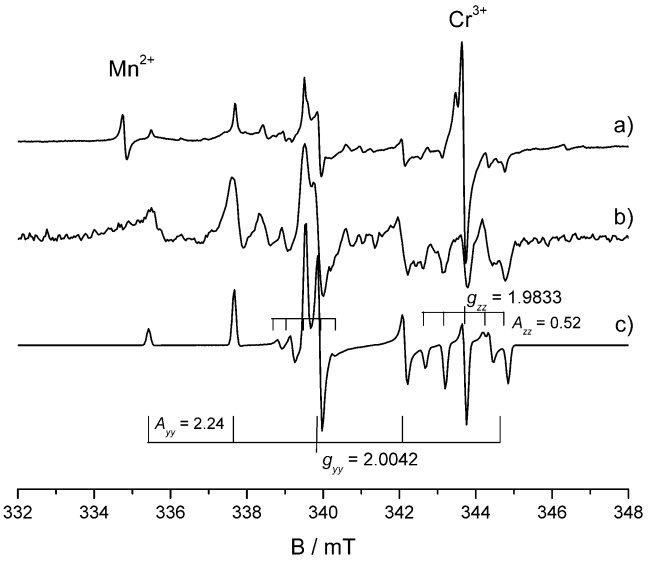

Figure 9.3. (a) CW X band EPR spectrum recorded at 77 K and 0.1 mW microwave power. (b) Two pulse echo detected EPR spectrum at 40 K. (c) Computer simulation of the EPR spectra.

In order to substantiate the interpretation of the spectrum and to obtain a better characterization of this centre, CW-EPR spectra were recorded at W band frequency (95 GHz). The spectrum recorded at high field (Fig. 9.4a) is complicated by the presence of Mn^{2+} and Cr^{3+} impurities; however, the multiline pattern characteristic of the N_2^- spectrum observed in X band is clearly visible. Furthermore, at this frequency, the g_{zz} component is markedly shifted towards high field so that the g_{zz} factor can be read off from the spectrum with considerable accuracy. The spectral feature at $g = 2.035$ observed in the X band spectrum becomes extremely broad at this frequency probably due to strain effects present in the polycrystalline systems. Moreover

a complex, structured feature at g = 2.021 becomes evident. The nature of these two signals is at the moment unclear, and specific experiments are currently being performed to interpret these features. Computer simulation of the W band spectrum (Fig. 9.4b) was thus limited to the N_2^- spectrum and was obtained using the figures deduced from the simulation of the X band echo-detected spectrum as starting values. In this way the same set of spin-Hamiltonian parameters simultaneously fits the spectra recorded at the two frequencies allowing confidence to be placed on the extracted figures. Minor mismatches are present which may be due to small heterogeneity, which was not taken into account in the simulation. The results are reported in Table 9.1 and provide firm evidence that the radical under observation is N_2^-, which, to the best of our knowledge, has never been observed in the bulk of MgO.

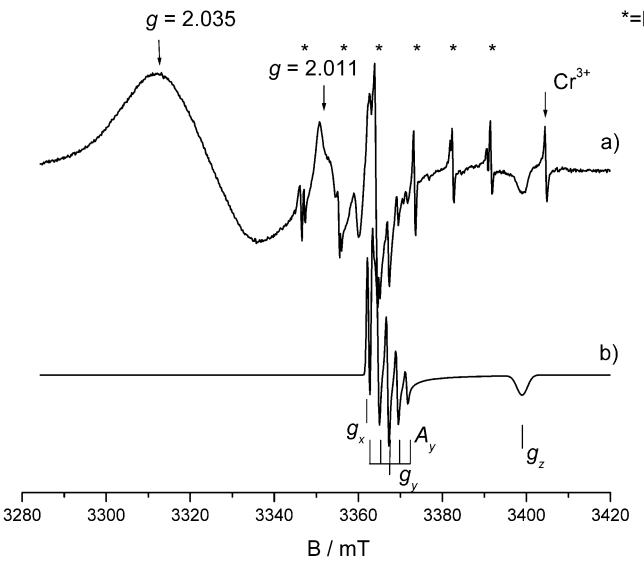

Figure 9.4. Experimental (a) and simulated (b) W-band EPR spectra of Mg_3N_2 oxidized at 1073 K for 20 h.

The N_2^- anion has been previously observed in the bulk of solid matrices including single crystals of various azides (K, Na, Ba) [486,487,488] or alkali-halides [489]. In general, the reported $\boldsymbol{g}$ and $\boldsymbol{A}$ tensors for these systems are remarkably similar to those found in this work (see Table 9.1). Also, they are in line with those found for the same species localized at the surface of MgO [491,492]. It should be noted that the different local coordination between bulk

and surface adsorbed species leads to a small but perceptible variation in the spin Hamiltonian parameters of the radical trapped in the bulk and adsorbed on the surface of MgO. This is amenable to the different symmetry of the local crystal fields experienced by the molecule in the two cases and is reflected in the $\boldsymbol{g}$ matrix components. The variation in the g_{xx} and g_{yy} values observed in this work with respect to those reported in Ref. [492] suggests that the π^*_y and π^*_x orbitals may be inverted. Elucidation of this aspect will require specific modelling of the two situations.

In Table 9.1 the most significant differences are found for the g_{zz} component, which shows different shifts from the free electron value. For instance, while for N_2^- in MgO the shift is relatively small, $\delta = 0.019$, the same radical in KCl exhibits a five times lager deviation, $\delta = 0.0958$, despite the same cubic structure of the host crystal.

Table 9.1. Experimental Spin-Hamiltonian Parameters for N_2^- in different host matrixes.

	g_{xx}	g_{yy}	g_{zz}	A_{xx} (G)	A_{yy} (G)	A_{zz} (G)	Ref.
N_2^- in MgO	2.0042	2.0021	1.9833	3.4	22.4	5.2	This work
N_2^- in KCl	1.9978	2.000	1.9065	21.3	5.0	6.1	489
N_2^- in KN_3	2.0008	2.0027	1.9832	3.8	12.0	4.0	486
N_2^- in NaN_3	≈2.00	≈2.00	1.75	11.0	23.5	3.9	487
N_2^- in $Ba(N_3)_2$	≈1.99	≈1.99	1.979	3.6	20.7	4.1	488
$^{14}N_2^-$ on MgO	2.0018	2.0042	1.9719	2.90	21.50	4.20	492
$^{14}N_2^-$ on CaO	2.0006	2.0048	1.9677	2.50	20.00	4.30	492

The g tensor elements reported in Table 9.1 are in agreement with those expected for the $^2\Pi_{1/2}$ state of an 11-electron radical like N_2^-. The electronic configuration of such a species (isoelectronic with NO and CO^-) is characterized by the presence of a single unpaired electron in the π antibonding orbitals of the molecule and the EPR spectrum can only be observed if the degeneracy of the two orbitals is lifted by an anisotropic electric field, such as that exerted by the low coordinated cations of an oxygen vacancy site. It should be noted that the same Coulombic forces are responsible for the stabilization of the N_2^- species, thus preventing dissociation into $N_2 + e^-$. The electronic configuration produces an orthorhombic g tensor whose elements can be obtained by adapting the equations of Zeller, Shuey and Känzig [498] (originally derived for $^2\Pi_{3/2}$ states), to the N_2^- case in agreement with the treatment performed by Brailsford *et al.* [489] for N_2^- in

KCl single crystal. A slightly simplified form of these equations, which are suited to the $^2\Pi_{1/2}$ state, with the unpaired electron in the π^*_y orbital (*vide infra*), are given as

$$g_{zz} = g_e - 2\lambda \sin 2\alpha \tag{9.2}$$

$$g_{yy} = g_e \cos 2\alpha + (\lambda / E)(1 + \cos 2\alpha + \sin 2\alpha) \tag{9.3}$$

$$g_{xx} = g_e \cos 2\alpha + (\lambda / E)(\cos 2\alpha - \sin 2\alpha - 1) \tag{9.4}$$

where λ is the spin–orbit coupling constant and E is the energy separation between the $^2\Pi$ ground state and a $^2\Sigma$ excited state admixed to the former by the spin–orbit interaction. The degeneracy of the π^*_y and π^*_x orbitals is lifted by the spin–orbit interaction, λ, and the orthorhombic crystal-field, Δ. The value of tan 2α is defined as λ/Δ. From the above equations it follows that all g factors should be less than g_e (2.0023) with g_{zz} showing the maximum shift as experimentally observed (Table 9.1).

The $\boldsymbol{A}$ tensor of the ^{14}N hyperfine may be written as in Eq. (2.40), where a_{iso} is the isotropic component (Fermi contact) of the hyperfine interaction and $\boldsymbol{T}$ is the anisotropic interaction term. Following the choice of signs adopted for the analysis of the hyperfine tensor of N_2^- radicals trapped in alkali halides and azides and on the surface of MgO, we assume $A_{yy} > 0$, while A_{xx} and $A_{zz} < 0$. This choice leads to a positive a_{iso}, in agreement with the results of theoretical modelling (*vide infra*).

The hyperfine tensor can thus be decomposed as follows:

$$^{N}A = \begin{vmatrix} -3.3 & & \\ & 22.2 & \\ & & -5.4 \end{vmatrix} = 4.5 + \begin{vmatrix} 1.4 & & \\ & -0.7 & \\ & & -0.7 \end{vmatrix} + \begin{vmatrix} -9.2 & & \\ & 18.4 & \\ & & -9.2 \end{vmatrix} \tag{9.5}$$

whereby the $\boldsymbol{T}$ tensor derived from Eq. (9.5) has been decomposed into two traceless components (2a, $-a$, $-a$) and ($-b$, 2b, $-b$) accounting for a partial admixture of the π_x and π_y orbitals via spin–orbit interactions. The largest value of the hyperfine tensor corresponds to the y direction determined by π^*_y, *i.e.*, the orbital constituting the SOMO.

Using the reported atomic value [371] of the dipolar ^{14}N constant as $B^o = 4/5 g_N \beta_n \langle r^{-3} \rangle_{2p}$ = 39.6 G, the spin density on the nitrogen 2p orbitals can be

assessed by direct comparison of the experimental *a* and *b* values to the atomic anisotropic coupling constant of nitrogen using the classic formula $\rho_{2p_y} = c^2_{2p_y} = b / B°$ and $\rho_{2p_x} = c^2_{2p_x} = a / B°$. The total spin density on the N_2^- molecule will be given by $\rho(N)_{total} = 2\left[\rho_{2p_x} + \rho_{2p_y} + c^2_{2s}\right] = 0.99$ indicating that the total spin density on the N atoms is close to unity. We remark that the N_2^- anion is positively charged with respect to the MgO lattice; therefore a compensation mechanism needs to be present. A possible pattern can be provided by transition metal ion impurities present in the sample. In particular the drastic reduction in the intensity of the EPR signal of Cr^{3+} upon oxidation of Mg_3N_2 (see Fig. 9.2) may be taken as indicative of such a compensation pathway.

The powder EPR spectra discussed so far do not allow the relation between the magnetic and crystallographic axes to be obtained; therefore no information on the geometrical arrangement of the radical within the crystal can be obtained. This limitation can be overcome by comparing experimental and computed spin Hamiltonian parameters on a suitable theoretical model (see Fig. 9.5 and Table 9.2).

In Table 9.2 we also report the computational results related to a similar system, N_2^- in KCl, which have been recently reported by Di Valentin and Pacchioni [499] and is discussed here for further analysis.

Table 9.2. Theoretical (B3LYP) and Experimental EPR parameters for N_2^- species in bulk MgO and KCl matrices.[a]

MgO	g_{xx}	g_{yy}	g_{zz}	a_{iso}	T_{xx}	T_{yy}	T_{zz}
Exp.	2.0043	2.0021	1.9833	4.5	-7.8	17.7	-9.9
N_2^-	2.0041	2.0023	1.9873	6.4	-8.5	16.7	-8.1
N_2^{-*} (+0.83 eV)[b]				7.1	16.8	-8.6	-8.2
KCl							
Exp.	1.9978	2.000	1.9065	3.4	17.9	-9.5	-8.4
N_2^-	2.0020	2.0067	1.9565	6.6	15.8	-8.1	-7.6
N_2^{-*} (+0.18 eV)[b]				8.0	-8.7	16.8	-8.2

[a] The *x*, *y* and *z* directions correspond to the [001], [1-10] and [110] crystallographic axis, respectively, for both the ***g*** and ***T*** tensors. The N_2^- internuclear axis is oriented along the [110] direction. The *x* and *y* assignment to the *g* and *T* matrix elements for the MgO powder samples has been done on the basis of the theoretical results. The axis orientations are defined in Fig. 9.5. Hyperfine coupling constants are in G.

[b] Differences in energy and ***T*** tensors are reported for the first N_2^- excited state in both MgO and KCl where the extra electron is in the perpendicular N_2 π^* state with respect to the ground state. See text for further details.

Calculations of N_2^- in bulk MgO confirm that the configuration with the N–N internuclear axis parallel to the [110] direction is more stable by 0.5 eV than the one oriented along the [100] direction. This energy difference is considerably larger than that previously found for N_2^- in KCl (30 meV) [499]. This is a relevant indication that the N_2^- species is free to rotate in KCl while is much less mobile in MgO where the lattice constant is smaller (~4.2 vs ~6.3 Å). Another important difference with respect to the N_2^- species in KCl is the molecular orbital hosting the unpaired electron: in KCl it is well established, on the basis of single crystal EPR measurements, that this electron occupies the π^* state lying in the *xz* plane, π_x^* (see Fig. 9.5 for axis orientation) [489].

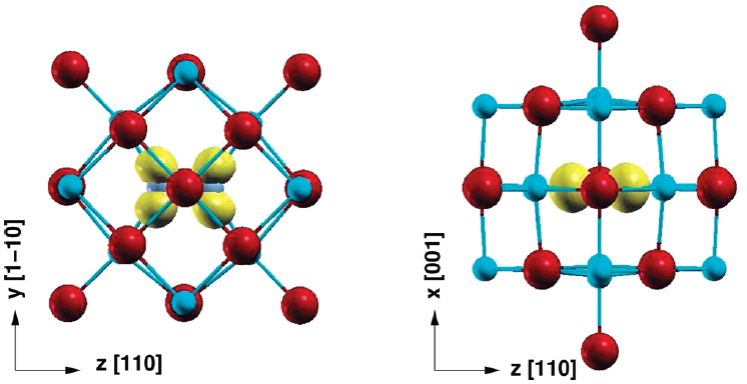

Figure 9.5. Top and side views of a N_2^- species in the bulk MgO as derived from cluster model DFT calculations. The spin density plot associated to the unpaired electron is shown. Magnesium atoms are in light blue, oxygen atoms in red and nitrogen atoms in grey.

This result is corroborated by theoretical calculations which indicate this as the ground state [499]. The configuration where the π_y^* orbital is occupied corresponds to the first excited state. On the contrary, in the case of MgO, in the ground state the unpaired electron is found to occupy the π^* level lying in the *yz* plane, π_y^*; in the first excited state the electron is in the π_x^* orbital. Thus, according to the DFT calculations the nature of the ground state is reversed in N_2^-/MgO and N_2^-/KCl. Unfortunately, the EPR experiments on polycrystalline MgO do not allow us to assign the component (*x* or *y*) of the π^* state where the unpaired electron resides. Therefore, in Table 9.2 the assignment has been done on the basis of the computational evidence.

In order to improve our understanding of this unexpected result, we

computed the first excited states for the two cases (see Table 9.2). The reported values have been determined as the total energy difference between ground and excited doublet Π state (vertical transition energy): 0.18 eV (N_2^-/KCl) and 0.83 eV (N_2^-/MgO). Notice that the energy required to switch the electron from one π^* state to the other is very different in the two cases, and in particular that the excitation energy in KCl is 4.6 times larger than in MgO. The $\pi_x^* - \pi_y^*$ excitation energy represents an estimate of the crystal field splitting Δ in these systems. It is interesting to introduce the computed Δ values in the simplified version of Eq. (9.2), $g_{zz} \approx g_e - 2\,\lambda/\Delta$, and estimate the g_{zz} component according to perturbation theory. This can then be compared with the experimental value and with the *g*-value computed *ab initio* using the approach by Neese [193] (see Table 9.2). Using $\lambda(N) = 74.2$ cm^{-1}, from Eq. (9.2) we obtain $g_{zz} = 1.9801$ for N_2^- in MgO and $g_{zz} = 1.9001$ for N_2^- in KCl. The experimental value measured for N_2^- in MgO is thus reproduced quantitatively both by a simplified perturbation theory approach, Eq. (9.2), and by an *ab initio* estimate (see Table 9.2). For N_2^- in KCl, however, the simplified approach provides a quantitative reproduction of the *g* value, 1.9001 (calc.) versus 1.9065 (exp.), while the *ab initio* result, 1.9565, Table 9.2, is only in qualitatively agreement.

This result indicates two things. First of all, g_{zz} of trapped N_2^- is a direct, powerful measure of the different crystal field strength in MgO and KCl and the different shift calculated and measured is directly related to the splitting of the π^* levels generated by the field. In particular, the *g*-shift and the splitting of the π^* orbitals are about 5 times larger in MgO than in KCl. Two factors contribute to this result: the shorter cation–anion distances and the larger nominal charges in MgO compared to KCl. Furthermore, while the π_y^* lobe points directly toward positive cations of the lattice, this is not the case for the π_x^* lobe (see Fig. 9.5). The second observation is that apparently a simplified approach based on perturbation theory, Eq. (9.2), provides a better description of the g_{zz} component than a fully *ab initio* approach. However, one should notice that this result can be partly fortuitous and that the shift in g_{zz} value goes as $1/\Delta$ so that for nearly degenerate π orbitals and small Δ values, as in N_2^-/KCl, small errors comparable in size with the intrinsic accuracy of the method, ±0.05 eV, may result in substantial *g*-shifts. The fact that the crystal field splitting is larger in MgO (with a consequent lower degree of mixing between ground and excited states) makes the use of a single determinant DFT approach more appropriate than for other nearly degenerate systems such as

N_2^- or O_2^- in KCl [489,499].

As a final remark we briefly comment on the excellent agreement between computed and experimental EPR hyperfine coupling constants (see Table 9.2). These quantities are very well described in both the isotropic and dipolar component for both MgO and KCl radicals. Altogether, the reproduction of the EPR parameters, ***g*** tensor and ***T*** tensor, for the system considered in this study, N_2^-/MgO can be considered excellent, showing the power of a combined theoretical–experimental approach for the characterization of these systems.

9.4 Conclusions

The oxidation of magnesium nitride, Mg_3N_2, results in the formation of polycrystalline MgO with NaCl cubic structure characterized by the presence of a number of defect centres. Among these, N_2^- molecular anions are clearly identified by a combination of CW and pulsed EPR experiments at 9.5 and 95 GHz and fully characterized in terms of electronic structure and spin distributions by a direct comparison of measured and computed EPR parameters. To this end DFT cluster model calculations have been performed.

The spin Hamiltonian parameters extracted from this study allow a direct comparison of the properties of this species with those of the analogous N_2^- species trapped in another ionic crystal, KCl allowing (a) to test the validity of *ab initio* methods to compute complex quantities like the ***g*** tensor of paramagnetic centres in solids and (b) to verify the information that can be extracted from EPR spectra, and in particular from the ***g*** tensor, on the strength of the crystal field of the host crystal.

The ground state of the molecule is found to be different in MgO and KCl as different components of the π^* orbitals are occupied in the oxide and in the chloride. Even more important, the computed separation between the ground state and the first excited state is much larger in MgO (about 0.8 eV) than in KCl (about 0.2 eV) in agreement with the different g_{zz} factors observed in the two host crystals. This effect is fully explained by first-order perturbation theory and well reproduced by *ab initio* values of the ***g*** tensor; it is consistent with the stronger crystal field of MgO due to a shorter lattice constant and to a larger formal charge of the ions.

Further study will be needed to understand the nature of $g = 2.035$ signal and the overall charge compensation mechanisms operating in the system.

CHAPTER 10

Summary and Conclusions

The aim of the work presented in this thesis was to provide insight into a number of properties influenced by defects and impurities in three doped metal oxides: zinc oxide, zirconium dioxide and magnesium oxide. A systematic study was carried out by means of a combined and multidisciplinary approach involving a localized basis sets method at the density functional theory level and a number of advanced experimental techniques. The effectiveness of the joint computational and experimental description at an atomistic level of a number of defects and related issues in semiconducting and insulating metal oxides is the major result of this work. The reliability of the method on different systems paves the way to successfully investigate almost every type of intrinsic and extrinsic defects in metal oxides providing fundamental informations for an effective defect engineering.

In the following we provide a summary of the main results achieved for the materials here investigated.

10.1 Zinc Oxide

Zinc oxide is a wide gap semiconductor with a post-synthesis unintentional *n*-type conductivity that severely hinders the achieving of *p*-type doping required for optoelectronics applications.

In Chapter 3, a number of well-known intrinsic (*i.e.*, oxygen vacancy, zinc

interstitial) and extrinsic (*i.e.*, hydrogen substitutional to oxygen and hydrogen interstitial) donors in zinc oxide have been addressed. The good agreement with previous plane-wave DFT studies and with available spectroscopic data has validated our theoretical approach to calculate optical, ε^{opt}, and thermodynamic, ε^{therm}, transition energy levels of bulk defects in different charge states. This method makes an efficient use of the Janak's theorem and allows a large simplification in the calculation of the transition energy levels using localized basis sets codes. Zinc interstitial and hydrogen impurities are confirmed to be shallow donor species, while oxygen vacancy induces deep donor states in the zinc oxide gap.

In Chapter 4, we provide an overview on the copper doped bulk ZnO. Substitutional copper to zinc is confirmed to be a deep acceptor defect and its hyperfine coupling tensor is computed for the first time. No significant magnetic order is found for this dopant on the basis of hybrid exchange-correlation functional calculations. Shallow donor states were experimentally observed upon the diffusion of copper particles, deposited on the O–ZnO $(000\bar{1})$ surface, into the bulk ZnO by a mild thermal treatment above room temperature. An ionization energy of 88 meV was measured through HREELS experiments (University of Bochum). Based on the very good agreement of this value with the computed thermodynamic transition energy level, we propose the shallow donor species to be interstitial copper in bulk ZnO. Finally, copper clustering is found to be favoured at a high impurity concentration since it reduces the cost of doping.

In Chapter 5, nitrogen doping is investigated on both polycrystalline and single crystal ZnO samples. In the former case, nitrogen defects were achieved upon annealing under ammonia atmosphere and studied through continuous wave and pulsed EPR measurements (University of Turin). Two nitrogen paramagnetic species were observed, namely, a monomeric and a dimeric species. In particular, the nature of the monomeric defect has been deeply investigated and characterized by the hyperfine and quadrupole coupling tensors, obtained from HYSCORE experiments. Different modes of insertion of nitrogen in the bulk of ZnO have been tested by means of DFT calculations. On the basis of the larger thermodynamic stability and the good agreement with the experimental EPR parameters, the monomeric species has been assigned to a nitrogen ion substituting a lattice oxygen ion.

Nitrogen doping was also achieved on the ZnO $(10\bar{1}0)$ surface upon ammonia sputtering followed by an oxidation treatment (University of

Bochum). The latter was proved to be crucial for breaking residual nitrogen-hydrogen bonds in the bulk sample by TDS measurements. Two optical transition levels of nitrogen species have been observed by HREEL spectroscopy at 0.8 eV and 2.7 eV. They have been attributed to an isolated nitrogen species and to a NH_x species, respectively. The calculation of the transition energy levels indicates that nitrogen produces deep acceptor levels in the gap in agreement with previous studies [365,366]. This would exclude nitrogen doping as a viable route to achieve *p*-type conductivity in ZnO. However, the bad agreement of computed transition levels with the HREELS data is still an open question. Taking into account also the unexpected negative *g* shift for the nitrogen monomeric species identified in the polycrystalline sample, our assignment of nitrogen impurities to nitrogen ions substituting lattice oxygen ions should be considered as tentative. Other theoretical models are currently under investigation in order to definitely settle the issue.

In Chapter 6 the reactivity of ZnO surfaces toward the only reagent capable of providing nitrogen doping in post-synthesis processes, *i.e.* ammonia, has been investigated for different coverages and samples (*i.e.* powder and single crystal). A good agreement between computed vibrational frequencies and IR-bands and electron energy loss peaks has allowed a thorough assignment of the adsorbates on the non polar mixed-terminated ZnO $(10\bar{1}0)$ surface. While at low coverage ammonia adsorbs molecularly, for the full monolayer coverage it is found to form an ordered adlayer with (2 x 1) periodicity presenting alternating molecular NH_3 and singly deprotonated NH_2 moieties adsorbed on cationic sites. The adsorption enthalpy has been observed to decrease with the coverage and this proves that the repulsive interactions between adsorbates are higher than attractive electrostatic interactions (*i.e.*, hydrogen bonds). Therefore repulsive interactions are probably the driving force for partial NH_3 dissociation at full coverage.

10.2 Zirconium Dioxide

The high-temperature tetragonal polymorph of zirconium dioxide is generally stabilized by impurities and finds a number of advanced technologically applications spanning from photocatalysis to gate dielectric material in metal-oxide semiconductor devices.

In Chapter 7 the titanium doping of tetragonal zirconium dioxide has been studied in order to rationalize the experimentally observed large band gap red-

shift of 1.3 eV. Substitutional and interstitial impurities have been investigated through hybrid functional calculations. While for interstitial titanium we observe defect states in the middle of the band gap, for a titanium ion substitutional to a zirconium lattice ion we observe a number of empty d-states just below the conduction band maximum (0.4 eV in a 5.7 eV computed band gap). Diluted and well-separated impurities are found to be favoured with respect to the formation of TiO_2 nano-phases. The calculation of the optical transition levels for a concentration of about 15% of titanium substitutional, comparable with the experimental one, provides computed optical absorption of 4.9 eV. The shift with respect to the pure ZrO_2 is of about 0.8 eV which is in broad agreement with the experimentally observed optical shift of 1.3 eV. The discrepancy between experimental and computed values of the absorption shift may be due to excitonic effects which are not taken into account in the present approach. Finally, we observe an electron transfer from neutral oxygen vacancy to a Ti^{4+} centre with formation of a Ti^{3+} species. Since the energy cost for the formation of an oxygen vacancy significantly decreases in the presence of the dopant (from 6.2 eV to 5.7 eV), Ti doping is predicted to favour oxygen deficiency.

10.3 Magnesium Oxide

The nitrogen doping of magnesium oxide has been recently proposed as a potential route to achieve room temperature ferromagnetism.

In Chapter 8 nitrogen impurities in bulk magnesium oxide have been investigated in different modes of insertion, namely substitutional and interstitial. In both cases, the defects are paramagnetic with a high degree of spin localization that may disfavour the formation of a ferromagnetic order at room temperature. The hyperfine coupling tensors are very similar so that the distinction of the two defect centres, based on EPR spectra only, is not definitive. The possible interaction with intrinsic defects, namely magnesium and oxygen vacancies, has also been considered. In both cases, an electron transfer has been observed and specifically nitrogen impurities behave as donors in the presence of magnesium vacancy and as acceptors in the presence of oxygen vacancy.

In Chapter 9 a trapped N_2^- radical anion has been indentified and investigated in a polycrystalline magnesium oxide sample achieved upon oxidation of magnesium nitride (University of Turin). A thorough

characterization of its electronic structure has been provided through continuous wave and pulsed EPR experiments at 9.5 and 95 GHz, in conjunction with quantum mechanical calculations. A theoretical comparison of the spin Hamiltonian parameters of the N_2^- radical anion obtained in this work with the analogous N_2^- species trapped in KCl has been performed in order to validate the *ab initio* method and to verify the information that can be extracted from EPR spectra (*e.g.*, the strength of the crystal field of the host crystal). The different g_{zz} factors, observed in the two host crystals, are found to agree with the different computed separation between the ground state and the first excited state in MgO (about 0.8 eV) and in KCl (about 0.2 eV). This effect is consistent with the stronger crystal field of MgO due to a shorter lattice constant and to a larger formal charge of the ions.

Publications

1. F. Gallino, G. Pacchioni, C. Di Valentin, *J. Chem. Phys.: "Transition levels of defect centers in ZnO by hybrid functionals and localized basis set approach",* **2010**, 133, 144512.

2. H. Qiu, F. Gallino, C. Di Valentin, Y. Wang, *Phys. Rev. Lett.*: *"Shallow donor states induced by in-diffused Cu in ZnO: a combined HREELS and hybrid DFT study"*, **2011**, 106, 066401.

3. F. Gallino, C. Di Valentin, *J. Chem. Phys*.: *"Copper Impurities In Bulk ZnO: A Hybrid DFT Study"*, **2011**, 134, 144506.

4. F. Gallino, C. Di Valentin, G. Pacchioni, M. Chiesa, E. Giamello, *J. Mater. Chem.: "Nitrogen impurity states in polycrystalline ZnO. A combined EPR and theoretical study",* **2010**, 20, 689.

5. F. Gallino, H. Noei, L. Jin, C. Di Valentin, Y. Wang, *"Combined Theoretical and Experimental Study on Nitrogen Doping of Zinc Oxide", in preparation.*

6. H. Noei, F. Gallino, L. Jin, C. Di Valentin, Y. Wang, *"Ammonia Adsorption on the ZnO (10-10) Surface", submitted.*

7. F. Gallino, C. Di Valentin, G. Pacchioni, *Phys. Chem. Chem. Phys.: "Band gap engineering of bulk ZrO_2 by Ti doping"*, **2011**, 13, 17667.

8. M. Pesci, F. Gallino, C. Di Valentin, G. Pacchioni, *J. Phys. Chem. C: "Nature of Defect States in Nitrogen-Doped MgO",* **2010**, 114, 1350.

9. F. Napoli, M. Chiesa, E. Giamello, M. Fittipaldi, C. Di Valentin, F. Gallino, G. Pacchioni, *J. Phys. Chem. C: "N_2^- Radical Anions Trapped in Bulk Polycrystalline MgO"*, **2010**, 114, 5187.

Bibliography

[1] V. E. Heinrich, P. A. Cox, *The Surface Science of Metal Oxides*, (Cambridge University Press, Cambridge, **1994**).
[2] P. A. Cox, *Transition Metal Oxides*, (Oxford University Press, Oxford, **1993**).
[3] J. L. G. Fierro, *Metal Oxides: Chemistry and Applications*, (CRC Press, Taylor & Francis Group, Boca Raton, **2006**).
[4] C. Noguera, *Physics and Chemistry at Oxide Surfaces*, (Cambridge University Press, Cambridge, **1996**).
[5] C. N. R. Rao, B. Raveau, *Transition Metal Oxides*, (Wiley-VCH, New York, **1998**).
[6] J. G. Bednorz, K. A. Müller, *Z. Physik*, **1986**, B64, 180.
[7] S. F. Matar, G. Campet, M. A. Subramanian, *Prog. Solid State Ch.*, **2011**, 39, 70.
[8] L. Pauling, *J. Am. Chem. Soc*., **1932**, 54, 3570.
[9] J. Mullay, *Struct. Bond*, **1987**, 66, 1.
[10] R. G. Pearson, *J. Am. Chem. Soc*., **1963**, 85, 3533.
[11] R. G. Pearson, *J. Chem. Educ*., **1999**, 76, 267.
[12] E. G. Seebauer, M. C. Kratzer, *Mater. Sci. Eng. R*, **2006**, 55, 57.
[13] S. B. Ogale, *Adv. Mater*., **2010**, 22, 3125.
[14] J. W. Fergus, *J. Mater. Sci*., **2003**, 38, 4259.
[15] Y. Zhang, A. Kolmakov, S. Chretien, H. Metiu, M. Moskovits, *Nano Lett*., **2004**, 4, 403.
[16] W. Baiqi, J. Liqiang, Q. Yichun, L. Shudan, J. Baojiang, Y. Libin, X. Baifu, F. Honggang, *Appl. Surf. Sci*., **2006**, 252, 2817.
[17] S. M. Hu, *Mater. Sci. Eng. R*, **1994**, 13, 105.
[18] M. Y. L. Jung, C. T. M. Kwok, R. D. Braatz, E. G. Seebauer, *J. Appl. Phys*., **2005**, 97, 063520.
[19] S. Guha, J. M. Depuydt, M. A. Haase, J. Qiu, H. Cheng, *Appl. Phys. Lett*., **1993**, 63, 3107.
[20] S. R. Kurtz, A. A. Allerman, E. D. Jones, J. M. Gee, J. J. Banas, B. E. Hammons, *Appl. Phys. Lett*., **1999**, 74, 729.
[21] E. C. Jones, E. Ishida, *Mater. Sci. Eng. R*, **1998**, 24, 1.
[22] C. Kilic, A. Zunger, *Appl. Phys. Lett*., **2002**, 81, 73.
[23] I. Tanaka, K. Tatsumi, M. Nakano, H. Adachi, F. Oba, *J. Am. Ceram. Soc.*, **2002**, 85, 68.
[24] C. G. Van de Walle, *Phys. Rev. Lett*., **2000**, 85, 1012.
[25] C. Kittel, A. H. Mitchell, *Phys. Rev*., **1954**, 96, 1488.
[26] J. M. Luttinger, W. Kohn, *Phys. Rev.*, **1955**, 97, 869.
[27] P. R. C. Kent, A. Zunger, *Phys. Rev. Lett*., **2001**, 86, 2613.
[28] P. R. C. Kent, A. Zunger, *Phys. Rev. B*, **2001**, 64, 115208.
[29] M. Stavola, *Identification of Defects in Semiconductors*, *Semiconductors and Semimetals*, vol 51B (Academic Press, San Diego, **1999**).

[30] A. Janotti, C. G. Van de Walle, *Rep. Prog. Phys*., **2009**, 72, 126501.
[31] M. D. McCluskey, S. J. Jokela, *J. Appl. Phys*., **2009**, 106, 071101.
[32] P. M. Mooney, *J. Appl. Phys*., **1990**, 67, R1.
[33] S. B. Zhang, S.-H. Wei, A. Zunger, *Phys. Rev. Lett.*, **2000**, 84, 1232.
[34] S. B. Zhang, S.-H. Wei, A. Zunger, *J. Appl. Phys.*, **1998**, 83, 3192.
[35] K. Honda, A. Fujishima, *Nature*, **1972**, 238, 37.
[36] Z. Zou, J. Ye, K. Sayama, H. Arakawa, *Nature*, **2001**, 414, 625.
[37] M. R. Hoffmann, S. T. Martin, W. Choi, D. W. Bahnemann, *Chem. Rev*., **1995**, 95, 69.
[38] D. Robert, S. Malato, *Sci. Total Environ*., **2002**, 291, 85.
[39] X. Chen, Y. Lou, S. Dayal, X. Qiu, R. Krolicki, C. Burda, C. Zhao, J. Becker, *Nanosci. Nanotechnol.*, **2005**, 5, 1408.
[40] C. Burda, Y. Lou, X. Chen, A. C. S. Samia, J. Stout, J. Gole, *NanoLett.*, **2003**, 3, 1049.
[41] X. Chen, C. Burda, *J. Phys. Chem. B*, **2004**, 108, 15446.
[42] X. Chen, Y. Lou, A. C. S. Samia, C. Burda, J. L. Gole, *Adv. Funct. Mater.*, **2005**, 15, 41.
[43] C. Di Valentin, E. Finazzi, G. Pacchioni, A. Selloni, S. Livraghi, M. C. Paganini, E. Giamello, *Chem. Phys.*, **2007**, 339, 44.
[44] A. M. Smith, S. Nie, *Acc. Chem. Res.*, **2010**, 43, 190.
[45] J. Osorio-Guillén, S. Lany, S. V. Barabash, A. Zunger, *Phys. Rev. Lett.*, **2006**, 96, 107203.
[46] P. Mahadevan, A. Zunger, D. Sarma, *Phys. Rev. Lett*., **2004**, 93, 177201.
[47] A. Franceschetti, S. V. Didiy, S. V. Barabash, A. Zunger, J. Xu, M. van Schilfgaarde, *Phys. Rev. Lett*., **2006**, 97, 047202.
[48] Y. Matsumoto, *Science*, **2001**, 291, 854.
[49] T. Fukumura, Z. Jin, A. Ohtomo, H. Koinuma, M. Kawasaki, *Appl. Phys. Lett.*, **1999**, 75, 3366.
[50] M. Venkatesan, C. B. Fitzgerald, J. G. Lunney, J. M. D. Coey, *Phy.Rev. Lett.*, **2004**, 93, 177206.
[51] T. Dietl, H. Ohno, F. Matsukura, J. Cibert, D. Ferrand, *Science*, **2000**, 287, 1019.
[52] T. Dietl, *Semicond. Sci. Technol*., **2002**, 17, 377.
[53] A. Zunger, S. Lany, H. Raebiger, *Phys.*, **2010**, 3, 53.
[54] E. A. Carter, *Science*, **2008**, 321, 800.
[55] P. Huang, E. A. Carter, *Annu. Rev. Phys. Chem.*, **2008**, 59, 261.
[56] C. J. Cramer, D. G. Truhlar, *Phys. Chem. Chem. Phys.*, **2009**, 11, 10757.
[57] C. R. A. Catlow, *Computer Modelling in Inorganic Crystallography*, (Academic Press, London, **1997**).
[58] M. Scheffler, *Lecture on: "Computational Materials Sciences from First Principles: Status, Achievements, Challenges"* (*DFT & Beyond, Hands-on Tutorial Workshop*, Berlin, **2011**).
[59] A. D. Becke, *J. Chem. Phys.*, **1993**, 98, 5648.
[60] C. Lee, W. Yang, R.G. Parr, *Phys. Rev. B*, **1988**, 37, 785.
[61] F. Corà, M. Alfredsonn, G. Mallia, D. S. Middlemiss, W. C. Mackrodt, R. Dovesi, R. Orlando, *Struct. Bond.*, **2004**, 113, 171.
[62] L. H. Tjeng, A. R. Vos, G. A. Sawatzky, *Surf. Sci.*, **1990**, 235, 269.
[63] N. B. Brookes, D. S.-L. Law, T. S. Padmore, D. R. Waeburton, G. Thorton, *Solid State Comm.*, **1986**, 57, 473.
[64] G. N. Raikar, P. J. Hardman, C. A. Muryn, G. van der Laan, P. L. Wincott, G. Thorton, D.

W. Bullett, *Solid State Comm.*, **1991**, 80, 423.
[65] P. J. Hardman, G. N. Raikar, C. A. Muryn, G. van der Laan, P. L. Wincott, G. Thorton, D. W. Bullett, P. A. D. M. A. Dale, *Phys. Rev. B*, **1994**, 49, 7170.
[66] U. Scherz, M. Scheffler, *Semicond. Semimetals*, **1993**, 38, 1.
[67] S. Lany, A. Zunger, *Phys. Rev. B*, **2008**, 78, 235104.
[68] C. G. Van de Walle, J. Neugebauer, *J. Appl. Phys*., **2004**, 95, 3851.
[69] R. Dovesi, R. Orlando, B. Civalleri, C. Roetti, V. R. Saunders, C. M. Zicovich-Wilson, *Z. Kristallogr*., **2005**, 220, 571.
[70] R. Dovesi, V. R. Saunders, C. Roetti, R. Orlando, C. M. Zicovich-Wilson, F. Pascale, B. Civalleri, K. Doll, N. M. Harrison, I. J. Bush, P. D'Arco, M. Llunell, *CRYSTAL 09 (CRYSTAL09 User's Manual)*, University of Torino, Torino, (**2009**).
[71] R. Dovesi, V. R. Saunders, C. Roetti, R. Orlando, C. M. Zicovich-Wilson, F. Pascale, B. Civalleri, K. Doll, N. M. Harrison, I. J. Bush, Ph. D'Arco, M. Llunell, *CRYSTAL 06 (CRYSTAL06 User's Manual)*, University of Torino, Torino, (**2006**).
[72] J. F. Janak, *Phys. Rev. B*, **1978**, 18, 7165.
[73] M. Born, R. Oppenheimer, *Ann. Phys.*, **1927**, 84, 0457.
[74] R. G. Parr, W. Yang, *Density-functional theory of atoms and molecules*, (Oxford University Press, New York, **1989)**.
[75] W. Koch, M. C. Holthausen, *A Chemist's Guide to Density Functional Theory* 2nd ed., (Wiley-VCH, Heidelberg, **2001)**.
[76] P. Hohenberg, W. Kohn, *Phys. Rev.*, **1964**, 136, B864.
[77] Y. A. Wang, N. Govind, E. A. Carter, *Phys. Rev. B*, **1999**, 60, 16350.
[78] S. S. Iyengar, M. Ernzerhof, S. N. Maximoff, G. E. Scuseria, *Phys. Rev. A*, **2001**, 63, 052508.
[79] W. Kohn, L. J. Sham, *Phys. Rev.*, **1965**, 140, 1133.
[80] S. Kurth, J. P. Perdew, P. Blaha, *Int. J. Quant. Chem.*, **1999**, 75, 889.
[81] J. P. Perdew, A. Ruzsinszky, J. Tao, V. N. Staroverov, G. E. Scuseria, G. I. Csonka, *J. Chem. Phys.*, **2005**, 123, 062201.
[82] F. Della Sala, *Lecture on: "Exchange-Correlation functionals for the ground state: from LDA up to the Optimized Effective Potential method"* (*DFT & Beyond, Hands-on Tutorial Workshop*, Berlin, **2011**).
[83] G. E. Scuseria, V. N. Staroverov, *Theory and Applications of Computational Chemistry: The First Forty Years*, (Elsevier, Amsterdam, **2005)**.
[84] J. P Perdew, S. Kurth, *A Primer in Density Functional Theory*, (Spinger-Verlag, Berlin, **2003**).
[85] E. J. Baerends, O. V. Gritsenko, *J. Phys. Chem. A*, **1997**, 101, 5383.
[86] J. P. Perdew, *Density Functional Theory of Molecules, Clusters, and Solids*, (Kluwer, Dordrecht, **1995**).
[87] J. P. Perdew, J. A. Chevary, S. H. Vosko, K. A. Jackson, M. R. Pederson, D. J. Singh, C. Fiolhais, *Phys. Rev. B*, **1992**, 46, 6671.
[88] J. P. Perdew, K. Burke, M. Ernzerhof, *Phys. Rev. Lett.*, **1996**, 77, 3865.
[89] B. Miehlich, A. Savin, H. Stoll, H. Preuss, *Chem. Phys. Lett.*, **1989**, 157, 200.
[90] Y. Zhang, W. Yang, *Phys. Rev. Lett*., **1998**, 80, 890.
[91] B. Hammer, L. B. Hansen, J. K. Norskov, *Phys. Rev. B*, **1999**, 59, 7413.

[92] J. P. Perdew, A. Zunger, *Phys. Rev. B*, **1981**, 23, 5048.
[93] R. Van Leeuwen, E. J. Baerends, *Phys. Rev. A*, **1994**, 49, 2421.
[94] J. P. Perdew, R. G. Parr, M. Levy, J. L. Jr. Balduz, *Phys. Rev. Lett.*, **1982**, 49, 1691.
[95] W. Yang, Y. Zhang, P. W. Ayers, *Phys. Rev. Lett*., **2000**, 84, 5172.
[96] M. J. Allen, D. J. Tozer, *Mol. Phys.*, **2002**, 100, 433.
[97] T. Grabo, T. Kreibich, S. Kurth, E. K. U. Gross, *Strong Coulomb Correlation in Electronic Structure: Beyond the Local Density Approximation*, (Gordon & Breach, Tokyo, **2000**).
[98] E. Engel, *A Primer in Density Functional Theory*, (Springer, Berlin, **2003**).
[99] A. D. Becke, *J. Chem. Phys*., **1998**, 109, 2092.
[100] T. van Voorhis, G. E. Scuseria, *J. Chem. Phys.*, **1998**, 109, 400.
[101] J. P. Perdew, S. Kurth, A. Zupan, P. Blaha, *Phys. Rev. Lett*., **1999**, 82, 2544.
[102] J. P. Perdew, *Chem. Phys. Lett.*, **1979**, 64, 127.
[103] A. Svane, O. Gunnarsson, *Phys. Rev. Lett.*, **1990**, 65, 1148.
[104] P. Strange, A. Svane, W.M. Temmerman, Z. Szotek, H. Winter, *Nature*, **1999**, 399, 756.
[105] D. Cremer, *Mol. Phys*., **2001**, 99, 1899.
[106] D. Cremer, M. Filatov, V. Polo, E. Kraka, S. Shaik, *Int. J. Mol. Sci*., **2002**, 3, 604.
[107] V. Polo, E. Kraka, D. Cremer, *Mol. Phys*., **2002**, 100, 1771.
[108] V. Polo, E. Kraka, D. Cremer, *Theor. Chem. Acc*., **2002**, 107, 291.
[109] J. Gräfenstein, E. Kraka, D. Cremer, *Phys. Chem. Chem. Phys*., **2004**, 6, 1096.
[110] J. Harris, *Phys. Rev. A*, **1984**, 29, 1648.
[111] A. D. Becke, *J. Chem. Phys*., **1993**, 98, 1372.
[112] O. Sinanoğlu, *Adv. Chem. Phys*., **1964**, 6, 358.
[113] D. K. W. Mok, R. Neumann, N. C. Handy, *J. Phys. Chem*., **1996**, 100, 6225.
[114] O. V. Gritsenko, P. R. T. Schipper, E. J. Baerends, *J. Chem. Phys*., **1997**, 107, 5007.
[115] V. N. Staroverov, G. E. Scuseria, J. Tao, J. P. Perdew, *J. Chem. Phys*., **2003**, 119, 12129.
[116] M. Ernzerhof, G. E. Scuseria, *J. Chem. Phys*., **1999**, 110, 5029.
[117] A. D. Boese, N.C. Handy, *J. Chem. Phys*., **2002**, 116, 9559.
[118] J. Heyd, G. E. Scuseria, M. Ernzerhof, *J. Chem. Phys*., **2003**, 118, 8207; **2006**, 124, 219906.
[119] J. Heyd, G.E. Scuseria, *J. Chem. Phys*., **2004**, 120, 7274; **2004**, 121, 1187.
[120] A. V. Krukau, O. A. Vydrov, A. F. Izmaylov, G. E. Scuseria, *J. Chem. Phys*., **2006**, 125, 224106.
[121] E. R. Batista, J. Heyd, R. G. Hennig, B. P. Uberuaga, R. L. Martin, G. E. Scuseria, C. J. Umrigar, J. W. Wilkins, *Phys. Rev. B*, **2006**, 74, 121102.
[122] J. Paier, M. Marsman, K. Hummer, G. Kresse, I. C. Gerber, J.G. Ángyán, *J. Chem. Phys*., **2006**, 124, 154709; **2006**, 125, 249901.
[123] J. P. Perdew, K. Schmidt, *Density Functional Theory and Its Application to Materials*, (AIP, New York, **2001**).
[124] J. Jaramillo, G. E. Scuseria, M. Ernzerhof, *J. Chem. Phys*., **2003**, 118, 1068.
[125] A. Görling, M. Levy, *Phys. Rev. B*, **1993**, 47, 13 105.
[126] A. Görling, M. Levy, *Phys. Rev. A*, **1994**, 50, 196.
[127] A. Görling, M. Levy, *Int. J. Quantum Chem*., **1995**, 29, 93.
[128] D. C. Langreth, J. P. Perdew, *Solid State Commun*., **1975**, 17, 1425.
[129] D. C. Langreth, J. P. Perdew, *Phys. Rev. B*, **1977**, 15, 2884.

[130] M. Fuchs, X. Gonze, *Phys. Rev. B*, **2002**, 65, 235109.
[131] A. I. Liechtenstein, V. I. Anisimov, J. Zaanen, *Phys. Rev. B*, **1995**, 52, R5467.
[132] V. I. Anisimov, F. Aryasetiawan, A. I. Liechtenstein, J. Phys.: Condens. Matter, **1997**, 9, 767.
[133] V. I. Anisimov, O. Gunnarsson, *Phys. Rev. B*, **1991**, 43, 7570.
[134] C. Pisani, R. Dovesi, *Intern. J. Quantum Chem*., **1980**, 17, 501.
[135] C. Pisani, R. Dovesi, C. Roetti, *Hartree-Fock ab-initio Treatment of Crystalline Systems: Lecture Notes in Chemistry*, Vol. 48 (Springer, Heidelberg, **1988**).
[136] E. Clementi, J. Mehl, *IBMOL 5 Program User's Guide*, (Publication RJ889, IBM Corporation **1971**).
[137] D. J. Hehre, W. A. Lathan, M. D. Newton, R. Ditchfield, A. Pople, *GAUSSIAN70 Program Number 236*, (QCPE, Indiana University, Bloomington, Indiana **1972**).
[138] M. Dupuis, D. Spangler, J. Wendoloski, *NRCC Software Catalog, Vol. 1, Program No. QG01 (GAMESS)* (**1980**).
[139] J. C. Slater, *Phys. Rev*., **1951**, 81, 385.
[140] S. H. Vosko, L. Wilk, M. Nusair, *Can. J. Phys.*, **1980**, 58, 1200.
[141] J. P. Perdew, Y. Wang, *Phys. Rev. B*, **1992**, 45, 13244.
[142] J. P. Perdew, A. Ruzsinsky, G. I. Csonka, O. A. Vydrov, G. E. Scuseria, L. A. Constantin, X. Zhou, K. Burke, *Phys. Rev. Lett*., **2008**, 100, 136406.
[143] Y. Zhao, D. G. Truhlar, *J. Chem. Phys*., **2008**, 128, 184109.
[144] Z. Wu, R. Cohen, *Phys. Rev. B*, **2006**, 73, 235116.
[145] J. Hafner, *J. Comput. Chem*., **2008**, 29, 2044.
[146] S. J. Clark, M. D. Segall, C. J. Pickard, P. J. Hasnip, M. J. Probert, K. Refson, M. C. Payne, *Z. Kristallogr*., **2005**, 220, 567.
[147] X. Gonze, B. Amadon, P.-M. Anglade, J. M. Beuken, F. Bottin, P. Boulanger, F. Bruneval, D. Caliste, R. Caracas, M. Cote, T. Deutsch, L. Genovese, P. Ghosez, M. Giantomassi, S. Goedecker, D. R. Hamann, P. Hermet, F. Jollet, G. Jomard, S. Leroux, M. Mancini, S. Mazevet, M. J. T. Oliveira, G. Onida, Y. Pouillon, T. Rangel, G. M. Rignanese, D. Sangalli, R. Shaltaf, M. Torrent, M. J. Verstraete, G. Zerah and J. W. Zwanziger, *Comput. Phys. Commun*., **2009**, 180, 2582.
[148] E. Hutter, M. Iannuzzi, *Z. Kristallogr*., **2005**, 220, 549.
[149] P. Pulay, *Mol. Phys*., **1969**, 17, 197.
[150] K. Doll, V. R. Saunders, N. M. Harrison, *Int. J. Quantum Chem*., **2001**, 82, 1.
[151] K. Doll, R. Orlando, R. Dovesi, *Theor. Chem. Acc*., **2006**, 115, 354.
[152] K. Doll, R. Dovesi, R. Orlando, *Theor. Chem. Acc*., **2004**, 112, 394.
[153] F. Pascale, C. M. Zicovich-Wilson, F. L. Gejo, B. Civalleri, R. Orlando, R. Dovesi, *J. Comput. Chem.*, **2004**, 25, 888.
[154] C. M. Zicovich-Wilson, F. J. Torres, F. Pascale, L. Valenzano, R. Orlando, R. Dovesi, *J. Comput. Chem*., **2008**, 29, 2268.
[155] S. Tosoni, F. Pascale, P. Ugliengo, R. Orlando, V. R. Saunders, R. Dovesi, *Mol. Phys.*, **2005**, 103, 2549.
[156] C. Pisani, S. Casassa, L. Maschio, M. Schütz, D. Usvyat, *CRYSCOR09 (CRYSCOR09 User's Manual)*, University of Torino, Torino (**2009**).
[157] B. Civalleri, Ph. D'Arco, R. Orlando, V. R. Saunders, R. Dovesi, *Chem. Phys. Lett.*, **2001**,

348**,** 131.
[158] M. J. Frisch, G. W. Trucks, H. B. Schlegel, G. E. Scuseria, M. A. Robb, J. R. Cheeseman, J. A. Jr. Montgomery, T. Vreven, G. Scalmani, B. Mennucci, V. Barone, G. A. Petersson, M. Caricato, H. Nakatsuji, M. Hada, M. Ehara, K. Toyota, R. Fukuda, J. Hasegawa, M. Ishida, T. Nakajima, Y. Honda, O. Kitao, H. Nakai, X. Li, H. P. Hratchian, J. E. Peralta, A. F. Izmaylov, K. N. Kudin, J. J. Heyd, E. Brothers, V. N. Staroverov, G. Zheng, R. Kobayashi, J. Normand, J. L. Sonnenberg, F. Ogliaro, M. Bearpark, P. V. Parandekar, G. A. Ferguson, N. J. Mayhall, S. S. Iyengar, J. Tomasi, M. Cossi, N. Rega, J. C. Burant, J. M. Millam, M. Klene, J. E. Knox, J. B. Cross, V. Bakken, C. Adamo, J. Jaramillo, R. Gomperts, R. E. Stratmann, O. Yazyev, A. J. Austin, R. Cammi, C. Pomelli, J. W. Ochterski, P. Y. Ayala, K. Morokuma, G. A. Voth, P. Salvador, J. J. Dannenberg, V. G. Zakrzewski, S. Dapprich, A. D. Daniels, M. C. Strain, O. Farkas, D. K. Malick, A. D. Rabuck, K. Raghavachari, J. B. Foresman, J. V. Ortiz, Q. Cui, A. G. Baboul, S. Clifford, J. Cioslowski, B. B. Stefanov, G. Liu, A. Liashenko, P. Piskorz, I. Komaromi, R. L. Martin, D. J. Fox, T. Keith, M. A. Al-Laham, C. Y. Peng, A. Nanayakkara, M. Challacombe, W. Chen, M. W. Wong, J. A. Pople, *GAUSSIAN03, Revision A.7*, Gaussian Inc.: Pittsburgh, PA (**2003**).
[159] B. G. Johnson, M. J. Fisch, *J. Chem. Phys*., **1994**, 100, 7429.
[160] W. J. Stevens, H. Basch, M. J. Krauss, *J. Chem. Phys*., **1984**, 81, 6026.
[161] B. G. Dick, A. W. Overhauser, *Phys. Rev.*, **1958**, 112, 90.
[162] P. V. Sushko, A. L. Shluger, R. C. Baetzold, C. R. A. Catlow, *J. Phys.: Condens. Matter*, **2000**, 12, 8257.
[163] J. P. Perdew, M. Levy, *Phys. Rev. Lett*., **1983**, 51, 1884.
[164] J. P. Perdew, M. Levy, *Phys. Rev. B*, **1997**, 56, 16021.
[165] S. Kümmel, L. Kronik, *Rev. Mod. Phys.*, **2008**, 80, 3.
[166] J. Muscat, A. Wander, N. M. Harrison, *Chem. Phys. Lett*., **2001**, 342, 397.
[167] M. Rohlfing, S. G. Louie, *Phys. Rev. Lett.*, **1998**, 80, 3320.
[168] K. Reuter, M. Scheffler, *Phys. Rev. B*, **2001**, 65, 035406.
[169] C. H. Patterson, *Phys. Rev. B*, **2006**, 74, 144432.
[170] P. Broqvist, A. Alkauskas, A. Pasquarello, *Phys. Rev. B*, **2009**, 80, 085114.
[171] A. Alkauskas, A. Pasquarello, *Physica B*, **2007**, 401-402, 670.
[172] M. Hedström, A. Schindlmayr, G. Schwarz, M. Scheffler, *Phys. Rev. Lett*., **2006**, 97, 226401.
[173] Note that: $\varepsilon^{\text{therm}}(+1/0) = \varepsilon^{\text{opt}}(+1/0) + E_{\text{rel}}$ and $\varepsilon^{\text{therm}}(0/-1) = \varepsilon^{\text{opt}}(0/-1) - E_{\text{rel}}$.
[174] D. C. Reynolds, D. C. Look, B. Jogai, C. W. Litton, G. Cantwell, W. C. Harsch, *Phys. Rev. B*, **1999**, 60, 2340.
[175] M. Leslie, M. J. Gillan, *J. Phys. C*, **1985**, 18, 973.
[176] G. Makov, M. C. Payne, *Phys. Rev. B*, **1995**, 51, 4014.
[177] F. Oba, A. Togo, I. Tanaka, J. Paier, G. Kresse, *Phys. Rev. B*, **2008**, 77, 245202.
[178] *CRC Handbook of Chemistry and Physics*, edited by D. R. Lide, 89th Ed. (CRC Press, Boca Raton, FL, **2008–2009**).
[179] A. Dwivedi, A.N. Cormack, *Philos. Mag.*, **1990**, 61, 1.
[180] C. M. Weinert, M. Scheffler, in *Defects in Semiconductors*, edited by H. J. von Bardeleben (Mater. Sci. Forum, 10–12, 25, **1986**).
[181] K. Reuter, M. Scheffler, *Appl. Phys. A*, **2004**, 78, 793.

[182] C. Stampfl, M. V. Ganduglia-Pirovano, K. Reuter, M. Scheffler, *Surf. Sci.*, **2002**, 500, 368.
[183] D.R. Stull, H. Prophet, *JANAF Thermochemical Tables*, 2nd ed. (U.S. National Bureau of Standards, Washington, DC, **1971**).
[184] V. V. Bannikov, I. R. Shein, A. L. Ivanovskii, *Tech. Phys. Lett.*, **2007**, 33, 541.
[185] I. S. Elfimov, S. Yunoki, G. A. Sawatzky, *Phys. Rev. Lett.*, **2002**, 89, 216403.
[186] K. Kenmochi, M. Seike, K. Sato, A. Yanase, H. Katayama-Yoshida, *Jpn. J. Appl. Phys.*, **2004**, 43, L934.
[187] V. Pardo, W. E. Pickett, *Phys. Rev. B*, **2008**, 78, 134427.
[188] A. Droghetti, C. D. Pemmaraju, S. Sanvito, *Phys. Rev. B*, **2008**, 78, 140404(R).
[189] I. S. Elfimov, A. Rusydi, S. I. Csiszar, Z. Hu, H. H. Hsieh, H. J. Lin, C. T. Chen, R. Liang, G. A. Sawatzky, *Phys. Rev. Lett.*, **2007**, 98, 137202.
[190] G. Pacchioni, F. Frigoli, D. Ricci, J. A. Weil, *Phys. Rev. B*, **2001**, 63, 054102.
[191] J. A. Weil, J. R. Bolton, J. E. Wertz, *Electron Paramagnetic Resonance*, (John Wiley & Sons, New York, **1994**).
[192] P. Pyykkö, *Mol. Phys.*, **2008**, 106, 1965.
[193] F. Neese, *J. Chem. Phys.*, **2001**, 115, 11080.
[194] P. Canepa, R. M. Hanson, P. Ugliengo, M. Alfredsson, *J. Appl. Cryst.*, **2011**, 44, 225.
[195] S. Tosoni, F. Pascale, P. Ugliengo, R. Orlando, V. R. Saunders, R. Dovesi, *Chem. Phys. Lett.*, **2004**, 396, 308.
[196] M. Merawa, P. Labeguerie, P. Ugliengo, K. Doll, R. Dovesi, *Chem. Phys. Lett.*, **2004**, 387, 453.
[197] P. Ugliengo, *ANHARM-A program to solve monodimensional Schrödinger equation*, **1989**, *unpublished.*
[198] S. F. Boys, F. Bernardi, *Mol. Phys.*, **1970**, 19, 553.
[199] L. Valenzano, B. Civalleri, S. Chavan, G. T. Palomino, C. O. Areán, S. Bordiga, *J. Phys. Chem.*, **2010**, 114, 11185.
[200] N. M. Atherton, *Principles of Electron Paramagnetic Resonance*, (Ellis Horwood PTR Pretince Hall, Physical Chemistry Series, U.K., **1993**).
[201] A. Schweiger, G. Jeschke, *Principles of Pulse Electron Paramagnetic Resonance*, (Oxford Un. Press, Oxford, **2001**).
[202] M. Chiesa, E. Giamello, *Encyclopedia of Analytical Chemistry*, **2000**, ed. R.A. Meyers, 12040.
[203] A. Schweiger, *Angew. Chem. Int. Ed. Engl*., **1991**, 30, 265.
[204] E. L. Hahn, *Phys. Rev.*, **1950**, 80, 580.
[205] L. G. Rowan, E. L. Hahn, W. B. Mims, *Phys. Rev.*, **1965**, 137, A61.
[206] P. Höfer, A. Grupp, H. Nebenführ, M. Mehring, *Chem. Phys. Lett.*, **1986**, 132, 279.
[207] T. Spałek, P. Pietrzyk, Z. Sojka, *J. Chem. Inf. Model*., **2005**, 45, 18.
[208] S. Stoll, A. Schweiger, *J. Magn. Reson*., **2006**, 178, 42.
[209] H. Ibach, *Electron Energy Loss Spectrometers*, (Springer-Verlag, Berlin, **1991**).
[210] R. Fuchs, K. L. Kliewer, *Phys. Rev. [Sect.] A*, **1965**, 140, 2076.
[211] P. A. Cox, W. R. Flavell, A. A. Williams, *Surf. Sci*., **1985**, 152/153, 784.
[212] H. Qiu, B. Meyer, Y. Wang, Ch. Wöll, *Phys. Rev. Lett.*, **2008**, 101, 236401.
[213] K.-H. Hellwege, O. Madelung, *Landolt-Bornstein, Semiconductors Physics of II-VI and I-VII Compounds* (Springer, New York, **1987**).

[214] W. A. Harrison, *Electronic Structure and the Properties of Solids: The Physics of the Chemical Bond* (Dover, New York, **1989**).
[215] S. M. Sze, K. Ng. Kwok, *Physics of Semiconductor Devices* (Wiley, Hoboken, NJ, **2006**).
[216] K. Huang, X. D. Xie, *Physics of Semiconductors* (Science Press, Beijing, **1958**).
[217] J. A. Konvalinka, J. J. F. Scholten, *J. Catal*., **1978**, 52, 547.
[218] C. M. Chan, R. Aris, W. H. Weinberg, *Appl. Surf. Sci.*, **1978**, 1, 360.
[219] A. M. De jong, J. W. Niemantsverdriet, *Surf. Sci.*, **1990**, 233, 355.
[220] J. B. Miller, H. R. Siddiqui, S. M. Gates, J. N. Jr. Russell, J. T. Jr. Yates, J. C. Tully, M. J. Cardillo, *J. Chem. Phys.*, **1987**, 87, 6725.
[221] V. P. Zhdanov, *Surf. Sci. Rep.*, **1991**, 12, 183.
[222] L. Hanley, O. Konienko, E. T. Ada, E. Fuoco, J. L. Trevor, *J. Mass Spectr*.**, 1999**, 34, 705.
[223] J. L. Falconer, J. A. Schwarz, *Catal. Rev.-Sci. Eng.*, **1983**, 25, 141.
[224] P. A. Redhead, *Vacuum*, **1962**, 12, 203.
[225] D. A. King, T. E. Madey, J. T. Jr. Yates, *J. Chem. Phys*., **1971**, 55, 3236.
[226] J. L. Taylor, W. H. Weinberg, *Surf. Sci.*, **1978**, 78, 259.
[227] H. Qiu, *Interaction of adsorbates with clean and metal-covered oxide surfaces: Vibrational spectroscopic studies, Ph.D. Dissertation*, (Ruhr Universität Bochum, **2009**).
[228] G. Rupprechter, *Annu. Rep. Prog. Chem., Sect. C: Phys. Chem*., **2004**, 100, 237.
[229] C. J. Hirschmugl, *Surf. Sci*., **2002**, 500, 577.
[230] B. E. Hayden, *Vibrational Spectroscopy of Molecules on Surfaces*, ed. Vol. 1 J. T. Yates, T. E. Madey (Wiley, New York, **1987**).
[231] Y. J. Chabal, *Surf. Sci. Rep*., **1988**, 8, 211.
[232] F. M. Hoffmann, *Surf. Sci. Rep*., **1983**, 3, 107.
[233] J. Kattner, H. Hoffmann, *Handbook of Vibrational Spectroscopy*, ed. J. M. Chalmers and P. R. Griffiths (Wiley, Chichester, **2002**).
[234] Y. Wang, A. Glenz, M. Muhler, Ch. Wöll, *Rev. Sci. Instrum*., **2009**, 80, 113108.
[235] H. Noei, Ch. Wöll, M. Muhler, Y. Wang, *J. Phys. Chem. B*, **2011**, 1115, 908.
[236] M. Xu, Y. K. Gao, E. M. Moreno, M. Kunst, M. Muhler, Y. Wang, H. Idriss, Ch.Wöll, *Phys. Rev. Lett*., **2011**, 106, 138302.
[237] J. Kiss, D. Langenberg, D. Silber, F. Traeger, L. Jin, H. Qiu, Y. Wang, B. Meyer, C. Wöll, *J. Phys. Chem. A*, **2011**, 115, 7180.
[238] H. Noei, H. Qiu, Y. Wang, E. Löffler, Ch. Wöll, M. Muhler, *Phys. Chem. Chem. Phys*., **2008**, 10, 7092.
[239] Y. Wang, R. Kovácik, B. Meyer, K. Kotsis, D. Stodt, V. Staemmler, H. Qiu, F. Traeger, D. Langenberg, M. Muhler, Ch. Wöll, *Ang. Chem*., **2007**, 119, 5722.
[240] Y. Wang, R. Kovácik, B. Meyer, K. Kotsis, D. Stodt, V. Staemmler, H. Qiu, F. Traeger, D. Langenberg, M. Muhler, Ch. Wöll, *Ang. Chem., Int. Ed.*, **2007**, 46, 5624.
[241] H. Noei, *Vibrational Spectroscopic Studies on Adsorption and Reactions over ZnO-based Catalysts, Ph.D. Dissertation*, (Ruhr Universität Bochum, **2010**).
[242] C. Klingshirn, *Chem. Phys. Chem.*, **2007**, 8, 782.
[243] Ü. Özgür, Ya. I. Alivov, C. Liu, A. Teke, M. A. Reshchikov, S. Doğan, V. Avrutin, S.-J. Cho, H. Morkoç, *J. Appl. Phys*.**, 2005**, 98, 041301.
[244] Ch. Wöll, *Prog. Surf. Sci*., **2007**, 82, 55.
[245] C. Klingshirn, J. Fallert, H. Zhou, J. Sartor, C. Thiele, F. Maier-Flaig, D. Schneider, H.

Kalt, *Phys. Status Solidi B*, **2010**, 247, 1424.
[246] W. Hirschwald, P. Bonasewicz, L. Ernst, M. Grade. D. Hofmann, S. Krebs, R. Littbarski, G. Neumann, M. Grunze, D. Kolb, H. J. Schulz, *Curr. Top. Mater. Sci*., **1981**, 7, 143.
[247] C. H. Bates, W. B. White, R. Roy, *Science*, **1962**, 137, 993.
[248] S. Desgreniers, *Phys. Rev. B*, **1998**, 58, 14102.
[249] D. C. Reynolds, D. C. Look, B. Jogai, *Solid State Commun.*, **1996**, 99, 873.
[250] O. Madelung, *Semiconductors—Basic Data 2nd Revised Edn* (Springer, Berlin, **1996**).
[251] D. C. Look, *Mater. Sci. Eng. B*, **2001**, 80, 383.
[252] A. Janotti, C. G. Van de Walle, *Phys. Rev. B*, **2007**, 76, 165202.
[253] S. F. J. Cox, E. A. Davis, S. P. Cottrell, P. J. C. King, J. S. Lord, J. M. Gil, H. V. Alberto, R. C. Vilão, J. P. Duarte, N. A. de Campos, A. Weidinger, R. L. Lichti, S. J. C. Irvine, *Phys. Rev. Lett.*, **2001**, 86, 2601.
[254] R . Asahi, T. Morikawa, K. A. Ohwaki, Y. Yaga, *Science*, **2001**, 293, 269.
[255] Ya. I. Alivov, E. V. Kalinina, A. E. Cherenkov, D. C. Look, B. M. Ataev, A. K. Omaev, M. V. Chukichev, D. M. Bagnall, *Appl. Phys. Lett*., **2003**, 83, 4719.
[256] D. C. Look, D. C. Reynolds, C. W. Litton, R. L. Jones, D. B. Eason, G. Cantwell, *Appl. Phys. Lett*., **2002**, 81, 1830.
[257] A. Tsukazaki, A. Ohtomo, T. Onuma, M. Ohtani, T. Makino, M. Sumiya, K. Ohtani, S. F. Chichibu, S. Fuke, Y. Segawa, H. Ohno, H. Koinuma, M. Kawasaki, *Nat. Mater.*, **2005**, 4, 42.
[258] S. J. Pearton, W. H. Heo, M. Ivill, D. P. Norton, T. Steiner, *Semicond. Sci. Technol*., **2004**, 19, R59.
[259] K.-S. Ahn, T. Deutsch, Y. Yan, C.-S. Jiang, C. L. Perkins, J. Turner, M. Al-Jassim, *J. Appl. Phys*., **2007**, 102, 023517.
[260] D. J. Keavney, D. B Buchholz, Q. Ma, R. P. H. Chang, *Appl. Phys. Lett*., **2007**, 91, 012501.
[261] D. B. Buchholz, R. P. H. Chang, J. H. Song, J. B. Ketterson, *Appl. Phys. Lett*., **2005**, 87, 082504.
[262] L. Shen, R. Q. Wu, H. Pan, G. W. Peng, M. Yang, Z. D. Sha, Y. P. Feng, *Phys. Rev. B*, **2008**, 78, 073306.
[263] G. Ertl, H. Knözinger, J. Weitkamp, *Handbook of Heterogeneous Catalysis*, (Weinheim, Verlag Chemie, **1997**).
[264] C. T. Campbell, *Surf. Sci. Rep*., **1997**, 27, 1.
[265] R. Lindsay, G. Thornton, *Topics Catal*., **2002**, 18, 15.
[266] E. I. Solomon, P. M. Jones, J. A. May, *Chem. Rev*., **1993**, 93, 2623.
[267] B. Meyer, D. Marx, *Phys. Rev. B*, **2003**, 67, 035403.
[268] Y. Wang, B. Meyer, X. Yin, M. Kunat, D. Langenberg, F. Traeger, A. Birkner, C. Wöll, *Phys. Rev. Lett*., **2005**, 95, 266104.
[269] B. Meyer, D. Marx, O. Dulub, U. Diebold, M. Kunat, D. Langenberg, C. Wöll, *Ang. Chem. Int. Ed*., **2004**, 43, 6642.
[270] Y. Yan, M.M. Al-Jassim, *Phys. Rev. B*, **2005**, 72, 235406.
[271] A. Wander, N. M. Harrison, *Surf. Sci*., **2000**, 457, L342.
[272] B. Meyer, *Phys. Rev. B*, **2004**, 69, 045416.
[273] P. W. Tasker, *J. Phys. C*, **1979**, 12, 4977.
[274] M. W. Finnis, *Phys. Status Solidi A*, **1998**, 166, 397.
[275] D. C. Look, B. Claflin, *Phys. Status Solidi B*, **2004**, 241, 624.

[276] A. Janotti, C. G. Van de Walle, *Appl. Phys. Lett*., **2005**, 87, 122102.
[277] S. Lany, A. Zunger, *Phys. Rev. Lett*., **2007**, 98, 045501.
[278] C. Di Valentin, G. Pacchioni, A. Selloni, *Phys. Rev. Lett*., **2006**, 97, 166803.
[279] A. Alkauskas, P. Broqvist, A. Pasquarello, *Phys. Rev. Lett*., **2008**, 101, 046405.
[280] P. Deák, B. Aradi, T. Frauenheim, E. Janzén, A. Gali, *Phys. Rev. B*, **2010**, 81, 153203.
[281] Y. Noel, C. M. Zicovich-Wilson, B. Civalleri, Ph. D'Arco, R. Dovesi, *Phys. Rev. B*, **2001**, 65, 014111.
[282] T. Homann, U. Hotje, M. Binnewies, A. Börger, K. D. Becker, T. Bredow, *Solid State Sci*., **2006**, 8, 44.
[283] R. Pandey, J. E. Jaffe, N. M. Harrison, *J. Phys. Chem. Solids*, **1994**, 55, 1357.
[284] J. S. Binkley, J. A. Pople, W. J. Hehre, *J. Am. Chem. Soc*., **1980**, 102, 939.
[285] D. M. Hofmann, A. Hofstaetter, F. Leiter, H. Zhou, F. Henecker, B. K. Meyer, S. B. Orlinskii, J. Schmidt, P. G. Baranov, *Phys. Rev. Lett*., **2002**, 88, 045504.
[286] A. R. Hutson, *Phys. Rev*., **1957**, 108, 222.
[287] A. Janotti, C. G. Van de Walle, *Nat. Mater*., **2007**, 6, 44.
[288] D. C. Look, J. W. Hemsky, J. R. Sizelove, *Phys. Rev. Lett*., **1999**, 82, 2552.
[289] K. Hoffmann, D. Hahn, *Phys. Status Solidi A*, **1974**, 24, 637.
[290] K. Vanheusden, C. H. Seager, W. L. Warren, D. R. Tallant, J. A. Voigt, *Appl. Phys. Lett*., **1996**, 68, 403.
[291] K. Vanheusden, W. L. Warren, C. H. Seager, D. R. Tallant, J. A. Voigt, B. E. Gnade, *J. Appl. Phys*., **1996**, 79, 7983.
[292] A. Hausmann, *Z. Phys*., **1970**, 237, 86.
[293] B. K. Meyer, H. Alves, D. M. Hofmann, W. Kriegseis, D. Forster, F. Bertram, J. Christen, A. Hoffmann, M. Strassburg, M. Dworzak, U. Haboeck, A. V. Rodina, *Phys. Stat. Sol. B***, 2004**, 241, 231.
[294] J. M. Smith, W. E. Vehse, *Phys. Lett*., **1970**, 31A, 147.
[295] W.-J. Lee, J. Kang, K. J. Chang, *Phys. Rev. B*, **2006**, 73, 024117.
[296] H. Ohno, *Science*, **1998**, 281, 951.
[297] P. V. Radovanovic, D. R. Gamelin, *Phys. Rev. Lett*., **2003**, 91, 157202.
[298] P. Sharma, A. Gupta, K. V. Rao, F. J. Owens, R. Sharma, R. Ahuja, J. M. O. Guillen, B. Johansson, G. A. Gehring, *Nature Mater*., **2003**, 2, 673.
[299] M. Kroll, U. Köhler, Surf. Sci., **2007**, 601, 2182.
[300] F. Herklotz, E. V. Lavrov, J. Weber, *Physica B*, **2009**, 404, 4807.
[301] R. Dingle, *Phys. Rev. Lett*., **1969**, 23, 579.
[302] N. Can, A. Cetin, R. Kibar, M. Ayvacikli, Ch. Buchal, P. D. Townsend, A. L. Stepanov, T. Karali, S. Selvi, *Nucl. Instrum. Methods Phys. Res. B*, **2006**, 249, 474.
[303] E. Mollwo, G. Müller, P. Wagner, *Solid State Commun*., **1973**, 13, 1283.
[304] Y. Kanai, *Jpn. J. Appl. Phys*., **1991**, 30, 703.
[305] S. Lany, A. Zunger, *Phys. Rev. B*, **2009**, 80, 085202.
[306] M. Ferhat, A. Zaoui, R. Ahuja, *Appl. Phys. Lett*., **2009**, 94, 142502.
[307] D. Huang, Y.-J. Zhao, D.-H. Chen, Y.-Z. Shao, *Appl. Phys. Lett*., **2008**, 92, 182509.
[308] L. M. Huang, A. L. Rosa, R. Ahuja, *Phys. Rev. B*, **2006**, 74, 075206.
[309] L.-H. Ye, A. J. Freeman, B. Delley, *Phys. Rev. B*, **2006**, 73, 033203.
[310] X. Feng, *J. Phys.-Condens. Mat*., **2004**, 16, 4251.

[311] M. S. Park, B. I. Min, *Phys. Rev. B*, **2003**, 68, 224436.
[312] M. D. Towler, R. Dovesi, V. R. Saunders, *Phys. Rev. B*, **1995**, 52, 10150.
[313] K. Doll, N.M. Harrison, *Chem. Phys. Lett*., **2000**, 317, 282.
[314] H. Ibach, *Phys. Rev. Lett.*, **1970**, 24, 1416.
[315] B. N. J. Persson, J. E. Demuth, *Phys. Rev. B*, **1984**, 30, 5968.
[316] U. Wahl, E. Rita, J. G. Correia, E. Alves, J. G. Soares, The ISOLDE Collaboration, *Phys. Rev. B*, **2004**, 69, 012102.
[317] R. E. Dietz, H. Kamimura, M. D. Sturge, A. Yariv, *Phys. Rev*., **1963**, 132, 1559.
[318] G. Müller, R. Helbig, *J. Phys. Chem. Solids*, **1971**, 32, 1971.
[319] Y. Yan, M. M. Al-Jassim, S. H. Wei, *Appl. Phys. Lett.*, **2006**, 89, 181912.
[320] E'_{rel} is the relaxation energy for the neutral charge state in the optimal charged state geometry, as defined in Sec. 2.1.5.1.
[321] I. Broser, M. Schulz, *Solid State Commun*., **1969**, 7, 651.
[322] C. A. Bates, P. E. Chandler, *J. Phys. C*, **1971**, 4, 2713.
[323] C. A. Bates, *Proc. Phys. Soc*., **1964**, 83, 465.
[324] W. C. Zheng, L. He, Y. Mei, *Philos. Mag*., **2009**, 89, 789.
[325] S.-Y. Wu, L.-H. Wei, Z.-H. Zhang, X.-F. Wang, Y.-X. Hu, *Sprectrochim. Acta Part A*, **2008**, 71, 1307.
[326] A. Hausmann, B. Schallenberger, R. Roll, *Z. Phys. B Con. Mat*., **1980**, 40, 1.
[327] O. N. Matamura, *J. Phys. Soc. Jpn.*, **1959**, 14, 108.
[328] S. Kossmann, B. Kirchner, F. Neese, *Mol. Phys*., **2007**, 105, 2049.
[329] K. J. De Almeida, Z. Rinkevicius, H. W. Hugosson, A. C. Ferreira, H. Agren, *Chem. Phys*., **2007**, 332, 176.
[330] D. L. Hou, X. J. Ye, H. J. Meng, H. J. Zhou, X. L. Li, C. M. Zhen, G. D. Tang, *Appl. Phys. Lett*., **2007**, 90, 142502.
[331] D. Chakraborti, J. Narayan, J.T. Prater, *Appl. Phys. Lett*., **2007**, 90, 062504.
[332] T. S. Herng S. P. Lau, S. F. Yu, H. Y. Yang, X. H. Ji, J. S. Chen, N. Yasui, H. Inaba, *J. Appl. Phys*., **2006**, 99, 086101.
[333] A. Meyer, F. Pascale, C. M. Zicovich-Wilson, R. Dovesi, *Int. J. Quantum Chem*., **2010**, 110, 338.
[334] A. Markovits, M. K. Skalli, C. Minot, G. Pacchioni, N. Lòpez, F. Illas, *J. Chem. Phys*., **2001**, 115, 8172.
[335] I. de P.R. Moreira, F. Illas, R. L. Martin, *Phys. Rev. B*, **2002**, 65, 155102.
[336] I. de P.R. Moreira, R. Dovesi, *Int. J. Quantum Chem*., **2004**, 99, 805.
[337] D. Muñoz, N. M. Harrison, F. Illas, *Phys. Rev. B*, **2004**, 69, 085115.
[338] L. J. de Jongh, R. Block, *Physica B*, **1975**, 69, 568.
[339] P. Gopal, N. A. Spaldin, *Phys. Rev. B*, **2006**, 74, 094418.
[340] T. S. Herng, D.-C. Qi, T. Berlijn, J. B. Yi, K. S. Yang, Y. Dai, Y. P. Feng, I. Santoso, C. Sánchez-Hanke, X. Y. Gau, A. T. S. Wee, W. Ku, J. Ding, A. Rusydi, *Phys. Rev. Lett*., **2010**, 105, 207201.
[341] C. D. Pemmaraju, R. Hanafin, T. Archer, H. B. Braun, S. Sanvito, *Phys. Rev. B*, **2008**, 78, 054428.
[342] The energy cost to form oxygen vacancies in ZnO has been largely debated in the past. We have determined an energy cost of 3.5 eV with respect to ½ O_2. For low oxygen chemical

potentials the formation energy decreases considerably and in the limit of oxygen poor conditions it becomes even slightly negative, –0.3 eV (see Sec. 3.3.3).
[343] J. D. Cox, D. D. Wagman, V. A.Medvedev, *CODATA Key Values for Thermodynamics*, (Hemisphere, New York, **1989**).
[344] C. Sudakar, J. S. Thakur, G. Lawes, R. Naik, V. M. Naik, *Phys. Rev. B*, **2007**, 75, 054423.
[345] S. Livraghi, M. C. Paganini, E. Giamello, A. Selloni, C. Di Valentin, G. Pacchioni, G. *J. Am. Chem. Soc*., **2006**, 128, 15666.
[346] X. Chen, S. S. Mao, *Chem. Rev.*, **2007**, 107, 2891.
[347] P. Fons, H. Tampo, A. V. Kolobov, M. Ohkubo, S. Niki, J. Tominaga, R. Carboni, F. Boscherini, S. Friedrich, *Phys. Rev. Lett.*, **2006**, 96, 045504.
[348] M. Pan, J. Nause, V. Rengarajan, R. Rondon, E. H. Park, I. T. Ferguson, *J. Electron. Mater*., **2007**, 36, 457.
[349] W. Liu, S. L. Gu, J. D. Ye, S. M. Zhu, Y. X. Wu, Z. P. Shan, R. Zhang, Y. D. Zheng, S. F. Choy, G. Q. Lo, X. W. Sun, *J. Cryst. Growth*, **2008**, 310, 3448.
[350] A. Zeuner, H. Alves, D. M. Hofmann, B. K. Meyer, A. Hoffmann, U. Haboeck, M. Strassburg, M. Dworzak, *Phys. Status Solidi B*, **2002**, 234, R7.
[351] C. H. Park, S. B. Zhang, S.-H. Wei, *Phys. Rev. B*, **2002**, 66, 073202.
[352] E.-C. Lee, Y.-S. Kim, Y.-G. Jin, K. J. Chang, *Phys. Rev. B*, **2001**, 64, 085120.
[353] J. Lægsgaard, K. Stokbro, *Phys. Rev. Lett.*, **2001**, 86, 2834.
[354] K. Iwata, P. Fons, A. Yamada, K. Matsubara, S. Niki, *J. Cryst. Growth*, **2000**, 209, 526.
[355] S. Moribe, T. Ikoma, K. Akiyama, Q. Zhang, F. Saito, S. Tero-Kubota, *Chem. Phys. Lett*., **2007**, 436, 373.
[356] J. Lu, Q. Zhang, J. Wang, F. Saito, M. Uchida, *Powder Technol*., **2006**, 162, 33.
[357] J. Sann, J. Stehr, A. Hofstaetter, D. M. Hofmann, A. Neumann, M. Lerch, U. Haboeck, A. Hoffmann, C. Thomsen, *Phys. Rev. B*, **2007**, 76, 195203.
[358] W. E. Carlos, E. R. Glaser, D. C. Look, *Phys. B*, **2001**, 308–310, 976.
[359] N. Y. Garces, N. C. Giles, L. E. Halliburton, G. Cantwell, D. B. Eason, D. C. Reynolds, D. C. Look, *Appl. Phys. Lett*., **2002**, 80, 1334.
[360] N. Y. Garces, L. Wang, N. C. Giles, L. E. Halliburton, G. Cantwell, D. B. Eason, *J. Appl. Phys*., **2003**, 94, 519.
[361] G. N. Aliev, S. J. Bingham, D. Wolverson, J. J. Davies, H. Makino, H. J. Ko, T. Yao, *Phys. Rev. B*, **2004**, 70, 115206.
[362] D. Pfisterer, J. Sann, D. M. Hofmann, M. Plana, A. Neumann, M. Lerch, B. K. Meyer, *Phys. Status Solidi B*, **2006**, 243, R1.
[363] S. B. Orlinskii, J. Schmidt, E. J. J. Groenen, P. G. Baranov, C. de Mello Denegá, A. Meijerink, *Phys. Rev. Lett.*, **2005**, 94, 097602.
[364] Y. Wang, Ch. Wöll, *Surf. Sci.*, **2009**, 603, 1589.
[365] J. L. Lyons, A. Janotti, C. G. Van de Walle, *Appl. Phys. Lett.*, **2009**, 95, 252105.
[366] S. Lany, A. Zunger, *Phys. Rev. B*, **2010**, 81, 205209.
[367] G. Jeschke, R. Rachmatullin, A. Shweiger, *J. Magn. Reson*., **1998**, 131, 261.
[368] C. Gonzalez, D. Block, R. T. Cox, A. Hervé, *J. Cryst. Growth*, **1982**, 59, 357.
[369] S. Larach, J. Turkevic, *J. Phys. Chem. Solids*, **1968**, 29, 1519.
[370] T. Giavani, H. Bildsoe, J. Skibsted, H. J. Jakobsen, *J. Phys. Chem. B*, **2002**, 106, 3026.
[371] J. A. J. Fitzpatrick, F. R. Manby, C. M. Western, *J. Chem. Phys*, **2005**, 122, 084312.

[372] O. F. Schirmer, *J. Phys. Chem. Solids*, **1968**, 29, 1407.
[373] R. K. Watts, W. C. Holton, M. De Wit, *Phys. Rev. B*, **1971**, 3, 404.
[374] A. Hausmann, B. Schallenberger, *Z. Phys. B: Condens. Matter Quanta*, **1978**, 31, 269.
[375] M. Torrent, D. G. Musaev, K. Morokuma, S. C. Ke, K. Warncke, *J. Phys. Chem. B*, **1999**, 103, 8618.
[376] F. Napoli, M. Chiesa, S. Livraghi, E. Giamello, S. Agnoli, G. Granozzi, C. Di Valentin, G. Pacchioni, *Chem. Phys. Lett.*, **2009**, 477, 135.
[377] S. J. Jokela, M. D. McCluskey, *J. Appl. Phys*., **2010**, 107, 113536.
[378] S. J. Jokela, M. D. McCluskey, *Phys. Rev. B*, **2007**, 76, 193201.
[379] D. E. Nicholson, *Nature*, **1960**, 186, 630.
[380] A. A. Tsyganenko, D. V. Pozdnyakov, V. N. Filimonov, *J. Mol. Struct.*, **1975**, 29 299.
[381] I. Yasumoto, *J. Phys. Chem.*, **1984**, 88, 4041.
[382] P. R. McGill, H. Idriss, *Langmuir*, **2008,** 24, 97.
[383] E. Román, J. L. de Segovia, *Surf. Sci*., **1991**, 251/252, 742.
[384] H. Ma, Y. Berthier, P. Marcus, *Appl. Surf. Sci*., **1999**, 153, 40.
[385] M. Casarin, C. Maccato, A. Vittadini, *Chem. Phys. Lett.*, **1999**, 300, 403.
[386] M. Schiek, K. Al-Shamery, M. Kunat, F. Traeger, Ch. Wöll, *Phys. Chem. Chem. Phys.*, **2006**, 8, 1505.
[387] Z. Chang, S. Haq, G. Thornton, *Surf. Sci.*, **2000**, 467, L841.
[388] B. E. Hayden, A. King, M. A. Newton, *J. Phys. Chem. B*, **1999**, 103, 203.
[389] B. Meyer, H. Rabaa, D. Marx, *Phys. Chem. Chem. Phys.* **2006**, 8, 1413.
[390] Y. Wang, M. Muhler, Ch. Wöll, *Phys. Chem. Chem. Phys.*, **2006**, 8, 1521.
[391] M. A. Henderson, *Surf. Sci. Rep.*, **2002**, 46, 5.
[392] J. Lin, P. M. Jones, M. D. Lowery, R. R. Gay, S. L. Cohen, E. I. Solomon, *Inorg. Chem*., **1992**, 31, 686
[393] T. Hasegawa, Y. Shirotori, K. Ozawa, K. Edamoto, K. Takahashi, *Appl. Surf. Sci.*, **2004**, 237, 352.
[394] K. Ozawa, K. Edamoto, *Surf. Sci. Lett.*, **2002**, 9, 717.
[395] K. Ozawa, T. Hasegawa, K. Edamoto, K. Takahashi, M. Kamada, *J. Phys. Chem. B*, **2002**, 106, 9380.
[396] J. B. L. Martins, E. Longo, O. D. Rodríguez Salmon, V. A. A. Espinoza, C. A. Taft, *Chem. Phys. Lett.*, **2004**, 400, 481.
[397] N. H. Moreira, G. Dolgonos, B. Aradi, A. L. da Rosa, T. Frauenheim, *J. Chem. Theo. Comput.*, **2009**, 5, 605.
[398] Q. Yuan, Y.-P. Zhao, L. Li, T. Wang, *J. Phys. Chem. C*, **2009**, 113, 6107.
[399] C. C. Li, Z. F. Du, L. M. Li, H. C. Yu, Q. Wan, T. H. Wang, *Appl. Phys. Lett.*, **2007**, 91, 032101.
[400] J. B. K. Law, J. T. L. Thong, *Nanotechnology*, **2008**, 19, 205502.
[401] C. M. Zicovich-Wilson, F. Pascale, C. Roetti, V. R. Saunders, R. Orlando, R. Dovesi, *J. Comput. Chem.*, **2004**, 25, 1873.
[402] F. Pascale, S. Tosoni, C. M. Zicovich-Wilson, P. Ugliengo, R. Orlando, R. Dovesi, *Chem. Phys. Lett.*, **2004**, 396, 308.
[403] P. Ugliengo, F. Pascale, M. Mérawa, P. Labéguerie, S. Tosoni, R. Dovesi, *J. Phys. Chem. B*, **2004**, 108, 13632.

[404] J. E. Jaffe, A. C. Hess, *Phys. Rev. B*, **1993**, 48, 7903.
[405] S. C. Abrahams, J. L. Bernstein, *Acta Crystallogr., Sec. B*, **1969**, B25, 1233.
[406] T. M. Sabine, S. Hogg, *Acta Crystallogr. Sec. B*, **1969**, B25, 2254.
[407] J. M. Leger, P. E. Tomaszewski, A. Atouf, A. S. Pereira, *Phys. Rev. B*, **1993**, 47, 14075.
[408] E. H. Kisi, C. J. Howard, *Key Eng. Mat.*, **1998**, 153–154, 1.
[409] L. K. Dash, N. Vast, P. Baranek, M.-C. Cheynet, L. Reining, *Phys. Rev. B*, **2004**, 70, 245116.
[410] O. Ohtaka, H. Fukui, T. Kunisada, T. Fujisawa, K. Funakoshi, W. Utsumi, T. Irifune, K. Kuroda, T. Kikegawa, *Phys. Rev. B*, **2001**, 63, 174108.
[411] S. Desgreniers, K. Lagarec, *Phys. Rev. B*, **1999**, 59, 8467.
[412] S. Shukla, S. Seal, *Int. Mater. Rev.*, **2005**, 50, 45.
[413] K. Tanabe, T. Yamaguchi, *Catal. Today*, **1994**, 20, 185.
[414] P. Charpentier, P. Fragnaud, D. M. Schleich, E. Gehain, *Solid State Ionics*, **2000**, 135, 373.
[415] D. R. Clarke, C. G. Levi, *Annu. Rev. Mater. Res*., **2003**, 33, 383.
[416] A. Meldrum, L. A. Boatner, R. C. Ewing, *Phys. Rev. Lett*., **2002**, 88, 025503.
[417] V. Fiorentini, G. Gulleri, *Phys. Rev. Lett*., **2002**, 89, 266101.
[418] E. J. Walter, S. P. Lewis, A. M. Rappe, *Surf. Sci.*, **2001**, 95, 44.
[419] E. V. Stefanovich, A. L. Shluger, C. R. A. Catlow, *Phys. Rev. B*, **1994**, 49, 11560.
[420] S. Chen, D. Wang, M. Yu, B. Hu, X. Wang, Y. Liu, Y. Yin, *Mater. Chem. Phys.*, **2007**, 103, 28.
[421] H. Jiang, R. I. Gomez-Abal, P. Rinke, M. Scheffler, *Phys. Rev. B*., **2010**, 81, 085119.
[422] T. H. Etsell, S. N. Flengas, *Chem. Rev.*, **1970**, 70, 339.
[423] P. Li, I.-W. Chen, J. E. Penner-Hahn, *J. Am. Ceram. Soc.*, **1994**, 77, 1281.
[424] E. G. Rauh, S. P. Garg, *J. Am. Ceram. Soc.*, **1980**, 63, 239.
[425] M. Hillert, *J. Am. Ceram. Soc.*, **1991**, 74, 2005.
[426] N. Mommer, T. Lee, J. A. Gardner, *J. Mater. Res.*, **2000**, 15, 377.
[427] G.-M. Rignanese, *J. Phys.: Condens. Matter*, **2005**, 17, R357.
[428] G. Dutta, K. P. S. S. Hembram, G. M. Rao, U. V. Waghmare, *J. Appl. Phys.*, **2008**, 103, 016102.
[429] H. Zhang, B. Gao, B. Sun, G. Chen, L. Zeng, L. Liu, X. Liu, J. Lu, R. Han, J. Kang, B. Yu, *Appl. Phys. Lett.*, **2010**, 96, 123502.
[430] Y. Cong, B. Li, B. Lei, W. Li, *J. Lumin.*, **2007**, 126, 822.
[431] H. R. Chauke, P. Murovhi, P. E. Ngoepe, N. H. de Leeuw, R. Grau-Crespo, *J. Phys. Chem. C*, **2010**, 114, 15403.
[432] S. Livraghi, F. Olivero, M. C. Paganini, E. Giamello, *J. Phys. Chem. C*, **2010**, 114, 18553.
[433] R. N. Correia, J. V. Emiliano, P. Moretto, *J. Mater. Sci.*, **1998**, 33, 215.
[434] J. W. Fergus, *Solid State Ionics*, **2006**, 177, 1529.
[435] B. M. Reddy, A. Khan, *Catal. Rev.-Sci. Eng.*, **2005**, 47, 257.
[436] D. M. Ramo, P. V. Sushko, J. L. Gavartin, A. L. Shluger, *Phys. Rev. B*, **2008**, 78, 235432.
[437] C. M. Zicovich-Wilson, R. Dovesi, *J. Phys. Chem. B*, **1998**, 102, 1411.
[438] T. Bredow, M. Lerch, *Z. Anorg. Allg. Chem.*, **2004**, 630, 2262.
[439] P. J. Hay, W. R. Wadt, *J. Chem. Phys*., **1985**, 82, 299.
[440] H. J. Monkhorst, J. D. Pack, *Phys. Rev. B*, **1976**, 13, 5188.
[441] C. J. Howard, R. J. Hill, B. E. Reichert, *Acta Cristallogr., Sect. B: Struct. Sci.*, **1988**, B44,

116.
[442] R. P. Ingel, D. Lewis III, *J. Am. Ceram. Soc.*, **1986**, 69, 325.
[443] B. Králik, E. K. Chang, S. G. Louie, *Phys. Rev. B*, **1998**, 57, 7027.
[444] A. S. Foster, V. B. Sulimov, F. L. Gejo, A. L. Shluger, R. M. Nieminem, *Phys. Rev. B*, **2001**, 64, 224108.
[445] T. Bredow, *Phys. Rev. B*, **2007**, 75, 144102.
[446] R. J. Ackermann, E. G. Rauh, C. A. Alexander, *High Temp. Sci.*, **1975**, 7, 304.
[447] R. H. French, S. J. Glass, F. S. Ohuchi, Y.-N. Xu, W. Y. Ching, *Phys. Rev. B*, **1994**, 49, 5133.
[448] M. Grüning, R. Shaltaf, G.-M. Rignanese, *Phys. Rev. B*, **2010**, 81, 035330.
[449] A. S. Foster, V. B. Sulimov, F. Lopez Gejo, A. L. Shluger, R. M. Nieminem, *J. Non-Crystall. Solids*, **2002**, 303, 101.
[450] A. A. Safonov, A. A. Bagatur'yants, A. A. Korkin, *Microelectron. Eng*., **2003**, 69, 629.
[451] T. L. Thompson, J. T. Jr. Yates, *Chem Rev.*, **2006**, 106, 4428.
[452] A. Fujishima, X. Zhang, D. A. Tryk, *Surf. Scie. Rep*., **2008**, 63, 515.
[453] K. Ueda, H. Tabata, T. Kawai, *Appl. Phys. Lett.*, **2001**, 79, 988.
[454] Y. Chen, M. M. Abraham, *J. Phys. Chem. Solids*, **1990**, 51, 747.
[455] G. Pacchioni, *Nanocatalysis*, ed. U. Heiz, U. Landman, (Springer, Berlin, 193, **2006**).
[456] F. Gao, J. Hu, C. Yang, Y. Zhen, H. Qin, L. Sun, X. Kong, M. Jiang, *Solid State Commun.*, **2009**, 149, 855.
[457] E. Giamello, M. C. Paganini, D. M. Murphy, A. M. Ferrari, G. Pacchioni, *J. Phys. Chem. B*, **1997**, 101, 971.
[458] E. A. Colbourn, *Surf. Sci. Rep*., **1992**, 15, 281.
[459] M. A. Nygren, L. G. M. Pettersson, Z. Barandiaran, L. Seijo,. *J. Chem. Phys.* **1994**, 100, 2010.
[460] G. Pacchioni, C. Sousa, F. Illas, F. Parmigiani, P. S. Bagus, *Phys. Rev. B*, **1993**, 48, 11573.
[461] M. Sterrer, T. Risse, H.-J. Freund, *Appl. Cat. A: Gen*., **2006**, 307, 58.
[462] G. Spoto, E. N. Gribov, G. Ricchiardi, A. Damin, D. Scarano, S. Bordiga, C. Lamberti, A. Zecchina, *Progr. Surf. Sci*., **2004**, 76, 71.
[463] A. Zecchina, D. Scarano, S. Bordiga, G. Ricchiardi, G. Spoto, F. Geobaldo, *Catal. Today*, **1996**, 27, 403.
[464] J. R. Schlup, S. Utamapanya, K. J. Klabunde, *Chem. Mat*., **1991**, 3, 175.
[465] S. Singh, E. Knözinger, K. H. Jacob, *Surf. Sci*., **1993**, 290, 175.
[466] S. Coluccia, M. Baricco, L. Marchese, G. Martra, A. Zecchina, *Spectrochim. Acta*, **1993**, 49A, 1289.
[467] J. Hu, Z. Zhang, M. Zhao, H. Qin, M. Jiang, *Appl. Phys. Lett.*, **2008**, 93, 192503.
[468] N. Kumar, D. Sanyal, A. Sundaresan, *Chem. Phys. Lett.*, **2009**, 477, 360.
[469] C. H. Yang, M. Samant, S. Parkin, **2009** *March APS American Physical Society Meeting*, Abstract V22.00004.
[470] C. Di Valentin, G. Pacchioni, A. Selloni, *Chem. Mater.*, **2005**, 17, 6656.
[471] M. I. McCarthy, N. M. Harrison, *Phys. Rev. B*, **1994,** 49, 8574.
[472] R. C. Whited, C. J. Flaten, W. C. Walker, *Solid state Commun.*, **1973**, 13, 1903.
[473] P. V. Sushko, A. L. Shluger, C. R. A. Catlow, *Surf. Sci.*, **2000**, 450, 153.
[474] C. Di Valentin, G. Pacchioni, A. Selloni, S. Livraghi, E. Giamello, *J. Phys. Chem. B*, **2005**,

109, 11414.
[475] C. Di Valentin, G. Pacchioni, A. Selloni, A., *Phys. Rev. B*, **2004**, 70, 085116.
[476] G. Pacchioni, *Solid State Sci.*, **2000**, 2, 161.
[477] G. Pacchioni, *Chem. Phys. Chem.*, **2003**, 4, 1041.
[478] B. H. Rose, L. E. Halliburton, *J. Phys. C.: Solid State Phys.*, **1974**, 7, 3891.
[479] P. Baranek, G. Pinarello, C. Pisani, R. Dovesi, *Phys. Chem. Chem. Phys.*, **2000**, 2, 3893.
[480] A. M. Ferrari, G. Pacchioni, *J. Phys. Chem.*, **1995**, 99, 17010.
[481] L. E. Halliburton, D. L. Cowan, W. B. Blake, J. E. Wertz, *Phys. Rev. B*, **1972**, 8, 1610.
[482] P. R. Underhill, T. E. Gallon, *Solid State Commun.*, **1982**, 43, 9.
[483] G. J. Schulz, *Rev. Mod. Phys.*, **1973,** 45, 423.
[484] G. L. Gutsev, P. B. Rozyczko, R. J. Bartlett, *J. Chem. Phys*., **1999,** 110, 5137.
[485] D. G. Truhlar, *Resonances*, (Am. Chem. Soc., Washington, D.C., **1984**).
[486] R. B. Horst, J. H. D. Anderson, E. Milligan, *J. Phys. Chem. Solids*, **1962**, 26, 157.
[487] E. Gelerinter, R. H. Silsbee, *J. Chem. Phys.*, **1966**, 45, 1703.
[488] P. L. Marinkas, R. H. Bartram, *J. Chem. Phys.*, **1968**, 48, 927.
[489] J. R. Brailsford, J. R. Morton, L. E. Vannotti, *J. Phys. Chem.*, **1969**, 50, 1051.
[490] M. Chiesa, M. C. Paganini, E. Giamello, D. M. Murphy, C. Di Valentin, G. Pacchioni, *Acc. Chem. Res*., **2006**, 39, 861.
[491] E. Giamello, M. C. Paganini, M. Chiesa, D. M. Murphy, R. Soave, G. Pacchioni, A. Rockenbauer, *J. Phys. Chem. B*, **2000**, 104, 1887.
[492] M. Chiesa, E. Giamello, D. M. Murphy, G. Pacchioni, M. C. Paganini, R. Soave, Z. Sojka, *J. Phys. Chem. B*, **2001,** 105, 497.
[493] A. M. Ferrari, R. Soave, A. D'Ercole, C. Pisani, E. Giamello, G. Pacchioni, G. *Surf. Sci.* **2001**, 479, 83.
[494] D. Ricci, G. Pacchioni, P. V. Sushko, A. L. Shluger, *Surf. Sci.*, **2003,** 542, 293.
[495] P. W. Atkins, M. R. C. Symons, *The Structure of Inorganic Radicals* (Elsevier, Amsterdam, **1967**).
[496] T. Morikawa, R. Asahi, T. Ohwaki, K. Aoki, Y. Taga, *Jpn. J. Appl. Phys.*, **2001**, 40, L561.
[497] S. Livraghi, M. R. Chierotti, E. Giamello, G. Magnaccia, M. C. Paganini, G. Cappelletti, C. L. Bianchi, *J. Phys. Chem. C*, **2008,** 112, 17244.
[498] M. R. Zeller, R. T. Shuey, W. Kanzig, *J. Phys. Radium*, **1967**, 28, 81.
[499] C. Di Valentin, G. Pacchioni, *Model. Simul. in Mater. Sci. and Eng.*, **2009**, 17, 084005.